SCUOLA
NORMALE
SUPERIORE

Classe di Scienze

Corso di perfezionamento in
FISICA

XXXIV ciclo

The D(M)M perspective on Flavour Physics

Settore Scientifico Disciplinare **FIS/02**

Candidato
dr. Ludovico Vittorio

Relatore	Supervisore interno
Prof. Dario Buttazzo	Prof. Enrico Trincherini

Anno accademico 2021/2022

To my mother and my father,
who have never stopped to support me

Abstract

Flavour Physics is a a sector of physics able to test the Standard Model of elementary particles with extreme precision. In fact, in the past fifty years lots of theoretical predictions of SM parameters and Flavour observables have been found to perfectly agree with the experiments. At present, however, this does not seem to be true in two fundamental cases, both related to semileptonic flavour transitions. On the one hand, the inclusive and exclusive determinations of the Cabibbo-Kobayashi-Maskawa parameter $|V_{cb}|$ are in tension with each other. This fact is often referred to as the $|V_{cb}|$ puzzle. On the other hand, a non-negligible discrepancy holds beteween the expectations and the measurements of the so-called Flavour Anomalies $R(D^{(*)})$ and $R(K^{(*)})$, which are the τ/μ and the μ/ℓ ratios of the branching fractions of the semileptonic $B \to D^{(*)}\ell\nu$ and $B \to K^{(*)}\ell^+\ell^-$ decays, respectively.

In this Thesis we will firstly describe a novel, non-perturbative and model-independent approach, *i.e.* the Dispersive Matrix method, to describe the hadronic Form Factors entering in the semileptonic charged-current B decays. Our most important findings are that both the $|V_{cb}|$ puzzle and the $R(D^*)$ anomalies are strongly lightened by applying the Dispersive Matrix method to the $B \to D^*\ell\nu$ decays, as will be described in Part I. In particular, for what concerns the CKM matrix element, this is in complete agreement with the indirect UTfit prediction for $|V_{cb}|$.

Then, we will extend the discussion to the analysis of Beyond the Standard Model effects in Flavour Physics, mainly motivated by the strong and still remaining $R(K^{(*)})$ anomalies. In particular, in Part II we will show the impact of several flavour observables on two explicit models, the Composite Higgs scenarios and the LeptoQuarks ones. A fundamental link exists between this Part and the previous one since, as we will explicitly appreciate, in the Beyond the Standard Model studies the Standard Model parameters are directly involved, thus the most precise are the theoretical estimates of these parameters, the strongest will be the bounds on the New Physics effects eventually affecting the flavour sector.

In the last Part, we will move to the study of the phenomenology of Dark Matter. Without any doubt, explaining the origin of the Dark Matter abundance is, at present, one of the most important and intriguing challenges of theoretical physics. In Part III we will firstly analyze the proofs of the existence of Dark Matter and then we will describe in detail the Weakly Interacting Massive Particle scenario. We will then show how Dark Matter and the Flavour problem can be related. To this end, we will study another model involving the thermal decays of Dark Matter. It assumes the existence of a precise flavour structure and the introduction of the LeptoQuarks, previously described in the context of Flavour Physics, in order to generate interactions between the Dark Matter and the Standard Model particles. As we will see in detail, both these scenarios will allow us to explain the observed value of the Dark Matter abundance.

This thesis is based on the work contained in the papers [1–12].

Contents

Chapter 1

Introduction

The Standard Model of particle physics is the fundamental theory of ElectroWeak and Strong interactions. It has allowed people in the past fifty years to develop a huge series of predictions with extraordinary precision, being in complete agreement with the experiments. However, the Standard Model has to be considered an Effective Field Theory which is valid only at low energies, *i.e.* below a certain energy cutoff. In fact, there exist several issues, which we are going to divide into two distinct categories, which do not find a clear explanation in this framework. On the one hand, we have several experimental evidences of phenomena not described by the Standard Model, namely the existence of Dark Matter in the Universe, the observed asymmetry between baryons and anti-baryons and finally the problem of the non-vanishing neutrino mass. On the other hand, there are many theoretical arguments that call for an extension of the Standard Model, *i.e.* the non-inclusion of gravitational interactions in the Standard Model, the absence of a precise justification of the equality in magnitude of proton and electron charges and then the problem of Naturalness, related to the observed Higgs mass.

For all these reasons, at present there is a constant effort to look for and study possible extensions of the Standard Model, namely Beyond the Standard Model scenarios, both on the experimental side and on the theoretical one. The final goal of these efforts is thus to find an UltraViolet completion of the Standard Model, *i.e.* a more fundamental theory in which we recover the Standard Model itself at low energies. In other words, we can think of the Standard Model as a particular case of a more general theory of Nature, in which in principle new interactions and new particles may emerge at high energies.

Experimental data plays a fundamental role in this game, since they indicate the places where, in principle, New Physics effects can emerge. In this sense, without any doubt one of the most interesting fields to be investigated is Flavour Physics. Precision measurements of flavour observables allow and will constantly allow us not only to test many properties of the Standard Model, say for instance the unitarity of the Cabibbo-Kobayashi-Maskawa matrix, but at the same time to find possible deviations with respect to the theoretical predictions within the Standard Model. Any such discrepancy, in fact, can be read as a potential and clear hint of New Physics affecting low-energy processes.

In the last twenty years an increasing amount of attention has been addressed to B physics, which studies the properties of B mesons and that will be enriched by new measurements of extraordinary precision in the next decades. In this Thesis, we will first of all focus our attention on the semileptonic charged-current B decays, with particular attention given to the $B \to D^{(*)}\ell\nu$ decays. These processes are of capital importance since they allow to extract the Standard Model parameters from experimental data with high precision and, at the same time, to test possible New Physics effects. In

fact, two phenomenological problems have arisen in the recent years. On the one hand, two different measurements of the Cabibbo-Kobayashi-Maskawa matrix element $|V_{cb}|$ – the exclusive and the inclusive determinations – are in tension with each other. This issue is the so-called $|V_{cb}|$ *puzzle*. On the other hand, these $b \to c$ transitions can give evidence to the existence of Lepton Flavour Universality Violation effects, since the theoretical estimates and the measurements of the τ/μ ratios of the branching fractions of these decays are in tension to each other.

As it is valid for all the semileptonic charged-current decays of mesons and hadrons, a central role in the theoretical estimate of the decay widths is played by the hadronic Form Factors, which encode all the informations about the strong dynamics of the quarks and are only functions of the momentum transfer. The question is: can the way in which these functions are parametrized be the cause of the aforementioned tensions? This will be the topic of the first Part of this Thesis, in which we will present a novel, non-perturbative and completely model-independent way to describe the Form Factors in the whole kinematical range, by using the results of the available Lattice Quantum-ChromoDynamics computations. We anticipate that our strategy allows us to lighten both the $|V_{cb}|$ puzzle and the Lepton Flavour Universality Violation problem with respect to previous studies present in literature.

The $B \to D^{(*)}\ell\nu$ decays, however, are not the only processes characterized by tensions between theory and experiments. A possible way to explain this kind of discrepancies, when present, is to assume the existence of New Physics effects. In this case, one can pursue two different approaches, *i.e.* to study Flavour Physics under an Effective Field Theory approach, which is completely model-independent, or through explicit New Physics models. The central question is whether some type of Beyond the Standard Model physics at the TeV scale can or cannot accomodate the existing tensions in the flavour sector.

This will be the topic of the second Part of this Thesis, which will thus face Flavour Physics from a Beyond the Standard Model point of view. In fact, we will describe the New Physics effects that all the possible flavour operators, which may arise in an extension of the Standard Model, can induce on low-energy processes in Flavour Physics. We will consider many $\Delta B = 1, 2$ transitions, for instance radiative B decays and $\bar{B} - B$ mixings, in order to compute the most important experimental constraints on New Physics coming from flavour observables. Furthermore, our findings will be applied to specific Beyond the Standard Model scenarios, such as the Composite Higgs one, and we will also investigate the flavour structure that these models can have. Let us finally highlight that, as it will be repeated several times throughout this work, the first and the second Parts of this Thesis are deeply related to each other. In fact, the more precise are the theoretical estimates of the Standard Model parameters (which is the goal of each precision physics study), the more stringent will be the bounds on New Physics affecting the flavour sector.

Note that this kind of theoretical studies is of capital importance in view of the incredible improvement in luminosities expected at future colliders. To make one example, the European community has developed a Future Circular Collider (FCC) programme [13–16], in accordance to the scientific strategy promoted by CERN, which consists both in a luminosity-frontier highest-energy lepton collider and in an energy-frontier hadron collider to be built in the next decades. What will be the physics opportunities of FCC? It will allow to uniquely study the properties of the ElectroWeak gauge bosons and the Higgs field and to develop a series of precision measurements sensitive to tiny deviations from the Standard Model. Moreover, FCC will give us the possibility to observe new particles with an extension in energy with respect to LHC by a factor of ~ 6. Fundamental examples are offered by Composite Higgs and Supersymmetric models, where for instance the gluinos will be discovered up to masses of close to 20 TeV and the vector modes in CH models up to masses close to 40 TeV. Summary plots for these scenarios are given in Figure 1.1. Note that this example is clearly not exhaustive, since

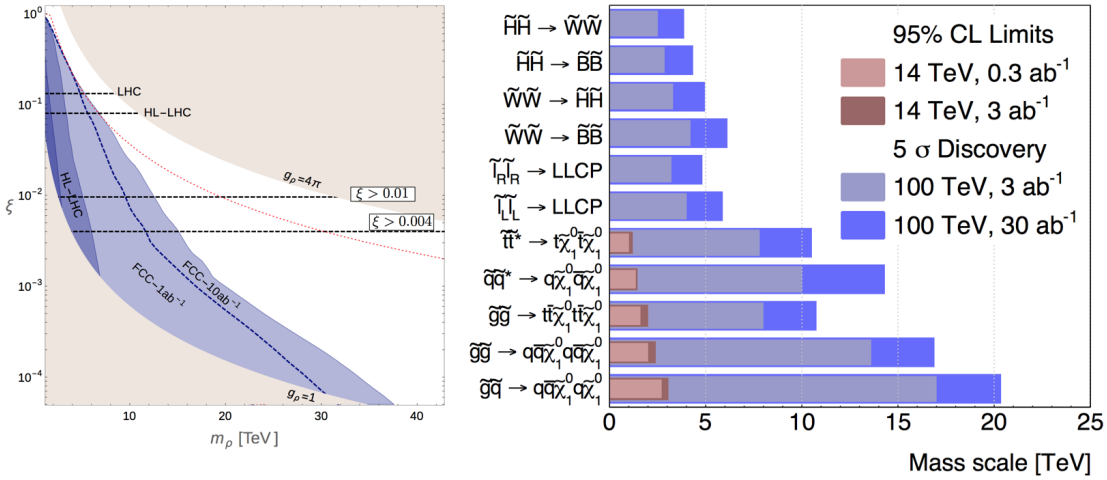

Figure 1.1: On the left side, current LHC and projected future High Luminosity LHC and FCC direct discovery reaches for heavy composite vector resonances decaying to dileptons or gauge boson pairs are shown. ξ is defined as the ratio of the Higgs vacuum expectation value and the compositeness scale. On the right side, direct FCC-hh 2σ and 5σ discovery reach for the supersymmetric sparticles are shown. Taken from [13].

many other examples of New Physics degrees of freedom, *i.e.* axions, sterile neutrinos and Z' gauge bosons, result to be affected by the direct discovery potential of FCC. Thus, for all these reasons we will investigate which will be the reach on NP coming from the future experiments in Flavour Physics and we will compare them with the prospects coming from these colliders.

A second fundamental challenge of particle physics, that also calls for an extension of the Standard Model as mentioned before, is the explanation of the observed abundance of Dark Matter in our Universe. In fact, while the existence of Dark Matter is a matter of fact, since it is confirmed by several astrophysical and cosmological probes, its nature is not clear. At present, the main hypotheses are that Dark Matter has an *elementary* or an *extended* nature.

In the third and last Part of this Thesis, we will investigate in detail the first possibility, which has attracted an incredible amount of attention from the experimental point of view in the development of direct and indirect searches for Dark Matter particles. We will firstly focus on one of the main attractive models proposed over the past decades, *i.e.* the Weakly Interacting Massive Particle (WIMP) scenario, which is able to reproduce the abundance of Dark Matter assuming its mass at the O(TeV) scale. We will try to close definitively the window on the WIMP paradigm by updating theoretical computations of their thermal masses and investigating the discovery potential of future experiments. Second, we will attempt a connection with the previous Parts of the Thesis, investigating possible relations between Dark Matter phenomenology and specific models of Flavour Physics. In this sense, we will propose a new model based on the thermal decays of Dark Matter, which is particularly intriguing since, as we will show, can be related to LeptoQuarks, new heavy degrees of freedom coupled to quarks and leptons which could have a central role in Beyond the Standard Model scenarios of flavour processes. The model of thermal decays constitutes a fundamental link between the study of Dark Matter and the one of Flavour Physics inside this Thesis, giving thus rise to an overall organic structure.

Among the various experimental strategies to look for Dark Matter particles, direct production at

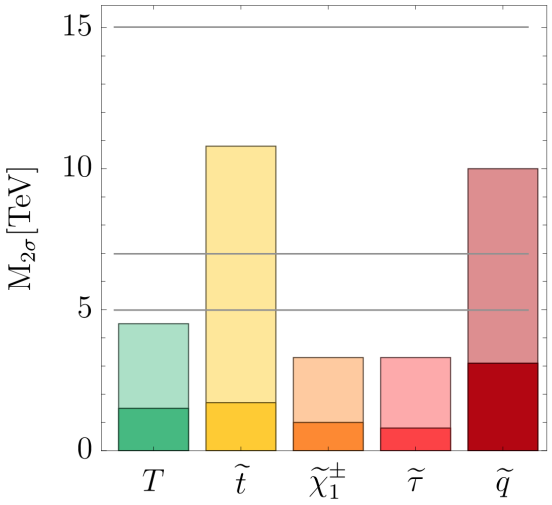

Figure 1.2: The 95% confidence level mass reach [17] for several Beyond the Standard Model particles, expected at the High Luminosity LHC (solid bars) and at the FCC proton-proton machine (shaded bars), is shown. This plot is taken from [9]. The potential discovery reach of a muon collider with center of mass energies equal to 10, 14 and 30 TeV are reported as horizontal lines.

colliders is one of the most important ones and will be deeply studied. In this Thesis, we will give particular emphasis to muon colliders [9], which are another example of the central role that future colliders will have to give a new insight on theoretical physics studies in the following decades. The muon collider strategy has to be considered as complementary to the FCC one. The fundamental idea is that muons can be made to collide in a compact ring *without* limitations coming from synchrotron radiation, while they are at the same time elementary and point-like particles. Thus, the center of mass collision energy can be entirely used to give rise to high-energy processes. Muon colliders are particularly effective in detecting ElectroWeak signals expected for purely ElectroWeak charged states. Figure 1.2, which is somehow complementary to Figure 1.1, shows this in detail. Here, the projected High Luminosity LHC mass reach and the 100 TeV FCC proton-proton collider one on several Beyond the Standard Model states are reported. Composite Higgs fermionic top-partners T and supersymmetric particles have been considered and, for each particle, the highest possible mass reach is reported. Note that the muon collider reach, displayed as horizontal lines for center of mass energies equal to 10, 14 and 30 TeV, exceeds the one of FCC for several Beyond the Standard Model candidates. A very similar example in this sense is then offered by the Weakly Interacting Massive Particles. They are perfect targets for experimental studies at muon colliders, given the pure ElectroWeak signals produced by their interactions. We will thus discuss about the important interplay existing between Dark Matter phenomenology and Collider Physics.

So, to summarize, the Thesis is organized as follows. In the first Part we will firstly investigate exclusive semileptonic B decays within the Standard Model. Then, we will extend the discussion to a more general perspective on Flavour Physics beyond the Standard Model in the second Part, analysing the relevant $\Delta F = 1, 2$ transitions both in a model-independent and in a model-dependent way. Finally, in the last Part we will focus on Dark Matter phenomenology and we will look for possible connections with Flavour Physics in the context of New Physics scenarios.

Chapter 2

The Standard Model and its flavour structure

The Standard Model (SM) of elementary particles describes three of the four fundamental forces existing in Nature, *i.e.* the strong, the weak and the electromagnetic interactions. It has been successfully tested during the past seventy years, since its theoretical predictions have been confirmed to an extraordinary level of precision and accuracy by the quasi-totality of the experiments. In this Section we will mainly review the flavour structure of the SM, specializing then the discussion on the fundamentals of the theory of ElectroWeak (EW) interactions. In this sense, the mechanism of production of the fermion masses will be presented, as well as the physical origin of the Cabibbo-Kobayashi-Maskawa (CKM) matrix and its impact on the Unitarity Triangle. Finally, we will show also the main physical properties and peculiarities of the Higgs boson.

2.1 The SM Lagrangian

The SM is characterized by a $SU(3) \times SU(2) \times U(1)$ symmetry group and the general expression of its renormalizable Lagrangian can be written as

$$\mathcal{L}_{SM} = \mathcal{L}_g + \mathcal{L}_f + \mathcal{L}_H + \mathcal{L}_Y, \tag{2.1}$$

where we have defined the following four Lagrangian substructures:

$$\begin{aligned}
\mathcal{L}_g &= -\frac{1}{4} G^a_\mu G^{a\mu\nu} - \frac{1}{4} W^b_{\mu\nu} W^{b\mu\nu} - \frac{1}{4} B_{\mu\nu} B^{\mu\nu}, && (2.2)\\
\mathcal{L}_f &= \sum_f \bar{\psi}_f i D^\mu_{(f)} \gamma_\mu \psi_f, && (2.3)\\
\mathcal{L}_H &= (D_{\mu(H)} H)^\dagger (D^\mu_{(H)} H) - V(H), && (2.4)\\
\mathcal{L}_Y &= Y^u_{ij} \bar{Q}^i_L u^j_R H^c + Y^d_{ij} \bar{Q}^i_L d^j_R H + Y^\ell_{ij} \bar{L}^i_L \ell^j_R H. && (2.5)
\end{aligned}$$

Eq. (2.2) contains the gauge interactions. $G_{\mu\nu}$, $W_{\mu\nu}$ and $B_{\mu\nu}$ are the field strength tensors for the $SU(3)$, $SU(2)$ and $U(1)$ symmetry groups, respectively, and can be expressed in terms of the single gauge fields as

$$\begin{aligned}
G^a_{\mu\nu} &= \partial_\mu g^a_\nu - \partial_\nu g^a_\mu + g_s f^{ajk}_{SU(3)} g^j_\mu g^k_\nu,\\
W^b_{\mu\nu} &= \partial_\mu W^b_\nu - \partial_\nu W^b_\mu + g_2 f^{b\alpha\beta}_{SU(2)} W^\alpha_\mu W^\beta_\nu,
\end{aligned}$$

$$B_{\mu\nu} \;=\; \partial_\mu B_\nu - \partial_\nu B_\mu .$$

$a, j, k = 1, \cdots, 8$ and $b, \alpha, \beta = 1, 2, 3$ represent, respectively, the indices in the adjoint representations of $SU(3)$ and $SU(2)$, whose structure constants are labeled as $f_{SU(3)}$ and $f_{SU(2)}$. Then, Eq. (2.3) represents all the fermions present in the SM, namely three generations of quarks and leptons. To be more specific, $f = \{Q_L^i, u_R^i, d_R^i, L_L^i, \ell_R^i\}$ (i is the generation index), where the Q_L^i represent the left-handed $SU(2)$ quark doublets, the u_R^i the d_R^i are the right-handed up-type and down-type quarks, the L_L^i represent the left-handed $SU(2)$ lepton doublets and finally the ℓ_R^i are right-handed leptons. We have also defined the covariant derivative $D^\mu_{(f)} \equiv \partial^\mu - ig_s g^{\mu a} \mathcal{T}^{a(f)} - ig_2 W^{\mu i} T^{i(f)} - ig_1 Y^{(f)} B^\mu$, where $\mathcal{T}^{a(f)}$ and $T^{i(f)}$ are the $SU(3)$ and $SU(2)$ generators in the representation chosen for the fermion ψ_f and $Y^{(f)}$ is its hypercharge. Eq. (2.4) describes the Higgs boson H, which is a scalar $SU(2)$ doublet with unit hypercharge. Thus, the covariant derivative here reads $D^\mu_{(H)} \equiv \partial^\mu - ig_2 W^{\mu\, i} \tau^i/2 - ig_1 B^\mu/2$, where τ^i ($i = 1, 2, 3$) are the Pauli matrices. $V(H)$ represents the Higgs potential, whose explicit expression can be found in the following Section. Finally, Eq. (2.5) describes the Yukawa interactions, where we have introduced the Yukawa matrices Y^u_{ij}, Y^d_{ij}, Y^ℓ_{ij} and we have defined $H^c \equiv i\sigma^2 H^*$.

Since it will be of fundamental importance in this Thesis, let us focus our attention on the flavour quantum numbers of the fields involved in the SM Lagrangian (2.1). The fermion part (2.3), the Higgs one (2.4) and the gauge one (2.2) are invariant under a global $U(3)_{Q_L} \times U(3)_{u_R} \times U(3)_{d_R} \times U(3)_{L_L} \times U(3)_{\ell_R}$ symmetry group, often referred to as $U(3)^5$ symmetry group. This is not true for the Yukawa terms (2.5). In fact, focusing for instance on the quark case, the Yukawa couplings break the $U(3)_{Q_L} \times U(3)_{u_R} \times U(3)_{d_R} \equiv U(3)^3$ group to the $U(1)_B$ one, which corresponds to the conservation of the baryonic number B.

2.2 ElectroWeak Interactions in the Standard Model

In this Section we will review the main properties of the ElectroWeak (EW) interactions within the SM. In particular, we will investigate the phenomenon of ElectroWeak Symmetry Breaking (EWSB), which is responsible for giving mass to SM fermions. In what follows, we will specialize our discussion only on the quark sector. We will also mention the origin and the physical meaning of the Cabibbo-Kobayashi-Maskawa (CKM) matrix.

2.2.1 Quark mixing and mass terms

In the previous Section 2.1, we have reviewed the matter content of the SM. A brief summary of the SM fermions can be found in Table 2.1, where we have specified their quantum numbers under the SM $SU(3) \times SU(2) \times U(1)$ symmetry group. Note that the hypercharge Y can be found through the simple relation

$$Q = \frac{Y}{2} + I_3,$$

where Q is the electric charge of a given particle and I_3 is the third component of the weak isospin.

It is clear from Table 2.1 that the quantum numbers of the quarks through the three generations are exactly the same. In fact, the physical property that allows us to distinguish them one from another is the mass. The Particle Data Group [18] quotes the following values:

$$\mathrm{m_u} = 2.16^{+0.49}_{-0.26}\,\mathrm{MeV}, \quad \mathrm{m_c} = 1.27 \pm 0.02\,\mathrm{GeV}, \quad \mathrm{m_t} = 172.76 \pm 0.30\,\mathrm{GeV},$$

$$\mathrm{m_d} = 4.67^{+0.48}_{-0.17}\,\mathrm{MeV}, \quad \mathrm{m_s} = 93^{+11}_{-5}\,\mathrm{MeV}, \quad \mathrm{m_b} = 4.18^{+0.03}_{-0.02}\,\mathrm{GeV}.$$

	SU(3)	SU(2)	U(1)
Q_L	**3**	**2**	+1/6
u_R	**3**	**1**	+2/3
d_R	**3**	**1**	-1/3
L_L	**1**	**2**	-1/2
ℓ_R	**1**	**1**	-1

Table 2.1: Quantum numbers of the SM fermions.

The u-, d- and s-quark masses are estimated in the $\overline{\text{MS}}$ scheme at a scale $\mu \approx 2\,\text{GeV}$, while the c- and the b-quark masses are the "running" masses in the same scheme [18]. Moreover, note that the value of the top mass is based on published direct measurements.

But how are these masses generated within the SM? The answer to this question is given by the so-called *Brout-Englert-Higgs mechanism* [19–21]. We start from the Higgs field H, which has been introduced in Eq. (2.5). We recall that the Higgs is a scalar weak isospin doublet with hypercharge $Y = 1$, which can be written as

$$H = \begin{pmatrix} \phi^+ \\ \phi^0 \end{pmatrix} = \begin{pmatrix} \frac{\pi_1 + i\pi_2}{\sqrt{2}} \\ \frac{v+\sigma+i\pi_3}{\sqrt{2}} \end{pmatrix}. \tag{2.6}$$

The complex fields ϕ^+ and ϕ^0 are the two components of the isospin doublet and can be expressed in terms of the real fields σ and $\vec{\pi} = (\pi_1, \pi_2, \pi_3)$. In Eq. (2.6) we have made explicit the Higgs expectation value $v \simeq 246\,\text{GeV}$ at the minimum of the potential

$$V(H) \equiv -\frac{\mu^2}{2} H^\dagger H + \frac{\lambda}{4!}(H^\dagger H)^2. \tag{2.7}$$

In this way, σ and $\vec{\pi}$ have a precise physical meaning: they represent the fluctuations of the field around this stationary point. Finally, by using the expression (2.6) we can re-write the weak isospin doublet H_c (appearing in Eq. (2.5)), which has hypercharge $Y = -1$, as

$$H_c \equiv (i\sigma_2)H^* = \begin{pmatrix} \phi^{0*} \\ -\phi^+ \end{pmatrix} = \begin{pmatrix} \frac{v+\sigma-i\pi_3}{\sqrt{2}} \\ -\frac{\pi_1+i\pi_2}{\sqrt{2}} \end{pmatrix}, \tag{2.8}$$

At this point, the EWSB allows us to give mass to the quarks. To see this, it is sufficient to set $\sigma = \vec{\pi} = 0$ (keeping only $v \neq 0$) and then re-express the Yukawa Lagrangian terms (2.5) as

$$\mathcal{L}_M = m^u_{ij} \bar{u}^i_L u^j_R + m^d_{ij} \bar{d}^i_L d^j_R + \text{h.c.} \tag{2.9}$$

The mass matrices m^u_{ij} and m^d_{ij} will be, in general, non-diagonal. One can show that, however, we can diagonalize a generic matrix A by using two unitary matrices. Hence, the diagonal form A_{diag} is related to the original one A through the relation

$$A_{\text{diag}} = U_L^\dagger A U_R \tag{2.10}$$

where the unitarity matrices U_L and U_R respect by definition the relations

$$U_L U_L^\dagger = I, \quad U_R U_R^\dagger = I.$$

Furthermore, one can also isolate all the phases eventually present in $A_{\rm diag}$ in order to make it a real matrix with all the eigenvalues positive-definite. This simple argument allows us to obtain the physical masses of the up-type and down-type quarks of each of the three generations through the diagonalization of the mass matrices m^u_{ij} and m^d_{ij}, namely

$$U^u_L m^u m^{u\dagger} U^{u\dagger}_L = U_R m^{u\dagger} m^u U^\dagger_R = (m^u_{\rm diag})^2, \tag{2.11}$$

$$U^u_L m^u U^{u\dagger}_R = m^u_{\rm diag}. \tag{2.12}$$

Analogous equations hold in the down-type quark sector.

2.2.2 The Cabibbo-Kobayashi-Maskawa matrix

The unitarity transformations induced by the matrices $U^{\{u,d\}}_L$ and $U^{\{u,d\}}_R$ have a precise impact on the quark fields. In particular, they allow us to define a *mass eigenstate* basis where

$$\tilde{u}_{L,R} = U^u_{L,R} u_{L,R}, \quad \tilde{d}_{L,R} = U^d_{L,R} d_{L,R}. \tag{2.13}$$

The important feature of these transformations is that they rotate quarks with different electric charges and with different chiralities in different ways. Note that, for the left-handed fermions, we can re-express the above transformations as

$$\tilde{u}_L = V_{CKM} U^d_L u_L, \quad \tilde{d}_L = U^d_L d_L, \tag{2.14}$$

where we have introduced the unitary *Cabibbo-Kobayashi-Maskawa* (CKM) matrix [22, 23] in the following way

$$V_{CKM} \equiv U^u_L U^{d\dagger}_L. \tag{2.15}$$

The physical meaning of the CKM matrix is clear from Eq. (2.15): it describes *quark mixing* in EW interactions. For this reason, the usual way to write it is

$$V_{CKM} = \begin{pmatrix} V_{ud} & V_{us} & V_{ub} \\ V_{cd} & V_{cs} & V_{cb} \\ V_{td} & V_{ts} & V_{tb} \end{pmatrix}. \tag{2.16}$$

Clearly, the dimension of this matrix depends on the number of existing quark generations and it can be described by four different parameters. This last point can be understood through the following argument. In the most general situation of a NxN unitary matrix, we have $N(N-1)/2$ Euler angles and $N^2 - N(N-1)/2 - (2N-1)$ independent phases. Setting $N = 3$, we are left with three Euler angles, that we will call θ_{12}, θ_{13} and θ_{23}, and one independent phase, which will be denoted as δ. Thus, an alternative parametrization of the matrix (2.16) is

$$V_{CKM} = \begin{pmatrix} C_{12}C_{13} & S_{12}C_{13} & S_{13}e^{-i\delta} \\ -S_{12}C_{23} - C_{12}S_{13}S_{23}e^{i\delta} & C_{12}C_{23} - S_{12}S_{13}S_{23}e^{i\delta} & S_{23}C_{13} \\ S_{12}S_{23} - C_{12}S_{13}C_{23}e^{i\delta} & -C_{12}S_{23} - S_{12}S_{13}C_{23}e^{i\delta} & C_{23}C_{13} \end{pmatrix} \tag{2.17}$$

where we have defined $C_{12} = \cos\theta_{12}$, $S_{12} = \sin\theta_{12}$ and so analogously for the other couples of subscripts. This formulation, often called the *standard parametrization*, emphazises that the CKM matrix is very similar to the identity one. In fact, the Euler angles have been experimentally measured and they have low values. From a mathematical point of view, the limit of zero angles brings exactly to $V_{CKM} = I$. As suggested by the presence of the phase δ, the 3x3 CKM matrix is in general

complex. In particular, if $\delta \neq 0$ there is a violation of CP symmetry in EW interactions. In fact, one can verify this statement by applying a CP transformation on the mass terms in Eq. (2.9) before the quark rotations (2.13)-(2.14). CP invariance is preserved only if the mass matrix is real. In this way, we have transferred the criterion for CP violation from the mass matrix to the CKM matrix.

Another possible way to describe the CKM matrix is offered by the so-called *Wolfenstein parametrization* [24]. The physical hint at the basis of this alternative formulation is that, since $S_{13} \ll S_{23} \ll S_{12} \ll 1$, it is reasonable to develop a perturbative expansion in powers of S_{12}. To be more specific, we introduce four new parameters λ, A, η and ρ, defined as

$$\begin{aligned} \lambda &\equiv S_{12} \simeq V_{us}, \\ A\lambda^2 &\equiv S_{23} \simeq V_{cb}, \\ A\lambda^3(\rho - i\eta) &\equiv S_{13}e^{-i\delta} \simeq V_{ub}, \end{aligned}$$

where the last relation holds for small δ. By putting all the ingredients together, we have the new form

$$V_{CKM} = \begin{pmatrix} 1-\lambda^2/2 & \lambda & A\lambda^3(\rho - i\eta) \\ -\lambda & 1-\lambda^2/2 & A\lambda^2 \\ A\lambda^3(1-\rho-i\eta) & -A\lambda^2 & 1 \end{pmatrix} + O(\lambda^4), \tag{2.18}$$

from which it is now evident that CP non-conservation is condensed in the terms of order λ^3 or higher. In conclusion, we can also consider higher order corrections in Eq.(2.18). By way of example, including terms $O(\lambda^5)$ we obtain the expression

$$V_{CKM} = \begin{pmatrix} 1-\lambda^2/2-\lambda^4/8 & \lambda + O(\lambda^7) & A\lambda^3(\rho - i\eta) \\ -\lambda + A^2\lambda^5[1-2(\rho+i\eta)]/2 & 1-\lambda^2/2-\lambda^4(1+4A^2)/8 & A\lambda^2 + O(\lambda^8) \\ A\lambda^3(1-\bar{\rho}-i\bar{\eta}) & -A\lambda^2 + A\lambda^4[1-2(\rho+i\eta)]/2 & 1-A^2\lambda^4/2 \end{pmatrix} \tag{2.19}$$

where $\bar{\rho}$ and $\bar{\eta}$ are slightly modified versions of the Wolfenstein parameters ρ and η and are related to them through the relations

$$\bar{\rho} = \left(1 - \frac{1}{2}\lambda^2\right)\rho, \quad \bar{\eta} = \left(1 - \frac{1}{2}\lambda^2\right)\eta. \tag{2.20}$$

2.2.3 The Unitarity Triangle

The unitarity of the CKM matrix (namely $V_{CKM}^\dagger V_{CKM} = I$) allows us to write down several orthogonality relations. Recalling Eq. (2.16), an example is offered by the relation

$$V_{ub}^* V_{ud} + V_{cb}^* V_{cd} + V_{tb}^* V_{td} = 0. \tag{2.21}$$

As the CKM matrix is in general complex, this expression can be interpreted as the sum of three vectors in the $(\bar{\rho}, \bar{\eta})$ complex plane. These vectors can be mapped in a *triangle*. The sides, the angles and also the area of the this triangle are physical quantities at all the effects, since their are invariant under an arbitrary change of phases of the quark fields.

To be more specific, the angles are defined in the following way:

$$\alpha \equiv \arg[-V_{td}V_{ub}V_{ud}^*V_{tb}^*] = \arg(-Q_{ubtd}), \tag{2.22}$$

$$\beta \equiv \arg[-V_{cd}V_{tb}V_{cb}^*V_{td}^*] = \arg(-Q_{tbcd}), \tag{2.23}$$

$$\gamma \equiv \arg[-V_{ud}V_{cb}V_{ub}^*V_{cd}^*] = \arg(-Q_{cbud}). \tag{2.24}$$

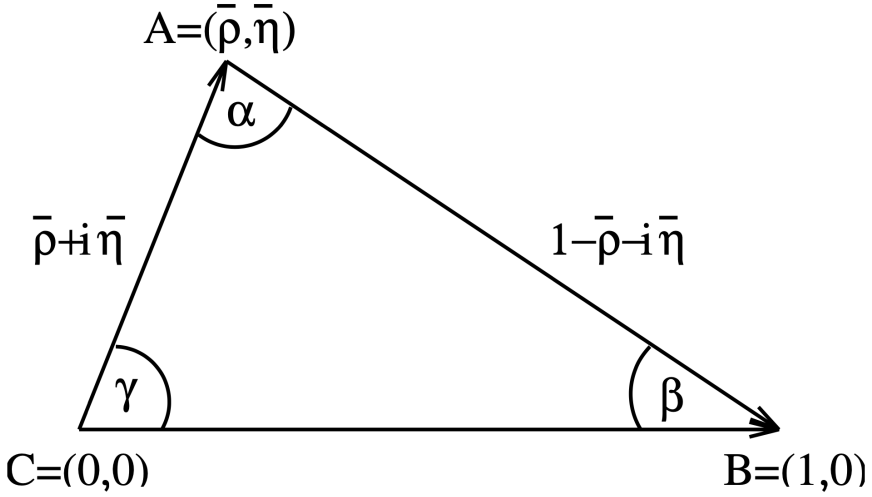

Figure 2.1: The unitarity triangle (2.21).

The quartets $Q_{\rho i \sigma j}$ are rephasing invariant quantities, defined as

$$Q_{\rho i \sigma j} \equiv V_{\rho i} V_{\sigma j} V^*_{\rho j} V^*_{\sigma i}, \quad \rho \neq \sigma,\, i \neq j. \tag{2.25}$$

The above angles, which satisfy the simple relation $\alpha+\beta+\gamma = \pi$, allows us to write down the equation of the unitarity triangle by taking the relation (2.21) and dividing it by the $V_{cd}V^*_{cb}$ term, obtaining

$$-\frac{V_{ud}V^*_{ub}}{V_{cd}V^*_{cb}} - \frac{V_{td}V^*_{tb}}{V_{cd}V^*_{cb}} = R_b e^{i\gamma} + R_t e^{-i\beta} = 1 \simeq (\bar\rho + i\bar\eta) + (1 - \bar\rho - i\bar\eta). \tag{2.26}$$

The graphical representation of the triangle can be found in Figure 2.1. Note that in the previous expression we have also defined the quantities

$$R_b \equiv |\frac{V_{ud}V^*_{ub}}{V_{cd}V^*_{cb}}| = \sqrt{\bar\rho^2 + \bar\eta^2}, \quad R_t \equiv |\frac{V_{td}V^*_{tb}}{V_{cd}V^*_{cb}}| = \sqrt{(1-\bar\rho)^2 + \bar\eta^2}.$$

Finally, the area is directly related to CP violation in EW decays. First of all, recalling Eq.(2.21), we can multiply this expression by $V^*_{cd}V_{cb}$ and, then, take the imaginary parts. In this way we obtain that

$$\mathrm{Im}\, Q_{udcb} = -\mathrm{Im}\, Q_{cbtd}.$$

Considering all the orthogonality relations, we find also that the imaginary parts of all the quartets are equal, up to a sign. Thus, in the Standard Model $|\mathrm{Im}\, Q\,|$ gives the strenght of CP violation. Secondly, we are interested in computing the area A_Δ of the unitarity triangle in Figure 2.1. As the height h of this triangle is given by

$$h = |V_{ud}V^*_{ub}| \sin\gamma,$$

we have that

$$A_\Delta = \frac{|V_{cd}V^*_{cb}| \times h}{2} = \frac{1}{2}|\mathrm{Im}\, Q_{udcb}\,|. \tag{2.27}$$

Thus, since all the $|\mathrm{Im}\, Q\,|$ are equal, all the unitarity triangles have the same area. Moreover, their area is a precise and quantitative test of CP non-conservation in EW decays.

2.2.4 Masses of the gauge bosons and weak interactions after EWSB

As explained before, EWSB is realized by setting $\sigma = \vec{\pi} = 0$ (keeping only $v \neq 0$) in Eqs. (2.6) and (2.8). In addition to the fermion masses, EWSB allows us to give masses to the gauge bosons. By expanding the covariant derivatives in the Higgs Lagrangian (2.4), one can demonstrate that the expressions of the $W^{\pm}$ and Z bosons read

$$m_W^2 = \frac{g^2 v^2}{4}, \quad m_Z^2 = \frac{m_W^2}{\cos^2\theta_w}, \tag{2.28}$$

where we have introduced the weak mixing angle θ_w, whose sine and cosine can be expressed as

$$\sin\theta_w = \frac{g_1}{\sqrt{g_1^2+g_2^2}}, \quad \cos\theta_w = \frac{g_2}{\sqrt{g_1^2+g_2^2}}.$$

After the EWSB previously discussed, we can also write down the following interaction terms in the Lagrangian:

$$\mathcal{L}_{int} = -\frac{g_2}{\sqrt{2}}\left(W^{+\mu} J_{\mu,\text{charged}} + W^{-\mu} J^{\dagger}_{\mu,\text{charged}}\right) - g_1 \cos\theta_W A^{\mu} J_{\mu,\text{EM}} - \frac{g_2}{\cos\theta_W} Z^{\mu} J_{\mu,\text{neutral}} \tag{2.29}$$

where the electro-magnetic, the neutral and the charged currents are defined as

$$J^{\mu}_{\text{EM}} = \sum_f Q_f \bar{f}_i \gamma^{\mu} f_i, \tag{2.30}$$

$$J^{\mu}_{\text{neutral}} = \sum_f \left[(I_{3f} - Q_f \sin^2\theta_W)\bar{f}^i_L \gamma^{\mu} f^i_L - Q_f \sin^2\theta_W \bar{f}^i_R \gamma^{\mu} f^i_R\right], \tag{2.31}$$

$$J^{\mu}_{\text{charged}} = \bar{u}^i_L V^{ij}_{CKM} \gamma^{\mu} d^j_L + \bar{\nu}^i_L \gamma^{\mu} \ell^i_L, \tag{2.32}$$

respectively. Note that in the above Equations the quark fields are described in the basis of the mass eigenstates (2.14).

In conclusion, in Eq. (2.29) a key feature of the SM emerges: while the weak neutral currents are invariant under the transformations defined in Eq. (2.13), the weak charged ones are modified by the rotations induced by the unitarity matrices U_L and U_R. In fact, these interactions couple quarks with different electric charges. Thus, the Flavour Changing Charged Currents (FCCCs) are proportional to the CKM matrix and are generated at tree-level, while the Flavour Changing Neutral Currents (FCNCs) are present only at loop level.

2.3 The properties and the misteries of the Higgs boson

As clear from the previous Sections, the Higgs boson, defined in Eq. (2.6), has a central role in the SM since it gives masses to the elementary particles through the EWSB. In the summer of 2012, an extraordinary discovery for High Energy Physics has been achieved: a new scalar particle with the mass of 125 GeV has been observed for the first time at LHC [25, 26]. This was precisely the Higgs boson. From the theoretical point of view, this has determined the triumph of the Brout-Englert-Higgs mechanism of the mass generation of the SM particles. At the same time, this discovery has given rise to one of the fundamental problems of the SM, *i.e.* the *Naturalness* issue or *hierarchy problem*.

A naïve explanation of this problem is offered by an Effective Field Theory (EFT) approach to the SM, that will be reviewed in depth in the following Chapter for its application to Flavour Physics.

The basic idea is that the SM is an *effective* theory of Nature, valid only at infrared (IR) energies. A more general theory of Nature, which is identical to the SM in the limit of low energies, thus exists. From the formal point of view, after having defined an ultraviolet (UV) energy scale as $\Lambda_{\rm UV}$ (*i.e.* the energy scale at which new particles/interactions arise), we can then express the SM Lagrangian as

$$\mathcal{L}_{\rm SM,eff} = \sum_i C_i \Lambda_{\rm UV}^{4-d_i} \mathcal{O}_i, \tag{2.33}$$

where each SM operator $\mathcal{O}_i$ has dimension d_i and is accompanied by a specific Wilson Coefficient (WC) C_i. The Higgs mass term, that we have written in the r.h.s. of Eq. (2.7), is the *only* operator in the SM having dimension 2. Hence, from an EFT point of view it will be enhanced by a factor $\Lambda_{\rm UV}^2$. Since the experiments tell us that the Higgs mass is 125 GeV, if the UV scale is very high the only way to recover the measured value is to impose a very small WC. In order words, a non-negligible *fine tuning* emerges. To be more specific with numbers, we would have to require $C \sim 10^{-28}$ for $\Lambda_{\rm UV}$ equal to the Grand Unification Theory (GUT) scale, namely $\Lambda_{\rm UV} \sim 10^{16}$ GeV. This issue is also referred to as the *radiative instability* of the Higgs.

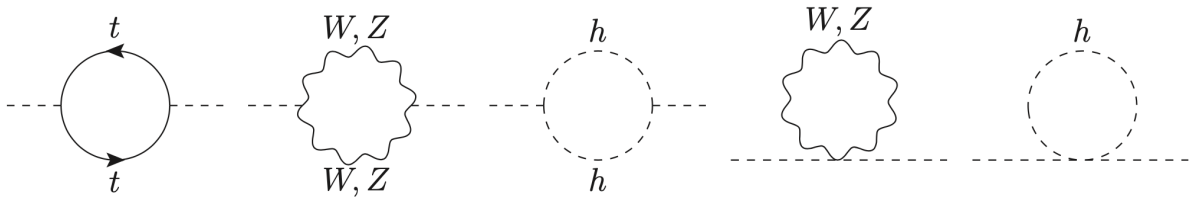

Figure 2.2: The SM loops contributing to the Higgs boson mass.

There is an alternative way to approach the problem of the radiative instability of the Higgs, that we are going to briefly mention. As we have explained in the previous Sections, EWSB is necessary to give a mass to the SM particles since the mass terms for these degrees of freedom are forbidden by the SM $SU(2) \times U(1)$ symmetry. For this reason, the masses of both fermions and vectors are proportional to the Higgs expectation value $v \simeq 246\,\text{GeV}$, since they have to vanish if we recover the $SU(2) \times U(1)$ symmetry. This proportionality holds also at loop-level since it comes from a symmetry argument, thus we can state that all the SM masses are protected from hypothetical uncontrolled radiative corrections. This argument is *not* true for the Higgs boson, which is the only scalar particle of the SM and has no symmetry protecting its mass term from being large. In other words, the Higgs mass is subject to radiative corrections which are proportional to the masses of the particles inside the loops. At this point, note that in the SM the only one-loop contributions to the Higgs mass are the ones in Figure 2.2. However, if new heavy degrees of freedom arise at an UV scale $\Lambda_{\rm UV}$, new diagrams will appear in addition to the SM ones. Following a Renormalization Group (RG) argument, one can demonstrate that a precise relation exists between the SM Higgs mass and the Higgs mass at the scale $\Lambda_{\rm UV}$, namely

$$m_h^2(\Lambda_{\rm IR}) \simeq m_h^2(\Lambda_{\rm UV}) - \kappa \Lambda_{\rm UV}^2 \log\left[\frac{\Lambda_{\rm UV}}{\Lambda_{\rm IR}}\right], \tag{2.34}$$

where $\Lambda_{\rm IR}$ is the typical low energy scale at which the SM is the correct theory of Nature and κ is an appropriate numerical factor that comes from the RG equations. Also in this formulation a non-negligible fine tuning arises, since, if the UV scale is very high, a very precise cancellation among the two terms in the r.h.s. of Eq. (2.34) is needed in order to obtain the measured Higgs mass.

In order to solve the hierarchy problem, one has to invoke the existence of New Physics (NP) effects arising at the TeV scale. The NP models of interest can be either weakly or strongly coupled. On the one hand, the major example of the first kind of scenarios is, without any doubt, Supersymmetry (SUSY). In this case, the loop quadratic divergences will be zero thanks to the presence of the sparticle loops. Thus, no radiative instability is present in this case. On the other hand, another possible solution, belonging to the second class of NP models, is offered by Composite Higgs (CH) theories. In this case, the assumption is that the Higgs boson is *not* an elementary field, but instead a composite bound state of a new strongly interacting sector. Since it is a bound state, in this case the Higgs will not be sensitive to UV effects, thus being free of the radiative instability problem. The CH scenarios will be more deeply investigated in Part II of this Thesis. To conclude, note that in both these examples, a symmetry has been introduced - supersymmetry, and the shift symmetry of Goldstone bosons - that protects the Higgs mass term from radiative corrections.

Part I

Flavour Physics Within the Standard Model

Chapter 3

The role of the Form Factors in $B \to D^{(*)}\ell\nu$ decays

In this Part, we will analyze in detail the semileptonic decays of the B mesons *i.e.* transitions whose final states are characterized by the presence of both leptons and hadrons. We will focus our attention on the FCCC processes, which, as explained in Chapter 2, are proportional to and thus offer the opportunity to determine the CKM matrix elements, which are free parameters of the SM. In this Chapter, we will focus on the *heavy-to-heavy* semileptonic B meson decays, namely $B \to D^{(*)}\ell\nu$ transitions (where ℓ denotes a generic lepton). In particular, we will illustrate the state-of-the-art and the central role of the hadronic Form Factors for phenomenology. Moreover, we will introduce and deeply describe a new method to describe them in the whole kinematical range.

3.1 The $|V_{cb}|$ puzzle and the $R(D^{(*)})$ anomalies

At present, exclusive semileptonic $B \to D^{(*)}\ell\nu$ decays are among the most important and challenging processes in the phenomenology of flavour physics. In fact, they allow to determine the SM parameters with high precision. In this sense, there are two reasons that justify their importance.

On the one hand, we have the so-called $|V_{cb}|$ *puzzle*, *i.e.* the tension between the inclusive [27–30] and the exclusive values of the CKM matrix element $|V_{cb}|$ [31–38]. Very synthetically, the difference between these two determinations is that, while the inclusive one comes from $B \to X_c\ell\nu$ decays, where X_c is a generic charmed meson (in other words, we are taking into consideration all possible final charmed mesons), the exclusive one is measured by choosing a specific B decay channel into a charmed meson. To be more specific, we can obtain exclusive estimates of $|V_{cb}|$ from different decay channels, *i.e.* $B \to D^{(*)}\ell\nu$, $B_s \to D_s^{(*)}\ell\nu$, $B \to J/\psi\ell\nu$ and finally $\Lambda_b \to \Lambda_c\ell\nu$. Note that in principle there are also further transitions that can be considered to this end, namely the ones involving excited mesons and baryons. Following the last 2021 report by the FLAG Collaboration [39], we have that $|V_{cb}|_{\text{excl}} \times 10^3 = 39.36 \pm 0.68$ (computed from $B \to D^{(*)}\ell\nu$ decays), while the last inclusive determination [30] corresponds to $|V_{cb}|_{\text{incl}} = 42.16 \pm 0.50$. Thus, a $\sim 3.3\sigma$ discrepancy exists between these two estimates.

On the other hand, a discrepancy exists between the theoretical expectation value and the measurements of the ratios $R(D^{(*)})$ [40], which are defined as

$$R(D^{(*)}) \equiv \frac{\Gamma(B \to D^{(*)}\tau\nu)}{\Gamma(B \to D^{(*)}\ell\nu)}, \tag{3.1}$$

where ℓ is a light lepton ($\ell = e, \mu$). The state-of-the-art for the $R(D^{(*)})$ anomalies can be seen in Figure 3.1, where the red area represents the average of all the measurements performed by Belle, BaBar and LHCb [41–49]. HFLAV quotes the following values for this average:

$$R(D)_{\text{exp}} = 0.339 \pm 0.026 \pm 0.014, \quad R(D^*)_{\text{exp}} = 0.295 \pm 0.010 \pm 0.010, \tag{3.2}$$

where the first error is statistical, while the second one is systematic. For what concerns the theoretical expectations, HFLAV takes into consideration the results of the computations in [50–52]. The first two results bring to the black cross in Figure 3.1, while the last one is the blue cross. The arithmetic average in this case is:

$$R(D)_{\text{th}} = 0.298 \pm 0.003, \quad R(D^*)_{\text{th}} = 0.252 \pm 0.005. \tag{3.3}$$

By comparing the Eqs. (3.2)-(3.3), one can see that $R(D)$ and $R(D^*)$ exceed the SM predictions by 1.4σ and 2.9σ, respectively. Considering the $R(D)$-$R(D^*)$ correlation of -0.38, the total difference with the SM predictions reported above corresponds to about 3.4σ.

Note that the ratios $R(D^{(*)})$ have a precise physical meaning, namely they are a test of Lepton Flavour Universality (LFU), which is one of the pillars of the SM. According to this principle, all the three types of charged lepton particles (namely the electrons, the muons and the taus) interact in the same way with the gauge bosons, independently of their generation. In other words, in the SM the gauge interactions are LFU. Any hint of violation of this principle can thus be interpreted, in a very clear way, as a hint of New Physics.

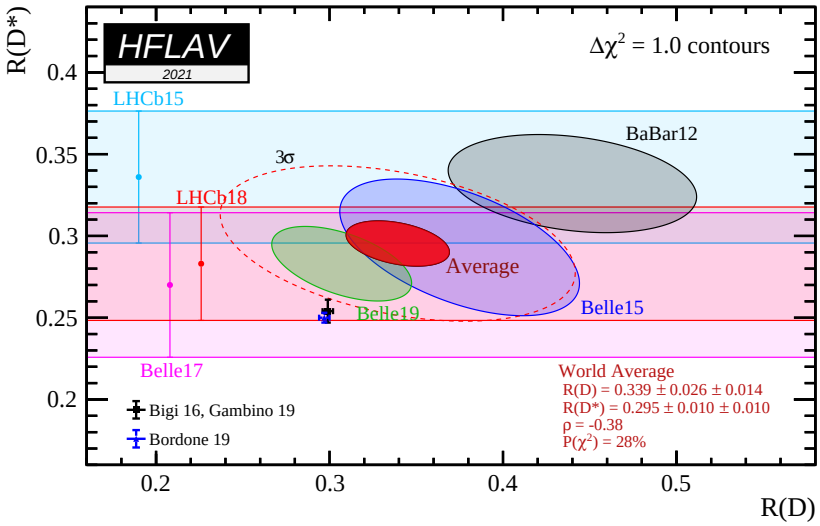

Figure 3.1: *Correlation plot of $R(D)$-$R(D^*)$ given by the HFLAV Collaboration [40] in the Spring 2021. The red area represents the world average of all measurements, while the blue and the black crosses are the two SM predictions described in the text. The plot shows a $\sim 3.4\sigma$ tension between theory and experiments.*

3.2 The role of the hadronic Form Factors

From the theoretical point of view, the extraction of $|V_{cb}|$ from exclusive $B \to D^{(*)}\ell\nu$ decays and the theoretical estimates of the $R(D^{(*)})$ ratios depend on the value and the shape of the Form Factors (FFs) entering the matrix elements and amplitudes. These functions encode the non-perturbative strong interactions between the quarks and, in principle, can be determined through lattice QCD (LQCD) computations. Let us now describe more specifically how the FFs influence the $B \to D^{(*)}\ell\nu$ decays and, in what follows, we will analyze separately the production of D and D^* mesons.

3.2.1 FFs and differential decay width of $B \to D\ell\nu$ decays

Defining the vector current $V^\mu \equiv \bar{b}\gamma^\mu c$, the structure of the hadronic matrix element reads

$$\langle D(p_D)\,|\,V^\mu\,|\,B(p_B)\rangle = f^+(q^2)\left(p_B^\mu + p_D^\mu - \frac{m_B^2 - m_D^2}{q^2}q^\mu\right) + f^0(q^2)\frac{m_B^2 - m_D^2}{q^2}q^\mu, \tag{3.4}$$

where

$$f^0(q^2) = \frac{q^2}{m_B^2 - m_D^2}f^-(q^2) + f^+(q^2). \tag{3.5}$$

and $q^\mu = p_B^\mu - p_D^\mu$ is the momentum transfer. The two FFs in Eq. (3.4) are constrained by the kinematical relation

$$f^0(0) = f^+(0), \tag{3.6}$$

which is a straightforward consequence of Eq. (3.5) at zero momentum transfer and ensures that the hadronic matrix element (3.4) is finite at the kinematic endpoint. Note that the axial current $A^\mu \equiv \bar{b}\gamma^\mu\gamma^5 c$ gives zero-contribution to $B \to D\ell\nu$ decays, as dictated by the Wigner-Eckart theorem.

A direct computation gives the final expression of the differential decay width

$$\begin{aligned}\frac{d\Gamma}{dq^2} = &\frac{G_F^2|V_{cb}|^2\eta_{EW}^2}{24\pi^3}\left(1 - \frac{m_\ell^2}{q^2}\right)^2 \\ &\times\left[|\vec{p}_D|^3\left(1 + \frac{m_\ell^2}{2q^2}\right)|f^+(q^2)|^2 + m_B^2|\vec{p}_D|\left(1 - \frac{m_D^2}{m_B^2}\right)^2\frac{3m_\ell^2}{8q^2}|f^0(q^2)|^2\right],\end{aligned} \tag{3.7}$$

where G_F is the Fermi constant, $\vec{p}_D$ the 3-momentum of the D meson, *i.e.*

$$|\vec{p}_D| = \left[\left(\frac{m_B^2 + m_D^2 - q^2}{2m_B}\right)^2 - m_D^2\right]^{1/2}, \tag{3.8}$$

$\eta_{EW} = 1 + \alpha\ln(M_Z/m_B)/\pi \simeq 1.0066$ the leading electromagnetic correction and m_ℓ the mass of the produced lepton. In the limit of produced massless lepton, the expression (3.7) simplifies to

$$\frac{d\Gamma}{dq^2} \simeq \frac{G_F^2|V_{cb}|^2\eta_{EW}^2}{24\pi^3}|\vec{p}_D|^3|f^+(q^2)|^2. \tag{3.9}$$

Another way to express the result (3.9) is

$$\frac{d\Gamma}{dw} \simeq \frac{G_F^2|V_{cb}|^2\eta_{EW}^2}{48\pi^3}\,\frac{4r\,m_D^3\,(m_B + m_D)^2\,(w^2-1)^{3/2}}{(1+r)^2}\,|f_+(w)|^2, \tag{3.10}$$

where $r \equiv m_D/m_B$ and we have also introduced the recoil variable w, defined as the scalar product of the 4-velocities of the B and the D mesons, *i.e.* $w \equiv v_B \cdot v_D$. This definition can be naturally adopted also for the $B \to D^*$ case. It is then straightforward to verify that the following one-to-one relation holds between the momentum transfer and the recoil

$$q^2 = m_B^2 + m_{D^{(*)}}^2 - 2 m_B m_{D^{(*)}} w. \tag{3.11}$$

3.2.2 FFs and differential decay width of $B \to D^*\ell\nu$ decays

The $B \to D^*$ case is more complicated than the $B \to D$ one since the D^* is a vector meson and, thus, is characterized by a polarization vector ϵ. According to the Wigner-Eckart theorem, both the vector the axial current give a non-zero contribution, namely

$$\begin{aligned}
\langle D^*(p,\epsilon)|\bar{c}\gamma^\mu\,(1 \mp \gamma_5)\,b|\bar{B}(p_B)\rangle \;=\; & -\frac{2}{m_B + m_{D^*}}\varepsilon^\mu_{\alpha\beta\gamma}\epsilon^{*\alpha}p^\beta q^\gamma V(q^2) \\
& \pm i\,\frac{2m_{D^*}}{q^2}(\epsilon^* \cdot q)q^\mu A_0(q^2) \\
& \mp \frac{i}{m_B - m_{D^*}}\left[(m_B - m_{D^*})\epsilon^{*\mu} - (\epsilon^* \cdot q)(p + p_B)^\mu\right] A_1(q^2) \\
& \mp i\,\frac{2m_{D^*}}{q^2}(\epsilon^* \cdot q)\left[\frac{q^2}{m_B^2 - m_{D^*}^2}(p + p_B)^\mu - q^\mu\right] A_3(q^2)\ ,
\end{aligned} \tag{3.12}$$

where we can also re-express $A_3(q^2)$ as

$$2\,m_{D^*}A_3(q^2) = [(m_B + m_{D^*})A_1(q^2) - (m_B - m_{D^*})A_2(q^2)]. \tag{3.13}$$

The four FFs $V(q^2), A_1(q^2), A_2(q^2), A_0(q^2)$ can be re-expressed in terms of a new set of FFs, called $f(q^2), g(q^2), \mathcal{F}_1(q^2), P_1(q^2)$, through the relations

$$V(w) = \frac{m_B + m_{D^*}}{2}g(w)\ , \tag{3.14}$$

$$A_1(w) = \frac{f(w)}{m_B + m_{D^*}}\ , \tag{3.15}$$

$$A_2(w) = \frac{1}{2}\frac{m_B + m_{D^*}}{(w^2 - 1)m_B m_{D^*}}\left[\left(w - \frac{m_{D^*}}{m_B}\right)f(w) - \frac{\mathcal{F}_1(w)}{m_B}\right]\ , \tag{3.16}$$

$$A_0(w) = \frac{1}{2}\frac{m_B + m_{D^*}}{\sqrt{m_B m_{D^*}}}P_1(w)\ , \tag{3.17}$$

where we have used Eq. (3.11).

The FFs are characterized by the following kinematical constraints (KCs). The first one applies at zero recoil and reads

$$\mathcal{F}_1(1) = (m_B - m_{D^*})f(1). \tag{3.18}$$

Instead, the second one applies in the opposite regime, namely at maximum recoil

$$P_1(w_{max}) = \frac{\mathcal{F}_1(w_{max})}{(1 + w_{max})(m_B - m_{D^*})\sqrt{m_B m_{D^*}}}, \tag{3.19}$$

where

$$w_{max} = \frac{m_B^2 + m_{D^*}^2}{2 m_B m_{D^*}},$$

under the assumption that the mass of the final state lepton is negligible. The latter KC (3.19) comes from requiring that $A_3(q^2=0) = A_0(q^2=0)$ (recall that zero momentum transfer is equivalent to maximum recoil). This condition ensures that the hadronic matrix element (3.12) is finite at the kinematic endpoint. On the contrary, the former KC (3.18) has a different physical origin. At zero recoil the D^* meson is at rest, thus we lose one degree of freedom (namely one of its helicities). One can explicitly demonstrate that this condition can be rephrased into the KC (3.18).

In conclusion, starting from the matrix element (3.12) we are able to compute the differential decay width of semileptonic $B \to D^*$ decays. It is interesting to note that the produced D^* strongly decays into a $D\pi$ pair and, thus, we have a four-body final state. The various helicity angles θ_l, θ_v, χ are defined in Fig. 3.2. Thus, the differential decays width reads

$$\begin{aligned}\frac{d\Gamma(B\to D^*(\to D\pi)\ell\nu)}{dw\, d\cos\theta_\ell\, d\cos\theta_v\, d\chi} &= \frac{G_F^2|V_{cb}|^2\eta_{EW}^2}{4(4\pi)^4} 3 m_B m_{D^*}^2 \sqrt{w^2-1}\left(1-2rw+r^2\right) \\ &\cdot B(D^*\to D\pi)\Big\{(1-\cos\theta_\ell)^2\sin^2\theta_v|H_+|^2 \\ &+ (1+\cos\theta_\ell)^2\sin^2\theta_v|H_-|^2 + 4\sin^2\theta_\ell\cos^2\theta_v|H_0|^2 \\ &- 2\sin^2\theta_\ell\sin^2\theta_v\cos 2\chi H_+H_- \\ &- 4\sin\theta_\ell(1-\cos\theta_\ell)\sin\theta_v\cos\theta_v\cos\chi H_+H_0 \\ &+ 4\sin\theta_\ell(1+\cos\theta_\ell)\sin\theta_v\cos\theta_v\cos\chi H_-H_0\Big\},\end{aligned} \tag{3.20}$$

where we have neglected the mass of the lepton and introduced the helicity amplitudes

$$H_0(w) = \frac{\mathcal{F}_1(w)}{\sqrt{m_B^2+m_D^2-2m_Bm_Dw}}, \quad H_\pm(w) = f(w) \mp m_B m_{D^*}\sqrt{w^2-1}\, g(w). \tag{3.21}$$

In order to obtain the final forms of the four differential decay widths $d\Gamma/dx$ (where $x = w, \cos\theta_l, \cos\theta_v, \chi$), we have simply to integrate on three of them in the expression (3.20). For instance, a simple calculation leads to the following expression for $d\Gamma/dw$

$$\frac{d\Gamma}{dw} = \frac{G_F^2|V_{cb}|^2\eta_{EW}^2 m_{D^*}^2}{48\pi^3 m_B}\sqrt{w^2-1}\left[2\,q^2(w)\left(f(w)^2 + m_B^2 m_{D^*}^2\left(w^2-1\right)g(w)^2\right) + \mathcal{F}_1(w)^2\right], \tag{3.22}$$

where $q^2(w)$ can be read from Eq. (3.11).

In conclusion, let us mention what happens in the case of production of a massive lepton, *i.e.* the τ. Eq. (3.20) takes a much more complicated form, however this goes beyond the scope of this Thesis since no measurement of the fourfold differential decay width in case of production of a τ-lepton is available at present. On the contrary, it is of capital importance to derive in this case the theoretical expression of $d\Gamma_\tau/dw \equiv d\Gamma(B\to D^*\tau\nu)/dw$, since it will directly enter in the computation of the $R(D^*)$ ratio (recall its definition in Eq. (3.1)). One can demonstrate that

$$\frac{d\Gamma_\tau}{dw} = \frac{d\Gamma_{\tau,1}}{dw} + \frac{d\Gamma_{\tau,2}}{dw}, \tag{3.23}$$

where we have defined

$$\begin{aligned}\frac{d\Gamma_{\tau,1}}{dw} &= \left(1-\frac{m_\tau^2}{q(w)^2}\right)^2\left(1+\frac{m_\tau^2}{2q(w)^2}\right)\times\frac{d\Gamma}{dw}, \\ \frac{d\Gamma_{\tau,2}}{dw} &= \frac{G_F^2|V_{cb}|^2\eta_{EW}^2 m_B^5}{32\pi^3}\frac{m_\tau^2(m_\tau^2-q(w)^2)^2 r^3(1+r)^2(w^2-1)^{3/2}P_1(w)^2}{q(w)^6}.\end{aligned}$$

Here $r \equiv m_{D^*}/m_B$ and $d\Gamma/dw$ has been written in Eq. (3.22).

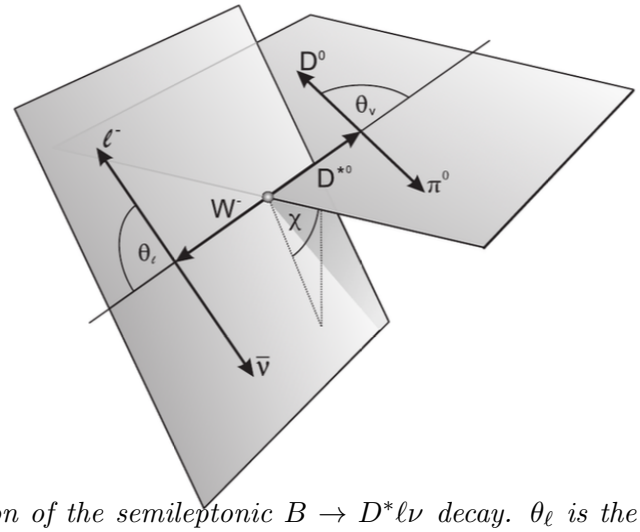

Figure 3.2: *Representation of the semileptonic $B \to D^*\ell\nu$ decay. θ_ℓ is the angle between the lepton and the direction opposite the B meson in the virtual W boson rest frame. θ_v is the angle between the D meson and the direction opposite the B meson in the D^* rest frame. χ is the angle between the two decay planes spanned by the $W-\ell$ and D^*-D systems in the B meson rest frame. Taken from [37].*

3.3 The Dispersive Matrix approach to the Form Factors

As clear from Eqs. (3.9)-(3.20), a correct description of the hadronic FFs is of crucial importance in order to compute the differential decay widths in a correct way. As explained in the previous Section, these functions encode all the informations about the strong interactions between the quarks and, in principle, can be computed on the lattice. In this sense, an improvement of the theory, mainly if not uniquely, for exclusive B decays is expected from progress in LQCD calculations of the relevant FFs.

One is, however, limited by the cutoff effects induced by the presence of a quark as heavy as the b-quark in calculations done at a finite lattice spacing a. Actually, most of the numerical simulations with heavy quarks are performed at a larger than about 0.05 fm, so that for the physical b-quark mass we have $m_b a \gtrsim 1$ and an extrapolation in m_b from unphysical values is necessary. In this context, discretisation errors affect the value of the FFs at zero recoil and make it difficult to study their momentum dependence at large recoil, namely at small q^2. For this reason, in some cases the dependence of the FFs on q^2 in the whole allowed kinematical region is supplemented by using also the results of QCD sum rules calculations at small q^2.

Let us make an explicit example. Results for the $B \to D\ell\nu$ FFs from LQCD [53,54], together with their uncertainties and correlations, are only available in the range $9.3\ \text{GeV}^2 \lesssim q^2 \lesssim 11.7\ \text{GeV}^2$, much smaller than the physical range, $0 \lesssim q^2 \lesssim 11.7\ \text{GeV}^2$. The same situation holds for the momentum-dependence of the FFs in $B \to D^*\ell\nu$ decays, where the results of the first computation on the lattice has recently appeared [55]. However, also in this case the kinematical region is always restricted at small recoil, namely in the region $w \leq 1.17$. In order to supply the lack of information from explicit LQCD calculations of the FFs in the full kinematical range, both the experimental analyses (in order to account for efficiencies and response functions) and the theoretical studies have to assume some parameterisation of the FFs. It is well possible then that the extraction of $|V_{cb}|$ from experiments is biased by the theoretical model adopted in the fits of the data.

In the past, some pioneering works [56–60] were devoted to the determination of model-independent bounds on the FFs entering in semileptonic charged-current decays of hadrons through the knowledge of the two-point functions $\Pi_V^{\mu\nu}(q) = i \int d^4x\, e^{iq\cdot x}\ \langle 0|\, T\{V^{\mu\dagger}(x)V^{\nu}(0)\}\,|0\rangle$, where $V^\mu(x)$ is the vector cur-

rent responsible for the transition under consideration. To be more specific, the authors derived precise constraints on the hadronic FFs from QCD dispersion relations, by exploiting the analiticity and positivity properties of $\Pi_V^{\mu\nu}(q)$. They used a QCD calculation of the aforementioned two-point function, by including both the perturbative contributions to two loops and the leading non-perturbative ones in their computation. These findings have then inspired the development of some parametrizations of the hadronic FFs, used in most of the phenomenological analyses present in literature. The three most popular parameterisations are called Boyd-Grinstein-Lebed (BGL) [61–63], Bourrely-Caprini-Lellouch (BCL) [64] and Caprini-Lellouch-Neubert (CLN) [65, 66], after the name of the authors. In order to give an overview of their features, BGL uses the same dispersive approach of Refs. [56–59] to constrain the FFs from first principles. The key idea is to develop power series expansions of the FFs and, then, to fit the available experimental and/or LQCD data to obtain bounds on the coefficients of the expansions. Although it is quite similar to BGL, BCL is characterized by a different structure of the power series expansion of the FFs, in order to ensure the proper scaling of the FFs themselves at large momentum transfer. Finally, CLN uses again dispersion relations to obtain bounds on the shape of the FFs and, then, combine them with the heavy quark symmetry, in order to provide new relations between the FFs near zero recoil.

In what follows we will deeply describe a novel way to describe the FFs in a non-perturbative and model-independent way, called the Dispersive Matrix Method (DMM). The original proposal was contained in the pioneering work by L. Lellouch [60]. It applies the dispersive techniques originally proposed in refs. [56–59] directly to lattice data and introduces a formalism to take into account the errors of the lattice results. In spite of the use of the FFs derived from first principles in LQCD, the proposal of Ref. [60] relies, for the unitarity constraints, on the *perturbative* calculation of the two-point current correlation functions. To our knowledge, in spite of the large use of the dispersive techniques discussed above, no one has systematically used the lattice two-point correlators computed non perturbatively in numerical simulations to constrain the FFs in semileptonic decays, not even in the original work [60]. Then, here we are going to present an extended study of the two- and three-point lattice correlation functions which will be used, together with the dispersive techniques, to constrain the lattice predictions for the FFs entering in semileptonic $B \to D^{(*)}\ell\nu$ decays.

3.3.1 Two-point correlation functions

The bounds on the different FFs are derived from the two-point functions of suitable currents. The starting point is the Fourier transform of the T-product of two hadronic currents, which generalizes the definition of the hadronic vacuum polarization (HVP) tensor. Assuming $x^0 > 0$ we have

$$\begin{aligned}\int d^4x\, e^{iq\cdot x}\ \langle 0|\, T\{J^{\mu\dagger}(x)J^{\nu}(0)\}\,|0\rangle &= \int d^4x\, e^{iq\cdot x} \sum_n \langle 0|\, J^{\mu\dagger}(x)\,|n\rangle\,\langle n|\, J^{\nu}(0)\,|0\rangle \\ &= \sum_n \int d^4x\, e^{iq\cdot x} e^{-ip_n\cdot x}\ \langle 0|\, J^{\mu\dagger}(0)\,|n\rangle\,\langle n|\, J^{\nu}(0)\,|0\rangle \qquad (3.24)\\ &= \sum_n (2\pi)^4\delta^{(4)}(q-p_n)\ \langle 0|\, J^{\mu\dagger}(0)\,|n\rangle\,\langle n|\, J^{\nu}(0)\,|0\rangle\ ,\end{aligned}$$

where p_n the 4-momentum of the intermediate n-particle state. A similar result can be derived for the case $x^0 < 0$. The completeness sum runs over all possible intermediate hadronic states and in particular we will focus our attention onto either a single-particle $B_c^{(*)}$-meson state or two-particle states composed by a B-meson and a $D^{(*)}$-meson. The link between the two-particle states appearing in the completeness sum (3.24) and the classification of the FFs introduced in Eqs. (3.4)-(3.12) is given

by the substitution

$$\langle D^{(*)}|J^\mu|B\rangle \to \langle B\, D^{(*)}|J^\mu|0\rangle\,, \tag{3.25}$$

which can be simply realised by inverting the sign of $p_{D^{(*)}}$ and by analytic continuation of the FFs in q^2 from $m_\ell^2 \leq q^2 \leq (m_B - m_{D^{(*)}})^2$ to $(m_B + m_{D^{(*)}})^2 \leq q^2 \leq \infty$. Thus, the amplitudes entering in semileptonic decays are strongly correlated to the T-product in Eq. (3.24), which is the reason why the latter is so important to constrain the FFs.

At this point, the Fourier transform of the T-product defines the following HVP tensors:

$$\begin{aligned}
\Pi_V^{\mu\nu}(q) &= i\int d^4x\, e^{iq\cdot x}\ \langle 0|\, T\{V^{\mu\dagger}(x)V^\nu(0)\}\,|0\rangle &(3.26)\\
&= (q^\mu q^\nu - g^{\mu\nu}q^2)\,\Pi_{1^-}(q^2) + q^\mu q^\nu\,\Pi_{0^+}(q^2)\,,\\
\Pi_A^{\mu\nu}(q) &= i\int d^4x\, e^{iq\cdot x}\ \langle 0|\, T\{A^{\mu\dagger}(x)A^\nu(0)\}\,|0\rangle &(3.27)\\
&= (q^\mu q^\nu - g^{\mu\nu}q^2)\,\Pi_{1^+}(q^2) + q^\mu q^\nu\,\Pi_{0^-}(q^2)\,,
\end{aligned}$$

where V^μ, A^μ are the vector and the axial 4-currents defined in the previous Section. Furthermore, the subscripts $0^\pm$,$1^\pm$ represent spin-parity quantum numbers of the intermediate states. The quantities $\Pi_{0^\pm}$,$\Pi_{1^\mp}$ are called *polarization functions*. In particular, the term proportional to Π_{0^+} (Π_{0^-}) represents the *longitudinal* part of the HVP tensor with vector (axial) 4-currents, while the term proportional to Π_{1^-} (Π_{1^+}) is the *transverse* contribution to the HVP tensor with vector (axial) 4-currents. Note finally that by inserting a completeness sum between the vector or axial 4-currents we are able to relate these expressions to Eq. (3.24). Thus, it is straightforward to state that the FFs introduced in Eqs. (3.4)-(3.12) enter in the imaginary parts of the polarization functions, accordingly to their spin-parity quantum numbers.

The imaginary parts of the longitudinal and transverse polarization functions are related to their derivatives with respect to q^2 by the dispersion relations

$$\begin{aligned}
\chi_{0^+}(q^2) &\equiv \frac{\partial}{\partial q^2}[q^2\Pi_{0^+}(q^2)] = \frac{1}{\pi}\int_0^\infty dz \frac{z\,\mathrm{Im}\Pi_{0^+}(z)}{(z-q^2)^2}\,,\\
\chi_{0^-}(q^2) &\equiv \frac{\partial}{\partial q^2}[q^2\Pi_{0^-}(q^2)] = \frac{1}{\pi}\int_0^\infty dz \frac{z\,\mathrm{Im}\Pi_{0^-}(z)}{(z-q^2)^2}\,, &(3.28)\\
\chi_{1^-}(q^2) &\equiv \frac{1}{2}\left(\frac{\partial}{\partial q^2}\right)^2[q^2\Pi_{1^-}(q^2)] = \frac{1}{\pi}\int_0^\infty dz \frac{z\,\mathrm{Im}\Pi_{1^-}(z)}{(z-q^2)^3}\,,\\
\chi_{1^+}(q^2) &\equiv \frac{1}{2}\left(\frac{\partial}{\partial q^2}\right)^2[q^2\Pi_{1^+}(q^2)] = \frac{1}{\pi}\int_0^\infty dz \frac{z\,\mathrm{Im}\Pi_{1^+}(z)}{(z-q^2)^3}\,.
\end{aligned}$$

In what follows we will denote by χ a generic susceptibility. From a dimensional point of view note that the longitudinal (scalar/pseudoscalar) susceptibilities $\chi_{0^\pm}$ are dimensionless, while the transverse (vector/axial) ones have dimension $[E]^{-2}$, where E is an energy. The imaginary parts of the polarization functions receive both one-particle and two-particle contributions, whose analytic expressions can be directly found in Appendix A.

3.3.2 Dispersive bounds from the DMM

First of all, let us describe the general ideas behind the dispersive method of Refs. [56]- [59] thanks to which one can obtain bounds for a generic FF $f(q^2)$. We define

$$t_\pm = (m_B \pm m_{D^{(*)}})^2 \tag{3.29}$$

and we use the analytic continuation of the amplitudes from the kinematical decay region, where $m_\ell^2 \leq q^2 \leq t_-$, to the single-meson or pair production region, where $m_{B_c}^2 \leq q^2$ or $t_+ \leq q^2$. By means of the dispersion relations we can use the two-point correlation functions computed in QCD to obtain the constraints on $f(q^2)$ and then use analyticity to translate these constraints into the physical FFs relevant for semileptonic decays.

The dispersion relations that we will consider in this work have already been introduced in Eqs. (3.28). We also recall that the derivatives of the various polarization functions can be determined in perturbative QCD *only* for values of q^2 that are far from the region of production of resonance states, namely

$$(m_b + m_c)\Lambda_{QCD} \ll (m_b + m_c)^2 - q^2, \tag{3.30}$$

where m_b and m_c are the bottom and charm quark masses, respectively. A possible choice is thus also the value $q^2 = 0$, which has been widely used in the past, particularly in all the calculations that used the perturbative expression of the susceptibilities $\chi(q^2)$. On the contrary, with a non-perturbative determination of the two-point correlation functions we can use the most convenient value of q^2 at disposal, namely the value which will allow the most stringent bounds on the FFs.

By inserting a complete set of states with the same quantum numbers of a generic current J we have[1]

$$\mathrm{Im}\Pi_{0^\pm,1^\mp} = \frac{1}{2}\sum_n \int d\mu(n)(2\pi)^4\delta^{(4)}(q - p_n)|\left\langle 0\right| J \left|n\right\rangle|^2, \tag{3.31}$$

where $d\mu(n)$ is the measure of the phase space for the set of states n. As the completeness sum is semi-positive definite, we can restrict our attention to a subset of hadronic states and thus produce a strict inequality. This consideration allows us to re-write the dispersion relations for $\chi(q^2)$ as

$$\frac{1}{\pi\,\chi(q^2)}\int_{t_+}^{\infty} dt \frac{W(t)|f(t)|^2}{(t-q^2)^3} \leq 1, \tag{3.32}$$

where $f(t)$ is the generic FF and $W(t)$ is a computable function that depends on the particular FF under consideration and is related to phase space factors. These have been given explicitly in Eqs. (A.7)-(A.10) for all the possible bilinears in Appendix B.

We can now use analyticity to turn the result (3.32) into a constraint for the semileptonic region. To achieve this goal, it is necessary that the integrand is analytic below the pair-production threshold $t < t_+$. To this end, we define the *conformal* variable z as

$$z(t, t_s) \equiv \frac{\sqrt{t_+ - t} - \sqrt{t_+ - t_s}}{\sqrt{t_+ - t} + \sqrt{t_+ - t_s}}, \tag{3.33}$$

which is real for $t_s < t_+$, zero for $t = t_s$ and a complex number on the unitary circle for $t \geq t_+$. We can remove the poles of the integrand of Eq.(3.32) by multiplying it by appropriate powers of the $z(t, t_s)$s, as determined by the positions t_s of the sub-threshold poles. Each pole has a distinct value of t_s, and the product $z(t, t_{s1})^{k_1} z(t, t_{s2})^{k_2} \ldots$ removes all of them. Hence, we re-express Eq. (3.32) as

$$\frac{1}{\pi}\int_{t_+}^{\infty} dt \left|\frac{dz(t,t_0)}{dt}\right| \times \left|\tilde{\Phi}(t,t_0)P(t)f(t)\right|^2 \leq 1, \tag{3.34}$$

where t_0 is an arbitrary point that we will define below. Here we have introduced the *Blaschke factor* $P(t)$, which is a product of many quantities of the form (3.33) at the position of the sub-threshold

[1] For simplicity we omit Lorentz indices and other complications that are immaterial for the present discussion.

poles (i.e., $t_s \leq t_+$), and the *outer function* $\tilde{\Phi}(t, t_0)$, which is defined for the vector/axial channel for instance as

$$\tilde{\Phi}(t, t_0) = \tilde{P}(t) \left[\frac{W(t)}{|dz(t, t_0)/dt|\, \chi_{1^\pm}(q^2)(t - q^2)^3} \right]^{1/2} . \tag{3.35}$$

In the last expression $\tilde{P}(t)$ represents a product of the $z(t, t_s)$'s and $\sqrt{z(t, t_s)}$'s that remove the sub-threshold singularities and cuts in the kinematical part $W(t)$. Regarding the choice of t_0 in Eq. (3.34), there are several possibilities which may be more or less convenient depending on the quantity at hand. In this Thesis, we will always choose $t_0 = t_-$, so that the allowed kinematic interval $[0, t_-]$ corresponds to the range $[z_{\max}, 0]$.

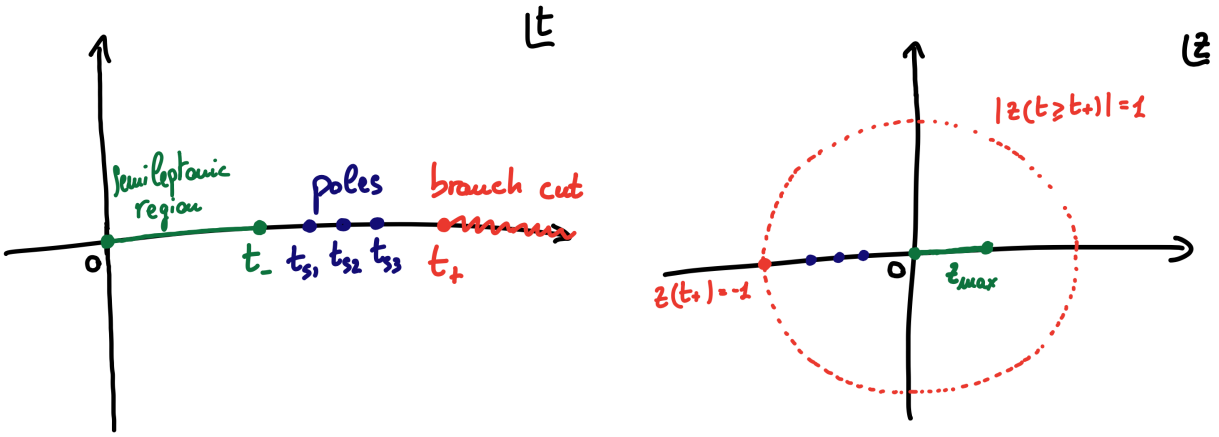

(a) (b)

Figure 3.3: Sketch of the analytic structure of the hadronic form factors as function of t (left panel) or as function of z (right panel). The green line represents the region relevant for semileptonic decays. The blue points are the isolated poles coming from one-particle states. In conclusion, the red branch cut in the left panel is caused by multi-particle states, *i.e.* states of two or more particles. This branch cut translates in the unit circle $|z| = 1$ in the right panel.

The DMM allows us to translate the information given by the susceptibility $\chi(q^2)$ into a bound on the FFs in the following way. Firstly, we make the transformation

$$\frac{1 + z}{1 - z} = \sqrt{\frac{t_+ - t}{t_+ - t_-}} , \tag{3.36}$$

or

$$z = \frac{\sqrt{\frac{t_+ - t}{t_+ - t_-}} - 1}{\sqrt{\frac{t_+ - t}{t_+ - t_-}} + 1} , \tag{3.37}$$

which exactly corresponds to $z = z(t, t_-)$, see Eq. (3.33). We thus map the complex t-plane into the unit disc in the variable z, whereas the integral around the cut in Eq. (3.34) becomes an integral around the unit circle. A graphical representation of the situation is shown in Figure 3.3 for clarity.

Then, a generic integral of the form given in Eq. (3.32) can be written as an integral over z [59]- [60]

$$\frac{1}{2\pi i} \int_{|z|=1} \frac{dz}{z} |\phi(z, q^2) f(z)|^2 \leq \chi(q^2) , \tag{3.38}$$

where the kinematical functions $\phi(z,q^2)$ for the different form factors entering $B\to D^{(*)}$ decays will be specified in Eq. (3.45) below. At this point, by introducing an inner product defined as

$$\langle g|h\rangle = \frac{1}{2\pi i}\int_{|z|=1}\frac{dz}{z}\bar{g}(z)h(z)\,, \tag{3.39}$$

where $\bar{g}(z)$ is the complex conjugate of the function $g(z)$, the inequality (3.38) can simply be written as

$$0\leq\langle\phi f|\phi f\rangle\leq\chi(q^2)\,, \tag{3.40}$$

where we have also used the positivity of the inner product. Following Refs. [59]- [60], we also define the function $g_t(z)$ as

$$g_t(z)\equiv\frac{1}{1-\bar{z}(t)z}\,, \tag{3.41}$$

where $\bar{z}(t)$ is the complex conjugate of the variable $z(t)$ defined in Eq. (3.37) and z is the integration variable of Eq. (3.39). It is then straightforward to show that

$$\langle g_t|\phi f\rangle=\phi(z(t),q^2)\,f\left(z(t)\right)\,,\qquad \langle g_{t_m}|g_{t_l}\rangle=\frac{1}{1-\bar{z}(t_l)z(t_m)}. \tag{3.42}$$

At this point, let us introduce the matrix

$$\mathbf{M}=\begin{pmatrix}\langle\phi f|\phi f\rangle & \langle\phi f|g_t\rangle & \langle\phi f|g_{t_1}\rangle & \cdots & \langle\phi f|g_{t_n}\rangle\\ \langle g_t|\phi f\rangle & \langle g_t|g_t\rangle & \langle g_t|g_{t_1}\rangle & \cdots & \langle g_t|g_{t_n}\rangle\\ \langle g_{t_1}|\phi f\rangle & \langle g_{t_1}|g_t\rangle & \langle g_{t_1}|g_{t_1}\rangle & \cdots & \langle g_{t_1}|g_{t_n}\rangle\\ \vdots & \vdots & \vdots & \vdots & \vdots\\ \langle g_{t_n}|\phi f\rangle & \langle g_{t_n}|g_t\rangle & \langle g_{t_n}|g_{t_1}\rangle & \cdots & \langle g_{t_n}|g_{t_n}\rangle\end{pmatrix}. \tag{3.43}$$

The values $t_1,\cdots,t_n$ will correspond to the squared 4-momenta at which the FFs have been computed non-perturbatively and that will be used as inputs for constraining the FF in regions non-accessible to the calculation. Note that the first matrix element in (3.43) is the quantity directly related to the susceptibility $\chi(q^2)$ through the dispersion relations, see Eq. (3.40). Taking for instance into consideration the $B\to D$ case, in terms of the longitudinal and transverse susceptibilities $\chi_{0^+}(q^2)$ and $\chi_{1^-}(q^2)$ we have that:

$$\begin{aligned}\langle\phi_0 f_0|\phi_0 f_0\rangle &\leq \chi_{0^+}(q^2)\,,\\ \langle\phi_+ f_+|\phi_+ f_+\rangle &\leq \chi_{1^-}(q^2)\,,\end{aligned} \tag{3.44}$$

where $\phi_{0,+}$ are kinematical functions

$$\begin{aligned}\phi_0(z,q^2) &= \sqrt{\frac{2n_I}{3}}\sqrt{\frac{3t_+t_-}{4\pi}}\frac{1}{t_+-t_-}\frac{1+z}{(1-z)^{5/2}}\left(\rho(0)+\frac{1+z}{1-z}\right)^{-2}\left(\rho(q^2)+\frac{1+z}{1-z}\right)^{-2}\,,\\ \phi_+(z,q^2) &= \sqrt{\frac{2n_I}{3}}\sqrt{\frac{1}{\pi(t_+-t_-)}}\frac{(1+z)^2}{(1-z)^{9/2}}\left(\rho(0)+\frac{1+z}{1-z}\right)^{-2}\left(\rho(q^2)+\frac{1+z}{1-z}\right)^{-3}\,,\end{aligned} \tag{3.45}$$

where n_I is an isospin Clebsch-Gordan factor and

$$\rho(q^2)\equiv\sqrt{\frac{t_+-q^2}{t_+-t_-}}\,. \tag{3.46}$$

When analyticity does not hold, i.e. when a FF has, for instance, N poles at $t = t_{P1}, t_{P2}, \cdots ..., t_{PN}$, it is sufficient to modify the kinematical function ϕ according to

$$\phi(z, q^2) \to \phi_P(z, q^2) \equiv \phi(z, q^2) \times \frac{z - z(t_{P1})}{1 - \bar{z}(t_{P1})z} \times \cdots \times \frac{z - z(t_{PN})}{1 - \bar{z}(t_{PN})z} \tag{3.47}$$

and the previous definitions will continue to be valid.

The positivity of the inner products (3.42) guarantees that the determinant of the matrix (3.43) is positive semi-definite, namely

$$\det \mathbf{M} \geq 0. \tag{3.48}$$

This condition can be rephrased in the second order inequality

$$\alpha \langle g_t | \phi f \rangle^2 + 2\beta \langle g_t | \phi f \rangle \leq \gamma \,, \tag{3.49}$$

with

$$\begin{aligned} \alpha &\equiv \det \mathbf{M}^{\{(1,1),(2,2)\}} \,, \\ \beta &\equiv \sum_{i=1}^{n} (-1)^{1+i} \det \mathbf{M}^{\{(1,1),(2,i+1)\}} \langle g_{t_i} | \phi f \rangle \,, \\ \gamma &\equiv \chi(q^2) \det \mathbf{M}^{\{(1,1)\}} - \sum_{i,j=1}^{n} (-1)^{i+j} \det \mathbf{M}^{\{(1,1),(i+1,j+1)\}} \langle g_{t_i} | \phi f \rangle \langle g_{t_j} | \phi f \rangle \,, \end{aligned} \tag{3.50}$$

where $\mathbf{M}^{\{(i_1,j_1),(i_2,j_2),\cdots\}}$ is the minor obtained by deleting the rows $i_1, i_2, \cdots$ and the columns $j_1, j_2, \cdots$. Calling Δ the discriminant of the inequality (3.49), one can show that

$$\Delta = \det \mathbf{M}^{\{(1,1)\}} \times \det \mathbf{M}^{\{(2,2)\}} \equiv \Delta_1 \times \Delta_2, \tag{3.51}$$

so that at the end the relevant quantities will only be $\alpha, \beta, \Delta_1, \Delta_2$. Note that α and Δ_2 are t-independent, *i.e.* they are given numbers once the susceptibility $\chi(q^2)$ and the lattice QCD inputs are chosen. On the contrary, β and Δ_1 are t-dependent. Moreover, only the quantities β and Δ_2 depend on the chosen value of q^2.

At this point, since $\Delta_1 \geq 0$ by construction, the inequality (3.49) will have an acceptable solution only when $\Delta_2 \geq 0$. If this condition, that we will call *unitarity filter*, is satisfied, by expressing the scalar product $\langle g_t | \phi f \rangle$ according to Eq. (3.42) we obtain the following unitarity constraints on the FF $f(t)$

$$f_{lo}(t, q^2) \leq f(t) \leq f_{up}(t, q^2) \,, \tag{3.52}$$

where

$$f_{lo(up)}(t, q^2) \equiv \frac{-\beta(t, q^2) \mp \sqrt{\Delta_1(t)\, \Delta_2(q^2)}}{\alpha\, \phi(z(t), q^2)} \,. \tag{3.53}$$

Thus, thanks to the dispersive bounds in Eqs. (3.52), by using a direct lattice measurement of the FFs at the points $t_1, t_2, \ldots, t_n$ and the two-point functions of the suitable currents we can constrain the FFs in regions of momenta not accessible to lattice simulations. Explicit analytical expressions for $f_{lo(up)}(t, q^2)$, which are very useful for their direct numerical evaluation, are given in Appendix C. Let us stress also that the unitarity filter $\Delta_2(q^2) \geq 0$ is t-independent, which implies that, when it is not satisfied, no prediction for $f(t)$ is possible at any value of t.

In the phenomenological applications present in this Thesis, we will always use the results of the computation of the FFs performed by other Collaborations. On the contrary, we have computed for

the first time on the lattice the susceptibilities relevant for the semileptonic B decays. In Appendix D the central ideas for their non-perturbative computations are shown and discussed.

In conclusion, we point out an interesting feature of the dispersive approach based on the matrix (3.43). When the momentum transfer t coincides with one of the data points, i.e. when $t \to t_j$, the determinant $\Delta_1(q^2) \to 0$ and the quantity $\beta/\alpha \to \phi(z(t_j), q^2) f(z(t_j))$, so that $f_{lo(up)}(t, q^2) \to f(z(t_j))$. In other words, the FF $f(t)$, obtained from the dispersive matrix method, reproduces exactly the given set of data points.

3.3.3 Statistical and systematic errors in the presence of kinematical constraints

Let us now discuss the treatment of the statistical errors and of the systematic effects when the bounds on the values of the FF $f(t)$ are derived using the values $f(t_i)$ computed at the points t_i with $i = 1, 2, \ldots, n$, and the appropriate susceptibility χ. Without any loss of generality, we consider in this Section the case of the semileptonic $B \to D$ decays, in which case we deal with the scalar $f_0(t)$ and vector $f_+(t)$ FFs. Recall that they have to fulfill the kinematical constraint (3.6).

Eq. (3.53) allows us to compute the lower/upper bounds of $f_{0(+)}(t)$ once we have chosen our set of input data, i.e. $\{\chi_{0^+(1^-)}, f_{0(+)}(t_1), \cdots, f_{0(+)}(t_n)\}$. Thus, the input data set is made of $2n+2$ quantities: the n values of the scalar FF f_0, the n values of the vector FF f_+ and the two susceptibilities χ_{0^+} and χ_{1^-}. For sake of simplicity we are considering the same number of data points for both the scalar and the vector FFs evaluated at the same series of values t_i ($i = 1, \cdots, n$). Our goal is to propagate the uncertainties related to these quantities into the evaluation of the FFs $f_{0(+)}(t)$ at a generic value of t.

In Ref. [60] L. Lellouch proposed a solution to this problem. His idea is as follows. Let us assume that the two FFs $f_+(t)$, $f_0(t)$ are distributed according to a normalized probability distribution, call it $\mathcal{P}_{in}(f_+, f_0)[d^n f_+][d^n f_0]$. Since the FFs have to respect both the unitarity filters and the KC between them, we can define the measure

$$d\mu(f_+, f_0) \equiv [d^n f_+][d^n f_0] \times \theta\left(\Delta_2^+\right) \theta\left(\Delta_2^0\right) \theta\left(f_{0,up}(0, q^2) - f_{+,lo}(0, q^2)\right) \theta\left(f_{+,up}(0, q^2) - f_{0,lo}(0, q^2)\right), \tag{3.54}$$

where $\theta(x)$ is the Heaviside theta function. At this point, we can also define the probability that the form factor $f_{+(0)}(t)$ takes a value inside an arbitrary interval $[\kappa_{lo}^{+(0)}, \kappa_{up}^{+(0)}]$ at momentum transfer t, *given that* $f_{+(0)}(0) \in [\max[f_{+,lo}(0), f_{0,lo}(0)], \min[f_{+,up}(0), f_{0,up}(0)]]$. These two probabilities (the one for f_+ and the one for f_0) allow then to plot *confidence level* bounds for each of the two FFs, assigning to them a precise statistical meaning.

In what follows we propose, instead, the following method, which is different from the one of Ref. [60]. We start by building up a multivariate Gaussian distribution with mean values and covariance matrix given respectively by $\{f_0(t_1), \cdots, f_0(t_n), f_+(t_1), \cdots, f_+(t_n)\}$ and $\Sigma_{ij} = \rho_{ij}\sigma_i\sigma_j$, where $f_{0(+)}(t_i)$ are the FFs extracted on the lattice, σ_i are the corresponding uncertainties, and ρ_{ij} is their correlation matrix (including also correlations between the two FFs). Since we are going to use data produced by other groups, that provide their values of $f_{0(+)}(t_i)$, σ_i and ρ_{ij}, we generate N_{boot} bootstrap events according to the expected probability distributions. In this case we generate N_{boot} values of the non-perturbative susceptibilities $\chi_{0^+(1^-)}$ through normal distributions defined by their mean values and standard deviations[2].

Then, for each bootstrap event we consider the $(n+1) \times (n+1)$ matrices $\mathbf{M}^0$ and $\mathbf{M}^+$ (see Eq. (3.43)) corresponding to the scalar and vector FFs, respectively. The positivity condition (3.51)

[2]If we have, instead, direct access to the data of the simulations, we can generate by ourself jackknife or bootstrap sets of all the quantities defined above. At the same time we use the non-perturbative susceptibilities evaluated on the same jackknife/bootstrap sets used to compute the values of the form factors $f_{0(+)}(t_i)$.

implies that both Δ_2^0 and Δ_2^+ should be positive. Thus, we compute $\Delta_2^{0(+)}$ and verify their signs. If either Δ_2^0 or Δ_2^+ results to be negative for a specific bootstrap, then the event is eliminated from the sample. From the physical point of view, this step can be read as a consistency check between all the input data, namely the susceptibilities and the FFs for that particular bootstrap. At the end of the procedure, we will be left with $\widetilde{N}_{boot} \leq N_{boot}$ events.

In order to satisfy the KC between the FFs, in the subset of the $\widetilde{N}_{boot}$ events satisfying the unitarity filters $\Delta_2^{0(+)} \geq 0$, we select only the $N^*_{boot} \leq \widetilde{N}_{boot}$ events for which the dispersive bands for f_0 and f_+ overlap each other at zero momentum trasfer. This corresponds to impose the conditions

$$\begin{aligned} f_{0,up}(0,q^2) &> f_{+,lo}(0,q^2)\ , \\ f_{+,up}(0,q^2) &> f_{0,lo}(0,q^2)\ , \end{aligned} \tag{3.55}$$

where $f_{lo,up}(t,q^2)$ were defined in Eq. (3.53) for a generic FF f. Omitting for simplicity the argument q^2 at which the susceptibilities $\chi_{0(+)}$ are calculated, the conditions (3.55) can then be rephrased as

$$\left|\phi_+(z(0))\,\beta_+(0) - \phi_0(z(0))\beta_0(0)\right| \leq \sqrt{\Delta_1(0)}\left[\phi_+(z(0))\,\sqrt{\Delta_2^+} + \phi_0(z(0))\,\sqrt{\Delta_2^0}\right]. \tag{3.56}$$

As already said, the above condition select $N^*_{boot} \leq \widetilde{N}_{boot}$ events. For each of the N^*_{boot} events we define

$$\begin{aligned} f^*_{lo}(0) &= \max[f_{+,lo}(0), f_{0,lo}(0)]\,, \\ f^*_{up}(0) &= \min[f_{+,up}(0), f_{0,up}(0)]\,, \end{aligned} \tag{3.57}$$

so that, putting $f(0) \equiv f_0(0) = f_+(0)$, one has

$$f^*_{lo}(0) \leq f(0) \ \leq f^*_{up}(0)\ . \tag{3.58}$$

We now consider the FF $f(0)$ to be uniformly distributed in the range given by Eq. (3.58) and we add it to the input data set as a new point at $t_{n+1} = 0$. To be more precise, for each of N^*_{boot} events we generate N_0 values of $f(0)$ with uniform distribution in the range $[f^*_{lo}(0), f^*_{up}(0)]$, obtaining a new sample having $\overline{N}_{boot} = N^*_{boot} \times N_0$ events, each of them satisfying by construction both the unitarity filters $\Delta_2^{0(+)} \geq 0$ and the KC (3.6).

We then consider two modified $(n+2)\times(n+2)$ matrices, $\mathbf{M}^0_C$ and $\mathbf{M}^+_C$, that have one more row and one more column with respect to matrices $\mathbf{M}^0$ and $\mathbf{M}^+$ and contain the common FF $f(t_{n+1}=0)$, namely matrices of the form

$$\mathbf{M}_C = \begin{pmatrix} \langle \phi f|\phi f\rangle & \langle \phi f|g_t\rangle & \langle \phi f|g_{t_1}\rangle & \cdots & \langle \phi f|g_{t_n}\rangle & \langle \phi f|g_{t_{n+1}}\rangle \\ \langle g_t|\phi f\rangle & \langle g_t|g_t\rangle & \langle g_t|g_{t_1}\rangle & \cdots & \langle g_t|g_{t_n}\rangle & \langle g_t|g_{t_{n+1}}\rangle \\ \langle g_{t_1}|\phi f\rangle & \langle g_{t_1}|g_t\rangle & \langle g_{t_1}|g_{t_1}\rangle & \cdots & \langle g_{t_1}|g_{t_n}\rangle & \langle g_{t_1}|g_{t_{n+1}}\rangle \\ \vdots & \vdots & \vdots & \vdots & \vdots & \vdots \\ \langle g_{t_n}|\phi f\rangle & \langle g_{t_n}|g_t\rangle & \langle g_{t_n}|g_{t_1}\rangle & \cdots & \langle g_{t_n}|g_{t_n}\rangle & \langle g_{t_n}|g_{t_{n+1}}\rangle \\ \langle g_{t_{n+1}}|\phi f\rangle & \langle g_{t_{n+1}}|g_t\rangle & \langle g_{t_{n+1}}|g_{t_1}\rangle & \cdots & \langle g_{t_{n+1}}|g_{t_n}\rangle & \langle g_{t_{n+1}}|g_{t_{n+1}}\rangle \end{pmatrix}. \tag{3.59}$$

For any point t at which we want to predict the allowed dispersive band of the FF $f(t)$ (which can be either $f_0(t)$ or $f_+(t)$) without directly determining it on the lattice, we compute the matrix $\mathbf{M}_C$ and using Eq. (3.53) we get $f_{lo}(t)$ and $f_{up}(t)$. This can be done for each of the N_0 events. Let us

indicate the result of the k-th extraction by $f_{lo}^k(t)$ and $f_{up}^k(t)$, respectively. Then, for each of the N_{boot}^* events the lower and upper bounds $\overline{f}_{lo}(t)$ and $\overline{f}_{up}(t)$ can be defined as

$$\begin{aligned} \overline{f}_{lo}(t) &= \min[f_{lo}^1(t), f_{lo}^2(t), \ldots, f_{lo}^{N_0}(t)] \,, \\ \overline{f}_{up}(t) &= \max[f_{up}^1(t), f_{up}^2(t), \ldots, f_{up}^{N_0}(t)] \,. \end{aligned} \tag{3.60}$$

At this point we can generate the bounds of the form factor $f(t)$. To achieve this goal, we combine all the N_{boot}^* results $\overline{f}_{lo,up}^i(t)$ $(i = 1, \cdots, N_{boot}^*)$ to generate the corresponding histograms and fit them with a Gaussian Ansatz. From these fits we extract the average values $f_{lo(up)}(t)$, the standard deviations $\sigma_{lo(up)}(t)$ and the corresponding correlation factor $\rho_{lo,up}(t) = \rho_{up,lo}(t)$, namely

$$f_{lo(up)}(t) = \frac{1}{N_{boot}^*} \sum_{i=1}^{N_{boot}^*} \overline{f}_{lo(up)}^i \,, \tag{3.61}$$

$$\sigma_{lo(up)}^2(t) = \frac{1}{N_{boot}^* - 1} \sum_{i=1}^{N_{boot}^*} \left[\overline{f}_{lo(up)}^i(t) - f_{lo(up)}(t)\right]^2 \,, \tag{3.62}$$

$$\rho_{lo,up}(t) = \rho_{up,lo}(t) = \frac{1}{N_{boot}^* - 1} \sum_{i,j=1}^{N_{boot}^*} \left[\overline{f}_{lo}^i(t) - f_{lo}(t)\right] \left[\overline{f}_{up}^j(t) - f_{up}(t)\right] \,. \tag{3.63}$$

Note that in the above procedure we are assuming that the bootstrap values of the FFs at each value of the momentum transfer are Gaussian distributed. From the practical point of view, we have explicitly verified for each decay channel we have taken into consideration that this is a very good approximation. In fact, we have checked that the distributions of the FFs events at different t values are well reproduced by Gaussian distributions. To giva an explicit example, in Chapter 4 we will analyze in depth this point for the $B \to D^* \ell \nu$ decays.

3.3.4 Combination of the lower and upper bounds for each FF

After the steps described before, for any choice for t we obtain from the bootstrap events (pseudogaussian) distributions for $f_{0,lo}(t)$, $f_{0,up}(t)$, $f_{+,lo}(t)$ and $f_{+,up}(t)$ as well as the corresponding mean values, standard deviations and correlations. We combine them according to the following procedure.

Let us consider a single bootstrap event in which f_L is the lower bound and f_U is the upper one for a generic FF at the given value of t (for sake of simplicity we omit the t-dependence for a while). We associate to the FF f a flat distribution between f_L and f_U, *i.e.*

$$P(f) = \frac{1}{f_U - f_L} \Theta(f - f_L) \Theta(f_U - f) \,, \tag{3.64}$$

where $f = f_{0(+)}$, $f_U = f_{0(+),up}$, $f_L = f_{0(+),lo}$ and Θ is the Heaviside step function. The mean value and the variance associated to the distribution (3.64) are respectively given by

$$\frac{1}{f_U - f_L} \int_{f_L}^{f_U} df \; f \, \Theta(f - f_L) \, \Theta(f_U - f) = \frac{f_U + f_L}{2} \,, \tag{3.65}$$

$$\frac{1}{f_U - f_L} \int_{f_L}^{f_U} df \; \left(f - \frac{f_U + f_L}{2}\right)^2 \Theta(f - f_L) \, \Theta(f_U - f) = \frac{(f_U - f_L)^2}{12} \,. \tag{3.66}$$

It is however necessary to average over the whole set of bootstrap events. Since the lower and the upper bounds of a generic FF are strongly correlated, we adopt a multivariate Gaussian distribution to describe them, *i.e.*

$$P_{LU}(f_L, f_U) = \frac{\sqrt{\det C^{-1}}}{2\pi}\; e^{-\frac{1}{2}\left[C^{-1}_{LL}(f_L - f_{lo})^2 + 2C^{-1}_{LU}(f_U - f_{up})(f_L - f_{lo}) + C^{-1}_{UU}(f_U - f_{up})^2\right]}\,, \tag{3.67}$$

where $f_{lo(up)}$ represents the mean of the lower (upper) bound over all the bootstrap events, given by Eq. (3.61), and C is the covariance matrix

$$C = \begin{pmatrix} \sigma^2_{lo} & \rho_{lo,up}\;\sigma_{lo}\sigma_{up} \\ \rho_{up,lo}\;\sigma_{lo}\sigma_{up} & \sigma^2_{up} \end{pmatrix} \tag{3.68}$$

with $\sigma_{lo(up)}$ and $\rho_{lo,up} = \rho_{up,lo}$ being given by Eqs. (3.62) and (3.63), respectively. In Eq. (3.67) the normalization has been chosen so that

$$\int_{-\infty}^{+\infty}\int_{-\infty}^{+\infty} df_U\, df_L\, P_{LU}(f_L, f_U) = 1\,. \tag{3.69}$$

Using the product of the distributions (3.64) and (3.67) we can compute the final values of the form factor $f(t)$ and its variance $\sigma^2_f(t)$ as

$$f(t) = \frac{f_{lo}(t) + f_{up}(t)}{2}\,, \tag{3.70}$$

$$\sigma^2_f(t) = \frac{1}{12}\left[f_{up}(t) - f_{lo}(t)\right]^2 + \frac{1}{3}\left[\sigma^2_{lo}(t) + \sigma^2_{up}(t) + \rho_{lo,up}(t)\,\sigma_{lo}(t)\,\sigma_{up}(t)\right]\,. \tag{3.71}$$

In conclusion, let us highlight here that the overall procedure described above can be easily extended also to the FFs $f(q^2), g(q^2), \mathcal{F}_1(q^2), P_1(q^2)$ entering $B \to D^*\ell\nu$ decays, keeping in mind that in this case these FFs have to respect the KCs shown in Eqs. (3.18)-(3.19).

3.3.5 What if only a small percentage of the bootstraps survive to the filters?

In some of the analyses of the lattice data that we are going to present we have encountered the following phenomenon. As clear from the previous discussion, for some of the bootstrap events no solution can be found, either because $\Delta_2 < 0$ or because there is no overlap between the regions allowed by the KCs. This may obviously happen for a statistical fluctuation of the sample at hand. When, however, the fraction of rejected bootstrap events is large, say much larger than 50%, we have to implement a procedure to increment the percentage of accepted bootstraps, otherwise it is legitimate to doubt about the statistical reliability of the final result for the FFs.

At present, we have developed two possible strategies to solve this problem.

- On the one hand, we can use a different statistical approach, like the *skeptical* one discussed in Refs. [67,68]. The basic idea is the following. Probability theory helps us in building up a model in which the values and uncertainties of the physical quantities about which we are in doubt are allowed to vary from the nominal ones. Obviously, the model is not unique, as not unique are the probability distributions that can be used. The simplest choice consists in enlarging the reported standard deviations σ_i of the measured points, by assuming the *true* standard deviations, call them σ^t_i, are related to the σ_i by a factor r_i, one for each of the measured points, *i.e.* $\sigma^t_i = r_i\,\sigma_i$, whereas the average values $\bar{f}_i$ are the same. All the points i are treated democratically and

fairly, *i.e.* our prior belief of each r_i has expected value equal to one; its prior distribution does not depend on the point; we are skeptical, and hence each r_i has *a priori* a wide range of possibilities described by a probability distribution, with a prior 100% standard uncertainty on r_i, i.e. $\sigma(r_i)/E[r_i] = 1$.

The simplest model is to introduce a Gamma probability distribution for the variable $r \geq 0$

$$P_{skept}(r) = \frac{1}{B\ \Gamma(A)} \left(\frac{r}{B}\right)^{A-1} e^{-r/B}\ . \tag{3.72}$$

The parameters A and B are fixed by imposing that this distribution has both mean value and variance equal to 1. A simple calculation shows that this request corresponds to the choice $A = B = 1$, i.e. $P_{skept}(r) = e^{-r}$. At this point, we slightly modify the procedure previously described, namely we build up a multivariate Gaussian distribution whose covariance matrix now is

$$\Sigma_{ij} = \rho_{ij}\sigma_i\sigma_j \times r^2, \tag{3.73}$$

where the σ's are the uncertainties of the measured points in the numerical simulation and ρ_{ij} the corresponding correlation matrix.

Thus, according to Eq. (3.72) we extract N_r values of r and, for each of them, N_b bootstrap events for both the FFs values and the susceptibilities. To decide whether a single bootstrap event is accepted or rejected, let us fix the bootstrap event, *i.e.* the i-th event N_i, and we consider N_i^r values of r. We check the unitarity constraint for all the FFs for each of the N_i^r events, then, we compute the lower and the upper bounds for the survived $\hat{N}_r^i \leq N_r^i$ events and check whether the KCs are verified or not. This second step will leave us with $\tilde{N}_r^i \leq \hat{N}_r^i$ bootstraps. Our prescription is thus the following: *the event N_i is considered as accepted if $\tilde{N}_r^i \neq 0$, namely if there exists at least one value of r which passes both the unitarity and the KC filters.* Adopting this ansatz, we see that a much larger fraction of the generated events is accepted.

At this point, we combine the values of the accepted r in a unique value. We proceed in three steps. For each bootstrap we compute the mean value of r over the $\tilde{N}_i^r$ extractions. Then, we find the r (among the $\tilde{N}_i^r$ extracted) closest to that mean value. Finally, we save the event corresponding to that r as representative of the bootstrap that we have fixed. Note that in this way we are guaranteed that the new bootstrap events will pass both the unitarity and the KC filters.

- On the other hand, we can adopt an *iterative procedure*. The idea is as follows. We start from a given dataset of points for the FFs and generate a sample of bootstrap events according to the their correlations. Then, we apply the unitarity filters of the DMM to the FFs. If they are satisfied only by a reduced number of bootstraps, on the subset of surviving events we recalculate the mean values, uncertainties and correlations of the FFs. The changes in the mean values and uncertainties turn out to be quite small, while the application of the unitarity filters has its major impact on the correlations among the FFs. Then, we repeat the generation of the bootstrap sample using the new input values and we apply again the unitarity filters. This procedure is repeated until the percentage of survived bootstraps is $\gtrsim 95\%$.

  It is clear that the same approach has to be developed also to properly take into account the KCs. Thus, we apply again the iterative procedure to increase each time the percentage of surviving events after imposing the filters corresponding to the KCs. Also in this case, we require a fraction of surviving events $\gtrsim 95\%$ after imposing all the filters.

3.3.6 Final observations

In order to conclude this Section, let us develop some final observations on the DMM.

First of all, with respect to the original proposal by L. Lellouch [60] and other previous studies, the main novelties in our procedure are as follows:

i) The non-perturbative determination of the relevant two-point current correlation functions on the lattice which are then used to implement the dispersive bounds;

ii) The possibility of implementing the constraints from the two-point correlation function computed non-perturbatively also in regions where the perturbative calculations used in previous analyses are non reliable and could not be used;

iii) The reduction of lattice artefacts in the two-point correlation functions using fixed-order perturbation theory on the lattice and in the continuum;

iv) A quite simpler treatment of the lattice uncertainties with respect to the method proposed in Ref. [60];

v) A new approach to a realistic estimate of the systematic errors present at small values of q^2, namely at large momenta of the final meson, based on the skeptical approach and/or the iterative procedure.

Secondly, it is interesting to compare the DMM with the other parametrizations introduced at the beginning of this Section, namely BGL, BCL and CLN. All the quantitative details about these parametrizations can be found in the Appendix B. With respect to BGL, BCL and CLN, we highlight the following important improvements:

i) Since no series expansion of the FFs at low-z is performed, the DMM is independent of any truncation error that, on the contrary, can occur in BGL, BCL or CLN. For completeness, note that according to Refs. [50,51,69] the truncation problem can be controlled in BGL and in BCL by imposing the unitarity bounds on the coefficients of the power series expansion of the FFs (these bounds are represented by Eq. (B.2) and Eq. (B.7) for BGL and BCL, respectively) and by repeating the fits at different truncation orders;

ii) Contrarily to BGL or BCL, where a truncated fit might be distorted by events which do not fulfill unitarity, in the DMM unitarity is *built-in*, hence a unitarity check of FFs data is developed independently of a particular parameterization. For completeness, also this problem can be controlled in BGL and BCL by imposing the unitarity bounds and by repeating the fits at different truncation orders;

iii) Having a set of lattice data for a FF evaluated at a series of values q_j^2 of the squared 4-momentum transfer ($j = 1, ..., N$), the DMM reproduces exactly each of the data point when $q^2 \to q_j^2$. In other words, it behaves like a fitting procedure passing exactly for the given data set.

iv) Finally, contrarily to CLN, the DMM is entirely based on first principles (*i.e.* LQCD evaluation of 2- and 3-point Euclidean correlators) and thus is independent of any approximate symmetry, as for instance the Heavy Quark Effective Theory (HQET).

For all these reasons, the DMM seems to us a very intriguing and interesting strategy for the description of the FFs in the whole kinematical range. However, for completeness, let us mention

also one theoretical limitation that affects this method. As clearly stated above, the DMM allows to compute the lower/upper bounds of a FF through Eq. (3.53) once we have chosen our set of input data. This set is composed by the susceptibility of a given spin-parity quantum channel and by the LQCD determinations of the FF at some values of the momentum transfer. Now, there is not a straightforward way to include the experimental determinations of the differential decay width of a given process among the aforementioned input data. In other words, it is not straightforward to include these measurements inside the original matrix in Eq. (3.43). Some preliminary results can be found in [70] in the case of production of a pseudoscalar meson. However, it will be very important for the future to overcome this problematic issue in a systematic way, by including also the cases of production of a vector meson or a baryon.

Let us now describe in detail the results of the phenomenological application of the DMM to the semileptonic $B \to D^{(*)}\ell\nu$ decays.

Chapter 4

The DMM analysis of the $b \to c$ quark transitions

In this Chapter we will firstly apply the Dispersive Matrix approach to describe the FFs entering in the $B \to D^{(*)}\ell\nu$ decays in the whole kinematical range. As stated in Chapter 3, for the $B \to D^{(*)}\ell\nu$ decays the kinematical regions accessible to LQCD calculations are still restricted to small values of the recoil. In this Thesis, in fact, we will make use of lattice computations in final form for $B \to D\ell\nu$ decays [71] and for the $B \to D^*\ell\nu$ ones [55], whose results are available at non-zero, although small, recoil. [1] Our fundamental assumption relies on a different treatment of the lattice results and of the experimental measurements. To be more specific, our approach is to use lattice calculations alone, combined with unitarity, to determine the dependence of the FFs on the momentum transfer. Then, we compute the theoretical expectations of the differential decay widths, to be compared with the experiment in order to determine $|V_{cb}|$. In what follows, we will treat separately the $B \to D\ell\nu$ and the $B \to D^*\ell\nu$ cases separately. Moreover, we will extend our analysis to other semileptonic heavy-to-heavy B decays, namely the $B_s \to D_s^{(*)}\ell\nu$ transitions. This study, in fact, will allow us to obtain new exclusive determinations of the CKM matrix elements $|V_{cb}|$, as well as to develop further tests of LFU.

4.1 $|V_{cb}|$ and $R(D)$ from $B \to D\ell\nu$ decays

Here we study semileptonic $B \to D$ decays in order to extract $|V_{cb}|$ and the ratio $R(D)$ through the DMM. The inputs are the FNAL/MILC data [71], summarized in the Table 4.1. There exists another lattice computation performed by the HPQCD Collaboration [73], however the HPQCD values of the FFs are compatible with the FNAL/MILC results within larger uncertainties. For this reason, they will not be considered in the following. For what concerns the susceptibilities, we use the results of our non-perturbative lattice computation, whose basic ideas have been described in Appendix D and whose results are contained in the last column of Table D.1.

In order to write down the matrices in Eq. (3.43) (or, equivalently, in Eq. C.3) for $f_{+,0}(z)$, we need the following kinematical functions

$$\phi_+(z) \;=\; \frac{8r^2}{m_B}\sqrt{\frac{16}{3\pi}}\,\frac{(1+z)^2\sqrt{1-z}}{\left[(1+r)(1-z)+2\sqrt{r}(1+z)\right]^5}\;, \tag{4.1}$$

[1] Note that, in the latter case, new results of LQCD computations of the FFs are expected by the JLQCD Collaboration [72].

	FNAL/MILC data
$f_+(1)$	1.1994(095)
$f_+(1.08)$	1.0941(104)
$f_+(1.16)$	1.0047(123)
$f_0(1)$	0.9026(072)
$f_0(1.08)$	0.8609(077)
$f_0(1.16)$	0.8254(094)

Table 4.1: *Values of the LQCD computations of the FFs $f_{+,0}(w)$ as reported by FNAL/MILC Collaboration in [71].*

$$\phi_0(z) \quad = \quad r(1-r^2)\sqrt{\frac{16}{\pi}}\,\frac{(1-z^2)\sqrt{1-z}}{\left[(1+r)(1-z)+2\sqrt{r}(1+z)\right]^4} \tag{4.2}$$

with $r \equiv m_D/m_B$. Note that they coincide with the expressions (3.45) under the choices $q^2 = 0$ and $n_I = 2$. Each of these kinematical functions is then modified according to Eq. (5.6) using the poles in Table III of [69].

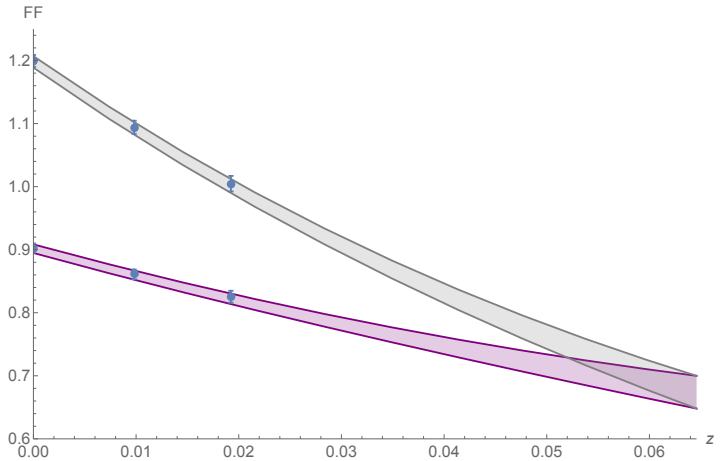

Figure 4.1: *The bands of the FFs entering $B \to D\ell\nu$ decays computed through the DMM. The colour code is (lower) violet band for $f_0(z)$, (higher) gray one for $f_+(z)$. The blue points are the FNAL/MILC data [71], summarized in Table 4.1.*

In Fig. 4.1 we show the bands of the FFs resulting from the DMM. In order to obtain these bands we had to use the sceptical approach, since only the $\sim 15\%$ of bootstraps is accepted. Following the prescription described in the previous Section and extracting 100 values of r (common to both FFs), we are able to recover all the generated bootstraps, which then contribute to the final bands of the FFs. The extrapolation at z_{max} is crucial in order to analyse experimental data. The matrix description gives the result

$$f(z_{max}) = 0.674 \pm 0.026, \tag{4.3}$$

which is compatible with the Light Cone Sum Rule (LCSR) estimate [74]

$$f(z_{max})_{\rm LCSR} = 0.65 \pm 0.08.$$

4.1.1 Extraction of $|V_{cb}|$

In order to obtain an updated value of $|V_{cb}|$ from $B \to D$ decays, we put together our description of the lattice FFs in the whole kinematical range and the experiments. Let us briefly describe the experimental state-of-the-art. The most recent measurement of the differential decay width $d\Gamma/dw$, see Eq.(3.10) for its theoretical expression, has been performed at Belle [75]. In Table II of this work, the authors report the results of the measurements, dividing the kinematical region into 10 bins in the recoil variable w. The correlation matrix of the systematic errors is also given. Following the procedure used in [76] to extract $|V_{cd}|$ and $|V_{cs}|$ in the case of the semileptonic $D \to \pi\ell\nu$ and $D \to K\ell\nu$ decays, we then re-express Eq. (3.9) as

$$|V_{cb}| = \sqrt{\frac{d\Gamma}{dq^2}|_{exp} \times \frac{24\pi^3}{G_F^2 \eta_{EW}^2 |\vec{p}_D|^3 |f^+(q^2)|^2_{th}}}. \tag{4.4}$$

Hence, we generate N_{boot} bootstraps of the experimental differential decay width for every bin in w through a multivariate Gaussian distribution and similarly we extract N_{boot} bootstrap events for the FFs $f_{+,0}(w)$ for each of the bins w_i $(i = 1, \cdots, 10)$. The mean value and the covariance matrix of the distribution can be directly computed through our DMM. Finally, we compute $|V_{cb}|$ for each recoil bin through the expression (4.4).

Let us now fix a particular bin. In order to extract a mean value and uncertainty for $|V_{cb}|$, we fit the histogram of these events with a normal distribution and save the values of the corresponding marginalized parameters. We then have 10 values of the CKM matrix element, one for each w bin. In order to compute the average of these quantities by taking appropriately into consideration the correlations, calling $\mathbf{C}$ the covariance matrix and $|V_{cb}|_i$ $(i = 1, \cdots, 10)$ the values of the CKM matrix element for each bin, it is sufficient to compute [77]

$$|V_{cb}| = \frac{\sum_{i,j=1}^{10} (\mathbf{C}^{-1})_{ij} |V_{cb}|_j}{\sum_{i,j=1}^{10} (\mathbf{C}^{-1})_{ij}}, \qquad \sigma^2_{|V_{cb}|} = \frac{1}{\sum_{i,j=1}^{10} (\mathbf{C}^{-1})_{ij}}. \tag{4.5}$$

The above formulæ can be used since the distributions of the bootstrap events of $|V_{cb}|$ for each bin are approximately Gaussian. Now, the application of Eq. (4.5) gives us the following result for $|V_{cb}|$

$$|V_{cb}| \times 10^3 = 41.0 \pm 1.2, \tag{4.6}$$

which is compatible with the most recent inclusive determination $|V_{cb}|_{\rm incl} = (42.16 \pm 0.50) \cdot 10^{-3}$ [30] at the 0.9σ level. In Fig. 4.2 we show the 10 values of the CKM matrix element, one for each w bin, and the final band corresponding to Eq. (4.6).

4.1.2 Determination of the $R(D)$ ratio

Finally, let us compute a theoretical estimate of the ratio $R(D)$, defined in Eq. (3.1). Since in the $B \to D$ case we have only two FFs to deal with, we can write the rather compact expression

$$R(D) = \frac{\int_{m_\tau^2}^{(m_B - m_D)^2} dq^2 |\vec{p}_D|^3 f_+^2(q^2) \left(1 - \frac{m_\tau^2}{q^2}\right)^2 \left[1 + \frac{m_\tau^2}{2q^2} + \frac{m_B^2}{|\vec{p_D}|^2} \left(1 - \frac{m_D^2}{m_B^2}\right)^2 \frac{3m_\tau^2}{8q^2} \frac{f_0^2(q^2)}{f_+^2(q^2)}\right]}{\int_0^{(m_B - m_D)^2} dq^2 |\vec{p}_D|^3 f_+^2(q^2)}, \tag{4.7}$$

where m_τ is the mass of the τ lepton and we have considered the electron and the muon as massless. Using the bootstrap events for the FFs extracted as explained before, we compute N_{boot} values of the

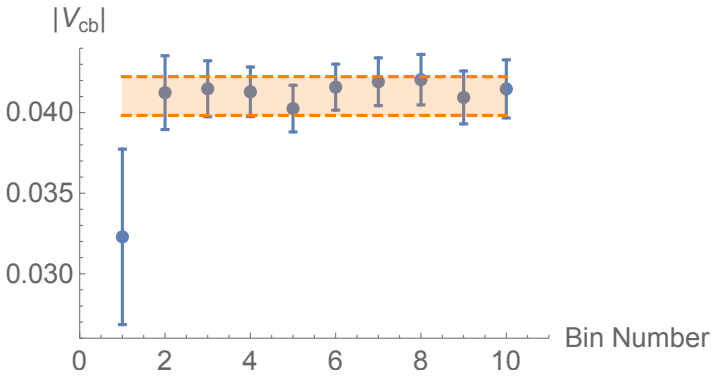

Figure 4.2: *Values of the CKM matrix element $|V_{cb}|$ resulting from the combination of the sceptical matrix description of the FFs and the experimental data by Belle. The orange band represents the result of the weighted mean described in the text.*

ratio $R(D)$, and fit the histogram of these events with a normal distribution, in order to obtain the expectation value and the uncertainty, as in Fig. 4.3. Our prediction is

$$R(D) = 0.296 \pm 0.008.$$

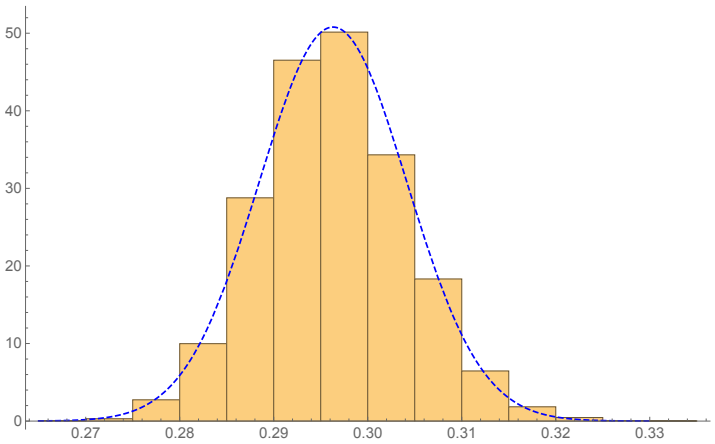

Figure 4.3: *The orange bins represent the PDF of the bootstrap events for $R(D)$. The dashed blue curve is the best Gaussian fit of the bootstraps themselves.*

4.2 $|V_{cb}|$ and $R(D^*)$ from $B \to D^* \ell \nu$ decays

Let us now apply the non-perturbative DMM to the semileptonic $B \to D^* \ell \nu$ decays. At present, the inputs for our matrices are the final results of the LQCD computations of the FFs provided by the FNAL/MILC Collaborations [55]. There, in the ancillary files, the authors give the synthetic values of the FFs $g(w), f(w), \mathcal{F}_1(w)$ and $\mathcal{F}_2(w)$ at three non-zero values of the recoil variable $(w-1)$, namely $w = \{1.03, 1.10, 1.17\}$, as well as their correlations. The FF $\mathcal{F}_2(w)$ is directly related to the pseudoscalar FF $P_1(w)$, which we will refer to hereafter, through the relation $P_1(w) = \mathcal{F}_2(w)\sqrt{r}/(1+r)$,

where $r \equiv m_{D^*}/m_B$. All the FNAL/MILC inputs are summarized in Table 4.2. Recall that these FFs have been introduced in Eqs. (3.14-3.17).

	FNAL/MILC data
$g(1.03)$ (GeV^{-1})	0.372 (14)
$g(1.10)$ (GeV^{-1})	0.331(13)
$g(1.17)$ (GeV^{-1})	0.291(17)
$f(1.03)$ (GeV)	5.80(11)
$f(1.10)$ (GeV)	5.52(11)
$f(1.17)$ (GeV)	5.27(16)

	FNAL/MILC data
$\mathcal{F}_1(1.03)$ (GeV^2)	18.85(36)
$\mathcal{F}_1(1.10)$ (GeV^2)	17.67(42)
$\mathcal{F}_1(1.17)$ (GeV^2)	16.62(67)
$P_1(1.03)$	0.978(29)
$P_1(1.10)$	0.860(29)
$P_1(1.17)$	0.763(39)

Table 4.2: *Values of the LQCD computations of the FFs $g(w), f(w), \mathcal{F}_1(w)$ and $P_1(w)$ as reported by FNAL/MILC Collaborations in [55].*

In order to write down the matrices in Eq. (3.43) (or, equivalently, in Eq. C.3) for the four FFs of interest, we need the following kinematical functions

$$\begin{aligned}
\phi_f(z) &= 4\,\frac{r}{m_B^2}\sqrt{\frac{2}{3\pi}}\,\frac{(1+z)(1-z)^{3/2}}{\left[(1+r)(1-z)+2\sqrt{r}(1+z)\right]^4}\,, \\
\phi_g(z) &= 16\,r^2\sqrt{\frac{2}{3\pi}}\,\frac{(1+z)^2}{\sqrt{1-z}\left[(1+r)(1-z)+2\sqrt{r}(1+z)\right]^4}\,, \\
\phi_{\mathcal{F}_1}(z) &= 4\,\frac{r}{m_B^3}\sqrt{\frac{1}{3\pi}}\,\frac{(1+z)(1-z)^{5/2}}{\left[(1+r)(1-z)+2\sqrt{r}(1+z)\right]^5}\,, \\
\phi_{P_1}(z) &= 16\,(1+r)r^{3/2}\sqrt{\frac{1}{\pi}}\,\frac{(1+z)^2}{\sqrt{1-z}\left[(1+r)(1-z)+2\sqrt{r}(1+z)\right]^4}
\end{aligned} \tag{4.8}$$

As for the $B \to D$ channel, the locations of the various $B_c^{(*)}$ poles are taken from Table III of Ref. [69] and the values of the susceptibilities are shown in the last column of Table D.1.

At this point, we start from a total of 12 data points for the FFs and generate a sample of 10^5 bootstrap events according to the given correlations. Then, we apply the unitarity filters of the DMM to all the FFs. They are satisfied only by a reduced number of bootstraps, namely the percentage of the surviving events is $\sim 1\%$ after imposing the three unitarity constraints on g, P_1 and $(f, \mathcal{F}_1)$. It is thus necessary to implement one of the procedures explained in the previous Section in order to increase the percentage of the accepted events. We choose the iterative procedure to achieve this goal. For this reason, on the subset of surviving events we recalculate the mean values, uncertainties and correlations of the FFs. The changes in the mean values and uncertainties turn out to be quite small, while the application of the unitarity filters has its major impact on the correlations among the FFs. We then repeat the generation of the bootstrap sample using the new input values and we apply again the unitarity filters. The overall procedure is iterated until the percentage of the accepted bootstraps is $\gtrsim 95\%$.

Recall that we have also to impose the two KCs that relate the FFs f and $\mathcal{F}_1$ at $w = 1$ and the FFs $\mathcal{F}_1$ and P_1 at $w = w_{max} = (1 + r^2)/(2r)$, shown in Eqs. (3.18)-(3.19). We apply again the iterative procedure to increase each time the percentage of surviving events after imposing these filters, requiring again a fraction of surviving events $\gtrsim 95\%$. The resulting dispersive bands of the FFs are shown in the whole range of values of the recoil w in Fig. 4.4. In particular, the extrapolations of the

FFs at $w = w_{max}$ read

$$f(w_{max}) = 4.19 \pm 0.31 \text{ GeV} , \tag{4.9}$$
$$g(w_{max}) = 0.180 \pm 0.023 \text{ GeV}^{-1} , \tag{4.10}$$
$$\mathcal{F}_1(w_{max}) = 11.0 \pm 1.3 \text{ GeV}^2 , \tag{4.11}$$
$$P_1(w_{max}) = 0.411 \pm 0.048 . \tag{4.12}$$

Our results can be compared with the results coming from LCSR [74] at $q^2 = 0$. In [74], the theoretical predictions are given in terms of the FFs V, A_1, A_2, appearing in the matrix element (3.12). Thanks to Eqs. (3.14-3.17), their results can be rephrased as

$$f(w_{max})|_{\text{LCSR}} = 4.37 \pm 0.66 \text{ GeV} ,$$
$$g(w_{max})|_{\text{LCSR}} = 0.19 \pm 0.04 \text{ GeV}^{-1} ,$$
$$\mathcal{F}_1(w_{max})|_{\text{LCSR}} = 16.0 \pm 2.1 \text{ GeV}^2 .$$

While the results for $f(w_{max})$ and $g(w_{max})$ are compatible to each other, wee see a $\sim 2\sigma$ tension in $\mathcal{F}_1(z_{max})$. This will have an important impact in the determination of both $|V_{cb}|$ and the $R(D^*)$ ratio.

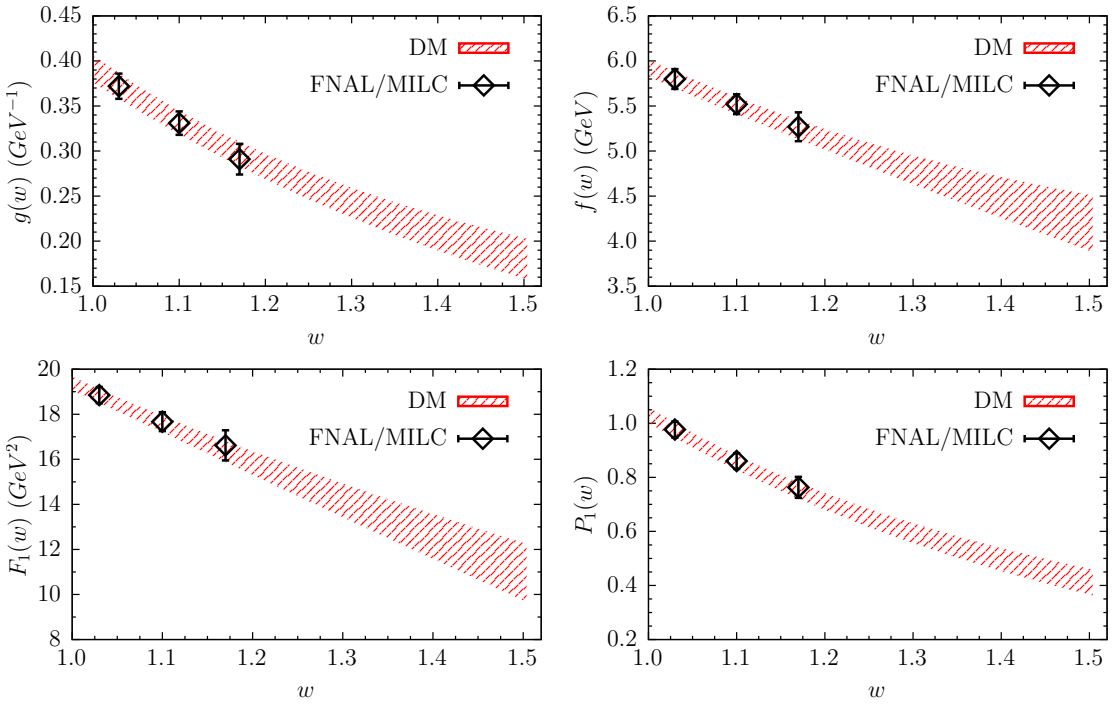

Figure 4.4: *The bands of the FFs $g(w)$, $f(w)$, $\mathcal{F}_1(w)$ and $P_1(w)$ computed by the DMM after imposing both the unitarity filter and the two KCs (3.18)-(3.19). The FNAL/MILC values [55] used as inputs for the DMM are represented by the black diamonds.*

Let us now discuss in detail the hypothesis of Gaussianity of the distribution of the bootstrap events of the FFs. In other words, let us discuss why the assumption that the distribution of the surviving events is Gaussian is a good approximation. We point out that the percentage of surviving events rapidly increases towards 100% after applying the Gaussian approximation at each step of the

iterative procedure. This is reassuring concerning the impact of the deviations from Gaussianity. In fact, if the filters would produce a non-negligible amount of non-Gaussian events (probably in the tails of the multivariate distribution), we would have observed a slow increase of the surviving events after each iteration and a saturation of the final percentage significantly below the 100% level.

We have performed a further check concerning the iterative procedure. Since the number of surviving events after the application of both the unitarity filters and the KCs is very limited, we have increased significantly the initial number of events from 10^5 to 10^7. In this way after the first iteration the number of surviving events is $\simeq 2500$, which may represent an acceptable size of the sample. In Fig. 4.5 we compare the DMM bands obtained after the first iteration starting from 10^7 events with those previously shown in Fig. 4.4, i.e. after the fifth iteration corresponding to a final sample with 10^5 events. The differences are quite limited.

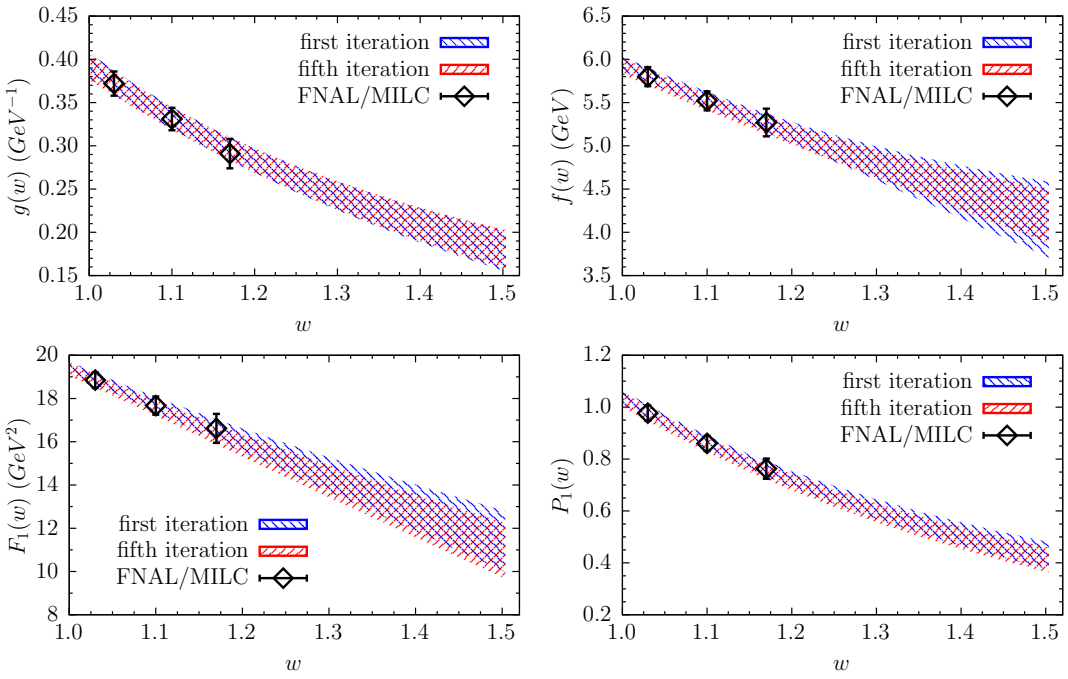

Figure 4.5: *The bands of the FFs $g(w)$, $f(w)$, $\mathcal{F}_1(w)$ and $P_1(w)$ computed by the DMM after the first iteration starting from 10^7 initial events (corresponding to $\simeq 2500$ surviving events) and after the fifth iteration (corresponding to a final sample with 10^5 events). The black diamonds represent the FNAL/MILC values [55] used as inputs for the DMM.*

4.2.1 Extraction of $|V_{cb}|$

Let us now use the dispersive bands of the FFs to extract $|V_{cb}|$ from the experimental data. For what concerns the experimental state-of-the-art, at present we have at our disposal two different measurements of the differential decay widths, both performed by the Belle Collaboration [37, 78]. The authors report the results of the measurements of the differential decay widths $d\Gamma/dx$, where x is one of the four kinematical variables of interest ($x = w, \cos\theta_l, \cos\theta_v, \chi$), by dividing the available region for each variable into 10 bins. The numerical values of these bins can be found in Table II of [37]. Recall that the various helicity angles are defined in Fig. 3.2.

Hence, we have globally 40 points for each of the two different measurements [37, 78]. The correlation matrices of the errors are also presented for both the measurements. Our strategy is thus the following. First of all, we compute the N_{boot} bootstraps of theoretical $d\Gamma/dx$ from the expression (3.20) using the dispersive bands of the FFs, *i.e.* by generating N_{boot} values of the FFs for each of the experimental bins through a multivariate Gaussian distribution. Then, we also generate an independent set of N_{boot} bootstrap values of the experimental differential decay widths for all the bins. For each of them, we fit the histogram of the resulting N_{boot} estimates of $|V_{cb}|$ with a normal distribution and save the corresponding mean value and uncertainty. Thus, we find 10 values of the CKM matrix element for each of the four kinematical variables $(w, \cos\theta_l, \cos\theta_v, \chi)$ and for each of the two experiments [37, 78], which are then averaged through the Eq. (4.5).

In Fig. 4.6 we show the bin-per-bin distributions of $|V_{cb}|$ for each kinematical variable x and for each experiment, together with their final weighted mean values. The latter ones are collected also in Table 4.3 together with the corresponding values of the reduced χ^2-variable, $\chi^2/(\text{d.o.f.})$, being the number of d.o.f. equal to 9. The important issue is that anomalous underestimates of the mean values of $|V_{cb}|$ can be observed in the case of some of the variables x, which correspond also to large values of the reduced χ^2-variable. This effect is well-known in literature and has been studied by Giulio D'Agostini in [79]. According to him, it can happen that "best fits to data which are affected by systematic uncertainties on the normalization factor have the tendency to produce curves lower than expected if the covariance matrix of the data points is used in the definition of the χ^2". In particular, this bias becomes unacceptable if the normalization error is large or a large number of data points are fitted.

experiment	$\|V_{cb}\|(x = w)$	$\|V_{cb}\|(x = \cos\theta_l)$	$\|V_{cb}\|(x = \cos\theta_v)$	$\|V_{cb}\|(x = \chi)$
Ref. [37]	0.0399 (12)	0.0411 (16)	0.0416 (16)	0.0414 (17)
$\chi^2/(\text{d.o.f.})$	1.72	1.10	1.21	1.45
Ref. [78]	0.0392 (9)	0.0399 (13)	0.0393 (11)	0.0418 (13)
$\chi^2/(\text{d.o.f.})$	1.62	2.41	3.77	0.79

Table 4.3: *Mean values and uncertainties of the CKM element $|V_{cb}|$ obtained by the correlated average (4.5) for each of the four kinematical variables x and for each of the two experiments [37, 78] adopting the original covariance matrices of the Belle experiments. The corresponding values of the reduced χ^2-variable, $\chi^2/(\text{d.o.f.})$, are also shown.*

We now illustrate a procedure that helps to overcome the possible aforementioned underestimation of $|V_{cb}|$. For each of the two Belle experiments, we consider the relative differential decay rates given by the ratios $(d\Gamma/dx)/\Gamma$ (where again $x = w, \cos\theta_l, \cos\theta_v, \chi$) for each bin by using the experimental data. In this way, we guarantee that the sum over the bins is exactly independent (bootstrap by bootstrap) of the choice of the variable x. Hence, we compute a *new* correlation matrix using the bootstrap events for the ratios $(d\Gamma/dx)/\Gamma$. The new correlation matrix has, by construction, four eigenvalues equal to zero, because the sum over the bins of each of the four variables x is always equal to unity. In other words, the number of independent bins for the ratios is 36 and not 40 for each experiment. Then, a *new* covariance matrix of the experimental data is constructed by multiplying the new correlation matrix by the original uncertainties associated to the measurements.

At this point, we repeat the whole procedure for the extraction of $|V_{cb}|$ using the new experimental

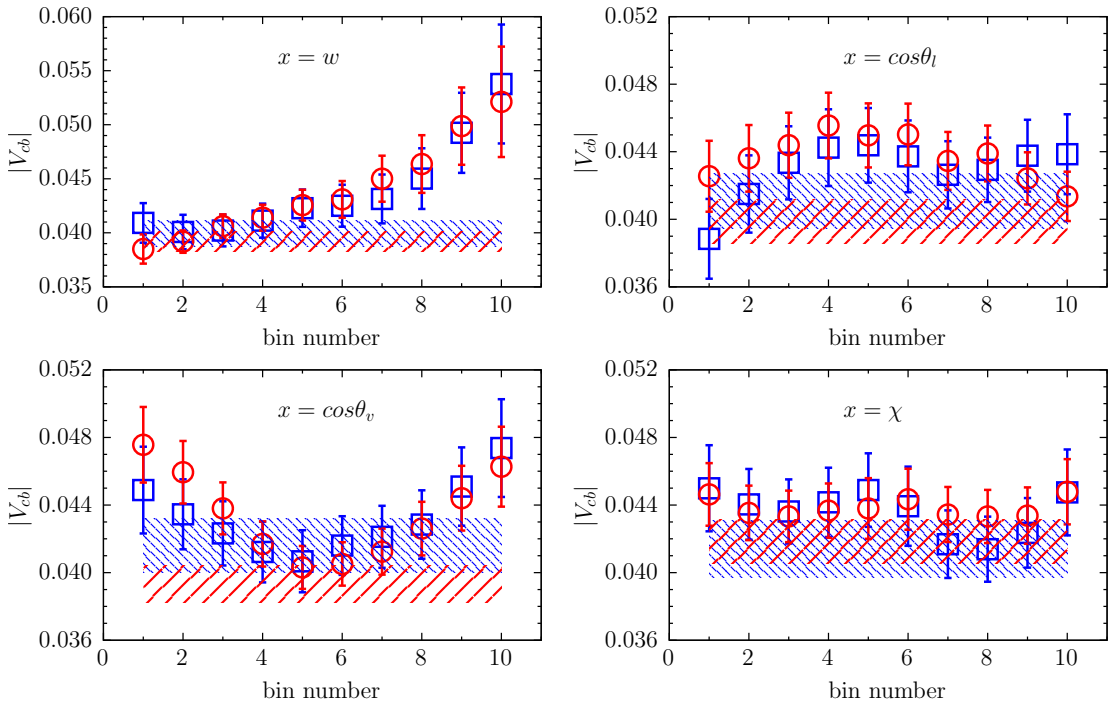

Figure 4.6: *The bin-per-bin estimates of $|V_{cb}|$ and their weighted means for each kinematical variable x and for each experiment adopting the original covariance matrices of the Belle experiments. The blue squares and the red circles correspond respectively to the first [37] and to the second [78] set of the Belle measurements. The dashed blue (red) bands are the weighted averages in the case of the blue squares (red circles) for each variable x.*

covariance matrices. In Fig. 4.7 we show the new bin-per-bin distributions of $|V_{cb}|$ for each kinematical variable x and for each experiment, together with their final weighted mean values. The latter ones are collected also in Table 4.4. A drastic improvement of the values of the reduced χ^2-variable is obtained for each of the kinematical variable x and for each of the two Belle experiments.

experiment	$\|V_{cb}\|(x = w)$	$\|V_{cb}\|(x = \cos\theta_l)$	$\|V_{cb}\|(x = \cos\theta_v)$	$\|V_{cb}\|(x = \chi)$
Ref. [37]	0.0405 (9)	0.0417 (13)	0.0422 (13)	0.0427 (14)
χ^2/(d.o.f.)	1.01	0.89	0.66	0.72
Ref. [78]	0.0394 (7)	0.0409 (12)	0.0400 (10)	0.0427 (13)
χ^2/(d.o.f.)	1.21	1.36	1.99	0.38

Table 4.4: *The same as in Table 4.3, but using the new experimental covariance matrices described in the text.*

Then, the eight mean values of $|V_{cb}|$ in Table 4.4 have to be averaged to obtain a final estimate. In order to avoid that the D'Agostini bias may affect our final result, we have decided to follow the conservative strategy described in Ref. [80]. To be more specific, we assign to all the $|V_{cb}|$ estimates

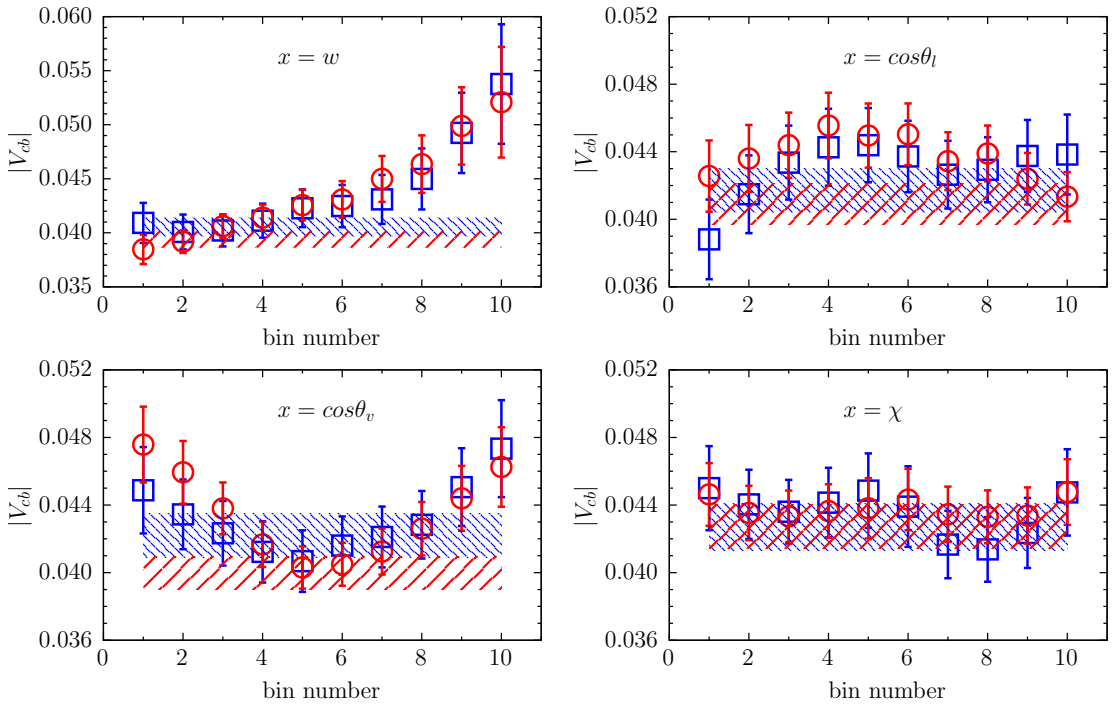

Figure 4.7: *The same as in Fig. 4.6, but using the new experimental covariance matrices described in the text.*

in Table 4.4 the same weight. Let us now define $\kappa \equiv |V_{cb}|$ to simplify the discussion. We assume that the observable κ has a distribution $\hat{f}(\kappa)$ given by $\hat{f}(\kappa) = (1/N)\sum_{k=1}^{N} \hat{f}_k(\kappa)$. Here $\hat{f}_k(\kappa)$ is the distribution provided by the bootstrap sample related to the k-th determination of the CKM matrix element, which is then characterized by central value κ_k and standard deviation σ_k. Thus we estimate the central value and the error for the observable κ through the mean value and the standard deviation of the distribution $\hat{f}(\kappa)$, which are given by the formulæ

$$\mu_\kappa = \frac{1}{N}\sum_{k=1}^{N} \kappa_k \ , \tag{4.13}$$

$$\sigma_\kappa^2 = \frac{1}{N}\sum_{k=1}^{N} \sigma_k^2 + \frac{1}{N}\sum_{k=1}^{N} (\kappa_k - \mu_\kappa)^2 \ , \tag{4.14}$$

where the second term in the r.h.s. of Eq. (4.14) accounts for the spread of the values of $|V_{cb}|$ corresponding to the various kinematical variables and experiments. We obtain for each of the two Belle experiments the averages

$$|V_{cb}| = (41.8 \pm 1.5) \cdot 10^{-3} \qquad \text{Ref. [37]} \tag{4.15}$$

$$= (40.8 \pm 1.7) \cdot 10^{-3} \qquad \text{Ref. [78]} \tag{4.16}$$

and by combining the two Belle experiments the final estimate

$$|V_{cb}| = (41.3 \pm 1.7) \cdot 10^{-3} \ , \tag{4.17}$$

which is compatible with the most recent inclusive determination $|V_{cb}|_{\rm incl} = (42.16 \pm 0.50) \cdot 10^{-3}$ [30] at the 0.5σ level. Without the modification of the experimental covariance matrices (i.e. using the eight mean values shown in Table 4.3) the final estimate of $|V_{cb}|$ would have read

$$|V_{cb}| = (40.5 \pm 1.7) \cdot 10^{-3} \ ,$$

which is still compatible with the most recent inclusive determination at the 1σ level.

At this point, let us note that there is another way to determine an exclusive value of $|V_{cb}|$ from semileptonic $B \to D^*$ decays. Starting from the unitarity bands of the FFs plotted in Figure 4.4, we can compute the theoretical expectation of the total decay width and we can then compare it with its measurements. From the experimental point of view, in fact, the Belle Collaboration has given its estimate of the branching ratio of semileptonic $B \to D^*$ decays for each of the two analyzes, namely $\mathcal{B}(B \to D^*\ell\nu) = (4.95 \pm 0.11 \pm 0.22) \times 10^{-2}$ [37] and $\mathcal{B}(B \to D^*\ell\nu) = (5.04 \pm 0.02 \pm 0.16) \times 10^{-2}$ [78,81]. Taking into consideration these values, our final results of the study of the total decay width read

$$|V_{cb}| = (42.9 \pm 1.8) \cdot 10^{-3} \qquad \text{Ref. [37]} \tag{4.18}$$

$$= (43.3 \pm 1.6) \cdot 10^{-3} \qquad \text{Ref. [78,81]} \tag{4.19}$$

Note that these values are by construction independent of all the correlations coming from the theory or from the experiment, since it is based on the analysis of the total decay width. Moreover, the values in Eq. (4.18) and Eq. (4.19) are compatible with the results coming from the study of the differential decay widths, namely the values in Eq. (4.15) and Eq. (4.16), respectively. According to us, this agreement is a strong indication of the robustness of our final estimate of $|V_{cb}|$, shown in Eq. (4.17).

Going back to Fig. 4.7, few comments naturally follow:

a) in the top left panel the value of $|V_{cb}|$ exhibits some dependence on the specific w-bin. The value obtained adopting a constant fit is dominated by the bins at small values of the recoil, where direct lattice data are available and the lenght of the momentum extrapolation is limited;

b) in the bottom left panel the value of $|V_{cb}|$ deviates from a constant behavior, as it is also signaled by the large value of the corresponding reduced χ^2-variable for the second set of the Belle measurements. Instead of a constant fit, we try a quadratic one of the form $|V_{cb}| \left[1 + \delta B \cos^2(\theta_v)\right]$, suggested by the structure of the differential decay rate $d\Gamma/d\cos(\theta_v)$ within the Standard Model. If the dependence of the experimental and theoretical decay rates upon $\cos(\theta_v)$ were the same, then the parameter δB would identically vanish. Instead we get a non-vanishing value of the parameter δB, namely: $|V_{cb}| = (41.1 \pm 1.4) \cdot 10^{-3}$ and $\delta B = 0.144 \pm 0.074$ for the first set [37] of the Belle measurements, and $|V_{cb}| = (40.8 \pm 1.0) \cdot 10^{-3}$ and $\delta B = 0.184 \pm 0.050$ for the second set [78]. The values of $|V_{cb}|$ are consistent with each other and also with the corresponding values obtained adopting a constant fit and shown in the fourth column of Table 4.4.

Both observations may be related to a different w-slope of the theoretical FFs based on the lattice results of Ref. [55] with respect to the Belle experimental data [37,78]. This crucial issue (a kind of a new *slope puzzle*) needs to be further investigated by forthcoming calculations of the FFs at non-zero recoil expected from the JLQCD Collaboration as well as by future improvements of the precision of the experimental data.

In conclusion, let us highlight the main features of our procedure to extract $|V_{cb}|$ from exclusive experiments. First of all, contrarily to other analyses present in literature, we choose to keep distinct the lattice and the experimental data. In other words, only LQCD computations are used in order to derive the allowed unitarity bands of the FFs as functions of the recoil thanks to the DMM. This is a

key issue since, by construction, theoretical computations of the FFs on the lattice are SM-like. This is not guaranteed for the experimental data which, in principle, can contain NP contributions. Thus, the experimental measurements are considered only for determining bin-per-bin estimates of $|V_{cb}|$. It can happen that the values of $|V_{cb}|$ deviate from a constant behavior and this will be signaled by a large value of the reduced χ^2-variable. This is in fact the case for the $d\Gamma/d\cos(\theta_v)$ distribution. As clearly discussed above, in that case the substitution of a constant fit with a quadratic one does not change the final value of $|V_{cb}|$, while pointing towards the existence of a different bin-dependent NP effect. This is demonstrated by the non-vanishing values of the δB parameters. Secondly, in our study the pseudoscalar FF $P_1(z)$ plays a central role in the determination of $|V_{cb}|$, although not explicitly appearing in Eq. (3.20) in the massless lepton limit. In fact, the KC (3.19) allows us to constrain the $\mathcal{F}_1(w)$ band obtaining a better precision in the region not explored by lattice computations, *i.e.* at large values of w.

4.2.2 Determination of the $R(D^*)$ ratio and the polarization observables

By using the unitarity bands of the FFs we can compute the pure theoretical expectation values of the ratio $R(D^*)$, defined in Eq. (3.1), as well as some polarization observables, namely the τ-polarization $P_\tau(D^*)$ and the longitudinal D^*-polarization $F_L(D^*)$. The expressiopns of these latter quantities in terms of the FFs can be read directly from [69, 82, 83]. Our final results thus read

$$R(D^*) = 0.275 \pm 0.008 \,, \tag{4.20}$$
$$P_\tau(D^*) = -0.529 \pm 0.007 \,, \tag{4.21}$$
$$F_L(D^*) = 0.414 \pm 0.012 \tag{4.22}$$

to be compared with the experimental values

$$R(D^*)|_{\rm exp} = 0.295 \pm 0.011 \pm 0.008 \qquad \text{Ref. [40]} \,, \tag{4.23}$$
$$P_\tau(D^*)|_{\rm exp} = -0.38 \pm 0.51^{+0.21}_{-0.16} \qquad \text{Ref. [84]} \,, \tag{4.24}$$
$$F_L(D^*)|_{\rm exp} = 0.60 \pm 0.08 \pm 0.04 \qquad \text{Ref. [85]} \,. \tag{4.25}$$

While the theoretical and the experimental values of $P_\tau(D^*)$ are in agreement (mainly due to the larger experimental uncertainty), the compatibility for $R(D^*)$ and $F_L(D^*)$ is at the $\sim 1.3\sigma$ and $\sim 2.1\sigma$ level, respectively. Note that the $R(D^*)$ anomaly results to be smaller with respect to the $\sim 2.5\sigma$ tension stated by HFLAV Collaboration [40]. In conclusions, our findings are summarized in Fig. 4.8.

4.3 The DMM applied to the $B_s \to D_s^{(*)}\ell\nu$ decays

In this Section we will apply the DMM to semileptonic $B_s \to D_s^{(*)}\ell\nu$ decays. From the theoretical point of view, these transitions are completely equivalent to the $B \to D^{(*)}\ell\nu$ ones, the only difference is that the quark spectator is a strange quark rather than a light one. In particular, one can define the FFs of interest for these transitions in a completely analogous way to Eqs. (3.4) and (3.12). For reasons of clarity, we will denote the FFs entering in semileptonic $B_s \to D_s^{(*)}\ell\nu$ with a s superscript. Note that these transitions are very important since they allow us to obtain complementary exclusive determinations of $|V_{cb}|$ and to further test LFU in $\Delta B = 1$ transitions.

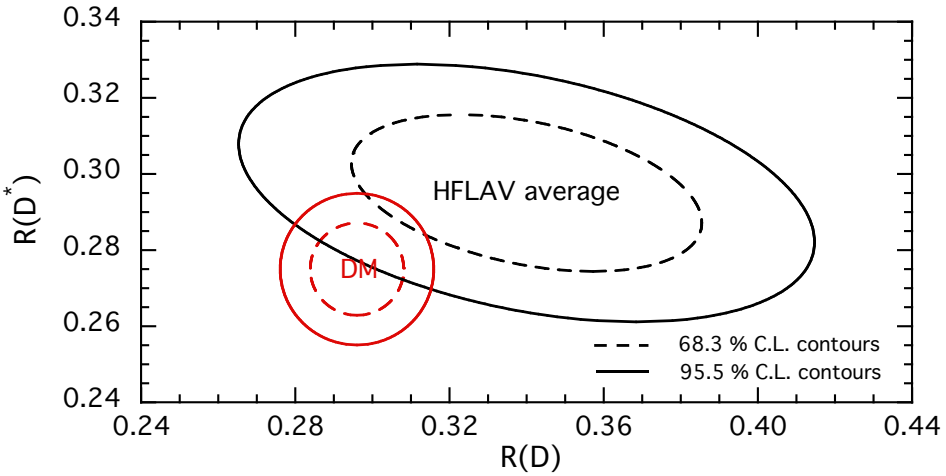

Figure 4.8: *The contour plots of the DMM results for the ratios $R(D)$ and $R(D^*)$, obtained respectively in Ref. [3] and in this work, compared with those corresponding to the experimental world averages from HFLAV [40].*

4.3.1 LQCD computations of the FFs and application of the DMM

The FFs entering semileptonic $B_s \to D_s^{(*)}\ell\nu_\ell$ decays have been computed on the lattice by the HPQCD Collaboration in Refs. [86,87], where the authors have made available the results of BCL fits of the FFs extrapolated to the physical b-quark point and to the continuum limit. The BCL fits of Refs. [86, 87] provide the FFs in their whole kinematical range, but, as far as statistical and systematic effects are concerned, LQCD computations are more precise and accurate at high values of q^2. Moreover, we want to use our DM method in order to extrapolate the shape of the FFs in their whole kinematical range, minimizing in this way the impact of any assumption about the momentum dependence of the FFs. Therefore, we select only three values of q^2 in the high-q^2 regime, namely at $q^2 \approx \{0.7, 0.85, 1.0\} \cdot q^2_{max}$, where $q^2_{max} = 11.6$ GeV^2 for the $B_s \to D_s\ell\nu_\ell$ decays and $q^2_{max} = 10.6$ GeV^2 for the $B_s \to D_s^*\ell\nu_\ell$ decays. Thus, from the marginalized values of the BCL coefficients we reconstruct the FFs in the high-q^2 regime in order to use them as inputs for the DM method. The mean values and uncertainties of the LQCD inputs are collected in Table 4.5 for the $B_s \to D_s\ell\nu_\ell$ decays and in Table 4.6 for the $B_s \to D_s^*\ell\nu_\ell$ decays.

q^2 (GeV^2)	$f_+^s(B_s \to D_s)$	$f_0^s(B_s \to D_s)$
8.5	1.021(28)	0.834(12)
10.0	1.108(34)	0.873(13)
11.6	1.209(41)	0.917(15)

Table 4.5: *Values of the vector $f_+^s(q^2)$ and scalar $f_0^s(q^2)$ FFs for the $B_s \to D_s\ell\nu_\ell$ decays, evaluated at $q^2 = \{8.5, 10.0, 11.6\}$ GeV^2 using the BCL fit computed by the HPQCD Collaboration in Ref. [86].*

We now apply the DM approach to the description of the FFs entering the semileptonic $B_s \to D_s^{(*)}\ell\nu_\ell$ decays. The non-perturbative values of the dispersive bounds corresponding to the $b \to c$ transition are the same ones adopted for the semileptonic $B \to D^{(*)}\ell\nu$ decays, namely the ones in the

q^2 (GeV^2)	$f^s(B_s \to D_s^*)$	$g^s(B_s \to D_s^*)$	$\mathcal{F}_1^s(B_s \to D_s^*)$	$P_1^s(B_s \to D_s^*)$
7.1	5.40(22)	0.341(35)	18.01(75)	0.781(42)
8.9	5.73(22)	0.369(38)	18.91(70)	0.861(45)
10.6	6.09(22)	0.401(44)	19.81(73)	0.949(51)

Table 4.6: *Values of the FFs $f^s, g^s, \mathcal{F}_1^s$ and P_1^s for the $B_s \to D_s^* \ell \nu_\ell$ decays, evaluated at $q^2 = \{7.1, 8.9, 10.6\}$ GeV^2 using the BCL fit computed by the HPQCD Collaboration in Ref. [87]. The FF P_1^s is dimensionless, while the FFs f^s, g^s and $\mathcal{F}_1^s$ are given in units of GeV, GeV^{-1} and GeV^2, respectively.*

last column of Table D.1. The kinematical functions associated to the semileptonic FFs reads

$$\begin{aligned} \phi_{f_0^s}(z,0) &= 2r(1-r^2)\sqrt{\frac{2n_I}{\pi}}\frac{(1-z^2)\sqrt{1-z}}{\left[(1+r)(1-z)+2\sqrt{r}(1+z)\right]^4}\,, \\ \phi_{f_+^s}(z,0) &= \frac{16r^2}{m_{B_s}}\sqrt{\frac{2n_I}{3\pi}}\frac{(1+z)^2\sqrt{1-z}}{\left[(1+r)(1-z)+2\sqrt{r}(1+z)\right]^5} \end{aligned} \tag{4.26}$$

with $r \equiv m_{D_s}/m_{B_s}$, and

$$\begin{aligned} \phi_{f^s}(z,0) &= 4\frac{r_*}{m_{B_s}^2}\sqrt{\frac{n_I}{3\pi}}\frac{(1+z)(1-z)^{3/2}}{\left[(1+r_*)(1-z)+2\sqrt{r_*}(1+z)\right]^4}\,, \\ \phi_{g^s}(z) &= 16r_*^2\sqrt{\frac{n_I}{3\pi}}\frac{(1+z)^2}{\sqrt{1-z}\left[(1+r_*)(1-z)+2\sqrt{r_*}(1+z)\right]^4}\,, \\ \phi_{\mathcal{F}_1^s}(z,0) &= 2\frac{r_*}{m_{B_s}^3}\sqrt{\frac{2n_I}{3\pi}}\frac{(1+z)(1-z)^{5/2}}{\left[(1+r_*)(1-z)+2\sqrt{r_*}(1+z)\right]^5}\,, \\ \phi_{P_1^s}(z,0) &= 8(1+r_*)r_*^{3/2}\sqrt{\frac{2n_I}{\pi}}\frac{(1+z)^2}{\sqrt{1-z}\left[(1+r_*)(1-z)+2\sqrt{r_*}(1+z)\right]^4} \end{aligned} \tag{4.27}$$

with $r_* \equiv m_{D_s^*}/m_{B_s}$. In Eqs. (4.26)-(4.27) n_I is a factor counting the number of spectator quarks and it is equal to $n_I = 1$ for the $B_s \to D_s^{(*)} \ell \nu_\ell$ decays [63]. For what concerns the poles, we refer to Appendix A of Ref. [86] for the $B_s \to D_s \ell \nu_\ell$ decays and to Table XII of Ref. [87] for the $B_s \to D_s^* \ell \nu_\ell$ decays.

At this point, we can implement the unitarity filters and the kinematical constraints in the DMM framework through a bootstrap analysis. For both decays the 100% of the generated bootstraps survive to the unitarity filters and this holds as well for each separate spin-parity quantum channel. The above results are not surprising. Indeed, the values of the dispersive bounds in Table D.1 are very conservative ones, since they sum up the contribution of all spectator quarks, both the light u- and d-quarks as well as the strange and the charm quarks. Thus, assuming small $SU(3)_F$ breaking effects in the FFs, we consider the alternative case in which the kinematical functions (4.26)-(4.27) are evaluated using $n_I = 3$. This is equivalent to leave unchanged all the kinematical functions, but to divide the dispersive bounds by three. The net result is that, as in the previous case, almost the 100% of the generated bootstraps survive to the new unitarity filters. Therefore, neither the skeptical nor the iterative procedures described in the previous Chapter need to be applied.

The resulting DM bands of the FFs are shown in Figs. 4.9 and 4.10. The extrapolations of the

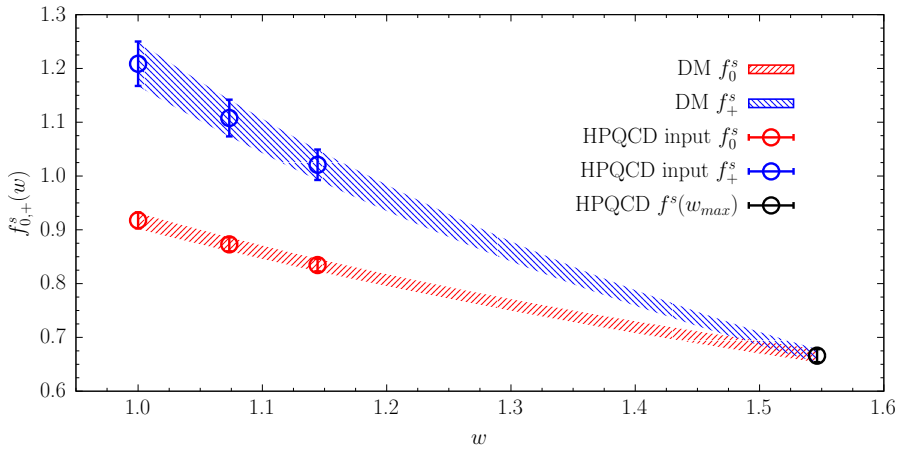

Figure 4.9: *The bands of the scalar and vector FFs entering the $B_s \to D_s\ell\nu_\ell$ decays computed through the DM method versus the recoil variable w. The blue band represents $f_+^s(w)$, while the red one is $f_0^s(w)$. The blue and red circles are the values of the FFs obtained by the HPQCD Collaboration in Ref. [86] and used as inputs for the DM method (see Table 4.5). The black circle represents the (common) value of the FFs at maximum recoil obtained by the HPQCD Collaboration in Ref. [86].*

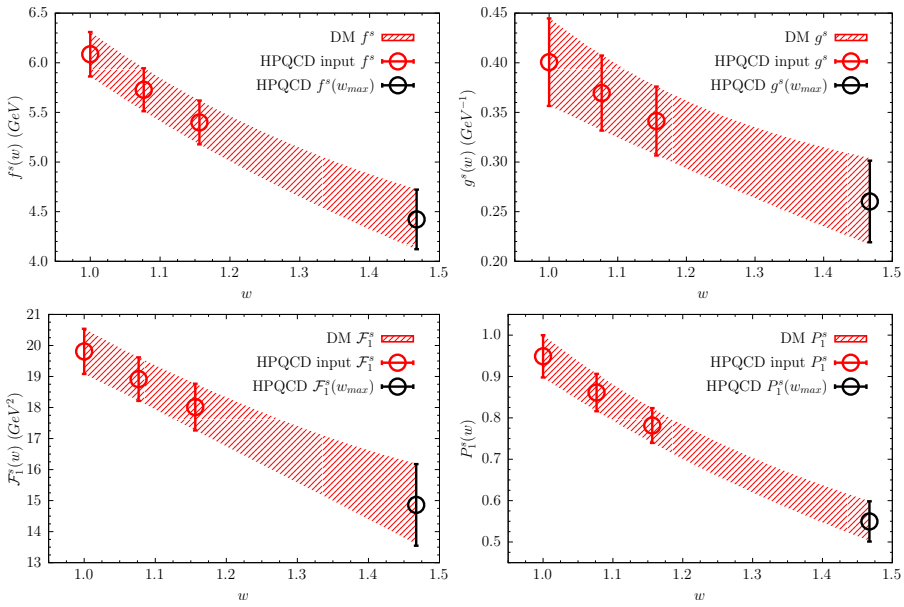

Figure 4.10: *The bands of the four FFs entering the $B_s \to D_s^*\ell\nu$ decays, i.e. $f^s(w)$, $g^s(w)$, $\mathcal{F}_1^s(w)$ and $P_1^s(w)$, computed through the DM method versus the recoil variable w. The red circles are the values of the FFs obtained by the HPQCD Collaboration in Ref. [87] and used as inputs for the DM method (see Table 4.6). The black circles represent the values of the FFs at maximum recoil obtained by the HPQCD Collaboration in Ref. [87].*

FFs at maximum recoil, which are important for the phenomenological applications which will be discussed in a while, read

$$f_+^s(w_{max}) = f_0^s(w_{max}) = 0.666 \pm 0.012 \ , \tag{4.28}$$

and

$$f^s(w^*_{max}) = 4.42 \pm 0.30\,\text{GeV}, \quad (4.29)$$
$$g^s(w^*_{max}) = 0.261 \pm 0.044\,\text{GeV}^{-1}, \quad (4.30)$$
$$\mathcal{F}_1^s(w^*_{max}) = 14.9 \pm 1.3\,\text{GeV}^2, \quad (4.31)$$
$$P_1^s(w^*_{max}) = 0.551 \pm 0.048\ , \quad (4.32)$$

which are consistent with the values of the BCL fits performed by the HPQCD Collaboration in Refs. [86, 87], as shown in Figs. 4.9-4.10.

4.3.2 Determination of $|V_{cb}|$

As far as the experimental measurements are concerned, the integrated branching fractions for both the $B_s \to D_s \ell\nu_\ell$ and the $B_s \to D_s^* \ell\nu_\ell$ processes have been determined in Ref. [88]. This allows us to determine $|V_{cb}|$ for the two channels using the theoretical estimate of the branching ratios based on the DM bands of the semileptonic FFs.

In Ref. [88] the LHCb Collaboration provided also a set of data concerning the differential decay rate $d\Gamma(B_s \to D_s^{(*)} \ell\nu_\ell)/dp_\perp$, where $p_\perp$ is the component of the final D_s-meson momentum (i.e., after the strong decay of the D_s^*-meson in the case of the $B_s \to D_s^* \ell\nu_\ell$ decays) perpendicular to the flight direction of the B_s-meson. The LHCb Collaboration carried out its own estimate of $|V_{cb}|$ by performing fits of the experimental data on $d\Gamma(B_s \to D_s^{(*)} \ell\nu_\ell)/dp_\perp$ based on either CLN or truncated BGL parameterizations of the semileptonic FFs. We make use of the latter fit to reconstruct the experimental data for $d\Gamma(B_s \to D_s^{(*)} \ell\nu_\ell)/dw$ and to get a further determination of $|V_{cb}|$.

Moreover, in Ref. [89] a different LHCb analysis produced the values of the unfolded decay widths for the $B_s \to D_s^* \ell\nu_\ell$ processes integrated in seven w-bins and normalized to the total decay rate. These data, together with the total branching fraction from Ref. [88], allow us to determine $|V_{cb}|$ adopting a bin-per-bin strategy, analogously to the $B \to D^{(*)}$ cases.

Let us examine these three different strategies in detail.

- **$|V_{cb}|$ from the integrated branching ratios of the $B_s \to D_s^{(*)} \ell\nu_\ell$ decays**

The LHCb Collaboration has measured the ratios of the branching fractions of the semileptonic $B_s \to D_s^{(*)} \mu\nu$ decays with respect to the $B \to D^{(*)} \mu\nu$ ones [88]. These measurements read

$$\frac{\mathcal{B}(B_s \to D_s \mu\nu)}{\mathcal{B}(B \to D \mu\nu)} = 1.09 \pm 0.05 \pm 0.06 \pm 0.05 = 1.09 \pm 0.09\ , \quad (4.33)$$

$$\frac{\mathcal{B}(B_s \to D_s^* \mu\nu)}{\mathcal{B}(B \to D^* \mu\nu)} = 1.06 \pm 0.05 \pm 0.07 \pm 0.05 = 1.06 \pm 0.10\ , \quad (4.34)$$

where the first error is statistical, the second one is systematic (including the uncertainty related to the choice of the CLN or BGL parameterization) and the third one is due to uncertainties of external inputs used in the measurements. Note that the LHCb data indicate that $SU(3)_F$ breaking effects on the branching ratios do not exceed the $\sim 10\%$ level. Then, the LHCb Collaboration adopted the measured values of $\mathcal{B}(B \to D^{(*)} \mu\nu)$ from PDG [90] to determine for the first time the branching ratios $\mathcal{B}(B_s \to D_s^{(*)} \mu\nu)$, obtaining

$$\mathcal{B}(B_s \to D_s \mu\nu) = (2.49 \pm 0.12 \pm 0.14 \pm 0.16) \cdot 10^{-2} = (2.49 \pm 0.24) \cdot 10^{-2}\ , \quad (4.35)$$

$$\mathcal{B}(B_s \to D_s^*\mu\nu) = (5.38 \pm 0.25 \pm 0.46 \pm 0.30) \cdot 10^{-2} = (5.38 \pm 0.60) \cdot 10^{-2} , \quad (4.36)$$

where the third error includes also the uncertainty related to the normalization of the branching fractions.

Using the latest PDG value for the B_s-meson lifetime, $\tau_{B_s} = (1.516 \pm 0.006) \cdot 10^{-12}$ s [90], one has

$$\Gamma^{\rm LHCb}(B_s \to D_s\mu\nu) = (1.08 \pm 0.10) \cdot 10^{-14} \text{ GeV} , \quad (4.37)$$

$$\Gamma^{\rm LHCb}(B_s \to D_s^*\mu\nu) = (2.34 \pm 0.26) \cdot 10^{-14} \text{ GeV} . \quad (4.38)$$

Thus, since

$$\Gamma(B_s \to D_s^{(*)}\mu\nu) = \int dq^2 \frac{d\Gamma}{dq^2}(B_s \to D_s^{(*)}\mu\nu) ,$$

we can use the DM bands for the FFs given in Figs. 4.9 and 4.10 to estimate the theoretical value of the total decay widths modulo $|V_{cb}|^2$, obtaining

$$\left[\Gamma(B_s \to D_s\mu\nu)/|V_{cb}|^2\right]^{\rm DM} = (6.04 \pm 0.23) \cdot 10^{-12} \text{ GeV} , \quad (4.39)$$

$$\left[\Gamma(B_s \to D_s^*\mu\nu)/|V_{cb}|^2\right]^{\rm DM} = (1.39 \pm 0.11) \cdot 10^{-11} \text{ GeV} . \quad (4.40)$$

In this way from Eqs. (4.37) -(4.38) we get the values

$$|V_{cb}| \cdot 10^3 = 42.3 \pm 2.1 \qquad \text{from } B_s \to D_s\ell\nu_\ell \text{ decays} , \quad (4.41)$$

$$= 41.0 \pm 2.8 \qquad \text{from } B_s \to D_s^*\ell\nu_\ell \text{ decays} . \quad (4.42)$$

- **$|V_{cb}|$ from the differential decay rates of the $B_s \to D_s^{(*)}\ell\nu_\ell$ decays**

In Ref. [88] the LHCb Collaboration fitted the $p_\perp$ distribution for both the $B_s \to D_s\ell\nu_\ell$ and the $B_s \to D_s^*\ell\nu_\ell$ processes by describing the semileptonic FFs either through a CLN or a truncated BGL parameterizations. The experimental data are not presented explicitly. Instead, the LHCb Collaboration provides the results of their own fits of the experimental data, i.e. their estimate of $|V_{cb}|$ and of the marginalized values of the parameters entering the CLN or the BGL parameterizations, together with the correlation matrix relating all these quantities to each other.

Using the results of their BGL fit we can reconstruct the experimental values of the differential decay width $d\Gamma^{\rm exp}(B_s \to D_s^{(*)}\ell\nu_\ell)/dw$ in a series of 14 values of the recoil w. Then, using the DM bands for the FFs given in Figs. 4.9 and 4.10 we evaluate the corresponding theoretical expectations modulo $|V_{cb}|^2$, i.e. $d\Gamma^{\rm DM}(B_s \to D_s^{(*)}\ell\nu_\ell)/dw$, to get a bin-per-bin estimate of $|V_{cb}|$, viz.

$$|V_{cb}|_j \equiv \sqrt{\frac{d\Gamma^{\rm exp}/dw_j}{d\Gamma^{\rm DM}/dw_j}} \qquad j = 1, 2, ..., 14 . \quad (4.43)$$

The results for $|V_{cb}|_j$ are shown in Fig. 4.11 as the black dots.

Using Eq. (4.5) with $N_{\rm bins} = 14$, we determine the value of $|V_{cb}|$ from a constant fit, obtaining the results

$$|V_{cb}| \cdot 10^3 = 42.4 \pm 1.9 \qquad \text{from } B_s \to D_s\ell\nu_\ell \text{ decays} , \quad (4.44)$$

$$= 41.9 \pm 2.2 \qquad \text{from } B_s \to D_s^*\ell\nu_\ell \text{ decays} , \quad (4.45)$$

shown in Fig. 4.11 as the red bands.

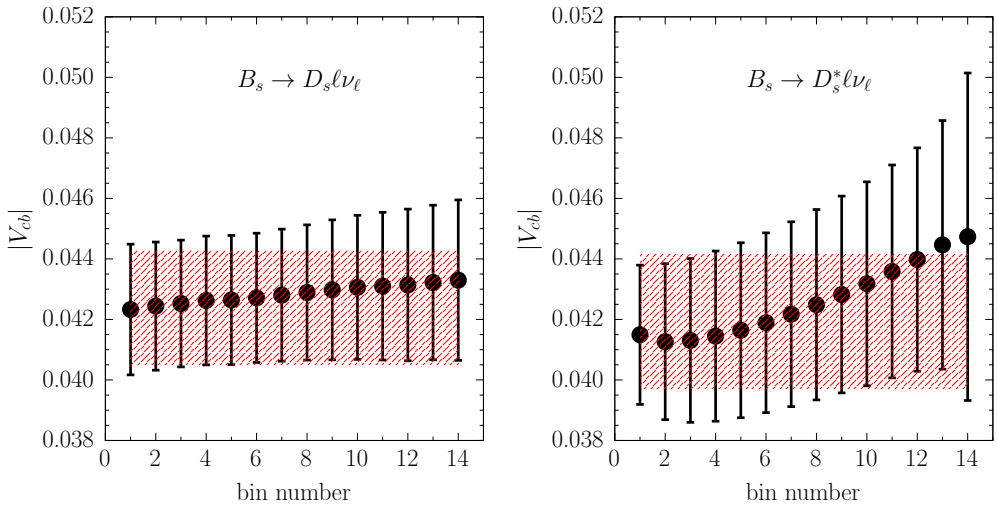

Figure 4.11: *Bin-per-bin estimates of $|V_{cb}|$ given by Eq. (4.43) using the LHCb data of Ref. [88] for the $B_s \to D_s \ell \nu_\ell$ (left panel) and $B_s \to D_s^* \ell \nu_\ell$ (right panel) decays. The red bands correspond to the results (4.44) (left panel) and (4.45) (right panel) obtained from the constant fit.*

- **$|V_{cb}|$ from the $B_s \to D_s^* \ell \nu_\ell$ data of Ref. [89]**

In Ref. [89] a different LHCb experiment has provided the values of the ratios

$$\Delta r_j \equiv \frac{\Delta\Gamma_j(B_s \to D_s^* \mu\nu)}{\Gamma(B_s \to D_s^* \mu\nu)} \qquad \text{j} = 1, 2, ..., 7 \tag{4.46}$$

between the decay rate $\Delta\Gamma_j(B_s \to D_s^* \mu\nu)$ integrated in each of seven w-bins with the total decay rate $\Gamma(B_s \to D_s^* \mu\nu)$. The experimental data are collected in Table 4.7 and compared with the corresponding predictions of the DM method based on the FFs of Fig. 4.10 obtained starting from the lattice inputs of Table 4.6. Our DM results turn out to be consistent with the corresponding ones calculated by HPQCD Collaboration in Ref. [87].

j-bin	1	2	3	4	5	6	7
Δw_j	0.1087	0.0601	0.0524	0.0505	0.0509	0.0588	0.0853
$\Delta r_j^{\rm LHCb}$	0.183(12)	0.144(8)	0.148(8)	0.128(8)	0.117(7)	0.122(6)	0.158(9)
$\Delta r_j^{\rm DM}$	0.1942(82)	0.1534(45)	0.1377(28)	0.1289(18)	0.1212(20)	0.1241(40)	0.1405(110)

Table 4.7: *Values of the ratios Δr_j given in Eq. (4.46) for each of the seven experimental w-bins of Ref. [89]. The w-bins and their widths Δw_j are given in the second and third rows, respectively. The forth row collects the experimental data from Ref. [89]. The last row corresponds to the theoretical results obtained using the FFs shown in Fig. 4.10 and determined by the DM method starting from the lattice inputs of Table 4.6.*

In Fig. 4.12 the differential decay rates $\Delta r_j/\Delta w_j = (\Delta\Gamma_j/\Delta w_j)/\Gamma$ are compared for each of the seven w-bins with the corresponding experimental data of Ref. [89]. It can be seen that the shape of the theoretical predictions is consistent with the one of the experimental data within ≈ 1 standard deviation.

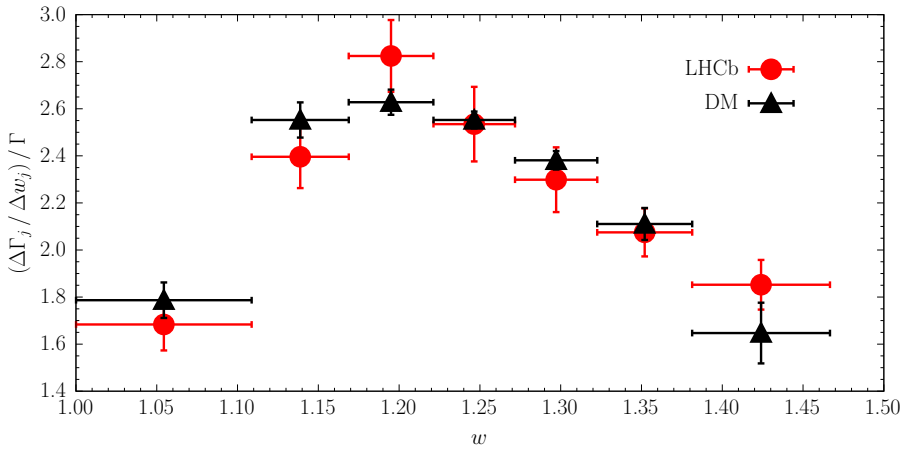

Figure 4.12: *The differential decay rate $\Delta r_j/\Delta w_j = (\Delta\Gamma_j/\Delta w_j)/\Gamma$, integrated for each of the seven experimental w-bins of Ref. [89] and normalized by the total decay rate, versus the recoil variable w. The red dots represent the LHCb experimental data of Ref. [89], while the black triangles are the predictions based on our DM approach starting from the lattice inputs of Table 4.6.*

Using the experimental value (4.38) for the total decay rate $\Gamma(B_s \to D_s^*\mu\nu)$ we can compute the experimental values of the (partially) integrated decay rate $\Delta\Gamma_j$ for each w-bin as

$$\Delta\Gamma_j^{exp} = \Delta r_j^{\rm LHCb} \cdot \Gamma^{\rm LHCb}(B_s \to D_s^*\mu\nu) \ . \tag{4.47}$$

The covariance matrix Γ_{ij}^{exp} for the decay rates $\Delta\Gamma_j^{exp}$ is evaluated by considering a sample of events for the ratios $\Delta r_j^{\rm LHCb}$ generated according to the experimental covariance matrix $R_{ij}^{\rm LHCb}$ provided in Ref. [89] and a Gaussian distribution for $\Gamma^{\rm LHCb}(B_s \to D_s^*\mu\nu)$ with mean value $\overline{\Gamma} = 2.34 \cdot 10^{-14}$ GeV and standard deviation $\sigma_{\overline{\Gamma}} = 0.26 \cdot 10^{-14}$ GeV. The latter distribution is uncorrelated with those of the ratios $\Delta r_j^{\rm LHCb}$, since it comes from a different LHCb experiment. A simple calculation yields

$$\Gamma_{ij}^{exp} = R_{ij}^{\rm LHCb}\left[\overline{\Gamma}^2 + \sigma_{\overline{\Gamma}}^2\right] + \Delta r_i^{\rm LHCb}\Delta r_j^{\rm LHCb}\sigma_{\overline{\Gamma}}^2 \ . \tag{4.48}$$

Notice that, since the sum of the ratio $\Delta r_j^{\rm LHCb}$ over the seven w-bins is equal to unity by construction, the covariance matrix $R_{ij}^{\rm LHCb}$ must have a null eigenvalue, so that the number of independent bins is six. This does not occur for the original covariance matrix provided in Ref. [89]. Thus, we generate a sample of events for the seven w-bins using the multivariate Gaussian distribution corresponding to the original covariance matrix of the ratios. Then, for each event we normalize the ratios by their sum over the bins and recalculate the covariance matrix, which has now properly a null eigenvalue. In what follows we make use of the corrected covariance matrix $R_{ij}^{\rm LHCb}$, though the numerical impact of the correction on the determination of $|V_{cb}|$ turns out to be negligible.

Using the DM bands of the FFs we now evaluate the theoretical predictions $\Delta\Gamma_j^{DM}$ (and the corresponding covariance matrix Γ_{ij}^{DM}) that can be compared with the experimental ones (4.47) to obtain the value of $|V_{cb}|$ for each of the seven w-bins, namely

$$|V_{cb}|_j \equiv \sqrt{\frac{\Delta\Gamma_j^{exp}}{\Delta\Gamma_j^{DM}}} \ . \tag{4.49}$$

The results for $|V_{cb}|_j$ are shown in Fig. 4.13 as the black dots. The covariance matrix C_{ij} for the quantities $|V_{cb}|_j$ can be calculated using (uncorrelated) samples of events for $\Delta\Gamma_j^{exp}$ and $\Delta\Gamma_j^{DM}$ generated according to their respective covariance matrices Γ_{ij}^{exp} and Γ_{ij}^{DM}.

Finally, we determine the value of $|V_{cb}|$ from a constant fit with $N_{\rm bins} = 7$. This procedure leads to the result

$$|V_{cb}| \cdot 10^3 = 38.6 \pm 2.7 \ , \tag{4.50}$$

shown in Fig. 4.13 as the red band. It can be seen that the central value of Eq. (4.50) lies well below

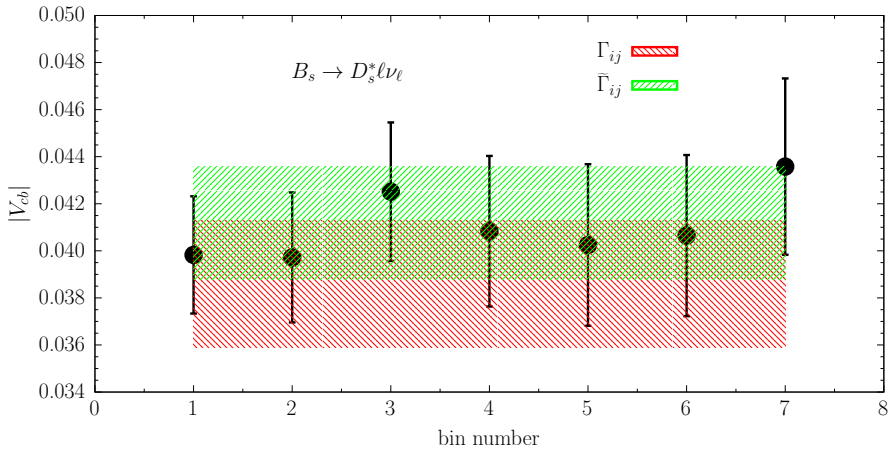

Figure 4.13: *Bin-per-bin estimates of $|V_{cb}|$ given by Eq. (4.49) using the LHCb data of Ref. [89]. The red and green bands correspond respectively to the values (4.50) and (4.52). They are obtained by a constant fit, using for the experimental data $\Delta\Gamma_j^{exp}$ the covariance matrices (4.48) (red bands) and (4.51) (green bands).*

the bin-per-bin data. This problem is well-known in literature [79] and it has the same origin of the one that we have already addressed for the $B \to D^* \ell \nu$ decays. The issue is related to the fact that best fits to data which are affected by an overall normalization uncertainty (like in our case $\sigma_{\overline{\Gamma}}$ for the quantities $\Delta\Gamma_j^{exp}$) have the tendency to produce curves lower than expected if the covariance matrix of the data points is used in the definition of the χ^2-variable. In particular, in Ref. [79] it was shown that in the case of a fit to a constant, a negative bias can be obtained, the absolute size of which is proportional to the number of degrees of freedom, to the square of the normalization uncertainty (i.e., to $\sigma_{\overline{\Gamma}}^2$) and to the differences between individual data points (i.e., in our case to the differences among the ratios $\Delta r_j^{\rm LHCb}$). In other words the observed negative bias is due to the term $\Delta r_i^{\rm LHCb} \Delta r_j^{\rm LHCb} \sigma_{\overline{\Gamma}}^2$ appearing in the r.h.s. of Eq. (4.48).

The above term, however, is necessary to guarantee the property $\sum_{i,j=1}^{N_{\rm bins}} \Gamma_{ij}^{exp} = \sigma_{\overline{\Gamma}}^2$, which follows from the fact that $\sum_{j=1}^{N_{\rm bins}} \Delta r_j^{\rm LHCb} = 1$ (or equivalently $\sum_{j=1}^{N_{\rm bins}} \Delta\Gamma_j^{exp} = \overline{\Gamma}$)[2]. Thus, since both the number of degrees of freedom and the normalization error $\sigma_{\overline{\Gamma}}$ cannot be modified, we neglect the differences between the ratios $\Delta r_j^{\rm LHCb}$ in the covariance matrix Γ_{ij}^{exp} by adopting the following modified covariance matrix

$$\widetilde{\Gamma}_{ij}^{exp} = R_{ij}^{\rm LHCb} \left[\overline{\Gamma}^2 + \sigma_{\overline{\Gamma}}^2 \right] + \frac{1}{N_{\rm bins}^2} \sigma_{\overline{\Gamma}}^2 \ , \tag{4.51}$$

which still fulfills the property $\sum_{i,j=1}^{N_{\rm bins}} \widetilde{\Gamma}_{ij}^{exp} = \sigma_{\overline{\Gamma}}^2$. Using the modified covariance matrix $\widetilde{\Gamma}_{ij}^{exp}$ the

[2]Notice that also the relation $\sum_{i,j=1}^{N_{\rm bins}} R_{ij}^{\rm LHCb} = 0$ holds as well, as we have explicitly checked.

constant fit yields now the result

$$|V_{cb}| \cdot 10^3 = 41.2 \pm 2.4 \ , \tag{4.52}$$

shown in Fig. 4.13 as the green band. The previous negative bias is now removed.

4.3.3 Lepton Flavour Universality and polarization observables

Analogously to what done for the $B \to D^{(*)}\ell\nu$ decays, we now compute the theoretical values of the τ/μ ratios $R(D_s^{(*)})$, the τ-polarization $P_\tau(D_s^*)$ and the D_s^* longitudinal polarization $F_L(D_s^*)$ using the DM bands of the FFs of Figs. 4.9 and 4.10 and developing a bootstrap analysis. Our results are

$$R(D_s) = 0.298\ (5) \ , \qquad R(D_s^*) = 0.250\ (6) \ , \tag{4.53}$$

$$P_\tau(D_s^*) = -0.520\ (12) \ , \qquad F_L(D_s^*) = 0.440\ (16) \ , \tag{4.54}$$

which can be compared with the corresponding results obtained before in the case of the semileptonic $B \to D^{(*)}\ell\nu_\ell$ decays, namely $R(D) = 0.296\ (8)$, $R(D^*) = 0.275\ (8)$, $P_\tau(D^*) = -0.529\ (7)$ and $F_L(D^*) = 0.414\ (12)$. It follows that $SU(3)_F$ breaking effects are negligible for all the above quantities except $R(D^*)$ and $R(D_s^*)$, which differ by $\approx 10\%$. Such a difference can be understood as a consequence of the different shapes of the semileptonic FFs entering the $B_{(s)} \to D^*_{(s)}\ell\nu_\ell$ decays.

4.4 Final observations

Let us here summarize our results of the DMM study of semileptonic charged current $B \to D^{(*)}\ell\nu$ decays and develop final comments and observations.

For what concerns the CKM matrix element $|V_{cb}|$, our final results can be summarized as

- for the $B \to D$ case:
$$|V_{cb}| \times 10^3 = 41.0 \pm 1.2; \tag{4.55}$$
- for the $B \to D^*$ case:
$$|V_{cb}| \times 10^3 = 41.3 \pm 1.7; \tag{4.56}$$
- for the $B_s \to D_s$ case:
$$|V_{cb}| \times 10^3 = 42.4 \pm 2.0; \tag{4.57}$$
- for the $B_s \to D_s^*$ case:
$$|V_{cb}| \times 10^3 = 41.4 \pm 2.6. \tag{4.58}$$

Note that the last two results come from an average of the results (4.41) and (4.44) for the semileptonic $B_s \to D_s\ell\nu_\ell$ decays and the results (4.42), (4.45) and (4.52) for the semileptonic $B_s \to D_s^*\ell\nu_\ell$ decays.

As already stated before, all these determinations are compatible with the most recent inclusive determination $|V_{cb}|_{\rm incl} = (42.16 \pm 0.50) \cdot 10^{-3}$. Let us now compare our value with other exclusive estimates. From the study of $B \to D\ell\nu$ decays, some of the results present in literature are

$$|V_{cb}|_{excl} \times 10^3 = 40.49 \pm 0.97 \qquad [50] \ ,$$

$$|V_{cb}|_{excl} \times 10^3 = 41.0 \pm 1.1 \qquad [91] \ ,$$

$$|V_{cb}|_{excl} \times 10^3 = 40.1 \pm 1.0 \qquad [92] \ .$$

All these determinations are compatible with and very similar to our result in Eq. (4.55), although in the analyses of Refs. [50, 91, 92] the lattice and the experimental data are fitted *all together* to constrain the shape of the FFs. We recall that in our study, instead, the two sources of information are always kept separate. It seems that in this case the two approaches bring to the same final result for $|V_{cb}|$. Let us finally highlight that Refs. [50, 92] use also the experimental data [93] published by BaBar Collaboration in their fits. Despite of this, Ref. [92] explicitly states that the fit is dominated by the more precise Belle data [75].

On the contrary, some results from the study of $B \to D^* \ell \nu$ decays read

$$\begin{aligned} |V_{cb}|_{excl} \times 10^3 &= 39.6^{+1.1}_{-1.0} \qquad [51] \ , \\ |V_{cb}|_{excl} \times 10^3 &= 39.56^{+1.04}_{-1.06} \qquad [94] \ , \\ |V_{cb}|_{excl} \times 10^3 &= 38.30 \pm 0.8 \qquad [92] \ , \end{aligned}$$

where the authors had implemented BGL-like analyses of the same experimental data, *without* the use of the FNAL/MILC final data in [55]. Moreover, in [55] the authors develop a combined BGL fit of their LQCD and the experimental data, obtaining

$$|V_{cb}|_{excl} \times 10^3 = 38.40 \pm 0.74 \qquad [55] \ .$$

All these determinations are compatible with each other, although there is a non-negligible tension with the inclusive value. Note also that these mean values are quite different from the one in Eq. (4.56). For our understanding, the reason of this discrepancy is the *different shapes of the FFs* induced by, on the one hand, the LQCD data plus unitarity and, on the other hand, the measurements of the differential decay widths. This is a key point and reflects the importance of keeping distinct the LQCD and the experimental data in $B \to D^* \ell \nu$ decays. In conclusion, for what concerns the $B \to D_s^{(*)} \ell \nu$ processes, the final results in Eqs. (4.57)-(4.58) are compatible with other exclusive determinations from these transitions, *i.e.* $|V_{cb}|^{\rm LHCb} \cdot 10^3 = 42.3 \pm 0.8 \pm 0.9 \pm 1.2 = 42.3 \pm 1.7$ [88] and $|V_{cb}|^{\rm HPQCD} \cdot 10^3 = 42.7 \pm 2.3$ [87].

Let us summarize our findings for the LFU observables. For what concerns the $R(D^{(*)})$ anomalies, in Figure 4.8 we have compared the DMM results $R(D) = 0.296 \pm 0.008$ and $R(D^*) = 0.275 \pm 0.008$ with the corresponding experimental world averages from HFLAV [40]. Our theoretical expectations are compatible with the experimental averages (3.2) at the $\sim 1.4\sigma$ level. Let us note that FNAL/MILC Collaborations have obtained a result for $R(D^*)$ which is very similar to ours, namely $R(D^*) = 0.273 \pm 0.010$ [55]. As the authors explicitly state in their work, this value is obtained with the imposition of both the KCs in Eqs. (3.18)-(3.19). Now, recalling the theoretical determinations in Eq. (3.3), we note a non-negligible tension between these values and the experimental ones in the $R(D^*)$ case. This is again due to the different slopes of the FFs induced by experiments with respect to the ones dictated by the combination of LQCD data plus unitarity. We have also determined the DMM estimates of the ratios $R(D_s) = 0.298(5)$ and $R(D_s^*) = 0.250(6)$, which have not been measured yet. We note that possible $SU(3)_F$ breaking effects can affect $R(D^*)$ and $R(D_s^*)$ at the $\approx 10\%$ level.

Chapter 5

The DMM perspective on heavy-to-light $B_{(s)}$ decays

In this Chapter, we will firstly study in detail the semileptonic heavy-to-light decays, *i.e.* the $B \to \pi\ell\nu_\ell$ and $B_s \to K\ell\nu_\ell$ decays, which allow to obtain exclusive determinations of the CKM matrix elements $|V_{ub}|$. We will address also the LFU issue for these decays. In the last Section, we will develop a comparison between the final DMM estimates of $|V_{cb}|$ and $|V_{ub}|$ and the determination of the same CKM matrix elements in the Unitarity Triangle Analysis (UTA) framework.

5.1 The DMM applied to the $B \to \pi\ell\nu_\ell$ and $B_s \to K\ell\nu_\ell$ decays

Let us now focus our discussion on the semileptonic heavy-to-light B decays, namely the $B \to \pi\ell\nu_\ell$ and $B_s \to K\ell\nu_\ell$ transitions. Since many years these processes are very intriguing mainly because a long-standing tension affects the inclusive and the exclusive determinations of the CKM matrix element $|V_{ub}|$. In fact, the most recent version of the FLAG report [39] quotes for the exclusive estimate of $|V_{ub}|$ the value $|V_{ub}|_{excl} \cdot 10^3 = 3.74\,(17)$ from $B \to \pi\ell\nu_\ell$ decays, while the inclusive determination performed by HFLAV [95] reads $|V_{ub}|_{incl} \cdot 10^3 = 4.19\,(12)\,(^{+11}_{-12})$, implying a $\sim 2\sigma$ discrepancy between them. However, a recent measurement of the inclusive value of $|V_{ub}|$ made by Belle [96] has changed the picture. In fact, the collaboration has presented the result of an average over four theoretical calculations (BLNP [97], DGE [98], GGOU [99], ADFR [100, 101]), which reads

$$|V_{ub}|_{incl} \cdot 10^3 = 4.10 \pm 0.09 \pm 0.22 \pm 0.15 \;\; [0.28] \;\; , \tag{5.1}$$

where the first two errors represent the statistical and systematic uncertainties respectively, the third one denotes the theoretical model uncertainty and the fourth one (in parenthesis) is their sum in quadrature. The FLAG review [39] then quotes the inclusive value $|V_{ub}|_{incl} \cdot 10^3 = 4.32\,(29)$, which differs from the exclusive one by $\simeq 1.7$ standard deviations. To have in mind other numerical estimates of $|V_{ub}|$, the last PDG review [90] quotes for its exclusive and inclusive determinations the values $|V_{ub}|_{excl} \cdot 10^3 = 3.70\,(10)_{\rm exp}\,(12)_{\rm th} = 3.70\,(16)$ from $B \to \pi\ell\nu_\ell$ decays and $|V_{ub}|_{incl} \cdot 10^3 = 4.13\,(12)_{\rm exp}\,(^{+13}_{-14})_{\rm th}\,(18)_{\rm model} = 4.13\,(26)$, which differ by $\simeq 1.4$ standard deviations. The aforementioned tension seems to be thus reduced, however a new model-independent exclusive estimate of $|V_{ub}|$ can help in shedding a new light on this issue and further reducing the difference between the inclusive and the exclusive estimates.

New analyses of the exclusive $b \to u$ transitions, claiming that their exclusive determinations of $|V_{ub}|$ are consistent with the estimate (5.1) at the $1 - 1.5\,\sigma$ level, also appeared [102–104]. Note that

the latter results were obtained by adopting for the hadronic Form Factors (FFs) the BCL or the Bharucha-Straub-Zwicky (BSZ) [105] parameterizations or the Padé approximants [106].

Our aim is, instead, to perform for the first time a study of these transitions through the DMM, which has been described in the previous Chapter. To this end, the FFs are taken from the results of the RBC/UKQCD [107] and FNAL/MILC [108] Collaborations for the $B \to \pi\ell\nu_\ell$ decays, and from RBC/UKQCD [107], HPQCD [109] and FNAL/MILC [110] Collaborations for the $B_s \to K\ell\nu_\ell$ decays. For what concerns the susceptibilities, instead, the final results of their non-perturbative computation can be found in Appendix D. For this reason, in what follows we will show the results of the DMM to the description of the FFs, then we will focus the discussion on the extraction of $|V_{ub}|$ from the experimental data and on the determination of LFU observables.

5.1.1 State-of-the-art of the LQCD computations of the FFs

As briefly stated before, the FFs entering semileptonic $B \to \pi$ decays have been studied by the RBC/UKQCD [107] and the FNAL/MILC [108] Collaborations. In the case of the $B_s \to K$ transition several LQCD computations of the FFs are available, namely from the RBC/UKQCD [107], HPQCD [109] and FNAL/MILC [110] Collaborations. For both channels the lattice computations of the FFs are available in the large-q^2 region, 17 GeV$^2 \lesssim q^2 \leq q^2_{max} \equiv (m_{B_{(s)}} - m_{\pi(K)})^2$. Note that these decays are pseudoscalar-to-pseudoscalar transitions exactly as the $B \to D$ ones, thus the definition of the hadronic FFs is the same of Eqs. (3.4)-(3.5).

The authors of Ref. [107] provide synthetic LQCD values of the FFs (together with their statistical and systematic correlations) at three values of q^2 in the large-q^2 regime, namely $q^2 = \{19.0, 22.6, 25.1\}$ GeV^2 for the $B \to \pi$ transition and $q^2 = \{17.6, 20.8, 23.4\}$ GeV^2 in the case of the $B_s \to K$ transition. These data can be directly used as inputs for our DMM. In the other works [108–110] the results of BCL fits of the FFs extrapolated to the continuum limit and to the physical pion point are available. Thus, from the marginalized BCL coefficients we evaluate the mean values, uncertainties and correlations of the FFs at the three values of q^2 given in Ref. [107]. The LQCD results used as inputs for our DMM are collected in Tables 5.1 and 5.2 for the $B \to \pi$ and $B_s \to K$ decays, respectively. In the next future new LQCD computations of the FFs are expected to become available [111, 112].

For both $B \to \pi$ and $B_s \to K$ decays we have also combined all the LQCD determinations of the FFs corresponding to the same values of the momentum transfer. Starting from N computations of the FFs with mean values $x_i^{(k)}$ and uncertainties $\sigma_i^{(k)}$ $(k = 1, \cdots, N)$ corresponding to a given value q_i^2 of the squared 4-momentum transfer, the *combined* LQCD average x_i and uncertainty σ_i are given by

$$x_i = \sum_{k=1}^{N} \omega^{(k)} x_i^{(k)}, \tag{5.2}$$

$$\sigma_i^2 = \sum_{k=1}^{N} \omega^{(k)} (\sigma_i^{(k)})^2 + \sum_{k=1}^{N} \omega^{(k)} (x_i^{(k)} - x_i)^2 \ , \tag{5.3}$$

where $\omega^{(k)}$ represents the weight associated to the k-th calculation ($\sum_{k=1}^{N} \omega^{(k)} = 1$). In what follows, we assume the same weight for all the computations, i.e. we consider the simple choice $\omega^{(k)} = 1/N$, following the strategy described in Ref. [80]. The reason of this choice is to obtain a conservative combination of the various LQCD computations of the FFs, in order to take into account hypothetical differences in the values of the FFs (and, thus, in their slopes) quoted by different lattice Collaborations. As we will see, this is in fact the case for semileptonic $B_s \to K$ decays. This issue has also been

already pointed out in Ref. [3], where a methodological study of preliminary LQCD computations of the FFs entering in semileptonic $B \to D^*$ decays was presented.

The results of Eqs. (5.2)-(5.3) are shown in the last columns of the Tables 5.1 and 5.2 for both the $B \to \pi$ and the $B_s \to K$ cases, respectively. Moreover, the covariance matrix C of the combined data can be easily evaluated in terms of the covariance matrices $C^{(k)}$ of each single LQCD computation as

$$C_{ij} \equiv \frac{1}{N}\sum_{k=1}^{N} C_{ij}^{(k)} + \frac{1}{N}\sum_{k=1}^{N}(x_i^{(k)} - x_i)(x_j^{(k)} - x_j) \ , \tag{5.4}$$

where the indices i and j run over the number of values of the 4-momentum transfer at which the LQCD computations of the FFs have been performed, namely $i, j = 1, 2, 3$.

	RBC/UKQCD	FNAL/MILC	Combined
$f_+^\pi(19.0\ \text{GeV}^2)$	1.21(10)(9)	1.17(8)	1.19(11)
$f_+^\pi(22.6\ \text{GeV}^2)$	2.27(13)(14)	2.24(12)	2.25(16)
$f_+^\pi(25.1\ \text{GeV}^2)$	4.11(51)(29)	4.46(23)	4.29(48)
$f_0^\pi(19.0\ \text{GeV}^2)$	0.46(3)(5)	0.46(3)	0.46(5)
$f_0^\pi(22.6\ \text{GeV}^2)$	0.68(3)(6)	0.65(3)	0.66(5)
$f_0^\pi(25.1\ \text{GeV}^2)$	0.92(3)(6)	0.86(3)	0.89(6)

Table 5.1: *Mean values and uncertainties of the LQCD computations of the FFs $f_{+,0}^\pi(q^2)$ obtained at three selected values of q^2 from the results of the RBC/UKQCD [107] and FNAL/MILC [108] Collaborations. For the RBC/UKQCD computations the first error is statistical while the second one is systematic. The last column contains the results of the combination procedure given in Eqs. (5.2)-(5.3) with $\omega^{(k)} = 1/N$.*

	RBC/UKQCD	HPQCD	FNAL/MILC	Combined
$f_+^K(17.6\ \text{GeV}^2)$	0.99(4)(5)	1.04(5)	1.01(4)	1.01(6)
$f_+^K(20.8\ \text{GeV}^2)$	1.64(6)(7)	1.68(7)	1.68(5)	1.67(8)
$f_+^K(23.4\ \text{GeV}^2)$	2.77(9)(11)	2.94(13)	2.91(9)	2.87(15)
$f_0^K(17.6\ \text{GeV}^2)$	0.48(2)(3)	0.53(3)	0.44(2)	0.48(4)
$f_0^K(20.8\ \text{GeV}^2)$	0.63(2)(4)	0.64(3)	0.59(1)	0.62(4)
$f_0^K(23.4\ \text{GeV}^2)$	0.81(2)(5)	0.79(4)	0.76(2)	0.79(5)

Table 5.2: *Mean values and uncertainties of the LQCD computations of the FFs $f_{+,0}^K(q^2)$ obtained at three selected values of q^2 from the results of the RBC/UKQCD [107], HPQCD [109] and FNAL/MILC [110] Collaborations. For the RBC/UKQCD computations the first error is statistical while the second one is systematic. The last column contains the results of the combination procedure given in Eqs. (5.2)-(5.3) with $\omega^{(k)} = 1/N$.*

5.1.2 Application of the DMM to the description of the FFs

Starting from Eq. (3.45), the kinematical functions ϕ_0 and ϕ_+ corresponding to the scalar and vector FFs of the $B_{(s)} \to \pi(K)$ decays are given by [63]

$$\begin{aligned}
\phi_0(z,0) &= \sqrt{\frac{2n_I}{3}}\sqrt{\frac{3t_+t_-}{4\pi}}\frac{1}{t_+-t_-}\frac{1+z}{(1-z)^{5/2}}\left(\sqrt{\frac{t_+}{t_+-t_-}}+\frac{1+z}{1-z}\right)^{-4}, \\
\phi_+(z,0) &= \sqrt{\frac{2n_I}{3}}\sqrt{\frac{1}{\pi(t_+-t_-)}}\frac{(1+z)^2}{(1-z)^{9/2}}\left(\sqrt{\frac{t_+}{t_+-t_-}}+\frac{1+z}{1-z}\right)^{-5}.
\end{aligned} \tag{5.5}$$

where $z \equiv z(t=q^2)$ is defined in Eq. (3.37) and n_I is an isospin Clebsh-Gordan factor equal to $n_I = 3/2$ for the $B \to \pi$ decays and to $n_I = 1$ for the $B_s \to K$ case. In order to take into account the B^* pole in the transverse channel, the transverse kinematical function ϕ_+ is modified as

$$\phi_+(z,0) \to \phi_+(z,0)\cdot\frac{z-z(m_{B^*}^2)}{1-z\,\bar{z}(m_{B^*}^2)} \tag{5.6}$$

with $m_{B^*} = 5.325$ GeV from the PDG [90]. The nonperturbative values of the susceptibilities (for the $b \to u$ quark current) relevant for the scalar $f_0(q^2)$ and vector $f_+(q^2)$ FFs are taken from Appendix D and read

$$\chi_{0^+}(0) = (2.04 \pm 0.20)\cdot 10^{-2}\,, \tag{5.7}$$

$$\chi_{1^-}(0) = (4.45 \pm 1.16)\cdot 10^{-4}\ \text{GeV}^{-2}, \tag{5.8}$$

respectively.

We now apply the DMM to the $B \to \pi$ decay using as inputs the lattice data of Table 5.1 corresponding to the three sets labelled RBC/UKQCD, FNAL/MILC and combined. A total of $5\cdot 10^4$ events are generated using the multivariate Gaussian distribution including the correlations among the LQCD data. It turns out that the unitarity bounds for both f_0^π and f_+^π as well as the KC $f_0^\pi(0) = f_+^\pi(0) \equiv f^\pi(0)$ are satisfied by $98-100\%$ of the events and, therefore, neither the skeptical nor the iterative procedures described in the previous Chapter need to be applied. In Figs. 5.1 and 5.2 we show the resulting bands of the two FFs. The extrapolation to $q^2 = 0$, which is crucial in order to analyze the experimental data, reads

$$\begin{aligned}
f^\pi(q^2=0)|_{\text{RBC/UKQCD}} &= -0.06 \pm 0.25\,, \\
f^\pi(q^2=0)|_{\text{FNAL/MILC}} &= -0.01 \pm 0.16\,, \\
f^\pi(q^2=0)|_{\text{combined}} &= -0.04 \pm 0.22\,.
\end{aligned}$$

The above results exhibit large uncertainties due to the long extrapolation from the high-q^2 region of the input data down to $q^2 = 0$. Let us stress here again that our results do not depend on any parameterization of the shape of the FFs. This is at variance with what happens with the BCL parameterizations of Refs. [107, 108], where the extrapolated mean values and uncertainties of the FFs at $q^2 = 0$ are plagued by instabilities with respect to the order of the truncation of the expansion. Our results for the FFs at $q^2 = 0$ are consistent within $1.4-1.8$ standard deviations with the recent estimate obtained in Ref. [102] using the LCSR, namely

$$f^\pi(q^2=0)_{\text{LCSR}} = 0.28 \pm 0.03.$$

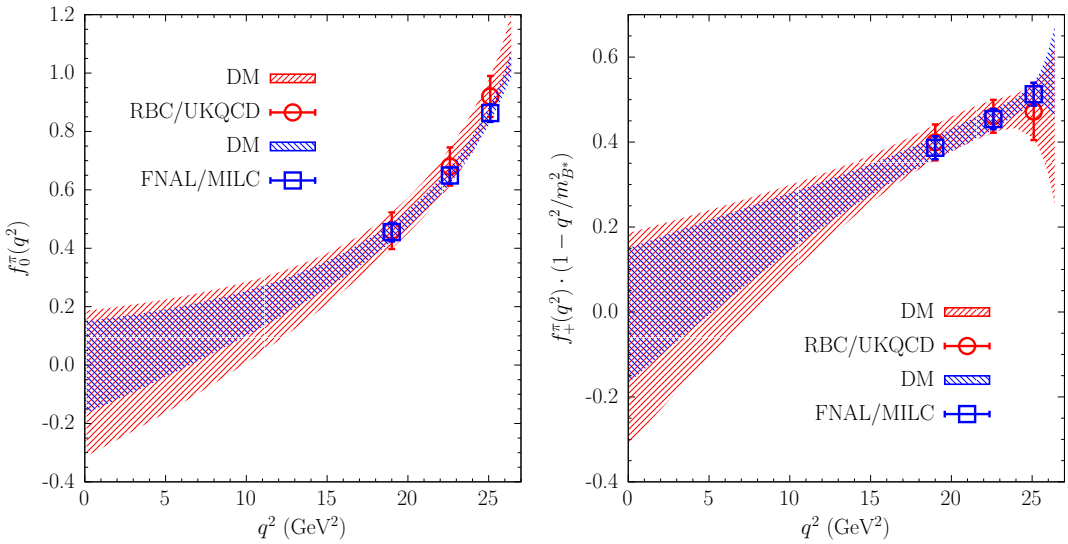

Figure 5.1: *The scalar $f_0^\pi(q^2)$ (left panel) and vector $f_+^\pi(q^2)$ (right panel) FFs entering the semileptonic $B \to \pi\ell\nu_\ell$ decays computed by the DMM as a function of the 4-momentum transfer q^2 using the LQCD inputs from RBC/UKQCD [107] and FNAL/MILC [108] Collaborations (see Table 5.1). For both FFs the red and blue bands correspond to the DMM results obtained at 1σ level using the RBC/UKQCD data (red circles) and FNAL/MILC (blue squares) data, respectively. In the right panel the vector FF is multiplied by the factor $(1-q^2/m_{B^*}^2)$ with $m_{B^*} = 5.325$ GeV.*

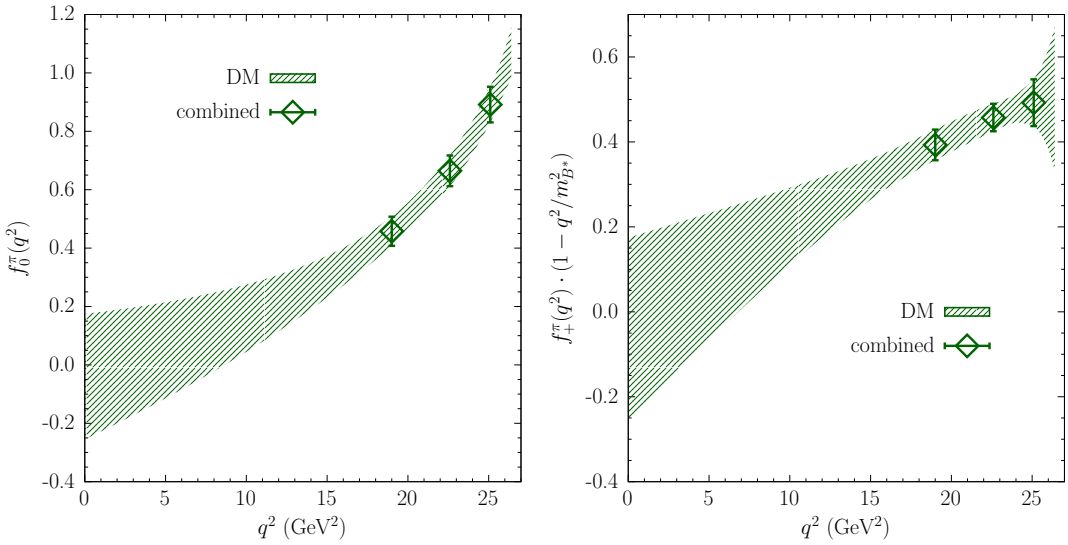

Figure 5.2: *The bands of the scalar $f_0^\pi(q^2)$ (left panel) and vector $f_+^\pi(q^2)$ (right panel) FFs entering the semileptonic $B \to \pi\ell\nu_\ell$ decays computed by the DMM method at 1σ level using as lattice inputs the combined LQCD data of Table 5.1, shown as green diamonds. In the right panel the vector FF is multiplied by the factor $(1-q^2/m_{B^*}^2)$ with $m_{B^*} = 5.325$ GeV.*

As for the semileptonic $B_s \to K$ decays few differences have to be considered with respect to the $B \to \pi$ case besides the obvious changes in the masses of the mesons involved. First, in the kinematical functions (3.45) the isospin factor n_I is now equal to unity instead of 3/2 as in the $B \to \pi$ case. This is due to the fact that in the $B_s \to K$ decays only the strange quark can be the spectator quark

of the transition. Second, following Refs. [107, 109, 110] a modification like the one in the Eq. (5.6) has to be applied also to $\phi_0(z,0)$ due to the presence of a scalar resonance $B^*(0^+)$ with a mass close to 5.68 GeV, lying below the pair production threshold located at $M_{B_s} + M_K \simeq 5.86$ GeV. For the susceptibilities $\chi_{0^+}(0)$ and $\chi_{1^-}(0)$ we adopt conservatively the same values of the $B \to \pi$ case.

We apply the DMM using as inputs the various sets of LQCD data of Table 5.2. A total of $5 \cdot 10^4$ events are generated using the multivariate Gaussian distributions including the correlations among the LQCD computations. As in the $B \to \pi$ case, the unitarity bounds for both f_0^K and f_+^K as well as the KC $f_0^K(0) = f_+^K(0) \equiv f^K(0)$ are satisfied by $98 - 100\%$ of the events. The dispersive bands for the FFs corresponding to the use of the combined LQCD data of Table 5.2 are shown in Fig. 5.3. Note the impact of the KC at $q^2 = 0$ on the extrapolation of the FFs in the low-q^2 region.

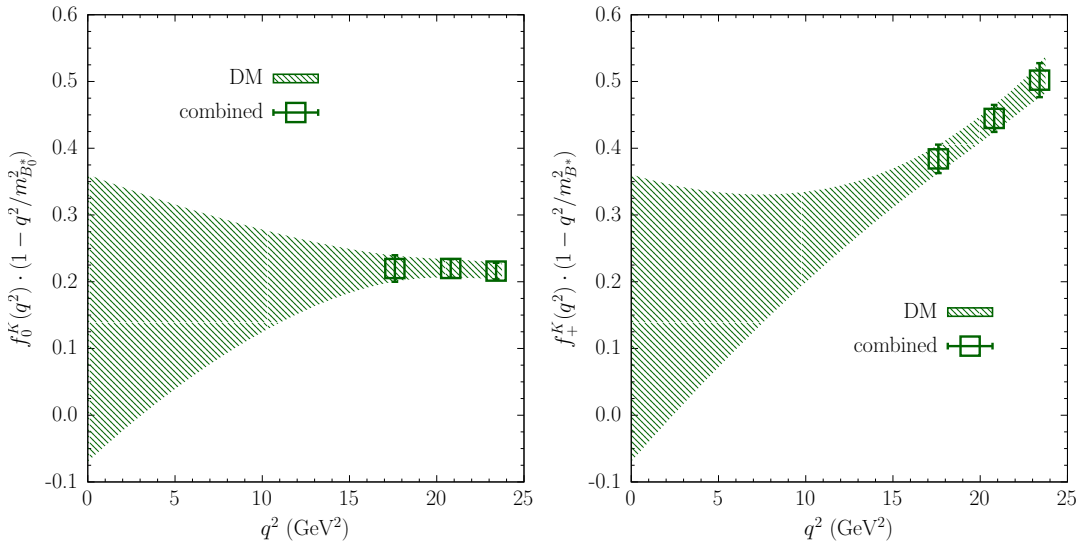

Figure 5.3: *The bands of the scalar $f_0^K(q^2)$ (left panel) and vector $f_+^K(q^2)$ (right panel) FFs entering the semileptonic $B_s \to K\ell\nu_\ell$ decays computed by the DMM at 1σ level using as inputs the combined LQCD data of Table 5.2, shown as green diamonds. In the left panel the scalar FF is multiplied by the factor $(1 - q^2/m_{B_0^*}^2)$ with $m_{B_0^*} = 5.68$ GeV, while in the right panel the vector FF is multiplied by the factor $(1 - q^2/m_{B^*}^2)$ with $m_{B^*} = 5.325$ GeV.*

The extrapolation of the FFs to $q^2 = 0$ reads

$$\begin{aligned} f^K(q^2=0)|_{\rm RBC/UKQCD} &= 0.08 \pm 0.15 \ , \\ f^K(q^2=0)|_{\rm HPQCD} &= 0.28 \pm 0.21 \ , \\ f^K(q^2=0)|_{\rm FNAL/MILC} &= 0.07 \pm 0.11 \ , \\ f^K(q^2=0)|_{\rm combined} &= 0.15 \pm 0.21 \ . \end{aligned}$$

The above results can be compared with the recent LCSR estimate of Ref. [113], which is

$$f^K(q^2=0)_{\rm LCSR} = 0.336 \pm 0.023 \ .$$

It can be seen that the results based on the RBC/UKQCD and FNAL/MILC data differ respectively by 1.7 and 2.4 standard deviations from the LCSR estimate, while the results based on the HPQCD data and the combined LQCD ones are in agreement thanks to larger mean values and uncertainties.

The DMM results presented so far indicate clearly that for both the $B \to \pi$ and $B_s \to K$ channels the extension of direct LQCD computations of the FFs toward values of q^2 lower than ~ 17 GeV^2 is crucial for improving the precision of their extrapolation to $q^2 = 0$ without resorting to the use of the experimental data.

5.1.3 New estimate of $|V_{ub}|$

In order to obtain $|V_{ub}|$ we use our results for the FFs in the whole kinematical range and the experimental data. For the semileptonic $B \to \pi$ decays the BaBar and the Belle Collaborations [114–117] have measured the *differential* branching ratios (BRs) in different bins of the 4-momentum transfer q^2. Instead, for the $B_s \to K$ decays only the ratio of the *total* branching fractions of the semileptonic $B_s \to K$ and $B_s \to D_s$ decays is available at present [118]. Since both the decays are pseudoscalar-to-pseudoscalar ones, the expression of the differential decay width is analogous to Eq. (3.7), *i.e.*

$$\begin{aligned}\frac{d\Gamma(B_{(s)} \to \pi(K)\ell\nu_\ell)}{dq^2} &= \frac{G_F^2|V_{ub}|^2}{24\pi^3}\left(1-\frac{m_\ell^2}{q^2}\right)^2\left[|\vec{p}_{\pi(K)}|^3\left(1+\frac{m_\ell^2}{2q^2}\right)|f_+^{\pi(K)}(q^2)|^2\right. \\ &+ \left. m_{B_{(s)}}^2|\vec{p}_{\pi(K)}|\left(1-r_{\pi(K)}^2\right)^2\frac{3m_\ell^2}{8q^2}|f_0^{\pi(K)}(q^2)|^2\right] , \end{aligned} \tag{5.9}$$

where explicitly the 3-momentum of the $\pi(K)$ meson in the $B_{(s)}$-meson rest frame is

$$|\vec{p}_{\pi(K)}| = m_{\pi(K)}\sqrt{\left(\frac{1+r_{\pi(K)}^2 - q^2/m_{B_{(s)}}^2}{2r_{\pi(K)}}\right)^2 - 1} \tag{5.10}$$

with $r_{\pi(K)} \equiv m_{\pi(K)}/m_{B_{(s)}}$.

- **$|V_{ub}|$ from $B \to \pi\ell\nu_\ell$ decays**

For the extraction of the CKM matrix element, we follow the procedure used both in the previous Chapter and in Refs. [3, 76] in the case of several semileptonic heavy-meson decays characterized by the production of a final pseudoscalar meson. In what follows, however, we will distinguish the two different channels that have been measured by the experiments, *i.e.* $B^0 \to \pi^-\ell^+\nu$ and $B^+ \to \pi^0\ell^+\nu$. Starting from the Eq. (5.9), for the generic i-th bin in q^2 we have [117]

$$|V_{ub}|_i = \sqrt{\frac{C_v}{\tau_{B^v}} \cdot \frac{\Delta\mathcal{B}|_i^{exp}}{\Delta\zeta_i}}, \tag{5.11}$$

where $\Delta\mathcal{B}|_i^{exp}$ is the experimental branching fraction and $\Delta\zeta_i$ the corresponding theoretical decay width (without $|V_{ub}|$ therein) in the given bin. Since $\left|\pi^0\right\rangle \equiv \left(\left|u\bar{u}\right\rangle - \left|d\bar{d}\right\rangle\right)/\sqrt{2}$, the isospin coefficient C_v is equal to 2 for the $B^+ \to \pi^0\ell^+\nu$ decays and to 1 for the $B^0 \to \pi^-\ell^+\nu$ transitions. Finally, τ_{B^v} is the lifetime of the decaying B-meson.

We generate N_{boot} bootstraps of the measured differential BR for each bin in q^2 and experiment [114–117] through a multivariate Gaussian distribution. Then, we extract N_{boot} bootstrap events for the vector FF $f_+(q^2)$ for each q^2-bin. In the latter case, the mean value and the covariance matrix of the distribution are those computed through our DMM. Thus, we compute N_{boot} values of $|V_{ub}|$ for each q^2-bin and each experiment through Eq. (5.11).

For any specific bin we fit the histogram of the resulting events of $|V_{ub}|$ with a normal distribution and store the values of the corresponding marginalized parameters, obtaining in this way mean values, uncertainties and correlations for $|V_{ub}|$ for each bin and experiment. We then evaluate the CKM matrix element $|V_{ub}|$ for the n-th experiment ($n = 1, \ldots, 6$ for the semileptonic $B \to \pi$ decays) through the following formulae

$$|V_{ub}|_n = \frac{\sum_{i,j}(\mathbf{C}^{-1})_{ij}|V_{ub}|_j}{\sum_{i,j}(\mathbf{C}^{-1})_{ij}}, \qquad \sigma^2_{|V_{ub}|_n} = \frac{1}{\sum_{i,j}(\mathbf{C}^{-1})_{ij}}, \tag{5.12}$$

where the indices i, j run over all the q^2-bins of the n-th experiment and $\mathbf{C}_{ij}$ is the covariance matrix among the bins. This is completely analogous to what done for the $B \to D$ decays, see Eq. (4.5). In Fig. 5.4 we show our results for $|V_{ub}|$ for each of the semileptonic $B \to \pi$ experiments, together with the mean values (5.12), adopting the DMM results for the FFs obtained using as inputs the combined LQCD data of Table 5.1. For each experiment the corresponding correlated mean values (5.12) are collected in Table 5.3.

experiment	BaBar 2011	BaBar 2012 ($B^0 \to \pi^-$)	BaBar 2012 ($B^+ \to \pi^0$)
$\|V_{ub}\| \cdot 10^3$	3.25 ± 0.33	3.58 ± 0.34	3.51 ± 0.46

experiment	Belle 2011	Belle 2013 ($B^0 \to \pi^-$)	Belle 2013 ($B^+ \to \pi^0$)
$\|V_{ub}\| \cdot 10^3$	3.74 ± 0.32	4.03 ± 0.41	3.64 ± 0.51

Table 5.3: *The correlated weighted averages (5.12) for each of the six experiments of Refs. [114–117]. The theoretical dispersive bands of the FFs correspond to the use of the combined LQCD data of Table 5.1 as inputs.*

Our final results for $|V_{ub}|$, evaluated making use of the averaging procedure given by Eqs. (5.2)-(5.3), read

$$\begin{aligned} |V_{ub}|^{B\pi}_{\text{RBC/UKQCD}} \cdot 10^3 &= 3.52 \pm 0.49 \ , \\ |V_{ub}|^{B\pi}_{\text{FNAL/MILC}} \cdot 10^3 &= 3.76 \pm 0.41 \ , \\ |V_{ub}|^{B\pi}_{\text{combined}} \cdot 10^3 &= 3.62 \pm 0.47 \ , \end{aligned} \tag{5.13}$$

which are consistent with the latest exclusive determination $|V_{ub}|_{excl} \cdot 10^3 = 3.70\,(16)$ from PDG [90]. Our uncertainties are larger than the PDG one, because we do not mix the theoretical calculations of the FFs with the experimental data to constrain the shape of the FFs in order to avoid possible biases. The rationale of this choice is the same one discussed in the previous Chapter during the study of semileptonic $B \to D^*$ decays.

- $|V_{ub}|$ **from** $B_s \to K\ell\nu_\ell$ **decays**

The LHCb Collaboration has observed for the first time the semileptonic $B_s \to K\ell\nu_\ell$ decays [118] and measured the ratio of the branching fractions of the $B_s^0 \to K^-\mu^+\nu_\mu$ and the $B_s^0 \to D_s^-\mu^+\nu_\mu$ processes,

$$R_{BF} \equiv \frac{\mathcal{B}(B_s^0 \to K^-\mu^+\nu_\mu)}{\mathcal{B}(B_s^0 \to D_s^-\mu^+\nu_\mu)} \ ,$$

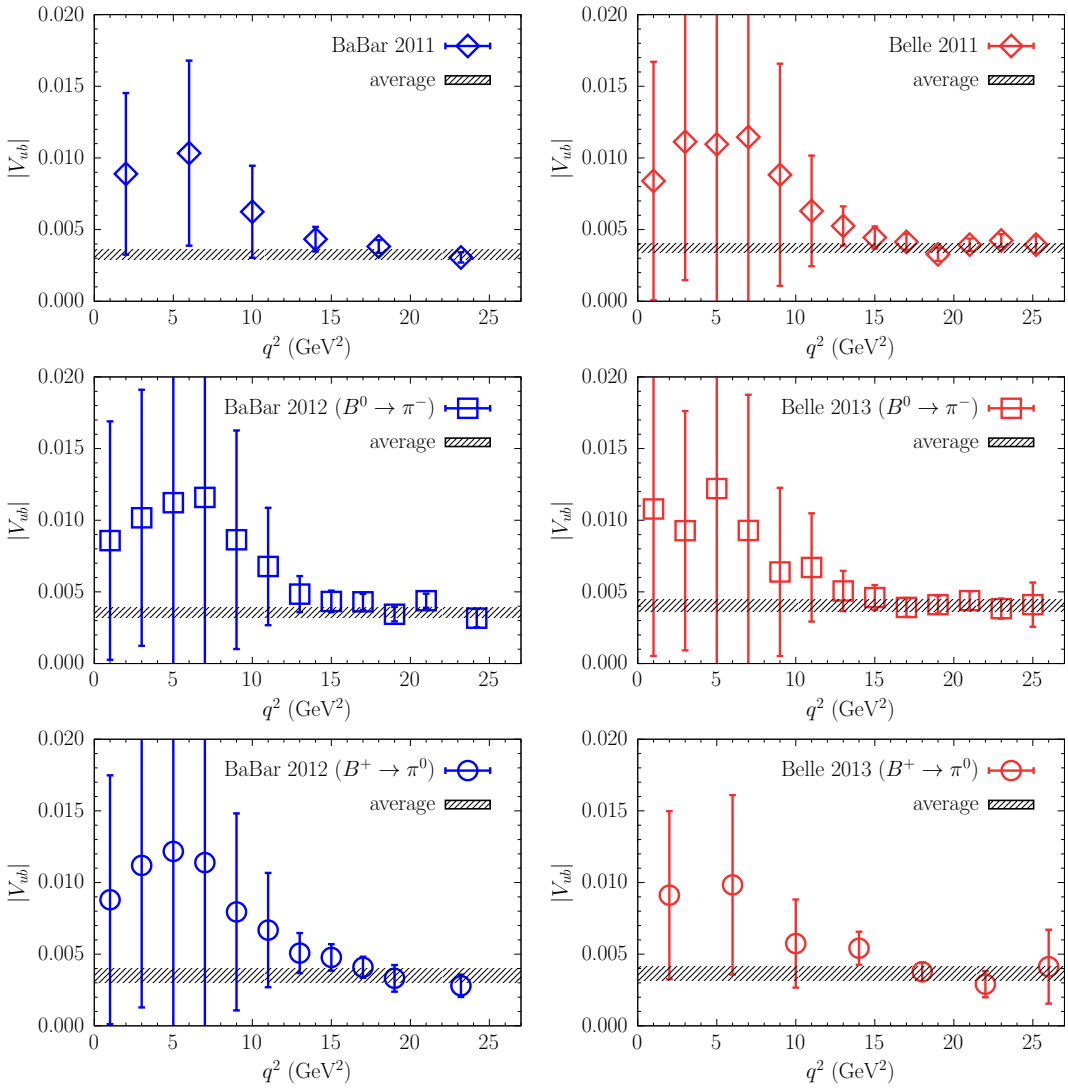

Figure 5.4: *Bin-per-bin estimates of $|V_{ub}|$ obtained using Eq. (5.11) for each of the six experiments of Refs. [114–117] specified in the insets of the panels as a function of q^2. The theoretical dispersive bands of the FFs correspond to the use of the combined LQCD data of Table 5.1 as inputs. The black dashed bands represent the correlated weighted averages (5.12) for each experiment, shown in Table 5.3.*

in two different q^2-bins, namely

$$R_{BF}(\text{low}) = (1.66 \pm 0.08 \pm 0.07 \pm 0.05) \cdot 10^{-3} \quad \text{for} \quad q^2 \leq 7\,\text{GeV}^2 \,, \tag{5.14}$$

$$R_{BF}(\text{high}) = (3.25 \pm 0.21^{+0.16}_{-0.17} \pm 0.09) \cdot 10^{-3} \quad \text{for} \quad q^2 \geq 7\,\text{GeV}^2 \,, \tag{5.15}$$

where the first error is statistical, the second one is systematic and the third one is due to the uncertainty on the $D_s^- \to K^+K^-\pi^-$ branching fraction.

In order to obtain an exclusive estimate of $|V_{ub}|$ we make use of the life time of the B_s-meson, $\tau_{B_s^0} = (1.516 \pm 0.006) \cdot 10^{-12}$ s [90], and of the experimental value of the branching ratio $\mathcal{B}(B_s^0 \to D_s^- \mu^+ \nu_\mu)$ measured by the LHCb Collaboration [88]

$$\mathcal{B}(B_s^0 \to D_s^- \mu^+ \nu_\mu) = (2.49 \pm 0.12 \pm 0.14 \pm 0.16) \cdot 10^{-2} \,,$$

where the first error is statistical, the second one is systematic and the third one is due to limited knowledge of the normalization branching fractions.

Then, we use the FFs obtained with our DMM to compute the differential decay width $d\Gamma/dq^2$ according to the formula (except $|V_{ub}|^2$) given in Eq. (5.9). Our results for $|V_{ub}|$ are collected in Table 5.4.

q^2-bin	RBC/UKQCD	FNAL/MILC	HPQCD	combined
low	6.70 ± 3.26	6.43 ± 2.03	3.57 ± 1.94	5.31 ± 3.02
high	4.20 ± 0.56	4.10 ± 0.38	3.54 ± 0.43	3.94 ± 0.59

Table 5.4: *Values of $|V_{ub}| \cdot 10^3$ extracted from the $B_s \to K\ell\nu_\ell$ decays measured at LHCb in the low ($q^2 \leq 7$ GeV^2) and high ($q^2 \geq 7$ GeV^2) q^2-bins using the dispersive bands for the theoretical FFs.*

Assuming (conservatively) that the systematic errors of the two experimental results (5.14)-(5.15) are 100% correlated (which corresponds to a correlation coefficient equal to 0.486 in the experimental, statistical plus systematic covariance matrix), the weighted averages of the two bins, carried out following Eqs. (5.2)-(5.3) for each set of FFs, read

$$\begin{aligned} |V_{ub}|^{B_sK}_{\rm RBC/UKQCD} \cdot 10^3 &= 3.93 \pm 0.46 \ , \\ |V_{ub}|^{B_sK}_{\rm FNAL/MILC} \cdot 10^3 &= 3.93 \pm 0.35 \ , \\ |V_{ub}|^{B_sK}_{\rm HPQCD} \cdot 10^3 &= 3.54 \pm 0.35 \ , \\ |V_{ub}|^{B_sK}_{\rm combined} \cdot 10^3 &= 3.77 \pm 0.48 \ , \end{aligned} \tag{5.16}$$

which are consistent with our results (5.13), obtained from the analysis of the $B \to \pi\ell\nu_\ell$ decays, and with the latest exclusive determination $|V_{ub}|_{excl} \cdot 10^3 = 3.70\,(16)$ from PDG [90]. We remind that the PDG uncertainty results from analyses in which theoretical calculations of the FFs and experimental data are mixed in order to constrain the shape of the FFs.

5.1.4 Theoretical estimate of $R^{\tau/\mu}_{\pi(K)}$, $\bar{\mathcal{A}}^{\ell,\pi(K)}_{FB}$ and $\bar{\mathcal{A}}^{\ell,\pi(K)}_{polar}$

In this Section we give pure theoretical estimates of various quantities of phenomenological interest, which are independent of $|V_{ub}|$, namely the ratio of the τ/μ differential decay rates $R^{\tau/\mu}_{\pi(K)}$, the normalized forward-backward asymmetry $\bar{\mathcal{A}}^{\ell,\pi(K)}_{FB}$ and the normalized lepton polarization asymmetry $\bar{\mathcal{A}}^{\ell,\pi(K)}_{polar}$.

The τ/μ ratio $R^{\tau/\mu}_{\pi(K)}$ is defined as

$$R^{\tau/\mu}_{\pi(K)} \equiv \frac{\Gamma(B_{(s)} \to \pi(K)\tau\nu_\tau)}{\Gamma(B_{(s)} \to \pi(K)\mu\nu_\mu)} \ , \tag{5.17}$$

where

$$\Gamma(B_{(s)} \to \pi(K)\ell\nu_\ell) = \frac{G_F^2|V_{ub}|^2}{24\pi^3} \int_{m_\ell^2}^{(m_{B_{(s)}} - m_{\pi(K)})^2} dq^2 \left[|\vec{p}_{\pi(K)}|^3 L_+ \left(\frac{m_\ell^2}{q^2}\right) |f_+^{\pi(K)}(q^2)|^2 \right.$$

$$+ \quad m^2_{B_{(s)}} \left(1 - r^2_{\pi(K)}\right)^2 |\vec{p}_{\pi(K)}| L_0 \left(\frac{m^2_\ell}{q^2}\right) |f_0^{\pi(K)}(q^2)|^2 \Bigg]$$

with m_ℓ being the lepton mass ($\ell = \tau, \mu$) and

$$L_+(x) = (1-x)^2 \left(1 + \frac{x}{2}\right) , \qquad L_0(x) = (1-x)^2 \frac{3x}{8} .$$

The forward-backward asymmetry $\mathcal{A}_{FB}^{\ell,\pi(K)}$ is defined as

$$\mathcal{A}_{FB}^{\ell,\pi(K)}(q^2) \equiv \int_0^1 \frac{d^2\Gamma}{dq^2 d\cos\theta_l} d\cos\theta_l - \int_{-1}^0 \frac{d^2\Gamma}{dq^2 d\cos\theta_l} d\cos\theta_l .$$

Note that θ_ℓ represents the angle between the final charged lepton and the $B_{(s)}$-meson momenta in the rest frame of the final state leptons. Since a direct computation of the two-fold differential decay width within the Standard Model gives the expression

$$\begin{aligned}
\frac{d^2\Gamma(B_{(s)} \to \pi(K)\ell\nu_\ell)}{dq^2 d\cos\theta_\ell} &= \frac{G_F^2 |V_{ub}|^2}{128\pi^3 m^2_{B_{(s)}}} \left(1 - \frac{m^2_\ell}{q^2}\right)^2 \\
&\cdot \Bigg\{ 4m^2_{B_{(s)}} |\vec{p}_{\pi(K)}|^3 \left(\sin^2\theta_\ell + \frac{m^2_\ell}{2q^2}\cos^2\theta_\ell\right) |f_+^{\pi(K)}(q^2)|^2 \\
&+ \frac{4m^2_\ell}{q^2}(m^2_{B_{(s)}} - m^2_{\pi(K)}) m_{B_{(s)}} |\vec{p}_{\pi(K)}|^2 \cos\theta_\ell \ \mathrm{Re}\left(f_+^{\pi(K)}(q^2) f_0^{*\pi(K)}(q^2)\right) \\
&+ \frac{m^2_\ell}{q^2}(m^2_{B_{(s)}} - m^2_{\pi(K)})^2 |\vec{p}_{\pi(K)}| |f_0^{\pi(K)}(q^2)|^2 \Bigg\} ,
\end{aligned} \tag{5.18}$$

one has

$$\begin{aligned}
\mathcal{A}_{FB}^{\ell,\pi(K)}(q^2) &= \frac{G_F^2 |V_{ub}|^2}{32\pi^3 m_{B_{(s)}}} \left(1 - \frac{m^2_\ell}{q^2}\right)^2 |\vec{p}_{\pi(K)}|^2 \frac{m^2_\ell}{q^2}(m^2_{B_{(s)}} - m^2_{\pi(K)}) \\
&\cdot \quad \mathrm{Re}[f_+^{\pi(K)}(q^2) f_0^{*\pi(K)}(q^2)] .
\end{aligned}$$

Then, the normalized forward-backward asymmetry $\bar{\mathcal{A}}_{FB}^{\ell,\pi(K)}$ is given by

$$\bar{\mathcal{A}}_{FB}^{\ell,\pi(K)} \equiv \frac{\int dq^2 \, \mathcal{A}_{FB}^{\ell,\pi(K)}(q^2)}{\int dq^2 \, d\Gamma^{\pi(K)}/dq^2} . \tag{5.19}$$

In conclusion, we compute also the lepton polarization asymmetry $\mathcal{A}_{polar}^{\ell,\pi(K)}$ defined as

$$\mathcal{A}_{polar}^{\ell,\pi(K)}(q^2) \equiv \frac{d\Gamma_-^{\pi(K)}}{dq^2} - \frac{d\Gamma_+^{\pi(K)}}{dq^2} ,$$

where [119]

$$\frac{d\Gamma_-^{\pi(K)}}{dq^2} = \frac{G_F^2 |V_{ub}|^2}{24\pi^3} \left(1 - \frac{m^2_\ell}{q^2}\right)^2 |\vec{p}_{\pi(K)}|^3 |f_+^{\pi(K)}(q^2)|^2 ,$$

$$\frac{d\Gamma_+^{\pi(K)}}{dq^2} = \frac{G_F^2|V_{ub}|^2}{24\pi^3}\left(1-\frac{m_\ell^2}{q^2}\right)^2\frac{m_\ell^2}{q^2}|\vec{p}_{\pi(K)}| \cdot \left[\frac{3}{8}\frac{\left(m_{B_{(s)}}^2-m_{\pi(K)}^2\right)^2}{m_{B_{(s)}}^2}|f_0^{\pi(K)}(q^2)|^2+\frac{1}{2}|\vec{p}_{\pi(K)}|^2|f_+^{\pi(K)}(q^2)|^2\right] .$$

The normalized lepton polarization asymmetry $\bar{\mathcal{A}}_{polar}^{\ell,\pi(K)}$ is finally given by

$$\bar{\mathcal{A}}_{polar}^{\ell,\pi(K)} \equiv \frac{\int dq^2\, \mathcal{A}_{polar}^{\ell,\pi(K)}(q^2)}{\int dq^2\, d\Gamma^{\pi(K)}/dq^2}. \tag{5.20}$$

In Tables 5.5 and 5.6 we collect our theoretical estimates of the quantities (5.17-5.20) for each set of LQCD computations of the FFs in the case of the $B \to \pi$ and $B_s \to K$ decays, respectively. Within the uncertainties our results are consistent with recent estimates [102, 120, 121] based on the BCL or BSZ parameterizations of the FFs.

	RBC/UKQCD	FNAL/MILC	combined
$R_\pi^{\tau/\mu}$	0.767(145)	0.838(75)	0.793(118)
$\bar{\mathcal{A}}_{FB}^{\mu,\pi}$	0.0043(39)	0.0018(14)	0.0034(31)
$\bar{\mathcal{A}}_{FB}^{\tau,\pi}$	0.219(25)	0.221(19)	0.220(24)
$\bar{\mathcal{A}}_{polar}^{\mu,\pi}$	0.985(11)	0.991(4)	0.988(9)
$\bar{\mathcal{A}}_{polar}^{\tau,\pi}$	0.294(87)	0.309(82)	0.301(86)

Table 5.5: *The theoretical values of the quantities (5.17-5.20) in the case of the semileptonic $B \to \pi\ell\nu_\ell$ decays with $\ell = \mu, \tau$ adopting the RBC/UKQCD, the FNAL/MILC and the combined LQCD data of Table 5.1 as inputs for our DMM.*

	RBC/UKQCD	FNAL/MILC	HPQCD	combined
$R_K^{\tau/\mu}$	0.845(122)	0.816(64)	0.680(134)	0.755(138)
$\bar{\mathcal{A}}_{FB}^{\mu,K}$	0.0032(18)	0.0024(12)	0.0059(29)	0.0046(28)
$\bar{\mathcal{A}}_{FB}^{\tau,K}$	0.257(14)	0.246(14)	0.278(19)	0.262(23)
$\bar{\mathcal{A}}_{polar}^{\mu,K}$	0.990(5)	0.992(4)	0.982(8)	0.986(7)
$\bar{\mathcal{A}}_{polar}^{\tau,K}$	0.172(54)	0.254(64)	0.112(79)	0.172(91)

Table 5.6: *The same as in Table 5.5, but in the case of the semileptonic $B_s \to K$ decays adopting the RBC/UKQCD, the FNAL/MILC, the HPQCD and the combined LQCD data of Table 5.2 as inputs for our DMM.*

As for the experimental side, only one measurement of $R_\pi^{\tau/\mu}$ by Belle is presently available, namely [122]

$$R_\pi^{\tau/\mu}|_{exp} = 1.05 \pm 0.51 , \tag{5.21}$$

which still has a large uncertainty compared to our theoretical ones. Note that the uncertainty on the above ratio expected by Belle II at 50 ab^{-1} of luminosity [123] is $\delta R_\pi^{\tau/\mu} \simeq 0.09$, which will be comparable to our present theoretical uncertainties.

5.2 Summary and comparison with UTfit

Let us finally summarize the DMM determination of the CKM matrix elements $|V_{cb}|$ and $|V_{ub}|$ from semileptonic charged-current B decays.

For what concerns $|V_{cb}|$, many exclusive estimates have been obtained in the previous Chapter through the application of the DMM to the semileptonic $B_{(s)} \to D_{(s)}^{(*)} \ell\nu$ transitions. An average of the estimates in Eqs. (4.55)-(4.58) give a very precise final DMM determination of this CKM matrix element, *i.e.*

$$|V_{cb}|_{\rm DMM} \cdot 10^3 = 41.4 \pm 0.8. \tag{5.22}$$

For what concerns $|V_{ub}|$, instead, we have obtained new exclusive estimates in a rigorous model-independent way through the study of the available lattice and experimental data concerning the semileptonic $B \to \pi$ and $B_s \to K$ decays. Our results for $|V_{ub}|$ can be summarized as

- from the semileptonic $B \to \pi$ decays

$$|V_{ub}| \cdot 10^3 = 3.62 \pm 0.47 \ ,$$

- from the semileptonic $B_s \to K$ processes

$$|V_{ub}| \cdot 10^3 = 3.77 \pm 0.48 \ .$$

They are compatible with each other and also consistent within 1σ level with the latest exclusive and inclusive determinations of $|V_{ub}|$, $|V_{ub}|_{excl} \cdot 10^3 = 3.70\,(16)$ and $|V_{ub}|_{incl} \cdot 10^3 = 4.13\,(26)$, taken from PDG [90]. Then, by averaging the above results corresponding to the $B \to \pi$ and $B_s \to K$ channels our final estimate of $|V_{ub}|$ reads

$$|V_{ub}|_{\rm DMM} \cdot 10^3 = 3.69 \pm 0.34 \ . \tag{5.23}$$

To conclude this Part of the Thesis, I think that it is very interesting to compare the DMM estimates in Eqs. (5.22)-(5.23) with the predictions coming from the analysis of the Unitarity Triangle, whose main properties have already been discussed in Chapter 2. This kind of study is very powerful since, within the Standard Model, it allows to determine precisely the SM parameters of the flavour sector, to test the compatibility of the experimental results with the theoretical calculations and finally, to predict (still unmeasured) flavour SM observables.

In the last twenty years, the **UT***fit* [124, 125] collaboration has been routinely updating the Unitarity Triangle analysis through global analyses of both theoretical and experimental data. In the last 2021 SM update [126], the predictions of the CKM matrix elements $|V_{cb}|$ and $|V_{ub}|$ from the SM global fits read

$$|V_{cb}|_{\rm UT} = 41.9 \pm 0.5, \qquad |V_{ub}|_{\rm UT} = 3.68 \pm 0.10. \tag{5.24}$$

The most important observations are the followings. First of all, these UT estimates are completely compatible with the DMM ones in Eqs. (5.22)-(5.23). Secondly, also the Unitarity Triangle Analysis (which is independent of the LQCD data of the FFs and the experimental data by the Belle Collaboration discussed in the previous Chapter) points towards a value of $|V_{cb}|$ which is higher with respect to the FLAG exclusive estimate [39] and, at the same time, compatible with the inclusive determination [30]. In the future years, without any doubt, the publication of new LQCD data and measurements will finally close the window on the CKM matrix element puzzles.

Part II

Flavour Physics Beyond the Standard Model

Chapter 6

An Effective Field Theory approach to Flavour Physics

In the previous Part we have developed a complete analysis of semileptonic charged current B decays within the SM in order to shed a new light on two important phenomenological problems affecting these transitions, *i.e.* the extraction of the CKM matrix elements $|V_{cb}|$ and $|V_{ub}|$ and the computation of the LFU observables, with particular attention given to the $R(D^{(*)})$ ratios. However, as it will be discussed in a while, the SM *cannot* be considered the complete theory of Nature and, thus, needs to be extended. In this sense, Flavour Physics offers a unique opportunity not only to test the the SM, as flavour observables are related to all the processes involving different generations of quarks and leptons, but also to study possible extensions of the SM itself. In fact, the measured flavour observables allow to put relevant constraints on the physical parameters of the BSM theories.

In this Chapter we will develop an EFT approach to Flavour Physics, which is particularly useful in constraining in a model-independent way the space of all the possible extensions of the SM. After having illustrated the reasons that justify the necessity to study NP models, we will see also which properties and symmetries the flavour structure of such scenarios have to respect. In fact, since the SM is the valid theory of Nature at low energies, all the SM predictions of the flavour observables, that can also be described in terms of NP operators, have to be recovered in this limit. This introductory Chapter will then allow us to review and study explicitly two BSM models that are very well-known in literature, namely the Composite Higgs in Chapter 7 and the LeptoQuarks in Chapter 8.

Note finally that a natural link exists between this Part of the Thesis and the previous one. As we will see, in the BSM studies many parameters of the SM are directly involved. In addition to the CKM matrix elements, which have been widely discussed in relation to semileptonic B decays, another example is offered for instance by the meson decay constants, computed by many Collaborations with numerical simulations on the lattice. For these reasons, *the more precise are the theoretical estimates of the SM parameters, the more stringent will be the bounds on the NP effects eventually affecting the flavour sector*. This is a fundamental issue to keep in mind especially in view of the improvement in sensitivity of future experiments.

6.1 Why is it necessary to go Beyond the Standard Model?

Although the Standard Model explains a series of phenomenological phenomena with incredible precision, there is, as stated in the Introduction, the necessity to consider possible NP extensions because of two sets of reasons.

- On the one hand, there are some experimental facts that do not find an explanation within the SM. Firstly, the presence of Dark Matter in our Universe, whose existence is justified by many astrophysical and cosmological observations, as we will see in Part III. Secondly, the asymmetry between baryons and anti-baryons, which is of fundamental importance in order to understand the history of our Universe but, at the same time, does not find a justification in the SM. In fact, although the baryonic number is violated by the sphalerons in a non-perturbative way, this fact is not sufficient to explain quantitatively the observed asymmetry.

- On the other hand, there are many theoretical arguments that we have to take into account. First of all, the Standard Model does not include gravity, since this interaction is not quantizable in ordinary field theory and gives birth to a non-renormalizable theory. Furthermore, it does not justify the equality in module of proton and electron charges. This fact is experimentally well-known and has been measured with an extremely high precision. In principle, it would be naturally explained in a GUT as a consequence of the zero traces of the generators of the GU symmetry group. Finally, there is the problem of Naturalness, that we have described in Chapter 2. To be extremely synthetic, in order to justify the measured mass of the Higgs within the SM, we should admit an incredible fine tuning of the parameters in the theory.

For all these reasons (and many other problems related to High Energy Physics), it is reasonable to consider the SM as an EFT valid at low energies. The EFT approach has been briefly introduced in Chapter 2 to explain the Naturalness problem. In what follows, we will apply it to Flavour Physics.

6.2 Effective Operators and BSM Flavour Physics

On the same spirit of Eq. (2.33), the Lagrangian of a generic UV extension of the SM can be sketched as

$$\mathcal{L}_{\text{eff}} = -\mathcal{H}_{\text{eff}} = \sum_i \frac{1}{\Lambda^2_{\text{UV}}} C_{\text{eff,i}} \mathcal{O}_{\text{eff,i}}, \tag{6.1}$$

where the WCs $C_{\text{eff,i}}$ are evaluated at some renormalization scale and Λ_{UV} is the NP energy scale. Note that here we are interested in dimension-6 operators. In fact, the ones with dimension equal or less than four can in principle have NP contributions, but these effects can be reabsorbed in the SM couplings, while the ones with higher dimension are more suppressed if the NP scale is large. Note that all the operators that enter in Eq. (6.1) have to respect some minimal requirements, *i.e.* the invariance under the SM $SU(3) \times SU(2) \times U(1)$ symmetry group and the conservation of both the baryonic and the leptonic numbers, which are symmetries of the SM too (although accidental).

At this point, in order to describe the quark transitions at low-energy, let us say at the scale of the bottom mass m_b, it is useful to define another EFT, described by the Weak Effective Hamiltonian

$$\mathcal{H} = -\frac{4G_F}{\sqrt{2}} \lambda_{\text{CKM}} \left[\frac{\alpha_{em}}{4\pi} \left(\sum_i C_i \mathcal{O}_i + \sum_i C'_i \mathcal{O}'_i \right) \right]. \tag{6.2}$$

The Wilson coefficients now can have contributions from both NP and heavy SM degrees of freedom. From the point of view of Feynman diagrams, the relevant operators contribute to interactions at the loop level within the SM. To be more specific, their contributions come from penguin (only for $\Delta F = 1$ interactions) or box (for both $\Delta F = 1$ and $\Delta F = 2$ processes) diagrams, as shown in Figure 6.1. For this reason, the corresponding quark transitions are *Cabibbo-suppressed*. In other words, since at least one W gauge boson is present inside these loops, we will always find a suppression of

these processes induced by the off-diagonal CKM matrix elements, which are the smallest ones as clear from the Wolfenstein structure (2.18). Note that this can be understood by looking at Eq.(6.2). In fact, the factor $\alpha_{em}/(4\pi)$ comes from the fact that, as stated above, the operators $\mathcal{O}_i^{(')}$ induce loop contributions and $\lambda_{\rm CKM}$ is the corresponding Cabibbo-suppression. The factor $4G_F/\sqrt{2}$ represents, instead, the SM scale. Then, the list of all the operators that contributes to a generic FCNC $q_i \to q_j$ is composed by:

- $\Delta F = 2$ operators, which are relevant for neutral meson-antimeson oscillations (we have chosen the basis as in [127])

$$\begin{aligned}
&\mathcal{Q}_1 = (\bar{q}_{Li}\gamma^\mu q_{Lj})(\bar{q}_{Li}\gamma^\mu q_{Lj}), && \mathcal{Q}_1^{'} = (\bar{q}_{Ri}\gamma^\mu q_{Rj})(\bar{q}_{Ri}\gamma^\mu q_{Rj})\\
&\mathcal{Q}_2 = (\bar{q}_{Ri} q_{Lj})(\bar{q}_{Ri} q_{Lj}), && \mathcal{Q}_2^{'} = (\bar{q}_{Li} q_{Rj})(\bar{q}_{Li} q_{Rj})\\
&\mathcal{Q}_3 = (\bar{q}^\alpha_{Ri} q^\beta_{Lj})(\bar{q}^\beta_{Ri} q^\alpha_{Lj}), && \mathcal{Q}_3^{'} = (\bar{q}^\alpha_{Li} q^\beta_{Rj})(\bar{q}^\beta_{Li} q^\alpha_{Rj})\\
&\mathcal{Q}_4 = (\bar{q}_{Ri} q_{Lj})(\bar{q}_{Li} q_{Rj}),\\
&\mathcal{Q}_5 = (\bar{q}^\alpha_{Ri} q^\beta_{Lj})(\bar{q}^\beta_{Li} q^\alpha_{Rj}).
\end{aligned} \tag{6.3}$$

  Note that (here and in what follows) the primed operators can be obtained from the unprimed ones through a $L \leftrightarrow R$ transformation;

- four-quark $\Delta F = 1$ operators, which are important for non-leptonic meson decays

$$\begin{aligned}
&\mathcal{O}_1^k = (\bar{q}_{Li}\gamma^\mu q_{Lj})(\bar{q}_{Lk}\gamma^\mu q_{Lk}), && \mathcal{O}_1^{'k} = (\bar{q}_{Ri}\gamma^\mu q_{Rj})(\bar{q}_{Rk}\gamma^\mu q_{Rk}),\\
&\mathcal{O}_2^k = (\bar{q}^\alpha_{Li}\gamma^\mu q^\beta_{Lj})(\bar{q}^\beta_{Lk}\gamma^\mu q^\alpha_{Lk}), && \mathcal{O}_2^{'k} = (\bar{q}^\alpha_{Ri}\gamma^\mu q^\beta_{Rj})(\bar{q}^\beta_{Rk}\gamma^\mu q^\alpha_{Rk}),\\
&\mathcal{O}_5^k = (\bar{q}_{Li}\gamma^\mu q_{Lj})(\bar{q}_{Rk}\gamma^\mu q_{Rk}), && \mathcal{O}_5^{'k} = (\bar{q}_{Ri}\gamma^\mu q_{Rj})(\bar{q}_{Lk}\gamma^\mu q_{Lk})\\
&\mathcal{O}_6^k = (\bar{q}^\alpha_{Li}\gamma^\mu q^\beta_{Lj})(\bar{q}^\beta_{Rk}\gamma^\mu q^\alpha_{Rk}), && \mathcal{O}_6^{'k} = (\bar{q}^\alpha_{Ri}\gamma^\mu q^\beta_{Rj})(\bar{q}^\beta_{Lk}\gamma^\mu q^\alpha_{Lk});
\end{aligned} \tag{6.4}$$

- $\Delta F = 1$ magnetic and chromomagnetic operators, which are relevant for radiative quark transitions

$$\begin{aligned}
&\mathcal{O}_7 = e m_{q_j}(\bar{q}_{Li}\sigma_{\mu\nu} q_{Rj})F^{\mu\nu}, && \mathcal{O}_7^{'} = e m_{q_i}(\bar{q}_{Ri}\sigma_{\mu\nu} q_{Lj})F^{\mu\nu},\\
&\mathcal{O}_8 = g_s m_{q_j}(\bar{q}_{Li}\sigma_{\mu\nu} q_{Rj})G^{\mu\nu}, && \mathcal{O}_8^{'} = g_s m_{q_i}(\bar{q}_{Ri}\sigma_{\mu\nu} q_{Lj})G^{\mu\nu};
\end{aligned} \tag{6.5}$$

- semileptonic $\Delta F = 1$ operators, important for semileptonic neutral-current meson decays

$$\begin{aligned}
&\mathcal{O}_9^k = (\bar{q}_{Li}\gamma^\mu q_{Lj})(\bar{\ell}_k\gamma^\mu \ell_k), && \mathcal{O}_9^{'k} = (\bar{q}_{Ri}\gamma^\mu q_{Rj})(\bar{\ell}_k\gamma^\mu \ell_k),\\
&\mathcal{O}_{10}^k = (\bar{q}_{Li}\gamma^\mu q_{Lj})(\bar{\ell}_k\gamma^\mu\gamma_5 \ell_k), && \mathcal{O}_{10}^{'k} = (\bar{q}_{Ri}\gamma^\mu q_{Rj})(\bar{\ell}_k\gamma^\mu\gamma_5 \ell_k).
\end{aligned} \tag{6.6}$$

First of all, note that the SM contributes only to some of these operators (in particular, the primed ones are very suppressed). Secondly, while the list of $\Delta F = 2$ operators contains all the independent operators that we can consider, for the $\Delta F = 1$ transitions we have reported only the operators relevant for the phenomenological applications that will be described in what follows. To be more specific, we have neglected all the (pseudo)scalar and tensor Lorentz structures. It has been shown that generalizing the $\Delta F = 1$ Lagrangian beyond the SM, namely considering all the operators of dimension-6 and invariant under the SM symmetry group, increases the total number of such operators up to ~ 120 [128,129]. To develop an explicit example for clarity, the $\Delta B = 2$ mixings are described by the effective Hamiltonian [130–132]

$$\mathcal{H}_{\Delta B=2} = \frac{G_F^2 m_W^2}{16\pi^2}(\lambda_{bq})^2 S_0(x_t)\mathcal{Q}_1, \tag{6.7}$$

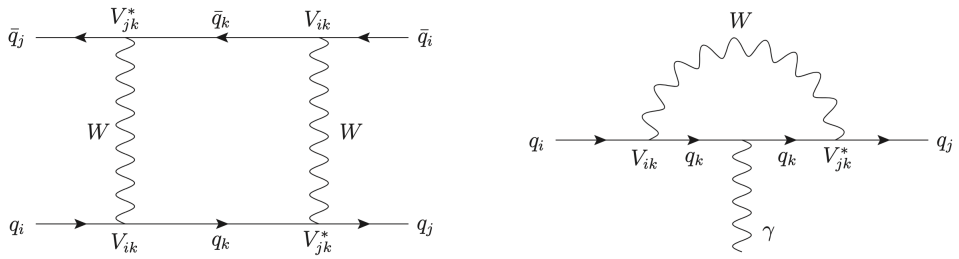

Figure 6.1: Examples of box (left) and penguin (right) Feynman diagrams Within the SM.

where $\lambda_{bq} \equiv V^*_{tb}V_{tq}$ and two possible choices for q can be made, *i.e.* $q = d, s$ for $B - \bar{B}$ mixing and for $B_s - \bar{B}_s$ one. Finally, $x_t \equiv m_t^2/m_W^2$ and $S_0(x_t)$ is a loop function that can be approximated as

$$S_0(x_t) \simeq 2.46 \left(\frac{m_t}{170\,\text{GeV}}\right)^{1.52} \simeq 2.31.$$

To conclude this Section, let us give a naive explanation of the robustness of the constraints on BSM scenarios that come from low-energy processes in flavour physics. Keeping again in mind the $\Delta B = 2$ transitions as an example, from Eqs. (6.1) and (6.7) it is clear that, if the WCs of the theory are $\mathcal{O}(1)$ factors, the ratio $1/(\Lambda^2_{UV}\, G_F)$ has to be tiny enough to give rise to the suppressions proportional to the CKM matrix elements. A central role in this game is evidently played by the uncertainties that affect both the theoretical expectation values and the measurements of particular flavour observables. This consideration is particularly relevant in view of the improvement in sensitivity expected at future experiments since, the most precise are the theoretical estimates of the SM parameters (such as the CKM matrix elements and the meson decay constants), the most stringent will be the bounds on NP coming from the flavour sector. We will see explicitly in detail the power of this kind of study in Composite Higgs scenarios in the next Chapter.

6.3 The Minimal Flavour Violation and the $U(2)^3$ frameworks

Before explicitly discussing two specific BSM models, *i.e.* Composite Higgs scenarios in Chapter 7 and LeptoQuarks in Chapter 8, it is instructive to speculate about the flavour structure of specific extensions of the SM. In other words, we can try to approach NP effects in flavour physics from the point of view of *flavour symmetries*.

To this end, let us summarize the physical meaning of the EFT approach to flavour physics just described. As stated before, we consider the SM as the right theory of Nature *only* at low energies, namely up to a certain scale Λ_{UV} (defined in Eq. (6.1)). Now, since the SM does *not* have an exact flavour symmetry because of the Yukawa interactions, it is an important task to identify a precise flavour structure for a BSM model. Note that in this game a central role is played by the numerical order of magnitude of the scale Λ_{UV}. As we have seen in Chapter 2, the hierarchy problem suggests that this scale should be $\mathcal{O}$(TeV). At the same time, however, we have to deal with the cases of excellent agreement between theoretical expectations and measurements of flavour observables. In general, this implies that, in order to maintain Λ_{UV} at the TeV scale, we are forced to assume that the flavour structure underlying the NP is highly non-generic. To be more specific, we have to find a NP flavour structure which is characterized both by a large symmetry group and some small symmetry breaking term. The Minimal Flavour Violation (MFV) scenario [133,134] suggests the most conservative choice

that we can develop in this sense: we hypothize that any extension of the SM must have the same flavour symmetry that the SM has in the limit of zero Yukawa terms, which corresponds to a

$$\mathcal{G}_q = U(3)_{Q_L} \times U(3)_{u_R} \times U(3)_{d_R} \tag{6.8}$$

symmetry group in the quark sector (as already stated in Chapter 2). In this way, the only symmetry breaking terms are precisely the quark Yukawa couplings. Note that, obviously, this is not the unique choice that we can do.

Let us explain how the MFV hypothesis works in detail. As stated above, the symmetry group $\mathcal{G}_q$ is broken by the Yukawa terms Y^u_{ij}, Y^d_{ij}, which have been introduced in Eq. (2.5). Thus, according to the MFV assumption we state that Y^u_{ij}, Y^d_{ij} are the only sources of symmetry breaking. From the mathematical point of view, this property can be rephrased in the assumption that Y^u_{ij}, Y^d_{ij} are *spurions*, *i.e.* fields that transform non-trivially under the symmetry group $\mathcal{G}_q$. Recalling Eq. (6.8), this can be achieved assuming that

$$Y^u \sim (3, \bar{3}, 1), \quad Y^d \sim (3, 1, \bar{3})$$

under $\mathcal{G}_q$. From the effective theory point of view, this means that minimal flavour violating theory must be characterized by high-dimensional operators that are built starting from the spurions Y^u_{ij}, Y^d_{ij} and are invariant under the $\mathcal{G}_q$ group.

Let us now introduce an important simplification in the description of MFV. We know that the SM Yukawas have a *hierarchical* structure, in other words all the eigenvalues of the Y^u_{ij}, Y^d_{ij} matrices are small, apart from the top Yukawa. Moreover, we know that the CKM matrix is almost a diagonal matrix, namely the off-diagonal terms are suppressed. For these two reasons, if we work in the basis where

$$Y^u = V^\dagger_{CKM}\, \mathrm{diag}(y_u,\, y_c,\, y_t), \quad Y^d = \mathrm{diag}(y_d,\, y_s,\, y_b),$$

we can reasonably assume that

$$[Y^u (Y^u)^\dagger]^n_{i \neq j} \simeq y_t^{2n} V^*_{ti} V_{tj}. \tag{6.9}$$

This means that, although in principle we can build up EFT operators with an arbitrarily high number of Yukawa fields, the net effect is that the NP terms in the amplitudes of flavour processes will have the same CKM suppression that we see in the SM. Recalling the $\Delta B = 2$ example, we can state that

$$\mathcal{A}^{\Delta B=2}_{\mathrm{MFV}} = (V^*_{ti} V_{tj})^2 \mathcal{A}^{\Delta B=2}_{\mathrm{SM}} \times \left[1 + a \frac{16\pi^2 m_W^2}{\Lambda^2_{UV}}\right], \tag{6.10}$$

where $\mathcal{A}^{\Delta B=2}_{\mathrm{SM}}$ is the SM $\Delta B = 2$ amplitude. By construction, from this flavour pattern it follows that the $\mathcal{O}(1)$ coefficient a is completely flavour independent, thus it would have the same value also for $\Delta S = 2$ transitions.

Let us finally note that MFV is *not* the unique possible hypothesis that we can assume. For instance, another interesting possibility is the so-called $U(2)^3$ flavour symmetry. This choice is again suggested by the matter content of the quark sector of the SM, which is characterized by an approximate $U(2)_{Q_L} \times U(2)_{u_R} \times U(2)_{d_R}$ symmetry acting only on the first two quark generations [135]. The quality of this approximate symmetry is guaranteed by the fact that the masses of the quarks of the first two generations and their mixings with the ones of the third generation are small with respect to the mass of the top. Note also that this symmetry would be exact if the aforementioned masses and mixings would be zero.

Let us briefly describe how the $U(2)^3$ symmetry works. The minimal scenario is to introduce some dimensionless parameters that are bidoublets under the group $U(2)_{Q_L} \times U(2)_{u_R} \times U(2)_{d_R}$, *i.e.*

$$\Delta_u = (2, \bar{2}, 1), \qquad \Delta_d = (2, 1, \bar{2}). \tag{6.11}$$

In this way, Δ_u and Δ_d allow to give masses to the up-type and down-type quarks of the first two generations by maintaining the full Lagrangian of the theory formally invariant. Since the quarks of the third generation are, by construction, singlets under $U(2)_{Q_L} \times U(2)_{u_R} \times U(2)_{d_R}$, the transformation properties in Eq. (6.11) ensure that their mixings with the quarks of the first two generations are exactly equal to zero. Since in reality this mixing is a small but non-zero one, one has to introduce in a minimal framework another spurion V whose transformation properties under $U(2)_{Q_L} \times U(2)_{u_R} \times U(2)_{d_R}$ are

$$V = (2, 1, 1). \tag{6.12}$$

Since we have introduced the minimal amount of spurions needed to realistically describe the SM parameters of the quark sector, this scenario (which is not unique) is often called *minimal* $U(2)^3$. As for the MFV case, this machinery can be adopted to compute the NP contributions to low-energy processes in flavour physics and to then compare them with data. Taking again as an example the $\Delta B = 2$ transitions, we would find the same CKM suppression of the SM with an expression analogous to Eq. (6.10), however, by construction, in this case the the coefficient a will be flavour dependent, thus giving different contributions to the mixings in the K and in the B sectors.

6.4 An instructive example: the flavour anomalies

At present, the EFT approach to Flavour Physics is one important tool to look for a BSM explanation of the *flavour anomalies*. As we have discussed before, they are a fundamental test of LFU, which has a more general importance in the context of BSM physics. In fact, it gives an important insight on the physical properties that a NP model must have. To make an explicit example, the NP responsible for the breaking of LFU has to be mainly coupled to the third generation of fermions, while having a small mixing with the light generations. Only under this assumption one can easily understand why no evidence of LFU violation has been observed so far in the extremely precise tests of LFU in the semileptonic decays of both kaons and pions.

In what follows, we are then going to examine the $R(D^{(*)})$ and the $R(K^{(*)})$ ratios separately, in order to give an idea of the NP effects that can affect these observables.

6.4.1 The $R(D^{(*)})$ ratios

In the previous Part, we have deeply investigate the SM computation of the $R(D^{(*)})$ ratios, defined in Eq. (3.1). In Chapter 4 we have presented an original way to describe the LQCD and experimental data available for the semileptonic $B \to D^{(*)}\ell\nu$ decays and we have thus found new values of the SM predictions of the LFU ratios, namely $R(D) = 0.296 \pm 0.008$ and $R(D^*) = 0.275 \pm 0.008$, which are compatible with the corresponding experimental averages at the $\sim 1.4\sigma$ level.

In the past few years, *i.e.* before the publication of the LQCD computations of the FFs by the FNAL/MILC Collaborations in [55], several studies have been developed instead in order to investigate which possible NP effects can enter in the $R(D^{(*)})$ ratios, motivated by the state-of-the-art reported by HFLAV Collaboration in Figure 3.1. As discussed in Chapter 4, the DMM values of the $R(D^{(*)})$ ratios are compatible with the corresponding world averages by HFLAV at the $\sim 1.5\sigma$ level. Nevertheless,

it is instructive to understand how hypothetical NP effects in the $R(D^{(*)})$ ratios can be described in a BSM scenario.

In the spirit of Eqs. (6.3)-(6.6), from an EFT point of view the NP amplitude of the semileptonic $B \to D^{(*)}\ell\nu$ transitions has to be written by considering a high number of operators, going beyond the $V-A$ structure of weak interactions of the SM. Following [82], a possible expression is

$$\begin{aligned}\mathcal{M} = \frac{G_F V_{cb}}{\sqrt{2}}[&(1+V_R+V_L)\langle D^{(*)}|\bar{c}\gamma^\mu b|B\rangle \bar{\ell}\gamma_\mu(1-\gamma_5)\nu \\ &+ (V_R - V_L)\langle D^{(*)}|\bar{c}\gamma^\mu\gamma_5 b|B\rangle\bar{\ell}\gamma_\mu(1-\gamma_5)\nu \\ &+ (S_R+S_L)\langle D^{(*)}|\bar{c}b|B\rangle\bar{\ell}(1-\gamma_5)\nu \\ &+ (S_R - S_L)\langle D^{(*)}|\bar{c}\gamma_5 b|B\rangle\bar{\ell}(1-\gamma_5)\nu \\ &+ T_L\langle D^{(*)}|\bar{c}\sigma^{\mu\nu}(1-\gamma_5)b|B\rangle\bar{\ell}\sigma_{\mu\nu}(1-\gamma_5)\nu],\end{aligned} \tag{6.13}$$

where we are assuming the absence of right-handed neutrinos in the theory. Here, we have introduced *new* (pseudo)scalar and tensor operators, each of them characterized by the WCs $V_{L,R}$, $S_{L,R}$, T_L. The corresponding hadronic matrix elements can be written as

$$\begin{aligned}\langle D(p_D)|\,\bar{c}b\,|B(p_B)\rangle &= \frac{q_\mu}{m_b - m_c}\,\langle D(p_D)|\,\bar{b}\gamma^\mu c\,|B(p_B)\rangle\,, \\ \langle D(p_D)|\,\bar{c}\sigma^{\mu\nu}(1\pm\gamma_5)b\,|B(p_B)\rangle &= i\frac{f_T(q^2)}{m_B+m_D}\left[(p_B+p_D)^\mu q^\nu - (p_B+p_D)^\nu q^\mu \pm i\epsilon^{\mu\nu\alpha\beta}(p_B+p_D)_\alpha q_\beta\right]\end{aligned} \tag{6.14}$$

for the $B \to D$ case and

$$\begin{aligned}\langle D^*(p_{D^*},\epsilon)|\,\bar{c}\sigma_{\mu\nu}b\,|B(p_B)\rangle &= \frac{\epsilon^*\cdot q}{(m_B+m_{D^*})^2}T_0(q^2)\epsilon_{\mu\nu\alpha\beta}p_B^\alpha p_{D^*}^\beta \\ &\quad + T_1(q^2)\epsilon_{\mu\nu\alpha\beta}p_B^\alpha\epsilon^{*\beta} + T_2(q^2)\epsilon_{\mu\nu\alpha\beta}p_{D^*}^\alpha\epsilon^{*\beta} \\ \langle D^*(p_{D^*},\epsilon)|\,\bar{c}\sigma_{\mu\nu}\gamma_5 b\,|B(p_B)\rangle &= i\frac{\epsilon^*\cdot q}{(m_B+m_{D^*})^2}T_0(q^2)(p_{B\mu}p_{D^*\nu} - p_{B\nu}p_{D^*\mu}) \\ &\quad + iT_1(q^2)(p_{B\mu}\epsilon^*_\nu - p_{B\nu}\epsilon^*_\mu) + iT_2(q^2)(p_{D^*\mu}\epsilon^*_\nu - p_{D^*\nu}\epsilon^*_\mu)\end{aligned} \tag{6.15}$$

for the $B \to D^*$ one. These are the only non-zero contributions to the amplitude accordingly to the Wigner-Eckart theorem, hence we have no axial and pseudoscalar effects for the $B \to D$ decays and no scalar one for the $B \to D^*$ ones. Putting these hadronic matrix elements together with the amplitude in Eq. (6.13), we are finally able to compute the differential decay widths of both the $B \to D\ell\nu$ and the $B \to D^*\ell\nu$ transitions. The explicit formulæ can be found in [82].

In conclusion, let us note that in the Eqs. (6.14)-(6.15) some new FFs naturally arise, namely $f_T(q^2)$ for the $B \to D$ decays and $T_0(q^2), T_1(q^2), T_2(q^2)$ for the $B \to D^*$ ones. Let us clearly state that the DMM, extensively described in Chapter 3, is perfectly appliable also to these FFs, which refer to the (pseudo)scalar and/or tensor spin-parity quantum channels. The only caveat is to compute the susceptibilities of the $b \to c$ current corresponding to those channels. In the future, this computation will be developed since new LQCD data for $f_T(q^2)$, computed on the lattice for high values of the momentum transfer, will be made public by the JLQCD Collaboration [72], while unfortunately $T_0(q^2), T_1(q^2), T_2(q^2)$ have not been computed on the lattice.

6.4.2 The $R(K^{(*)})$ ratios

Other flavour observables which are very important for BSM studies are the $R(K^{(*)})$ ratios, that, as the $R(D^{(*)})$ ones, represent a fundamental test of LFU in the SM. The $R(K^{(*)})$ ratios are defined as

$$R(K^{(*)}) \equiv \frac{\Gamma(B \to K^{(*)}\mu^+\mu^-)}{\Gamma(B \to K^{(*)}e^+e^-)} \tag{6.16}$$

and represent possible clear imprints of New Physics affecting the $b \to s\ell^+\ell^-$ quark transitions. Although we will not develop in this Thesis a systematic study and computation of these ratios Within-the-SM, note that semileptonic $B \to K^{(*)}\ell^+\ell^-$ decays are induced by FCNCs, thus they cannot arise at tree level in the SM and, instead, occur at one-loop level through penguins and box diagrams. In fact, as clearly stated in the previous Section, this property is shared by all the transitions induce by the operators in Eqs. (6.3)-(6.6).

The state-of-the-art of the available measurements of the $R(K^{(*)})$ ratios is shown in Figures 6.2a-6.2b. Note that, from the theoretical point of view, within the SM we naïvely expect that $R(K^{(*)})|_{\rm SM} = 1$. In particular, we can state that $R(K^{(*)})$ are *independent of perturbative and non-perturbative QCD contributions*, since they cancel out in the ratio. As clear from Figures 6.2a-6.2b, the evidence of LFU violation in semileptonic $B \to K^{(*)}\ell^+\ell^-$ decays comes from the LHCb measurements [136, 137]. To be more specific, the experimental data for $R(K)^{[1.1,6]}$, $R(K^*)^{[1.1,6]}$, $R(K^*)^{[0.045,1.1]}$ deviate from the SM expectation by 3.1σ, 2.5σ, $2.3\,\sigma$, respectively.

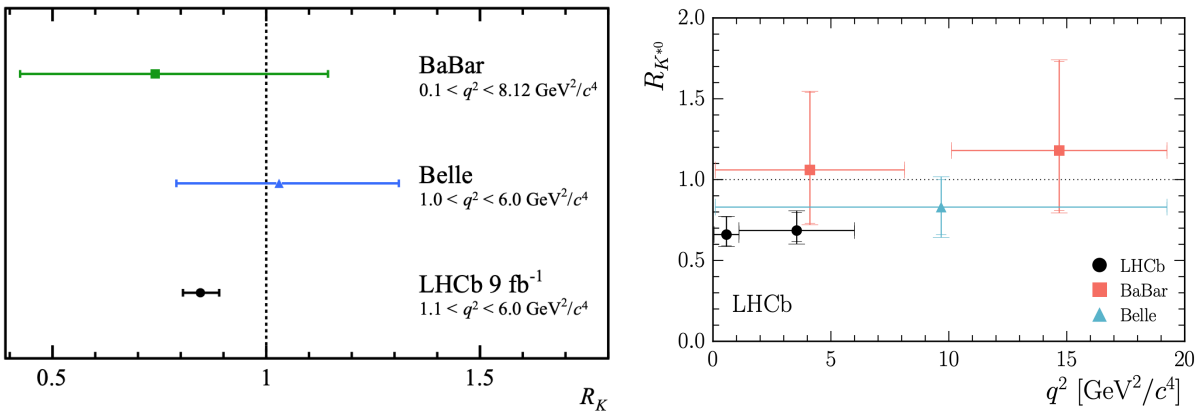

(a) (b)

Figure 6.2: State-of-the-art of the measurements of the $R(K^{(*)})$ ratios. (a) Comparison between the measurements of the $R(K)$ ratio as performed by LHCb [136], BaBar [138] and Belle [139] Collaborations. The naïve SM expectation is highlighted as a dashed line. Taken from [136]. (b) Comparison between the measurements of the $R(K^*)$ ratio by LHCb, Babar [140] and Belle [141] Collaborations. Also in this case, the naïve SM expectation is highlighted as a dashed line. Taken from [137].

As we will see more explicitly in the following Chapters, in order to explain the aforementioned discrepancies one can invoke the existence of NP effects. Thus, one can estimate the magnitude of the NP contributions to the WCs of the operators of interest that is necessary to justify the $R(K^{(*)})$ anomalies. One can show that, in the limit of heavy NP, SM and BSM effects in the $R(K^{(*)})$ ratios can be described by looking only at SM dipole operator $\mathcal{O}_7$ in Eq. (6.5) and at the four vector operators in Eq. (6.6). Some very recent analyses of the available experimental data can be found in [142, 143].

6.5 New bounds on the Wilson Coefficients from Flavour Physics

Starting from the general effective Lagrangian (6.1), we can now constraint the entity of the NP contributions to the WCs by comparing theoretical expectations and measurements of flavour observables. Note that these constraints will be completely model-independent, since we will not invoke any explicit BSM model. They will be then applied to CH models in the following Chapter.

In what follows, from the experimental point of view we will use expected improved uncertainties as quoted by both LHCb Upgrade II [144] and Belle II [145]. This will allow us to obtain more stringent bounds on possible NP effects affecting low-energy processes in Flavour Physics.

Let us examine in detail the low-energy processes in Flavour Physics that can be affected by BSM effects and let us constraint the corresponding NP contributions to the WCs in a model independent way.

- $b \to s\ell^+\ell^-$**: contributions to** $C^{(')}_{9,NP}$ **and** $C^{(')}_{10,NP}$

The main bounds on the real and imaginary parts of the Wilson coefficients $C^{(')}_{9,NP}$ and $C^{(')}_{10,NP}$ (whose corresponing operators have been defined in Eq. (6.6)) come from the process $B \to K^{(*)}\mu^+\mu^-$. For what concerns LHCb Upgrade II, in [144] a plot with the expected sensitivity for $C^{'}_{9,NP}$ and $C^{'}_{10,NP}$ is presented. We will consider the *SM scenario*, *i.e.* the mean values of $\mathrm{Re}(C^{'}_{9,NP})$, $\mathrm{Re}(C^{'}_{10,NP})$ are set equal to zero. This is the most conservative choice we can make, since under this assumption the NP scenario is maximally disfavoured. Hence, we extrapolate the following bounds at 2σ level:

$$\mathrm{Re}(C^{'}_{9,NP}) = 0.00 \pm 0.14, \quad \mathrm{Re}(C^{'}_{10,NP}) = 0.00 \pm 0.09. \tag{6.17}$$

Note that, for a direct application to the CH scenario, it is necessary to run these coefficients at the TeV scale [146]. For ease of comparison with Eq. (6.1), throughtout this Chapter we define $c_{i,NP}$ as the NP contribution to C_i at the scale $\Lambda_{UV} = 1\,\mathrm{TeV}$. In this way, by recalling the normalization of the weak effective Hamiltonian in Eq. (6.2) we have that

$$\mathrm{Re}(c^{(')}_{i,NP}) = -\,\mathrm{Re}(C^{(')}_{i,NP}) \times \left(-\frac{4G_F}{\sqrt{2}}\lambda_{bs}\frac{\alpha_{em}}{4\pi} \times (1\,\mathrm{TeV})^2\right), \quad i = 9, 10. \tag{6.18}$$

Another source of information comes from the analysis of the angular observables related to the $B \to K^*\mu^+\mu^-$ decay. In [147] the authors adopt the expected statistics at the various upgrades of LHCb, including also the Upgrade II at 300 fb^{-1}, and the one corresponding to Belle II at 50 ab^{-1} in order to obtain a new estimate of the bounds for $\mathrm{Re}(C_{9,NP})$ and $\mathrm{Re}(C_{10,NP})$. As usual, we fix the mean values of these coefficients to zero, in order to maximally disfavour NP scenarios, and we get their uncertainties from Table VI of [147] (case of z^3 fit). Thus, the most stringent constraints at 2σ level are:

$$\mathrm{Re}(C_{9,NP}) = 0.00 \pm 0.39, \quad \mathrm{Re}(C_{10,NP}) = 0.00 \pm 0.38. \tag{6.19}$$

In particular, that Table refers to the expected statistics at LHCb Upgrade I at 50 fb^{-1} but the authors claim that the difference between the predicted sensitivity in this case and the one at LHCb Upgrade II at 300 fb^{-1} (or the one at Belle II at 50 ab^{-1}) is completely negligible for phenomenological applications since the precision on the determination on the Wilson coefficients is already saturated by the uncertainties on the form factors that enter the description of $B \to K^*\ell\ell$ transitions. Note that also in this case we translate the values (6.19) of the Wilson coefficients $C_{9(10),NP}$ into the ones of $c_{9(10),NP}$ at the 1 TeV scale adopting the relation (6.18).

- $B_{d,s} - \bar{B}_{d,s}$ **mixing**

For what concerns the $B_{d,s} - \bar{B}_{d,s}$ mixings, the starting point consists in modifying the expression of M_{12}^q in the SM and keeping fixed the one of Γ_{12}^q (in what follows it will be implicit that $q = d, s$) [148]. To be more specific, following the UTfit collaboration [149,150] we can describe the NP contributions to the mixing amplitudes as

$$\frac{M_{12}^{q,full}}{M_{12}^{q,SM}} = C_{B_q} e^{2i\phi_{B_q}}, \tag{6.20}$$

where $M_{12}^{q,full}$ refers to the full theory (SM+NP). Now, the BSM contributions in the Eqs. (6.20)-(6.24) can be linked to the WCs associated to the effective operators in Eq. (6.3). In what follows, we will focus our attention on $Q_V^{bqLL} \equiv \mathcal{Q}_1$ and $Q_S^{bqLR} \equiv \mathcal{Q}_4$, which are dimension-six operators. Thus, we re-write these terms responsible for the $\Delta B = 2$ transitions in the effective Lagrangian as

$$\mathcal{L}^{NP} = \frac{c_V^{bqLL}}{\Lambda^2} Q_V^{bqLL} + \frac{c_S^{bqLR}}{\Lambda^2} Q_S^{bqLR}, \tag{6.21}$$

where Λ indicates the scale of NP.

Let us now examine which bounds on the WCs in Eq. (6.21) can be obtained starting from the expected improvements in sensitivity at both LHCb Upgrade II and Belle II.

i) *Vector operator in B_d mixing*

We adopt the results by UTfit Collaboration as reported in Table 157 of [145]. As usual, we consider the NP quantities in Eq. (6.20) as centered in their SM values. Thus, using the values of the predicted uncertainties by UTft we have at 2σ

$$C_{B_d} = 1.00 \pm 0.06, \quad \phi_{B_d} = (0.0 \pm 1.2)^\circ.$$

In order to set a constraint on c_V^{bdLL}, we fix $c_S^{bdLR} = 0$ and impose that $|\mathcal{A}_{NP}^{mixing}| \leq |\mathcal{A}_{SM}^{mixing}|$ [151], being $\mathcal{A}$ the amplitude of the $\Delta F = 2$ process. Recalling the expression (6.7), this implies that

$$\Lambda \geq \frac{|c_V^{bdLL}|^{1/2}}{|\lambda_{db}||C_{B_d} e^{2i\phi_{B_d}} - 1|^{1/2}} \times \frac{4\pi}{G_F m_t \sqrt{S_0}}. \tag{6.22}$$

Note that the enhancement factor $1/|\lambda_{db}|$ disappears in the MFV (or $U(2)$) models described in the previous Section, since in this case the NP terms have the same CKM suppression of the SM ones.

Now, to obtain the most conservative upper bound on c_V^{bdLL}, we also fix $\phi_{B_d} = 0$ and consider the maximal deviation of C_{B_d} from the unity, *i.e.* $\Delta C_{B_d} \equiv C_{B_d} - 1 = 0.06$ at 2σ. Fixing the NP scale $\Lambda = 1\,\text{TeV}$, the resulting numerical bound on the Wilson coefficient will thus be

$$\text{Re}(c_V^{bdLL}) < 2.1 \times 10^{-7}. \tag{6.23}$$

ii) *Vector operator in B_s mixing*

In this case, we use the results from the CKMfitter Collaboration [152][1]. We fix $\sigma_s = 0$ to obtain the most conservative bound (also in this case the scalar contribution is set equal to zero, *i.e.* $c_S^{bsLR} = 0$) and we link the quantity h_s (defined in Eq. (6.24)) to the WC c_V^{bsLL} through the relation

$$h_s \simeq 1.5 \, \frac{\mathrm{Re}(c_V^{bsLL})}{|\lambda_{sb}|^2} \, \frac{(4\pi)^2}{G_F \Lambda^2}. \tag{6.26}$$

Given that at 2σ level the authors find $h_s < 0.06$, fixing again $\Lambda = 1\,\mathrm{TeV}$ the numerical result for the Wilson coefficient reads

$$\mathrm{Re}(c_V^{bsLL}) < 4.6 \times 10^{-6}. \tag{6.27}$$

iii) *Scalar operator in $B_{d,s}$ mixing*

Finally, for what concerns c_S^{bqLR} (again $q = d,\, s$), we have to switch off the contribution of the vector operator in the NP Lagrangian, *i.e.* $c_V^{bqLL} = 0$.

In what follows, we will use some of the results present in [153], where the authors study in detail the NP contributions of a heavy neutral gauge boson Z' and of a neutral scalar H to $\Delta F = 2$ processes. To be more specific, the Tables 5 and 6 of this work show the central values of the hadronic matrix elements of the relevant operators, computed for different values of the scale Λ and for both the B_d and the B_s cases. Thus, for our purposes it is sufficient to compute the ratio

$$\frac{< Q_S^{bqLR} >}{< Q_V^{bqLL} >} \equiv \kappa_q, \quad (q = d, s) \tag{6.28}$$

since, being the value of $M_{12}^{q,full}$ directly fixed by C_{B_d} or h_s, Eq. (6.28) will directly imply that

$$\mathrm{Re}(c_S^{bqLR}) = \frac{\mathrm{Re}(c_V^{bqLL})}{\kappa_q}, \quad (q = d, s). \tag{6.29}$$

Numerically, the corresponding results read

$$\kappa_d = 6.3, \quad \kappa_s = 6.1,$$

from which it follows through the bounds (6.23) and (6.27) that

$$\mathrm{Re}(c_S^{bdLR}) < 3.3 \times 10^{-8}, \qquad \mathrm{Re}(c_S^{bsLR}) < 7.5 \times 10^{-7}. \tag{6.30}$$

- **Contributions to $C_{7,NP}^{(\prime)}$**

At this point, let us finally examine the observables that enter in the determination of the NP contribution to the WCs $C_{7,NP}^{(\prime)}$, which are associated to the operators in Eq. (6.5).

[1]The CKMfitter Collaboration describes the deviation of M_{12}^q from its SM expression as

$$M_{12}^{q,full} = M_{12}^{q,SM}(1 + h_q e^{2i\sigma_q}). \tag{6.24}$$

By a direct comparison of the equations (6.20) and (6.24), it is clear that the quantities describing NP can be linked to each other through the relation

$$1 + h_q e^{2i\sigma_q} = C_{B_q} e^{2i\phi_{B_q}}. \tag{6.25}$$

i) *Inclusive $b \to s\gamma$ radiative decays*

For the radiative decays it is convenient to study the ratio between the decay width in the full theory and in the SM only [154]. In this way all the numerical factors cancel out and we are left only with the expression

$$\frac{\Gamma_{full}}{\Gamma_{SM}} = \frac{|C_7|^2 + |C_7'|^2}{|C_{7,SM}|^2} = \frac{|C_{7,SM} + C_{7,NP}|^2 + |C'_{7,NP}|^2}{|C_{7,SM}|^2} \tag{6.31}$$

where all the WCs are considered at the scale μ_b. Note that in the SM $C_{7,SM}(\mu_b) = -0.304$ [155]. Considering NP at a scale $m_* = 1$ TeV as a reference, it is necessary to run the WCs so that

$$C^{(\prime)}_{7,NP}(\mu_b) = \left(\frac{\alpha_S(m_*)}{\alpha_S(m_t)}\right)^{\frac{16}{21}} \left(\frac{\alpha_S(m_t)}{\alpha_S(\mu_b)}\right)^{\frac{16}{23}} \times C^{(\prime)}_{7,NP}(m_*), \tag{6.32}$$

being α_S the strong coupling constant.

Let us turn back to Eq.(6.31). In order to fit the NP WCs, we consider the experimental Branching Ratio as the estimate valid in the full theory. The theoretical SM expectation reads [156]

$$BR_{\rm SM} = (3.36 \pm 0.23) \times 10^{-4}. \tag{6.33}$$

For the experimental value, as usual we choose the mean value equal to the theoretical one and we then consider the expected sensitivity at Belle-II with 50 ab^{-1}, that is $\delta BR_{\rm exp} = 3.2\%$.

ii) *Exclusive $b \to s\gamma$ radiative decays*

We will focus our attention onto the processes $B^0 \to K^*\gamma$ and $B_s^0 \to \phi\gamma$, which we will refer to generically as $B_q \to V\gamma$. The starting point is the time-dependent CP asymmetry [157], that reads

$$A_{CP}(t) = \frac{S_{V\gamma}\sin(\Delta m_q t) + C_{V\gamma}\cos(\Delta m_q t)}{\cosh(\Delta\Gamma_q t/2) - A_{\Delta\Gamma}(B_q \to V\gamma)\sinh(\Delta\Gamma_q t/2)}, \tag{6.34}$$

where $S_{V\gamma}$ is the mixing-induced CP asymmetry, $C_{V\gamma}$ is the direct CP one and finally $A_{\Delta\Gamma}(B_q \to V\gamma)$ is the mass-eigenstate rate asymmetry.

First of all, note that in the $B^0 \to K^*\gamma$ case $A_{\Delta\Gamma}$ can be neglected because of the tiny value of $\Delta\Gamma_d$. Thus, we may consider its contribution only in the $B_s^0 \to \phi\gamma$ case. In order to fit the NP Wilson coefficients, it is necessary to consider the relation between the time integrated BR and the theoretical contribution *in absence of* mixing, *i.e.*

$$BR_{\rm int}(B_s^0 \to \phi\gamma) = \left(\frac{1 - A_{\Delta\Gamma}(B_s^0 \to \phi\gamma) \times \frac{\tau_{B_s}\Delta\Gamma_{B_s}}{2}}{1 - (\frac{\tau_{B_s}\Delta\Gamma_{B_s}}{2})^2}\right) BR_{\rm full}(B_s^0 \to \phi\gamma), \tag{6.35}$$

where $BR_{\rm full}(B_s^0 \to \phi\gamma)$ is directly related to the WCs through the relation [158]

$$BR_{\rm full}(B_s^0 \to \phi\gamma) = \tau_{B_s}\frac{G_F^2\alpha_{EM}|\lambda_{sb}|^2}{32\pi^4} M_{B_s}^3 m_b^2 \left(1 - \frac{m_\phi^2}{M_{B_s}^2}\right)^3 |T_1(0)|^2 \times (|C_7|^2 + |C_7'|^2), \tag{6.36}$$

being as usual $\lambda_{sb} \equiv V_{ts}^* V_{tb}$. τ_{B_s} and M_{B_s} represent respectively the lifetime and the mass of the B_s meson, while m_b is the bottom mass (all these values are taken from the PDG [159]).

Note that $T_1(0)$ represents the tensor form factor which enters $B_s^0 \to \phi\gamma$ transition, evaluated at $q^2 = 0$. Furthermore, we need the SM prediction for the time integrated Branching Ratio, *i.e.*

$$BR_{\rm int}(B_s^0 \to \phi\gamma) = (4.31 \pm 0.86) \times 10^{-5}. \tag{6.37}$$

For what concerns $A_{\Delta\Gamma}$, we choose its central value equal to the SM prediction $A_{\Delta\Gamma,th} = 0.031 \pm 0.021$ and its uncertainty equal to the statistical one expected at LHCb Upgrade II, that is $\delta A_{\Delta\Gamma} = 0.02$. However, from the numerical point of view, the relative constraint on the Wilson coefficients appears to be very weak with respect to the others, hence we will not consider it in the following steps.

Secondly, another relevant source of information is $S_{K^*\gamma}$, which is defined as [160]

$$S_{K^*\gamma} = \frac{2{\rm Im}\left[e^{-i\phi_d}(\mathcal{A}_L^*\bar{\mathcal{A}}_L + \mathcal{A}_R^*\bar{\mathcal{A}}_R)\right]}{|\mathcal{A}_L|^2 + |\mathcal{A}_R|^2 + |\bar{\mathcal{A}}_L|^2 + |\bar{\mathcal{A}}_R|^2} \simeq \frac{2}{|C_7|^2 + |C_7'|^2}{\rm Im}\left(e^{-i\phi_d}C_7C_7'\right). \tag{6.38}$$

In the above expression there are two physical amplitudes, which describe the exclusive transition $B^0 \to K^*\gamma$ and are characterized by different polarizations of the photon, *i.e.*

$$\bar{\mathcal{A}}_{L(R)} = \mathcal{A}(\bar{B}^0 \to K^*\gamma_{L(R)}), \quad \mathcal{A}_{L(R)} = \mathcal{A}(B^0 \to \bar{K}^*\gamma_{L(R)}). \tag{6.39}$$

Moreover, the angle ϕ_d represents the phase of the amplitude for $B_d - \bar{B}_d$ mixing. It can be fixed through the relation

$$\sin(\phi_d) = S_{\psi K_S}, \tag{6.40}$$

where we have considered at the r.h.s. $S_{\psi K_S} = 0.69 \pm 0.02$, obtained from $b \to c\bar{c}s$ processes [161]. Note finally that the last approximate equality in (6.38) follows from the expressions of the decay amplitudes, which are functions of the WCs.

In order to fit the WCs, as usual we fix the central value of $S_{K^*\gamma}$ to the SM one, *i.e.* $S_{K^*\gamma,th} = -0.023 \pm 0.016$ [160], which takes into account also the contributions from soft-gluon emission. Thus, we express this quantity as

$$S_{K^*\gamma} \simeq S_{K^*\gamma,th} + \frac{2}{|C_7|^2 + |C_{7,NP}'|^2}{\rm Im}\left(e^{-i\phi_d}C_7C_{7,NP}'\right), \tag{6.41}$$

so that all the NP contributions will be encoded by the WCs and in the SM limit we will recover the SM prediction $S_{K^*\gamma,th}$. We finally adopt as uncertainty the sensitivity quoted by Belle-II at 50 ab^{-1}, that is $\delta S_{K^*\gamma} = 0.030$.

iii) *Exclusive $b \to s\ell\ell$ observables*

The process $B \to K^*\ell\ell$ offers another last constraint for the determination of bounds on $C_7^{(\prime)}$. The fourfold differential amplitude of this decay is defined in terms of several angular functions, that depend on the so-called transversity amplitudes $A_{\perp,\parallel,0,t}(q^2)$. These amplitudes are functions of the Wilson coefficients and of the form factors entering $B \to K^*\ell\ell$ decays. Starting from them, we can define two quantities, called $A_T^{(2)}$ and $A_T^{(Im)}$, which are particularly sensitive to right-handed currents in NP scenarios.

To be more specific, they are defined as [162]:

$$A_T^{(2)}(q^2) \;=\; \frac{|A_\perp(q^2)|^2 - |A_\parallel(q^2)|^2}{|A_\perp(q^2)|^2 + |A_\parallel(q^2)|^2}, \tag{6.42}$$

$$A_T^{(Im)}(q^2) \quad = \quad -2\frac{\text{Im}\left(A_\parallel^L(q^2)A_\perp^{L*}(q^2)+A_\parallel^R(q^2)A_\perp^{R*}(q^2)\right)}{|A_\perp(q^2)|^2+|A_\parallel(q^2)|^2}. \tag{6.43}$$

They assume a very simple form in the very low-q^2 limit, *i.e.*

$$\lim_{q^2\to 0} A_T^{(2)}(q^2) = \frac{2\,\text{Re}(C_7C_7'^*)}{|C_7|^2+|C_7'|^2}, \qquad \lim_{q^2\to 0} A_T^{(Im)}(q^2) = \frac{2\text{Im}\,(C_7C_7'^*)}{|C_7|^2+|C_7'|^2}. \tag{6.44}$$

These formulæ have to be considered as asymptotic, since for increasing q^2 the contributions of the other WCs, *i.e.* $C_{9,10}^{(\prime)}$, become not neglibible.

In order to reach very small values of the quadratic transferred momentum, which are thus of capital importance to find contributions to right-handed currents beyond the SM, Belle-II will study the $B\to K^*e^+e^-$ channel with high precision and will measure the observables (6.42)-(6.43) with sensitivities

$$\delta A_T^{(2)} = 0.066, \quad \delta A_T^{(Im)} = 0.064$$

in the kinematical range $q^2\in[0.002,1.12]\,\text{GeV}^2$. Since the formulæ (6.44) are valid only in the $q^2\to 0$ limit, we will adopt the following expressions in order to constrain the WCs $C_7^{(\prime)}$:

$$A_T^{(2)}(q^2)\simeq< A_{T,SM}^{(2)} > + \frac{2\,\text{Re}(C_7C_{7,NP}'^*)}{|C_7|^2+|C_{7,NP}'|^2}, \quad A_T^{(Im)}(q^2)\simeq< A_{T,SM}^{(Im)} > + \frac{2\text{Im}\,(C_7C_{7,NP}'^*)}{|C_7|^2+|C_{7,NP}'|^2}, \tag{6.45}$$

where q^2 now vary in the range $[0.002,1.12]\,\text{GeV}^2$ and the SM values have to be considered as means in that kinematical region. In this way, all the NP contributions will be encoded by the WCs and in the SM limit we will recover the SM predictions for $A_T^{(2)}$ and $A_T^{(Im)}$, which can be found in [157, 163] and read

$$< A_{T,SM}^{(2)} >= 0.033^{+0.021}_{-0.019}, \quad < A_{T,SM}^{(Im)} >= (0.3\pm 0.2)\times 10^{-3}.$$

Note finally that the presence of $C_{9,10}^{SM}$ in the NP contributions can be safely neglected for the low values of q^2 under consideration, since they would produce a negligible effect of the order of around 5%.

At this point, the aforementioned observables can be fitted all together in order to find the marginalized values of $\text{Re}\left(C_{7,NP}'\right)$ and $\text{Im}\left(C_{7,NP}'\right)$, after having set $C_{7,NP}$ equal to zero. The inverse situation (*i.e.* marginalization of $\text{Re}\,(C_{7,NP})$ and $\text{Im}\,(C_{7,NP})$) is numerically not so interesting as the other one for the following reason. In the plane $\text{Re}\,(C_{7,NP})-\text{Im}\,(C_{7,NP})$ the constraints are represented by the branching ratio of the $b\to s\gamma$ inclusive interaction and by the branching ratio of the exclusive $B\to K^*\mu^+\mu^-$ decay. For what concerns the former case, the uncertainty associated to the theoretical computation of the branching ratio, which is $\delta BR_{th}=6.8\%$, does not allow a high precision in constraining the real and imaginary parts of $C_{7,NP}$. An identical situation occurs also in the latter case, since the improvement in the sensitivity of LHCb Upgrade II and Belle II in the measurement of $BR(B\to K^*\mu^+\mu^-)$ is saturated by the hadronic uncertainties associated to the form factors, which enters the definition of this branching ratio.

For the reasons explained above, we focus our attention onto the marginalization of $\text{Re}\left(C_{7,NP}'\right)$ and $\text{Im}\left(C_{7,NP}'\right)$. In Figure 6.3 we show all the observables of interest for our fit. The marginalized

values are centred in zero (as we want in order to maximally disfavour NP contributions) and have the following uncertainties

$$\sigma\left[\mathrm{Re}\left(C'_{7,NP}\right)\right] = 0.015, \quad \sigma\left[\mathrm{Im}\left(C'_{7,NP}\right)\right] = 0.014, \tag{6.46}$$

which will be applied to the CH scenario in what follows. Furthermore, we can use the relation (6.18) in order to run the values of the real and the imaginary parts of $c'_{7,NP}$ at the 1 TeV scale, obtaining the following upper bounds on the WCs at 95% confidence level:

$$|\,\mathrm{Re}(c'_{7,NP})| < 2.4 \times 10^{-5}, \quad |\mathrm{Im}\,(c'_{7,NP})| < 2.3 \times 10^{-5}. \tag{6.47}$$

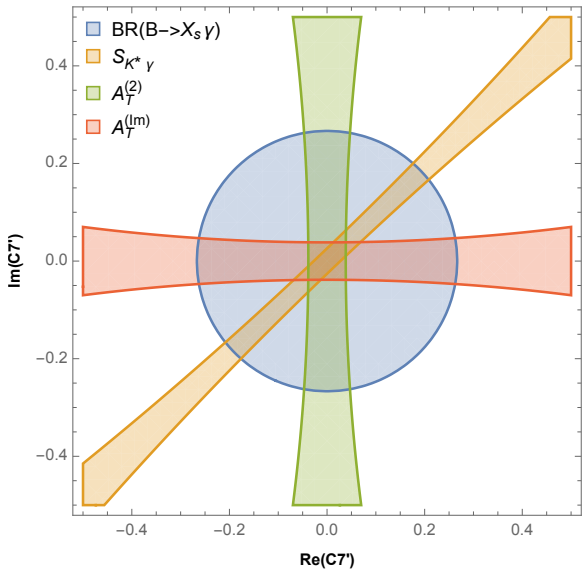

Figure 6.3: The correlation plot Re $\left(C'_{7,NP}\right)$ VS Im $\left(C'_{7,NP}\right)$ at 95% confidence level.

Table 6.1: Upper bounds on the WCs at the energy scale of 1 TeV at 95% confidence level. In bold we indicate the constraints relevant for applications to Composite Higgs, which will be developed in the following Chapter.

	Upper bounds on WC at 1 TeV	
Process	WC	Bound
$B \to K^* \ell\ell$	$\lvert \mathrm{Re}\,(c_{9,NP}) \rvert$	3.2×10^{-4}
	$\lvert \mathrm{Re}\,(\mathbf{c_{10,NP}}) \rvert$	$\mathbf{3.1 \times 10^{-4}}$
	$\lvert \mathrm{Re}(c'_{9,NP}) \rvert$	1.1×10^{-4}
	$\lvert \mathrm{Re}(c'_{10,NP}) \rvert$	7.3×10^{-5}
$\bar{B}_d - B_d$	$\lvert \mathrm{Re}\left(\mathbf{c_V^{bdLL}}\right) \rvert$	$\mathbf{2.1 \times 10^{-7}}$
$\bar{B}_d - B_d$	$\lvert \mathrm{Re}\left(\mathbf{c_S^{bdLR}}\right) \rvert$	$\mathbf{3.3 \times 10^{-8}}$
$\bar{B}_s - B_s$	$\lvert \mathrm{Re}\left(\mathbf{c_V^{bsLL}}\right) \rvert$	$\mathbf{4.6 \times 10^{-6}}$
$\bar{B}_s - B_s$	$\lvert \mathrm{Re}\left(\mathbf{c_S^{bsLR}}\right) \rvert$	$\mathbf{7.5 \times 10^{-7}}$
$b \to s\gamma$	$\lvert \mathrm{Re}(c'_{7,NP}) \rvert$	2.4×10^{-5}
	$\lvert \mathrm{Im}\,(\mathbf{c'_{7,NP}}) \rvert$	$\mathbf{2.3 \times 10^{-5}}$

Chapter 7

Explicit models I: Composite Higgs

In this Chapter we will analyse the bounds on Composite Higgs (CH) scenarios as a particular example of physics beyond the SM that is motivated by the hierarchy problem, and has an expected NP scale around the TeV. In particular, we will review these bounds in view of the increase in precision of experiments at the colliders in the future decade. To achieve this goal, we will firstly review the motivations for CH models and the theory underlying them. Then, we will describe in detail the application of CH to flavour physics, presenting original results about the aforementioned bounds and developing interesting comparisons with the state-of-the-art at present. Note that this kind of study is deeply related to the results of analyses Within the SM. In fact, the more precise are the theoretical estimates of the SM parameters (for instance the CKM matrix elements), the more stringent will be the bounds on NP coming from the flavour sector.

7.1 Theoretical framework

7.1.1 The Higgs as a pseudo Nambu-Glodstone boson (pNGB)

In Chapter 2 we have discussed the main properties of the Higgs boson, as well as its radiative instability problem. Let us here discuss a possible (although not unique) solution to this issue, precisely the CH scenario. The fundamental idea underlying this framework is the possibility to consider the Higgs boson *not* as an elementary particle (as seems from the experiments) *but* as a composite bound state of a new strongly-interacting sector. This situation would be analogous to what happens in Quantum Chromo-Dynamics (QCD), where there are many scalar particles that are bound states of quarks and antiquarks under a strongly-interacting sector, which is the QCD itself. Furthermore, as in that case, also the composite Higgs will be characterized by an appropriate compositeness scale, call it m_*, above which it will not be sensitive to UltraViolet (UV) effects and thus thanks to which we will be able to naturally generating its mass. Let us then present in what follows the main theoretical features of CH scenarios [164, 165].

The starting point of our review is to consider a new strong composite sector, characterized by a global Lie group $\mathcal{G}$. We assume that a spontaneous $\mathcal{G} \to \mathcal{G}'$ symmetry breaking occurs, leading to the appearance of massless Goldstones living in the co-set $\mathcal{G}/\mathcal{G}'$. The situation is graphically represented in the most general situation in Figure 7.1a, where we have called $\mathcal{H}_0$ the gauged subgroup of $\mathcal{G}$. Note that the unbroken subgroup $\mathcal{G}'$ is assumed to contain the SM group $\mathcal{G}_{SM} = SU(2)_L \times U(1)_Y$ and that a doublet of $SU(2)_L$, *i.e.* the Higgs, has to be present in the co-set $\mathcal{G}/\mathcal{G}'$.

Let us now consider the simplest example to deal with, namely the so-called Minimal Composite Higgs Model (MCHM) [166], in which the aforementioned Lie groups are $\mathcal{G} = SO(5)$ and $\mathcal{G}' = SO(4)$.

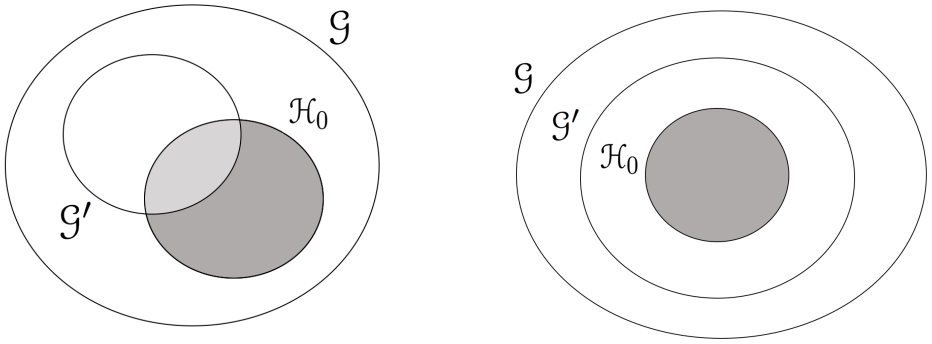

(a) (b)

Figure 7.1: (a) Sketch of the group algebra in the most general situation. The dark gray area represents the group $\mathcal{H}_0/\mathcal{G}'$, where the eaten Goldstones live, while the light gray area is the unbroken group $\mathcal{G}^{'} \cap \mathcal{H}_0$. (b) Sketch of the group algebra in the two-step symmetry breaking description. In this special case, $\mathcal{G}^{'} \cap \mathcal{H}_0 = \mathcal{H}_0$.

The $SO(5) \to SO(4)$ symmetry breaking will give rise to 4 real massless Goldstones, transforming as the fundamental representation of $SO(4)$ and leaving in the co-set $SO(5)/SO(4)$, which is equivalent to a 4-sphere S^4. Moreover, given the exact relation

$$SO(4) = \frac{SU(2)_L \times SU(2)_R}{\mathbb{Z}_2},$$

we can already think about these Goldstones as the real components of a $SU(2)_L$ doublet, *i.e.* again the Higgs. In addition to this, let us choose the following basis for the $SO(5)$ generators:

$$T^{a_L,a_R}_{ij} = -\frac{i}{2}\left(\frac{1}{2}\epsilon^{abc}(\delta^b_i\delta^c_j - \delta^b_j\delta^c_i) \pm (\delta^a_i\delta^4_j - \delta^a_j\delta^4_i)\right), \tag{7.1}$$

$$T^{\hat{a}}_{ij} = -\frac{i}{\sqrt{2}}(\delta^{\hat{a}}_i\delta^5_j - \delta^{\hat{a}}_j\delta^5_i), \tag{7.2}$$

so that the 6 "unbroken" generators T_a span the $SO(4)$ algebra while the remaining "broken" four $T^{\hat{a}}$ span the co-set $SO(5)/SO(4)$ algebra. Hence, we can parametrize the Goldstones originating from the $SO(5) \to SO(4)$ symmetry breaking as

$$\phi = \phi_0 e^{i\sqrt{2}T^{\hat{a}}\Pi^{\hat{a}}/f}, \quad \phi_0 = (0,0,0,0,1)^T, \tag{7.3}$$

being f an analogous of the pion decay constant of QCD.

At this point, we are ready to describe the EWSB in CH scenarios. To achieve this goal, we will compare two different descriptions, namely the two-step breaking VS the vacuum misalignment (the latter being firstly introduced in [167–169]). According to the first viewpoint, we assume that the gauged subgroup $\mathcal{H}_0$ is aligned with the unbroken subgroup $\mathcal{G}'$, as in Figure 7.1b. In MCHM, we will thus have $H_0 = SU(2)_L \times U(1)_Y \subset SO(4)_g = SO(4)$, where the last equality follows properly by the assumption of alignment. At this point, recalling Eq. (7.3) the Goldstones read

$$\phi = (\hat{\Pi}_1 \sin(\Pi/f), \hat{\Pi}_2 \sin(\Pi/f), \hat{\Pi}_3 \sin(\Pi/f), \hat{\Pi}_4 \sin(\Pi/f), \cos(\Pi/f))^T, \tag{7.4}$$

where

$$\Pi \equiv \sqrt{\sum_{\hat{a}} (\Pi^{\hat{a}})^2}, \quad \Pi^{\hat{a}} \equiv \frac{\Pi^a}{\Pi}.$$

Note that in this game the $SO(4)_g$ subgroup acts on the first four components of (7.4). Hence, assuming in total generality that

$$\langle \Pi_i \rangle = 0 \ \ (i = 1, 2, 3), \quad \langle \Pi_4 \rangle \neq 0, \tag{7.5}$$

from Eq. (7.4) it follows that

$$\langle \phi \rangle = (0, 0, 0, \sin\theta, \cos\theta)^T, \quad \theta \equiv \frac{\langle \Pi \rangle}{f}. \tag{7.6}$$

Looking at the first three components of (7.6), it is clear that the assumption of non-zero Vacuum Expectation Value (VEV) has brought us down to a $SO(3)$ subgroup, *i.e.* we have realized the two-step symmetry breaking $SO(5) \to SO(4) \to SO(3)$. At this point, we are ready to explain the second viewpoint of EWSB, namely the vacuum misalignment. In fact, from Eq. (7.5) it is evident that the Π_i $(i = 1, 2, 3)$ are precisely NGBs that will form the longitudinal polarizations of the gauge boson $W^{\pm}, Z^0$ while the remaining one Π_4, having a non-zero VEV, will be identified with the Higgs boson. We can thus re-express ϕ in order to clearly distinguish these different degrees of freedom. It can be demonstrated that a valid new parametrization reads

$$\phi = \begin{pmatrix} \sin\left(\theta + \frac{h(x)}{f}\right) \exp\left(i \frac{\chi^k A^k}{v}\right) \cdot (0, 0, 0, 1)^T \\ \cos\left(\theta + \frac{h(x)}{f}\right) \end{pmatrix},$$

where $h(x)$ is properly the Higgs boson, A^k are the generators of $SO(4)/SO(3)$ and finally χ^k are the Goldstones eaten by the $SU(2)_L \times U(1)_Y$ gauging. At this point, the concept of misalignment is clear. In fact, the angle θ, defined in Eq. (7.6), represents the misalignment between $SO(4)$ and the gauged $SO(4)_g$. There is only one of such angles since there is only one non-eaten Goldstone, *i.e.* the physical Higgs, which in fact can be thought as a coordinate on the 4-sphere S^4 and whose VEV gives the precise position and the entity of the misalignment of the true vacuum with respect to $SO(4)_g$. In Figure 7.2 there is a graphical representation of the mechanism just illustrated. Note that in the so-called decoupling limit, namely $\theta \to 0$, we recover precisely the SM since the composite sector is decoupled from the low-energy physics.

7.1.2 Partial compositeness

Until now, in our discussion we have never referred to the SM fermions which, together with the SM gauge bosons, constitute the so-called elementary sector. To this end, in this Paragraph we will firstly discuss the idea of partial compositeness, which was introduced for the first time in [170]. The starting point consists in writing down in the Lagrangian the terms describing the interaction between the elementary fermions and the composite sector. Contrarily to technicolor models, where one usually assumes bilinear interaction terms, in this context we will assume a *linear* coupling, which for the quarks will have the form

$$\mathcal{L}_{int} = \lambda(\bar{q} \cdot \mathcal{O} + h.c.) = \lambda_q \bar{q}_L \mathcal{O}_L + \lambda_u \bar{u}_R \mathcal{O}_{u_R} + \lambda_d \bar{d}_R \mathcal{O}_{d_R} + h.c. \tag{7.7}$$

The fundamental difference with respect to technicolor is that the composite operators $\mathcal{O}_L$, $\mathcal{O}_{u_R}$, $\mathcal{O}_{d_R}$ are now fermionic, rather than scalar. This feature of the model allows us to state that both the

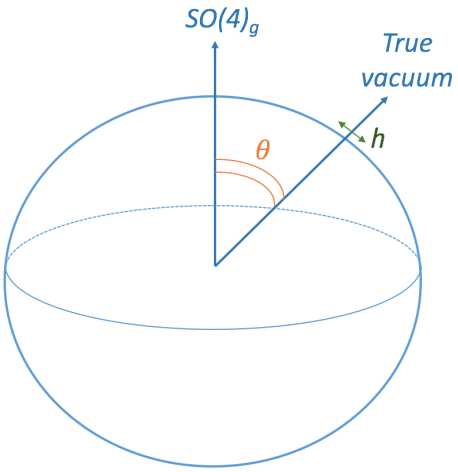

Figure 7.2: Graphical representation of the vaccum misalignment in the case of the MCHM. See the text for all the details.

large hierarchies in the quark masses and the large value of the top mass can be generated in a completely natural way. Moreover, although flavour changing four-fermion operators could in principle be obtained through the exchange of composite modes, a sort of GIM suppression is guaranteed, so that these operators are sufficiently small for the light quarks and leptons.

According to this picture, the CH scenario allows us to obtain a light enough Higgs (as required by the experiments) without falling into any hierarchical problem, as on the contrary happens for instance in technicolor models. But why then the name of *partial compositeness*? The interesting consequence of assuming linear couplings for the SM fermions interactions is precisely the fact that new mixings between the elementary quarks and the composite modes emerge. In this way, the physical SM particles result to be linear combinations of the elementary and the composite degrees of freedom. To be more specific, we assume that a composite operator $\mathcal{O}$ (as one of those appearing in Eq. (7.7)) has the right quantum numbers to have a non-zero matrix element of the form

$$\langle 0 \,|\, \mathcal{O} \,|\, \chi_n^r \rangle = \Delta_n u_r(p) e^{ip\cdot x}, \tag{7.8}$$

being χ_n^r a set of massive composite modes and u_r a spinor. Thus, at low energies the interaction Lagrangian (7.7) will take the structure

$$\mathcal{L}_{int} = \sum_n \Delta_n (\bar{q} \cdot \chi_n + h.c.), \tag{7.9}$$

where it is evident the appearance of mixings between the elementary and the composite states. Now, for simplicity let us hereafter take into consideration only the first composite mode. Thus the full Lagrangian (kinetic and interaction terms) will have the form

$$\mathcal{L} = \bar{\psi}_L i\not{\partial}\psi_L + \bar{\chi}(i\not{\partial} - m)\chi + \Delta(\bar{\psi}_L \chi_R + h.c.). \tag{7.10}$$

We can diagonalize the structure (7.10) simply developing a rotation, *i.e.*

$$\begin{pmatrix} \psi_L \\ \chi_L \end{pmatrix} = \begin{pmatrix} \cos\phi & \sin\phi \\ -\sin\phi & \cos\phi \end{pmatrix} \begin{pmatrix} \psi_L \\ \chi_L \end{pmatrix},$$

being $\tan\phi \equiv \Delta/m$ and $m_* \equiv \sqrt{m^2+\Delta^2}$. The physical meaning of the angle ϕ is the parametrization of the degree of partial compositeness. Thus, the heavier is the fermion, the more composite it is! In fact, the aforementioned rotation brings the Lagrangian (7.10) to the new form

$$\mathcal{L} = \bar{\psi} i\not{\partial}\psi + \bar{\chi}(i\not{\partial} - m_*)\chi, \tag{7.11}$$

so that the physical particles result to be combinations of the ψ, χ eigenstates, namely

$$|light\rangle = \cos\phi\,|\psi\rangle + \sin\phi\,|\chi\rangle\,, \tag{7.12}$$

$$|heavy\rangle = -\sin\phi\,|\psi\rangle + \cos\phi\,|\chi\rangle\,. \tag{7.13}$$

As we will see in the following Section, FP will allow us to put stringent constraints on the fermion modes degree of freedom, in particular their mass, through phenomenology. In conclusion, note that analogous considerations hold also for the gauge sector in QCD with the so-called $\gamma - \rho$ mixing.

7.1.3 The 1S1C hypothesis

At this point, it is necessary to write down the Lagrangian that allows us to describe all the fields in the CH scenario. Remember that on the one hand we have the *composite* sector, in which there are the NGB Higgs Ψ and the massive modes, while on the other hand we have the *elementary* sector, with the SM gauge fields and the quark and lepton fields.

In what follows we will present the so-called *One Scale One Coupling (1S1C)* hypothesis, called in this way for the reasons that will be clear in what follows. For what concerns the composite sector Lagrangian, we write

$$\begin{aligned}\mathcal{L} = &\frac{m_*^4}{g_*^2}\mathcal{L}_{tree}\left(\frac{\partial}{m_*}, \frac{g_*\Pi}{m_*}, \frac{g_*\sigma}{m_*}, \frac{g_*\Psi}{m_*^{3/2}}\right) \\ &+ \frac{g_*^2\hbar}{16\pi^2}\frac{m_*^4}{g_*^2}\mathcal{L}_{one-loop}\left(\frac{\partial}{m_*}, \frac{g_*\Pi}{m_*}, \frac{g_*\sigma}{m_*}, \frac{g_*\Psi}{m_*^{3/2}}\right) + \cdots,\end{aligned} \tag{7.14}$$

where we have assumed the presence of vector modes σ and fermion modes Ψ. The first term is the tree level contribution while the second one is the one loop term. The reason of the name 1S1C relies simply on the presence of only two parameters in the above Lagrangian, namely the typical resonance scale m_* and the typical resonance coupling g_*.

The 1S1C hypothesis can be interpreted also in an interesting way by developing an exercise of dimensional analysis. To this end, it is fundamental *not* to work in natural units. In this case, the Lagrangian density dimension reads

$$\mathcal{L} = \frac{[\hbar]}{L^4},$$

being L a lenght, so that the canonically normalized composite fields have dimensions

$$[\Pi] = [\sigma] = \frac{[\hbar]^{1/2}}{L}, \quad [\Psi] = \frac{[\hbar]^{1/2}}{L^{3/2}}.$$

Hence, it follows that

$$[m_*] = L^{-1}, \quad [g_*] = [\hbar]^{-1/2}.$$

Thanks to these considerations, we can rephrase the 1S1C hypothesis as the one in which the scale m_* and the coupling g_* are the only dimensionful parameters of the theory, so that the Lagrangian

can have only the form (7.14) since it is the unique possibility in virtue of dimensional analysis. The most important consequence of this consideration is the structure of the low-energy Effective Field Theory (EFT) that we find by integrating out the heavy resonance fields. In fact, if the heavy modes are integrated out at tree level, again m_* and g_* will be the unique dimensionful parameters in the thoery, thus dimensional analysis tells us that the Lagrangian structure (7.14) must be respected also by the EFT Lagrangian. In a EFT Lagrangian, the composite fields σ, Ψ will thus indicate the lightest modes present in the theory, as will be clear in the FP analysis contained in the following Section.

In conclusion, we want to include in our description also the SM elementary fields, *i.e.* the gauge fields A_μ and the fermions ψ. Also in this case dimensional analysis will show the way to proceed correctly. In fact, recalling the partial compositeness idea explained above, in the 1S1C assumption the full EFT Lagrangian in CH scenarios can only read

$$\begin{aligned}\mathcal{L}_{EFT} = &\frac{m_*^4}{g_*^2}\mathcal{L}_{tree}\left(\frac{\partial}{m_*}, \frac{g_*\Pi}{m_*}, \frac{g_*\sigma}{m_*}, \frac{g_*\Psi}{m_*^{3/2}}, \frac{g\cdot A_\mu}{m_*}, \frac{\lambda\cdot\psi}{m_*^{3/2}}\right) \\ &+ \frac{g_*^2\hbar}{16\pi^2}\frac{m_*^4}{g_*^2}\mathcal{L}_{one-loop}\left(\frac{\partial}{m_*}, \frac{g_*\Pi}{m_*}, \frac{g_*\sigma}{m_*}, \frac{g_*\Psi}{m_*^{3/2}}, \frac{g\cdot A_\mu}{m_*}, \frac{\lambda\cdot\psi}{m_*^{3/2}}\right) + \dots\end{aligned} \tag{7.15}$$

7.1.4 Possible representations of the fermion modes

The fermion modes Ψ, that have been introduced in Eq. (7.14), can have different representations. This choice allows to obtain new constraints on CH scenarios from the low-energy processes in flavour physics, which is precisely the goal of the following Section. In what follows, we will briefly describe three different cases [171], assuming that the global symmetry respected by the strong sector is $SU(3)\times SU(2)_L \times SU(2)_R \times U(1)$, which includes the custodial symmetry.

i) *Doublet model*: we hypothize that the SM left-handed quarks q_L mix with composite vector-like $SU(2)_L$ doublet, call them Q, one per generation. On the contrary, the SM right-handed quarks u_R and d_R couple both to a unique $SU(2)_R$ doublet, call it R. The relevant Lagrangian terms will thus be

$$\mathcal{L}_Y^D = Y^{ij}\,\mathrm{tr}\left[\bar{Q}_L^i \mathcal{H} R_R^j\right] + \text{h.c.}, \tag{7.16}$$

$$\mathcal{L}_{mix}^D = m_Q^j \lambda_L^{ij}\bar{q}_L^i Q_R^j + m_R^i\lambda_{Ru}^{ij}\bar{U}_L^i u_R^j + m_R^i\lambda_{Rd}^{ij}\bar{D}_L^i d_R^j, \tag{7.17}$$

where the first row contains the Yukawa terms of the composite particles, while the second one the mixing terms with the SM fields. Note that we have defined $\mathcal{H} \equiv (i\sigma_2 H^*, H)$ and $R = (U\ \ D)^T$.

ii) *Triplet model*: we hypothize that the SM left-handed quarks q_L mix with a composite state, call it L, that is a doublet both under $SU(2)_L$ and $SU(2)_R$, while the SM right-handed quarks u_R and d_R couple both to a composite $SU(2)_R$ triplet, call it R. To preserve the left-right symmetry of the theory, we will have to deal also with another particle which is a triplet of $SU(2)_L$, call it $R^{'}$. The Lagrangian terms now read

$$\mathcal{L}_Y^T = Y^{ij}\,\mathrm{tr}\left[\bar{L}_L^i \mathcal{H} R_R^j\right] + Y^{ij}\,\mathrm{tr}\left[\mathcal{H}\bar{L}_L^i R^{'j}_R\right] + \text{h.c.}, \tag{7.18}$$

$$\mathcal{L}_{mix}^T = M_L^j\lambda_L^{ij}\bar{q}_L^i Q_R^j + m_R^i\lambda_{Ru}^{ij}\bar{U}_L^i u_R^j + m_R^i\lambda_{Rd}^{ij}\bar{D}_L^i d_R^j \tag{7.19}$$

where Q is the T_{3R} doublet in L and, on the contrary, U and D are the components of R with charge 2/3 and 1/3, respectively.

iii) *Bidoublet model*: we hypothize that the SM left-handed quarks q_L mix with two composite states, call them L_U and L_D, which are both doublets under $SU(2)_L$ and $SU(2)_R$ but differ for the value of their charge X. The SM right-handed quarks u_R and d_R couple to two composite singlets of both $SU(2)_L$ and $SU(2)_R$, call them U and D, which again differ for the values of their charge X. In Lagrangian terms we have that

$$\mathcal{L}_Y^{BD} = \left(Y_U^{ij}\,\mathrm{tr}\big[\bar{L}_U^i \mathcal{H}\big]_L U_R^j + \mathrm{h.c.}\right) + (U \to D), \tag{7.20}$$

$$\mathcal{L}_{mix}^{BD} = m_{Qu}^j \lambda_{Lu}^{ij} \bar{q}_L^i Q_{Ru}^j + m_U^i \lambda_{Ru}^{ij} \bar{U}_L^i u_R^j + (U,\, u \to D,\, d), \tag{7.21}$$

where Q_u and Q_d are components of L_U and L_D, respectively.

To summarize all the properties of the fields just introduced, in Figure 7.3 we show their quantum numbers and the model in which they enter.

model		$SU(3)_c$	$SU(2)_L$	$SU(2)_R$	$U(1)_X$
doublet	Q	**3**	**2**	**1**	$\frac{1}{6}$
	R	**3**	**1**	**2**	$\frac{1}{6}$
triplet	L	**3**	**2**	**2**	$\frac{2}{3}$
	R	**3**	**1**	**3**	$\frac{2}{3}$
	R'	**3**	**3**	**1**	$\frac{2}{3}$
bidoublet	L_U	**3**	**2**	**2**	$\frac{2}{3}$
	L_D	**3**	**2**	**2**	$-\frac{1}{3}$
	U	**3**	**1**	**1**	$\frac{2}{3}$
	D	**3**	**1**	**1**	$-\frac{1}{3}$

Figure 7.3: Quantum number of the composite fermions introduced in the Eqs.(7.16)-(7.21). To compute the X charge, it is sufficient to consider the expression $Y = T_{3R} + X$, where Y is the hypercharge. Taken from [171].

7.2 New bounds on fermion resonances from Flavour Physics

Starting from the effective Lagrangian (7.15), we are able to describe the interactions of the composite degrees of freedom with the SM fields. Such interactions can give rise to BSM contributions to several processes in Flavour Physics. A direct comparison between the theory and the experiments allows then us to put important constraints to the physical parameters of CH scenarios, that is precisely the goal of this Section.

Note that, to achieve this goal, we will apply the results of the EFT study developed in the previous Chapter to the specific case of CH models. In Table 6.1 we have summarized all the bounds obtained on the WCs (at the 1 TeV scale). The ones relevant for applications to Composite Higgs are shown in bold. All these results will be rephrased, in what follows, on new bounds on the mass m_Ψ of the composite fermions, that have been introduced in the previous Section. Now, the SM up-type Yukawas can be related to the strong ones as:

$$y_u = Y_U s_{Lu1} s_{Ru1}, \qquad y_c = Y_U s_{Lu2} s_{Ru2}, \qquad y_t = Y_U s_{Lu3} s_{Ru3}, \tag{7.22}$$

where we have defined

$$s^{ii}_{\{L,R\}} = \frac{\lambda_{\{L,R\}i}}{\sqrt{1+(\lambda_{\{L,R\}i})^2}}.$$

Recall that the composite-elementary mixings $\lambda_{\{L,R\}}$ have been defined in the Eqs.(7.16)-(7.21). Having in mind that expressions analogous to (7.22) hold for the down-type quarks, we can also express the CKM matrix elements as $V_{ij} \sim s_{Li}/s_{Lj}$ $(i<j)$ for the doublet and the triplet representations of the fermion modes, while as $V_{ij} \sim s_{Ldi}/s_{Ldj} \pm s_{Lui}/s_{Luj}$ for the bidoublet one. Thus, in the doublet and the triplet representations we have only one free parameter, namely $x_t \equiv s_{L3}/s_{Ru3}$, while in the bidoublet case we have two free quantities, *i.e.* $x_t \equiv s_{Lt}/s_{Rt}$ and $z \equiv s_{Lt}/s_{Lb}$. All these quantities will be often used in the computations developed in the remaining part of this Chapter.

At this point, one question naturally arises: how can we ensure the hierarchical structure of the SM Yukawas in Eq. (7.22) (and analogously for the down-type ones) while being consistent with the stringent flavour constraints on higher-dimension operators? Basically, there are two possible ways.

- We assume that the strong Yukawas $Y_{U,D}$ have an anarchic structure, in other words all their matrix elements are of similar order. This is the so-called *anarchic* scenario, that has been widely studied in literature, see for instance [172–179]. In this case, the hierarchical form of the SM Yukawas is thus generated by the composite-elementary mixings $s_{\{L,R\}}$ (or, equivalently, $\lambda_{\{L,R\}}$), which must then be hierarchical.

- We assume a specific flavour structure for the strong sector. In this case, all the physical quantities related to the strong sector are characterized by a precise flavour symmetry. The most famous and possible choices are the $U(3)^3$ models (that are MFV frameworks) and the $U(2)^3$ ones, which have been described in Chapter 6. Note that, in these cases, the composite-elementary mixings are the *only* sources of breaking of the flavour symmetry of the composite sector.

At this point, in what follows we will firstly recall how the composite resonances enter both the tree level $\Delta F = 2$ FCNCs and the coupling of the SM gauge bosons. Then, we will compute the bounds on m_Ψ corresponding to each of the processes involving B-mesons previously studied, namely $b \to s\ell^+\ell^-$, $B_{d,s}$ mixing and finally $b \to s\gamma$.

- **Flavour changing Z couplings**

In CH scenarios, flavour changing Z couplings arise and are directly linked to the modified Zbb coupling [171]. Firstly, we write that coupling as

$$\begin{aligned}&\frac{g}{c_w}\bar{b}\gamma^\mu\left[\left(g^{L,SM}_{Zbb}+\delta g^L_{Zbb}\right)P_L+\left(g^{R,SM}_{Zbb}+\delta g^R_{Zbb}\right)P_R\right]bZ_\mu = \\ &\frac{g}{c_w}\bar{b}\gamma^\mu\left[\left(-\frac{1}{2}+\frac{1}{3}s^2_w+\delta g^L_{Zbb}\right)P_L+\left(\frac{1}{3}s^2_w+\delta g^R_{Zbb}\right)P_R\right]bZ_\mu,\end{aligned} \tag{7.23}$$

where s_w, c_w are the sine and the cosine of the Weinberg angle and $g \equiv g_2$. Secondly, we consider the diagrams of interest in order to compute $\delta g^{L,R}_{Zbb}$. The two relevant diagrams (for each helicity case) are characterized by two insertions of the Higgs VEV $< h > \equiv v$ in correspondence of the mixings between elementary and composite fermions (Figure 7.4a) or of the $\rho - Z$ one, being ρ a vector mode Figure

7.4b). Putting together the elementary-composite mixings, the propagators, the $\rho - Z$ coupling and (only in the first case) the composite Yukawas, we obtain the final expressions

$$\begin{aligned} \delta g^L_{Zbb} &= \frac{v^2 Y_D^2 x_t y_t}{2M_D^2 Y_U} a + \frac{v^2 g_\rho^2 x_t y_t}{4 m_\rho^2 Y_U} b, \\ \delta g^R_{Zbb} &= \frac{v^2 Y_D^2 y_b^2 Y_U}{2M_D^2 x_t y_t Y_D^2} c + \frac{v^2 g_\rho^2 y_b^2 Y_U}{4 m_\rho^2 x_t y_t Y_D^2} d, \end{aligned} \tag{7.24}$$

where the values of the coefficients a, b, c, d depend on the fermion representation, see Table 7.1.

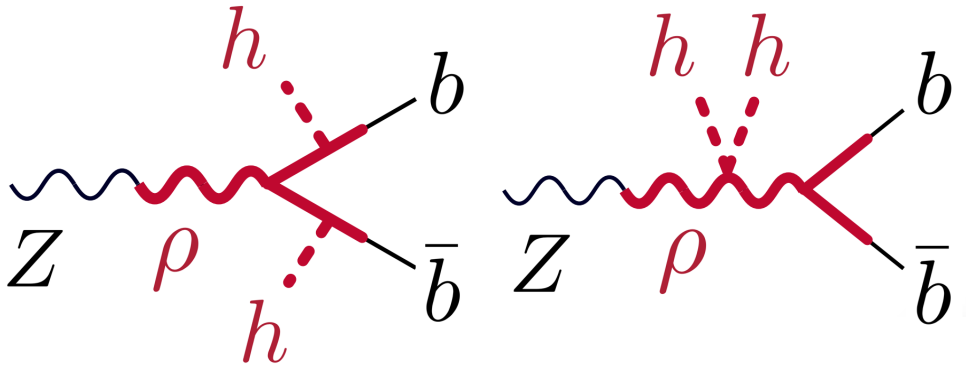

(a) (b)

Figure 7.4: The two relevant Feynman diagrams to determine the BSM contributions to flavour changing Z couplings in CH scenarios. The bold purple lines represent the (both fermion and vector) composite degrees of freedom, while the purple dotted lines are the Higgs insertions.

Table 7.1: Values of the coefficients a, b, c, d in Eq. (7.24) for the various fermion representations: doublet (D), triplet (T) and bi-doublet (BD).

	D	T	BD
a	1/2	0	$1/(2z^2)$
b	1/2	0	$1/z^2$
c	-1/2	-1/2	0
d	-1/2	-1	0

Since we are interested in the Zbs case, we have to take into account a modification in one elementary-composite mixing with respect to the $\delta g^{L,R}_{Zbb}$ case. Since

$$s_L^{2D} = V_{ts} \times s_L^{3D}, \tag{7.25}$$

$$s_R^{2D} = \frac{y_s}{Y_D s_L^2} = \frac{y_s}{Y_D V_{ts} s_L^3} = \frac{y_s}{Y_D V_{ts}} \sqrt{\frac{Y_U}{x_t y_t}} = \frac{m_s}{m_b V_{ts}} \times \frac{y_b}{Y_D} \sqrt{\frac{Y_U}{x_t y_t}} = \frac{m_s}{m_b V_{ts}} \times s_R^{3D}, \tag{7.26}$$

being s_L^{3D} and s_R^{3D} the analogous elementary-composite mixings in the Zbb case, we can state that

$$\delta g^L_{Zbs} \sim V_{ts}\, \delta g^L_{Zbb}, \qquad \delta g^R_{Zbs} \sim \frac{m_s}{m_b V_{ts}}\, \delta g^R_{Zbb}. \tag{7.27}$$

In order to constrain the fermion mass m_Ψ from modified Z couplings, it is sufficient to relate $\delta g^{L,R}_{Zbs}$ to the WCs $c^{(\prime)}_{9,NP}, c^{(\prime)}_{10,NP}$. In fact, one can show that

$$-\frac{g^2}{c_w^2}\frac{1}{m_Z^2}\delta g^{L(R)}_{Zbs} \times \left(-\frac{1}{2} + 2s_w^2\right) = c^{(\prime)}_{9,NP}, \tag{7.28}$$

$$-\frac{g^2}{c_w^2}\frac{1}{m_Z^2}\delta g^{L(R)}_{Zbs} \times \left(+\frac{1}{2}\right) = c^{(\prime)}_{10,NP}, \tag{7.29}$$

where the quantities in parenthesis in the are linear combinations of the left-handed and the right-handed $Z\mu\mu$ couplings in the SM. The numerical study shows that the right coupling δg^R_{Zbs} (related to the primed Wilson coefficients $c^{'}_{9(10),NP}$) gives a weaker bound on m_Ψ with respect to the one coming from the left coupling δg^L_{Zbs} (related instead to the unprimed Wilson coefficients $c_{9(10),NP}$). Furthermore, Eqs. (7.28)- (7.29) show that the constraints from the coefficients $c^{(\prime)}_{10,NP}$ are stronger than the ones by $c^{(\prime)}_{9,NP}$ due to the enhancement by the axial (or equivalently $L-R$) coupling of the Z to the muon pair.

Let us briefly discuss what happens for the various choices of the flavour pattern of the strong sector. Eq. (7.27) is valid only for the anarchic scenario. For the $U(2)^3$ models, we do not have sizable flavour-changing right-handed Z coupling, while the flavour-changing left-handed one has the same structure present in Eq. (7.27) if a further assumption is made. In fact, by construction in $U(2)^3$ models the mixings can be chosen diagonal, *but not* proportional to the identity matrix. For this reason, in $U(2)^3$ computations one has to consider an additional parameter, let us call it r_b [171], which can be in principle complex. Thus, we recover Eq. (7.27) for the left-handed coupling in $U(2)^3$ models *if* we require r_b to be $\mathcal{O}(1)$. Finally, in $U(3)^3$ models no modification of both the flavour-changing left-handed and the flavour-changing right-handed couplings arise, as a consequence of the symmetry pattern chosen.

In conclusion, in Table 7.3 we show the lower bounds on m_Ψ resulting from the constraints on $c_{10,NP}$. Note that, if we set $z = 1$, the bi-doublet model value results enhanced by a factor ~ 1.15 with respect to the corresponding doublet one.

- $\Delta F = 2$ **processes**

In CH theories, a new contribution to $\Delta F = 2$ interactions comes from an exchange of vector modes between four fermions at tree level (without the insertion of Higgs VEVs). In this sense, the WCs introduced in Eq. (6.21) can be expressed as

$$c^{bqAB}_{V(S)} = \frac{g_\rho^2}{m_\rho^2} g_A^{bq} g_B^{bq} \gamma^{bqAB}_{V(S)}, \tag{7.30}$$

where $A, B = L, R$ and $g^{bq}_{A(B)}$ are functions of the various elementary-composite mixings. The values of the coefficients $\gamma^{bqAB}_{V(S)}$ follow from group theory considerations, thus depend on the flavour pattern associated to the strong sector and on the particular representation of the fermion modes. Their values can be found in the Appendix A of [171].

At this point, since

$$\frac{g_\rho^2}{m_\rho^2} = \frac{1}{f^2} = \frac{Y^2}{m_\Psi^2}, \tag{7.31}$$

we can use the upper bounds on the WCs $c_{V(S)}^{bqAB}$, previously obtained, in order to set a lower bound on the mass m_Ψ of the fermion modes. Let us consider separately the NP contribution to the vector and to the scalar WCs.

i) *Contribution to the vector WC* c_V^{bqLL}

In this case, the elementary-composite mixings read

$$g_L^{bq} = s_L^b s_L^q \sim V_{tb} V_{tq}^\dagger s_{L3}^2 \sim V_{tb} V_{tq}^\dagger \frac{x_t y_t}{Y} \quad (q = d, s). \tag{7.32}$$

Note that under the assumption $Y_U = Y_D \equiv Y$ there is no difference in this expression between the doublet, triplet and bidoublet fermion representations. From Eq. (7.30) we thus have

$$m_\Psi = \sqrt{\frac{\gamma_V^{bqLL} (V_{ti} V_{tj}^\dagger x_t y_t)^2}{c_V^{bqLL}}} \quad (q = d, s). \tag{7.33}$$

Hence, the upper bounds on the Wilson coefficients (6.23) and (6.27) become lower bounds on the mass of the fermion modes, whose values are reported in Table 7.3.

For what concerns the flavour symmetry of the strong sector, these expressions are in general valid for both the anarchic scenario and the $U(3)^3$ models. In these cases, then, the NP terms in the amplitudes will have the same CKM suppression that we see in the SM, as discussed in Eq. (6.10) in the previous Chapter. In $U(2)^3$ models, instead, this statement is true *if* the additional parameter r_b (that we have previously described) is real, otherwise in principle a new phase can arise from NP contributions. In other words, Eqs. (7.32)-(7.33) are still valid in $U(2)^3$ models *if* r_b is a real and $\mathcal{O}(1)$ parameter.

ii) *Contribution to the scalar WC* c_S^{bqLR}

Here we are interested also to the right-handed elementary-composite mixings, which read

$$g_R^{bq} = s_{Rd}^b s_{Rd}^q \sim (z^2) \frac{y_b y_q}{Y x_t y_t V_{tb} V_{tq}^\dagger} \quad (q = d, s), \tag{7.34}$$

where again $Y_U = Y_D \equiv Y$ and the factor z^2 in parenthesis applies only in the bidoublet representation. Hence, from Eq. (7.30) we finally find that

$$m_\Psi = \sqrt{(z^2) \frac{y_b y_q}{c_S^{bqLR}}}, \quad (q = d, s). \tag{7.35}$$

Note that in this case $\gamma_S^{bqLR} = 1$ for every choice of the fermion representation. In conclusion, the resulting lower bounds on the mass of the fermion modes are reported in Table 7.3.

For what concerns the flavour pattern of the strong sector, this bound is valid only in the anarchic scenario. By construction, in both the $U(3)^3$ and the $U(2)^3$ the right-handed contributions are zero.

- **Right-handed W couplings**

The composite modes enter radiative B decays, *i.e.* $b \to s\gamma$ transitions, since a BSM right-handed W coupling to the quarks arise. We will be interested only in the one-loop IR contribution to the Wilson coefficients $C_7^{(\prime)}$ [154], which can be directly related to m_Ψ as follows. Let us compute the effect of the right-handed Wtb (Wts) coupling to C_7 ($C_7^\prime$) by writing this coupling in the Lagrangian of the theory. Consider for example the Wtb case (the other one is completely analogous). This coupling takes the form

$$\frac{g}{\sqrt{2}}\delta g^R_{Wtb}(\bar{t}\gamma^\mu P_R b)W_\mu. \tag{7.36}$$

Similarly to the Zbb case, the two relevant diagrams are characterized by two insertions of the Higgs VEV $< h > \equiv v$ in correspondence of the mixings between elementary and composite fermions or of the $\rho - W$ one, being ρ a vector mode. From the point of view of Feynman diagrams, the situation is completely equivalent to what seen for flavour changing Z coupling in Figure 7.4.

Putting together the elementary-composite mixings, the propagators, the $\rho - W$ coupling and (only in the first case) the composite Yukawas, we obtain the final expression

$$\delta g^R_{Wtb} = \frac{v^2}{2}\frac{y_b Y_U}{m_Q^2 x_t}a + \frac{g_\rho^2 v^2}{4m_\rho^2}\frac{y_b}{Y_D x_t}b, \tag{7.37}$$

where again the values of the coefficients a, b depend on the choice of fermion representation, see Table 7.2. Thus, the quantity (7.37) is related to the WCs as

$$C_7 = \frac{m_t}{m_b}\frac{\delta g^R_{Wtb}}{V_{tb}}G_{loop}(\frac{m_t^2}{m_W^2}), \tag{7.38}$$

where G_{loop} is a loop-function, in particular $G_{loop}(m_t^2/m_W^2) \simeq -0.78$.

Table 7.2: Values of the coefficients a, b in Eq. (7.37) for the various fermion representations: doublet (D), triplet (T) and bi-doublet (BD).

	D	T	BD
a	1	1	$-2\, x_t y_t/Y$
b	1	1	0

Furthermore, we can also find a relation involving $C_7^\prime$ rather than C_7, *i.e.* an expression analogous to Eq. (7.38). In order to determine δg^R_{Wts}, we have to take into account a different elementary-composite mixing with respect to the δg^R_{Wtb} case, while the rest of the computation is identical. Recalling equation (7.26), since

$$s_R^{2D} = \frac{m_s}{m_b V_{ts}} \times s_R^{3D}, \tag{7.39}$$

being s_R^{3D} the elementary-composite mixing in the Wtb case, it is clear that

$$C_7^\prime = \frac{m_t}{m_b}\frac{m_s}{m_b V_{ts}^2}\delta g^R_{Wtb}G_{loop}(\frac{m_t^2}{m_W^2}). \tag{7.40}$$

Hence, the IR contribution to $C_7^\prime$ is enhanced by a factor $\frac{m_s}{m_b V_{ts}^2}$ with respect to the C_7 case.

In Table 7.3 we show the lower bounds on m_Ψ resulting from Eq. (7.40) by taking into consideration the upper bound at 2σ on the imaginary part of C_7', which is slightly smaller than the one on its real part. This bound is valid only in the anarchic scenario since, by construction, in the $U(3)^3$ and the $U(2)^3$ models no NP contributions to the right-handed W couplings arise.

Table 7.3: Lower bounds on m_Ψ (in TeV) in the anarchic model from all the processes studied in these sections. The results are presented for different choices of the fermion representation: doublet (D), triplet (T) and bi-doublet (BD). Under the assumptions described in the main text, the bounds from Q_V^{bdLL} and Q_V^{bsLL} apply also in the $U(3)^3$ scenarios, while the ones from Q_V^{bdLL}, Q_V^{bsLL} and $\mathcal{O}_{10}$ are still valid in the $U(2)^3$ models.

Operators	Lower bounds on m_Ψ (TeV) D	T	BD
$\mathcal{O}_{10}$	$8.7\sqrt{Y x_t}$	—	$10.0\sqrt{Y x_t}/z$
Q_V^{bdLL}	$7.7\,x_t$	$11.1\,x_t$	$11.1\,x_t$
Q_S^{bdLR}	2.3	2.3	$2.3\,z$
Q_V^{bsLL}	$8.0\,x_t$	$11.5\,x_t$	$11.5\,x_t$
Q_S^{bsLR}	2.1	2.1	$2.1\,z$
$\mathcal{O}_7'$	$3.7\sqrt{Y}/\sqrt{x_t}$	$3.7\sqrt{Y}/\sqrt{x_t}$	3.7

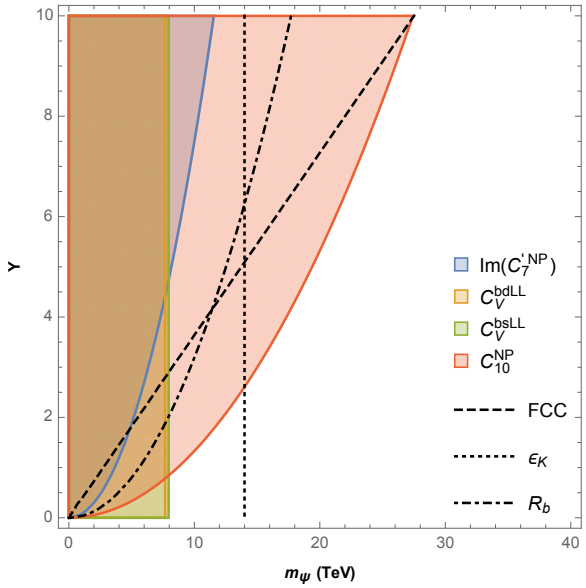

Figure 7.5: The correlation plot m_Ψ(TeV) VS Y choosing the doublet model as fermion representation (we have set $x_t = 1$). The constraints from Re$\left(c_S^{bdLR}\right)$ and Re$\left(c_S^{bsLR}\right)$ are not shown. All these constraints are valid in the anarchic scenario. Under the assumptions described in the main text, the bounds from C_V^{bdLL} and C_V^{bsLL} apply also in the $U(3)^3$ scenarios, while the ones from C_V^{bdLL}, C_V^{bsLL} and $C_{10}^{\rm NP}$ are still valid in the $U(2)^3$ models.

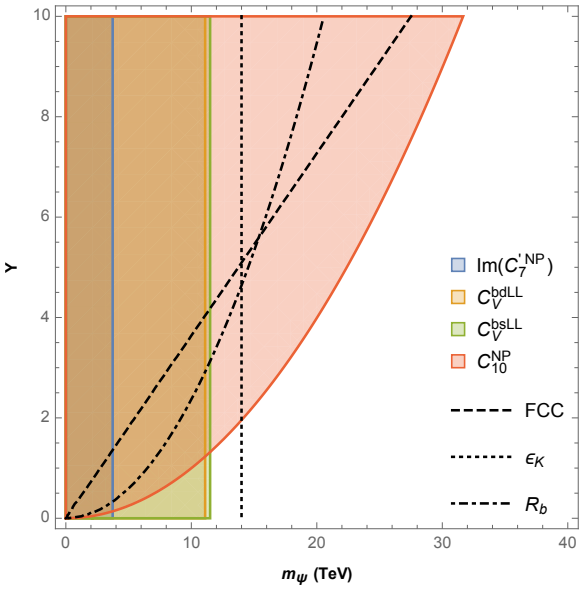

Figure 7.6: The correlation plot m_Ψ(TeV) VS Y choosing the bidoublet model as fermion representation (we have set $z = x_t = 1$). Also in this case the constraints from Re $\left(c_S^{bdLR}\right)$ and Re $\left(c_S^{bsLR}\right)$ are not shown. The same considerations present in the caption of Figure 7.5 apply for the various possible flavour patterns of the strong sector.

7.2.1 Summary plots

In this Section we show a summary of all the results found until now (and shown in Table 7.3) as correlation plots of the fermion mass m_Ψ VS the Yukawa coupling in the strong sector Y. We will study two possible choices of the fermion representation, *i.e.* the doublet model and the bidoublet one, separately.

In Figure 7.5 we show our results in the doublet model. Here the results in the "D" column of Table 7.3 are graphically represented, according to the color code described in Figure 7.5 itself. Since x_t is a free parameter varying in the range

$$\frac{y_t}{Y} < x_t < \frac{Y}{y_t},$$

we make the conservative choice $x_t = 1$. Note that there are other indirect bounds present in this plot, represented as black curves. The dashed one results from the indirect Higgs coupling constraints expected at FCC-ee [13], corresponding to $\xi \equiv v^2/f^2 = 0.004$. The dotted line comes from the chiral enhancement to ϵ_K expected from the scalar operator Q_S^{sdLR}, as shown in [171]. Finally, the dot-dashed curve corresponds to the bound from the Z partial width into b quarks, *i.e.* from R_b, that emerges from a modification of the Zbb couplings in CH [171]. Note that, contrarily to the first one, these two last bounds are expected not to improve so much in the future decade, given the very high precision with which the related physical quantities have been measured until now.

At this point, few observations are in order. First of all, the most important message is that the bounds coming from flavour physics result to be comparable to the ones coming from the other indirect searches, in some cases even stronger. To be more specific, the constraint from the WC C_{10}^{NP} is the most solid one, being less stringent than the one from ϵ_K only in the range $Y \lesssim 2$. In particular, these

two bounds push the fermion mass m_Ψ in the range $O(15-20)$ TeV, so that we can finally state that in not-completely natural CH models the doublet model is characterized by a huge predictivity.

In Figure 7.6 we show the analogous correlation plot choosing instead the bidoublet model. Here we use the results presented in the "BD" column in Table 7.3, preserving the same colour code of Figure 7.5. In addition to x_t, another free parameter $z \geq 1$ has to be fixed, hence we choose the values $x_t = z = 1$ in order to not further enhance the ϵ_K constraint. Here the situation is very similar to the doublet case, thus we observe again the fundamental role of the limits coming from phenomenology and flavour physics. The main differences are the stronger bound of the $\Delta B = 2$ transitions, slightly weaker than the ϵ_K one, and the more stringent constraint from C_{10}^{NP} with respect to the one in the doublet model, in particular for what concerns the high-Y region.

Chapter 8

Explicit models II: LeptoQuarks

In this Section we will review the main motivations for and physical properties of the LeptoQuarks (LQs). In the past five years, these BSM degrees of freedom have received a lot of interest especially in relation to the flavour anomalies, which we have described from an EFT point of view in Chapter 6. As we will see, many theoretical studies have been developed in order to explain the discrepancy between expectations and measurements observed in these observables through LQs. While we have proposed in Chapter 4 a study of the semileptonic $B \to D^{(*)}\ell\nu$ decays that allow to lighten the tension in the $R(D^{(*)})$ case, this is not the same for the $R(K^{(*)})$ ratios. Thus, we will review the results of other studies about the impact of the LQs on the analysis of the LFU observables in semileptonic B decays. Finally, we will mention possible UV completions of these theories, which allow also to link CH scenarios and LQs to each other. Note that this Section of review is also functional to the description of a particular Dark Matter model mediated by LQs, as we will describe in the following Part III.

8.1 Theoretical Framework

8.1.1 Candidates and Nomenclature

The LeptoQuarks were originally introduced by Pati and Salam in the 70s [180–182] and then further studied in the last forty years, see for instance [183–190]. They are BSM degrees of freedom that can turn leptons into quarks and viceversa, thus having the fundamental property of unifying matter.

In what follows, we will develop a classification of all the possible LQs that one can define, specifying their quantum numbers under the SM $SU(3) \times SU(2) \times U(1)$ gauge group [191]. In this sense, it is important to define the *fermion number* $F = 3B + L$, where B and L are the baryon and lepton number, respectively. We have a totality of six scalar and six vector LQs, that are shown in Table 8.1. Let us explain the rationale of such a classification and the main properties of these BSM particles.

First of all, since a LQ couples a quark and a lepton, which are triplets and singlets under $SU(3)$, respectively, all the LQs candidates have the same representation under $SU(3)$. The assignment of the dimensionality under $SU(2)$ is, instead, not trivial, since both quarks and leptons are doublets or singlets (according to their chirality) under $SU(2)$. From group theory considerations, this implies that a LQ can be a triplet, a doublet or a singlet under $SU(2)$ and this choice is specified by the subscript of the symbol associated to each LQ candidate. Furthermore, it can happen that many LQs share the same $SU(3)$ and $SU(2)$ quantum numbers, but having different values of the hypercharge Y. To highlight such a difference, a tilde or a bar is used in the LQ symbol. To explicitly compute the LQ candidates hypercharge, group theory considerations are again straightforward. In fact, since

Table 8.1: Classification of all the possible scalar (S) and vector (V) LQs, respectively [191].

Symbol	$(SU(3), SU(2), U(1))$	S/V	Fermion number
S_3	($\bar{3}$,3,1/3)	S	-2
R_2	(3,2,7/6)	S	0
$\tilde{R}_2$	(3,2,1/6)	S	0
$\tilde{S}_1$	($\bar{3}$,1,4/3)	S	-2
S_1	($\bar{3}$,1,1/3)	S	-2
$\bar{S}_1$	($\bar{3}$,1,-2/3)	S	-2
U_3^μ	($\bar{3}$,3,2/3)	V	0
V_2^μ	($\bar{3}$,2,5/6)	V	-2
$\tilde{V}_2^\mu$	($\bar{3}$,2,-1/6)	V	-2
$\tilde{U}_1^\mu$	(3,1,5/3)	V	0
U_1^μ	(3,1,2/3)	V	0
$\bar{U}_1^\mu$	(3,1,-1/3)	V	0

Y is an additive quantity, it is sufficient to compute the value of the hypercharge of the contraction of the particular quark and lepton representations associated to each LQ candidate.

In conclusion, note that in many UV completions of the theory incorporating one of these mediators, the LQs arise with partners of similar mass but different representations under the SM $SU(3) \times SU(2) \times U(1)$ gauge group. For this reason, one often considers two or more LQ candidates for developing phenomenological applications to low-energy processes in Flavour Physics. These facts will be deeply investigated and discussed in the following Sections.

8.1.2 The vector U_1^μ and the scalars S_1 and S_3

The general expressions of the LQs couplings to the SM particles (namely the Higgs, the gauge bosons and the quark-lepton pairs) can be found in the Appendices of [191]. Here we will examine some illustrative examples, *i.e.* the vector LQ U_1^μ and the scalar ones S_1 and S_3, since they have a central role in the phenomenological applications to several flavour observables.

Let us thus start from this latter case. From Table 8.1 we see that the quantum numbers of U_1^μ under the SM gauge group are $(3, 1, 2/3)$, thus its interactions with the left-handed quarks Q_i and leptons L_α have the following Lagrangian structure:

$$\mathcal{L}_U \supset g_U (J_U^\mu U_{1,\mu} + h.c.), \quad J_U^\mu \equiv \beta_{i\alpha} \bar{Q}_i \gamma^\mu L_\alpha, \tag{8.1}$$

where i, α are flavour indices. The structure of the 4-current J_U^μ depend on the matrixes $\beta_{i\alpha}$, whose expressions are influenced by the particular flavour structure that we decide to assign to our model. In other words, there will be a certain number of complex parameters which J_U^μ depends on, whose definition fix the flavour structure of the theory. Moreover, we can obtain the form of the effective Lagrangian by integrating out the LQ U_1^μ field, thus obtaining

$$\mathcal{L}_{U,\text{eff}} \supset -\frac{|g_U|^2}{2M_U^2} \beta_{i\alpha} \beta_{j\beta}^* \left[(\bar{Q}^i \gamma_\mu \sigma^a Q^j)(\bar{L}^\beta \gamma^\mu \sigma^a L^\alpha) + (\bar{Q}^i \gamma_\mu Q^j)(\bar{L}^\beta \gamma^\mu L^\alpha) \right], \tag{8.2}$$

where M_U is the LQ mass.

The same considerations can be developed for the scalar LQs S_1 and S_3, whose quantum numbers are $(\bar{3},1,1/3)$ and $(\bar{3},3,1/3)$, respectively. Using the same notation adopted in Eqs. (8.1)-(8.2), their interactions can be written in Lagrangian form as

$$\mathcal{L}_S \supset g_1\beta_{1,i\alpha}(\bar{Q}^{c\,i}\epsilon L^\alpha)S_1 + g_3\beta_{3,i\alpha}(\bar{Q}^{c\,i}\epsilon\sigma^b L^\alpha)S_3^b + h.c., \tag{8.3}$$

where we have defined $\epsilon \equiv i\sigma^2$ and $Q^c \equiv C\bar{Q}^T$. Moreover, S_3^b are the three components of S_3 under $SU(2)$. Also in this case the mixing matrices $\beta_{1,i\alpha}$ and $\beta_{3,i\alpha}$ depend on the flavour structure of the theory and are, in general, different to each other. We can obtain the expression of the effective Lagrangian by integrating out the two scalar LQs, obtaining

$$\begin{aligned}\mathcal{L}_{S,\text{eff}} \supset &-\left(\frac{|g_1|^2}{4M_{S_1}^2}\beta_{1,i\alpha}\beta_{1,j\beta}^* - \frac{|g_3|^2}{4M_{S_3}^2}\beta_{3,i\alpha}\beta_{3,j\beta}^*\right)\left[(\bar{Q}^i\gamma_\mu\sigma^a Q^j)(\bar{L}^\beta\gamma^\mu\sigma^a L^\alpha)\right] \\ &+\left(\frac{|g_1|^2}{4M_{S_1}^2}\beta_{1,i\alpha}\beta_{1,j\beta}^* + 3\frac{|g_3|^2}{4M_{S_3}^2}\beta_{3,i\alpha}\beta_{3,j\beta}^*\right)\left[(\bar{Q}^i\gamma_\mu Q^j)(\bar{L}^\beta\gamma^\mu L^\alpha)\right],\end{aligned} \tag{8.4}$$

where M_{S_1} and M_{S_3} are the masses of the scalar LQs S_1 and S_3, respectively.

8.2 Phenomenological applications to the flavour anomalies

In the recent few years, lots of papers in literature have analyzed the impact of LQs on the study of Flavour observables in a BSM framework. In what follows, we will review a very illustrative example in this sense, *i.e.* the flavour anomalies, whose EFT description has been illustrated in Chapter 6. To simplify the discussion, we will limit ourselves to consider the results of the papers [192, 193], where the authors have considered the simple scenario of a vector LQ U_1^μ. We anticipate that these models will be studied more in detail in Chapter 11, however we give here an introduction for convenience.

8.2.1 Effective interactions of the vector LQ U_1^μ with the SM fields

In view of phenomenological applications, it is important to write down an effective Lagrangian to describe the interactions of the LQ U_1^μ with the SM particles. The authors of [192,193] have considered a slightly more general case than the one in Eq. (8.1), namely the possibility that the LQ can interact also with right-handed fields. From the mathematical point of view, the resulting fermion current will thus take the new form

$$J_\mu = \frac{1}{\sqrt{2}}[\beta_L^{i\alpha}(\bar{Q}_L^i\gamma_\mu L_L^\alpha) + \beta_R^{i\alpha}(\bar{d}_R^i\gamma_\mu e_R^\alpha)], \tag{8.5}$$

where a new hermitian matrix $\beta_R^{i\alpha}$ has been introduced. Now, without loss of generality they have chosen for the $SU(2)$ doublets the following mass eigenstate basis:

$$Q_L^i = (V_{ji}^* u_L^j \quad d_L^i)^T, \qquad L_L^i = (\nu_L^i \quad e_L^i)^T,$$

where V_{ji} is the CKM matrix. In this way, they have expressed the matrices $\beta_L^{i\alpha}$, $\beta_R^{i\alpha}$ with the following form [192, 193]:

$$\beta_L = \begin{pmatrix} 0 & 0 & \beta_L^{d\tau} \\ 0 & \beta_L^{s\mu} & \beta_L^{s\tau} \\ 0 & \beta_L^{b\mu} & 1 \end{pmatrix}, \qquad \beta_R = \begin{pmatrix} 0 & 0 & 0 \\ 0 & 0 & 0 \\ 0 & 0 & \beta_R^{b\tau} \end{pmatrix}, \tag{8.6}$$

This is a very simple model, since one is retaining the *minimal* number of couplings that influence the flavour anomalies, while setting all the other entries equal to zero. Moreover, one is assuming that a hierarchy between these couplings exists, in accordance with the CKM flavour structure. In other words, $\beta_L^{d\tau}$, $\beta_L^{s\mu} \ll \beta_L^{s\tau}$, $\beta_L^{b\mu} \ll 1$ and finally $\beta_R^{b\tau} = \mathcal{O}(1)$.

Under these assumptions, the authors of [192,193] can finally integrate out the LQ U_1^μ and obtain the following compact expression for the effective Lagrangian (that can be consider a generalization of Eq. (8.2))

$$\begin{aligned}\mathcal{L}_{U,eff} = -2C_U[&-2(\beta_L^{i\alpha})^*\beta_R^{l\beta}(\bar{L}_L^\alpha e_R^\beta)(\bar{d}_R^l Q_L^i) + h.c. + \beta_R^{i\alpha}(\beta_R^{l\beta})^*(\bar{e}_R^\beta\gamma_\mu e_R^\alpha)(\bar{d}_R^i\gamma^\mu d_R^l) \\ &+ \frac{1}{2}\beta_L^{i\alpha}(\beta_L^{l\beta})^*(\bar{L}_L^\beta\gamma_\mu L_L^\alpha)(\bar{Q}_L^i\gamma^\mu Q_L^l) + \frac{1}{2}\beta_L^{i\alpha}(\beta_L^{l\beta})^*(\bar{L}_L^\beta\sigma^a\gamma_\mu L_L^\alpha)(\bar{Q}_L^i\sigma^a\gamma^\mu Q_L^l)].\end{aligned} \tag{8.7}$$

Here we have defined $C_U \equiv g_U^2/(4M_U^2)$, by reabsorbing the energy scale of Eq. (6.1) directly inside the WC.

8.2.2 The influence of U_1^μ on the flavour anomalies

In order to see the effect of the vector LQ U_1^μ on the flavour anomalies, the authors of [192,193] have developed the EFT approach to the $R(D^{(*)})$ and the $R(K^{(*)})$ ratios that we have described in Chapter 6. Let us examine the two cases separately.

For what concerns $R(D^{(*)})$, in this simplified model the vector LQ U_1^μ induce important contributions to these flavour observables at tree-level. Note that, in this sense, a sizable effect comes from the right-handed coupling $\beta_R^{b\tau}$ (defined in Eq. (8.6)). By recalling the discussion developed in Chapter 6, the easiest way to estimate the effect of U_1^μ to $R(D^{(*)})$ is to use the following approxiamte formulæ [192]:

$$R(D) \simeq R(D)^{SM} \times \left\{1 + 2C_U v^2 \,\mathrm{Re}\left[(1 - 1.5\eta_s(\beta_R^{b\tau})^*)\left(1 + \frac{V_{cs}}{V_{cb}}\beta_L^{s\tau} + \frac{V_{cd}}{V_{cb}}\beta_L^{d\tau}\right)\right]\right\}, \tag{8.8}$$

$$R(D^*) \simeq R(D^*)^{SM} \times \left\{1 + 2C_U v^2 \,\mathrm{Re}\left[(1 - 0.14\eta_s(\beta_R^{b\tau})^*)\left(1 + \frac{V_{cs}}{V_{cb}}\beta_L^{s\tau} + \frac{V_{cd}}{V_{cb}}\beta_L^{d\tau}\right)\right]\right\}, \tag{8.9}$$

where the factor $\eta_s \sim 1.8$ takes into account the running of the scalar operator in Eq.(8.7).

For what concerns instead $R(K^{(*)})$, they have to consider the U_1^μ contributions both at tree level and the one loop level. To simplify the discussion, in Eq. (8.6) they have assumed a vanishing coupling of the LQ to the electrons, thus U_1^μ will affect at tree level only the $b \to s\mu\mu$ and the $b \to s\tau\tau$ transitions. This translates into the following NP contribution to the WCs C_9 and C_{10} (see Eq. (6.6) for the definition of the corresponding operators) [192, 193]

$$C_9^{NP,\ell\ell} = -C_{10}^{NP,\ell\ell} = -\frac{2\pi}{\alpha V_{tb}V_{ts}^*}C_U v^2 \beta_L^{s\ell}(\beta_L^{b\ell})^*. \tag{8.10}$$

Note finally that there is also, as mentioned before, a loop level contribution to $b \to s\ell\ell$ transitions, that give rise to another NP contribution to C_9, namely [194]

$$C_9^{NP,loop} \simeq -\frac{1}{V_{tb}V_{ts}^*}\frac{2}{3}C_U v^2 \beta_L^{s\tau}(\beta_L^{b\tau})^* \log[m_B^2/M_U^2]. \tag{8.11}$$

Although not explicitly reviewed in this Thesis, note that the flavour structure (8.6) will influence and induce important contributions also to other low-energy processes in flavour physics, as for instance the leptonic $B_c \to \tau\nu$ and $B \to \tau\nu$ decays.

8.2.3 Summary plots

In Figure 8.1 the results of the very recent analysis in [193] of the flavour anomalies in this simplified U_1^μ model are shown. The authors have defined

$$\delta R(K^{(*)}) = \frac{R(K^{(*)}) - R(K^{(*)})^{SM}}{R(K^{(*)})^{SM}}, \quad \delta R(D^{(*)}) = \frac{R(D^{(*)}) - R(D^{(*)})^{SM}}{R(D^{(*)})^{SM}}, \tag{8.12}$$

where the theoretical estimates $R(D^{(*)})^{SM}$ correspond to the HFLAV estimates in Eq. (3.3), while the $R(K^{(*)})^{SM}$ ones have been read from [195]. For what concerns instead the experimental values, the $R(D^{(*)})$ ones correspond to the HFLAV averages in Eq. (3.2), while the $R(K^{(*)})$ ones are the LHCb measurements of these quantities [136, 137] (which are also shown in Figure 6.2). As clear from Figure 8.1, there is a good agreement between the model and the data for both the choices of $\beta_R^{b\tau}$ that have been studied in [193], namely $\beta_R^{b\tau} = 0$ (left panel) and $\beta_R^{b\tau} = -1$ (right panel). The authors comment also on the fact that the scenario with $\beta_R^{b\tau} = -1$ is a bit disfavoured than the one with $\beta_R^{b\tau} = 0$ since the theoretical expectation of $R(D^*)$ reported by HFLAV Collaboration is lower in mean value with respect to its experimental average. For the readers who are interested in this point, this is clear from the explicit fit results reported by the authors in Table 3.2 of [193].

In conclusion, note that in literature many other (more or less recent) similar studies are present, often with different flavour assumptions. See for instance [196–201] for the $R(D^{(*)})$ ratios, [202–209] for the $R(K^{(*)})$ ones and [210–213] for their combined explanation.

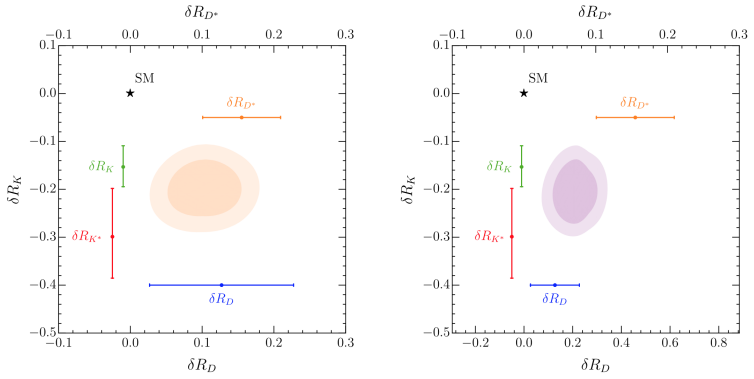

Figure 8.1: The coloured areas are the 1σ and 2σ regions preferred for explaining the $R(D^{(*)})$ and $R(K)$[1.1,6] anomalies. The authors have adopted, in the $R(D^{(*)})$ case, the theoretical and the experimental averages stated by the HFLAV Collaboration, see Eqs. (3.2)-(3.3). The orange area (left figure) corresponds to the choice $\beta_R^{b\tau} = 0$, while the purple one (right figure) to $\beta_R^{b\tau} = -1$. Taken from [193].

8.3 Possible UV completions of the LQs theory

To conclude this review about LQs, let us examine a couple of examples of UV completion of the theory, which is a very challenging topic. We know that LQs unify matter, pointing then towards possible gauge coupling unification theories [214–216]. It is thus necessary to develop a mechanism that can, in principle, unify the scalar LQs with the Higgs. This is not a simple task since the scalar LQs may, in principle, mediate proton decay, which is subjected to very strong constraints. In other

words, we have to ensure that the Higgs (which is a doublet of $SU(2)$), has to be light, while, at the same moment, an associated scalar LQ (which is, by construction, a triplet of $SU(3)$) has to be heavy enough to satisfy the bounds on the proton lifetime. This issue is often called the *doublet-triplet splitting problem*. The main difficulty here is that the doublet and the triplet live in the same representation, thus a large mass splitting between them is unnatural. So: which UV completion of the theory can ensure a solution to these problems?

A first possibility is offered by SUSY. From the point of view of the field content of a supersymmetric theory, each of the known fundamental particles of the SM has a so-called *superpartner*, whose spin differs from its one by 1/2 unit. This means that each fermion will have a scalar superpartner and viceversa. In the simplest realization of a theory with such a symmetry, called the *Minimal Supersymmetric Standard Model* (MSSM), this property brings to new 32 distinct masses corresponding to (yet) undiscovered degrees of freedom [217]. The link with the LQs is that the the scalar partners of all the quarks have the same quantum numbers of the LQs themselves. However, the MSSM is characterized by another fundamental property, the so-called *R-parity* or *matter parity* [218–222], which has the role of ensuring the conservation of the baryon and the lepton numbers as a postulate and *not* as an accidental symmetry, like it is in the SM. Again, this issue is a consequence of the experimental non-observation of the proton decay, as discussed for instance in [223–225]. Turning back to LQs, the unification of quarks and leptons within the SUSY framework requires the violation of the R-parity. These topics have been widely discussed in the literature, see for instance [226–236].

A second possible UV completion is offered, instead, by the CH framework, which we have deeply discussed in the previous Chapter 7. The idea is the following. As we have seen there, in these scenarios a new strongly-coupled sector breaks (spontaneously) a global symmetry and, thus, the Higgs arise as a composite pNBG. In the UV regime, this mechanism can be realized by introducing new heavy degrees of freedom, called the *hyper quarks* Ψ^i_{CH}, which are vector-like and are also charged under a (asymptotically free) gauge group, called the *hyper colour* $\mathcal{G}_{CH}$. Note that the hyper quarks have to respect a fundamental property, namely to be charged under the EW $SU(2)_L \times U(1)_Y$ group [237–244]. At this point, one can also hypothize that they are charged also under the $SU(3)$ group (as the LQs are). In this way, one can obtain the scalar S_1 and S_3 as pNGBs, or the vector U_1 and U_3 as composite vectors [245, 246].

Part III

Dark Matter and its connection with Flavour Physics

Chapter 9

The existence and the detection of Dark Matter

The majority of the amount of matter that constitutes our Universe is represented by non-baryonic matter, namely the so-called *Dark Matter* (DM). The existence of DM has been demonstrated by several astrophysical and cosmological probes, although at present its nature is completely unknown. Observations suggest, however, that whatever Dark Matter candidate has to respect the following physical properties and constraints:

- it can interact gravitationally and, more specifically, it must have the ability to form gravitational clusters;
- it must be stable on cosmological time scales, since we can observe it and, thus, it cannot have decayed by now;
- it has to be *dark*, then it cannot (or can very weakly) interact electromagnetically with photons;
- it cannot interact strongly with other particles, given the experimental bounds arising from Big Bang Nucleosynthesis (BBN);
- it must have the same relic density that has been measured by Planck, *i.e.* [247]

$$\Omega_{DM} h^2 = 0.11933 \pm 0.00091, \tag{9.1}$$

  where h represents the dimensionless Hubble constant.

In what follows, we will firstly review the main probes of the existence of Dark Matter and, considering that it can suffer only gravitational and weak interactions, the possible experimental ways to detect it.

9.1 Rotation curves of the galaxies

The first evidence for the existence of DM is represented by the distribution of the masses inside the clusters of galaxies. Following the same ideas of the articles of Zwicky on the subject [248, 249], the mass of a cluster can be derived through the *virial theorem*, according to which, assuming that the total moment of inertia of the galaxies is zero in the center of mass frame, the kinetic energy K and the potential energy U are related by the simple relation $2K + U = 0$. Moreover, if the mass distribution

is spherical, the potential energy can be expressed as $U = -GM^2/R$ (where M and R are the mass and the radius of the cluster of galaxies, respectively), so that the virial theorem can be written as

$$< v^2 >= \frac{GM}{R},$$

where $< v^2 >$ represents the velocity dispersion of the galaxies inside the cluster.

Thus, one would expect this physical quantity to behave as $< v^2 > \propto 1/R$ at large distances from the center of the cluster. This can be verified experimentally, since $< v^2 >$ is three times the velocity dispersion along the line of sight, which can be determined through the Hubble law. However, a typical result is shown in Figure 9.1. for the Triangulum Galaxy (or M33 galaxy). Here, the dashed line represents the naïve theoretical expectation, while the solid one corresponds to the effectively measured rotation curve. The only way to explain this behaviour is to assume the existence of much more matter than only the visible one, namely the DM, inside the observed galaxy.

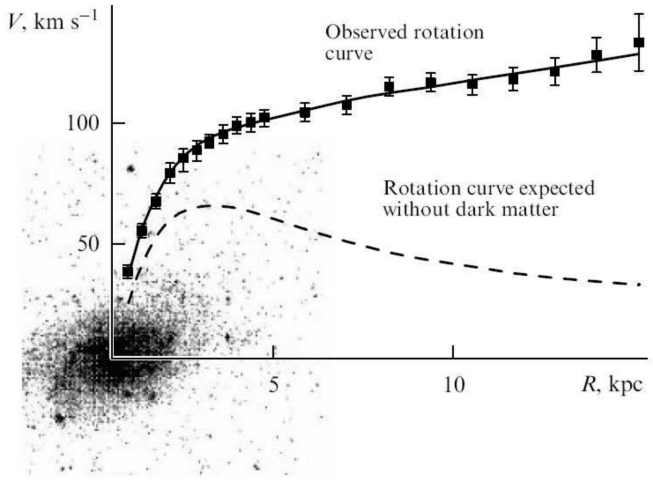

Figure 9.1: Rotation curve of the Triangulum Galaxy, taken from [250].

9.2 Gravitational lensing

A second important probe of the existence of Dark Matter is the so-called *gravitational lensing*, which is a consequence of one of the most important tests of General Relativity, *i.e.* the deflection of light.

It is well-known that the trajectory of a massless particle, let us say for example a photon, can be influenced and modified by the presence of a massive body. The resulting expression and numerical value of the deflection angle can be exactly computed in General Relativity, for instance in presence of a Schwarzschild background. From the historical point of view, the first observation of the deflection of light was developed in 1919 by Eddington, Dayson and Davidson during a solar eclypse. They measure the *apparent* position of a source behind the Sun during the eclypse, in which moment the light coming from this source was able to reach the Earth thanks to the huge reduction of the solar luminosity. They then computed the deflection angle of the light trajectory by comparing the measured position of the source with another one, observed precisely when the Earth is on the opposite side of its revolutionary orbit around the Sun.

The same physical phenomenon is at present often used to study the distribution of DM inside both galaxies and clusters. According to the level of distortion of the image observed, gravitational lensing is divided into two opposite regimes, *i.e.* the weak and the strong lensing [251]. The two different cases are graphically represented in Figure 9.2. The weak lensing, which is extremely common in the Universe, is generated in regions where the massive body (namely *the lens*) is located further away from the line of sight from the observer to the light source. For this reason, it produces only small image distortions and, in fact, can be detected only through a statistical study of a huge number of lensed sources. On the contrary, the strong lensing, which is much more rare than the weak one, occurs when the massive body is located very near to the line of sight, thus producing high magnifications and multiple images. Note that the strong lensing effects can readily be associated to specific and dense mass distributions, in fact they are often studied in order to detect DM halos.

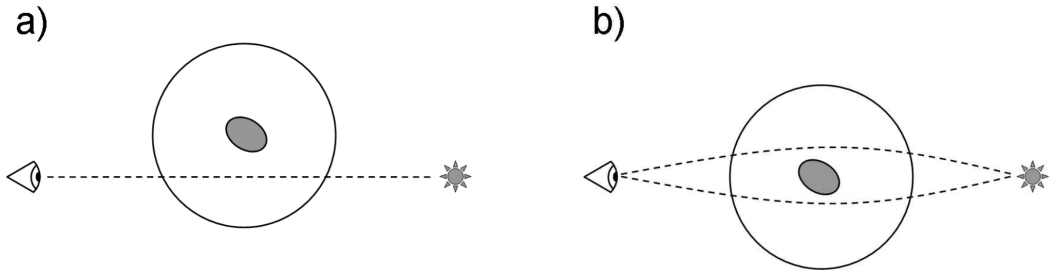

Figure 9.2: Graphical representations of weak (a) and strong (b) gravitational lensing. The lens is illustrated as a gray elliptical galaxy, surrounded by a DM halo (which extends to the outer circle). In the weak lensing case, the lens lies far from the line of sight (dashed line) between the observer (eye) and the light source (star), thus only a single image is produced, subject to mild magnification and distortion. On the contrary, in the strong lensing case the line of sight is aligned with the dense central ellipse. For this reason, the light from the source reaches the observer by following different paths, then generating separate images in the sky. Taken from [251].

9.3 Bullet Cluster

There is also another proof of the existence of Dark Matter, which can be considered direct and empirical, that has to be mentioned, namely the Bullet Cluster (1E0657-558). It represents an important example of colliding clusters. The majority of the baryonic mass present inside these clusters is in the form of intergalactic gas, which reached very high temperatures because of the collision. This increase of temperature has determined a huge emission of X-rays, which are detectable through a X-ray telescope. This is an observational strategy to detect the matter distribution of the colliding clusters and generates the pink area in Figure 9.3. At the same time, the total mass of the Bullet Cluster can be reconstructed by weak lensing, since both the clusters act like gravitational lenses, and thus detectable through an optical telescope. The corresponding matter distribution is represented by the blue area in Figure 9.3.

The entity of the pink and the blue areas allows one to state that a non-negligible tension exists between the distribution of ordinary matter and the total mass of the Bullet Cluster, as clearly shown in [252, 253]. A direct and natural explanation of this discrepancy is the existence of non-baryonic

matter inside the clusters. Note that the debate on this issue is still on-going. In fact, the theoretical expectation (that do not reproduce the observation) coming from the numerical cosmological simulations in the ΛCDM model seems not to be stable under the change of some properties of the codes themselves, such as the size of the simulated model box.

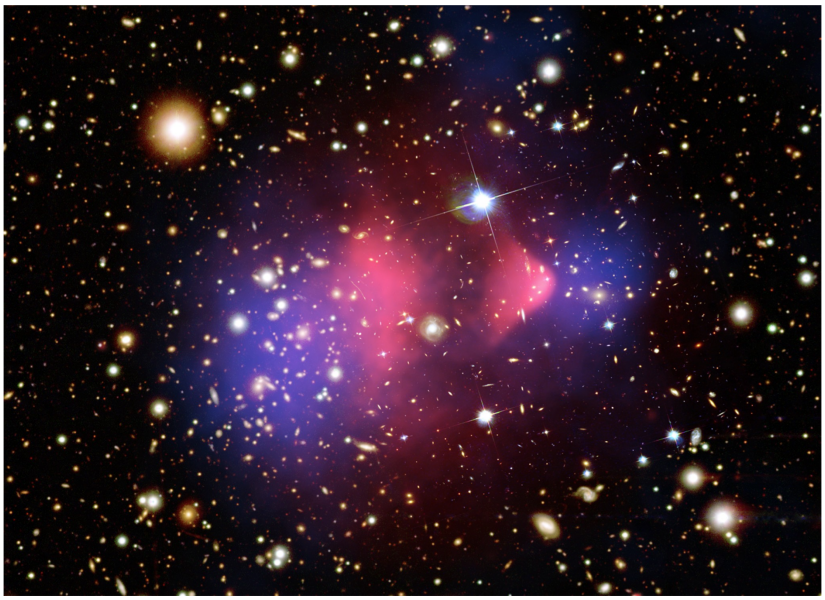

Figure 9.3: Image of the Bullet Cluster. See the text for details about the physical meaning of the pink and the blue areas.

9.4 An instructive example: the WIMP paradigm

Let us highlight that, both in what follows and in the following Chapters, we will specialize the discussion on the assumption of an *elementary* nature of DM [254]. This is not the unique possibility. In fact, there are other models that hypothize the existence of *extended* objects as DM. In this sense probably the best example is offered by the Primordial Black Holes [255–257], which have gained increasing interest in the recent few years [258–260] after the first detections of Gravitational Waves from black hole binaries.

At present, there exist many models of DM candidates of elementary nature which can explain the observed abundance of DM in our Universe (9.1) and which have all the properties discussed at the beginning of this Chapter. Among them, without any doubt the most famous one is represented by Weakly Interacting Massive Particles (WIMPs). In this Section, we will give an introduction to the physics underlying the WIMP scenario and we will then extend the discussion to two possible generalizations, *i.e.* the inclusion of bound states in Chapter 10 and the thermal decays of DM in Chapter 11.

In the standard scenario, one assumes that in the early universe WIMPs were produced in collisions between particles of the thermal plasma. In fact, in this phase of the history of the Universe the termperatures were very high, $T \gg m_\chi$ (where m_χ is the WIMP mass), thus the colliding SM particles pairs had enough energy to create efficiently WIMPs. Note that also the inverse reactions, *i.e.* the

ones that convert WIMPs into SM particles, were initially in equilibrium with the aforementioned production processes. To summarize, we are considering annilihation processes of the form DM DM $\leftrightarrow$ SM SM, whose common rate can be indicated as

$$\Gamma_{ann} = \langle \sigma_{ann} v \rangle n_{\chi}^{eq}, \tag{9.2}$$

where σ_{ann} represents the WIMP annihilation cross section and v is the relative velocity of the WIMPs. Moreover, n_{χ}^{eq} is the WIMP number density at the thermal equilibrium and, finally, the brackets indicate an average over the WIMP thermal distribution.

Now, during the expansion of the Universe the temperature decreased. In particular, WIMPs decoupled from the thermal plasma when $T < m_{\chi}$. Thus, in this phase their abundance lowered and lowered, until "freezing out" when the expansion rate of the Universe became larger than the WIMP annihilation rate, *i.e.* when $H > \Gamma_{ann}$, where H denotes the Hubble constant. Note that the expression *freeze out* has a precise meaning: when $H > \Gamma_{ann}$, the annihilation of WIMPs ceased and, thus, the number of WIMPs in a comoving volume remained approximately constant.

From a quantitative point of view, some numerical estimates can be developed by describing the evolution of the WIMP density through the Boltzmann equation, namely

$$\frac{dn_{\chi}}{dt} + 3Hn_{\chi} = -\langle \sigma_{ann} v \rangle \left[(n_{\chi})^2 - (n_{\chi}^{eq})^2 \right], \tag{9.3}$$

where t is time. An alternative formulation is also possible. From the law of entropy conservation, namely

$$\frac{ds}{dt} = -3Hs, \tag{9.4}$$

where s represents the entropy density, we can rephrase the Boltzmann equation (9.3) as

$$\frac{dY}{dx} = \frac{1}{3H} \frac{ds}{dx} \langle \sigma_{ann} v \rangle (Y^2 - Y_{eq}^2), \tag{9.5}$$

where we have defined the abundance $Y \equiv n/s$ and the variable $x \equiv m/T$. Recalling that in cosmology the entropy density is $s = 2\pi^2 g_* T^3/45$, where g_* counts the number of relativistic degrees of freedom, one can solve numerically the Boltzmann equation (9.5) by imposing the initial condition $Y = Y_{eq}$ at $x \simeq 1$, in order to compute the present WIMP abundance Y_0. In Figure 9.4 we show the final result for illustrative purposes. This plot allows us to finally summarize what said before. At the freeze out temperature (T_{fo}), since the WIMP annihilation rate becomes of the order of the Hubble expansion rate, the WIMP annihilation becomes negligible and, thus, the WIMP abundance per comoving volume reaches its final value. Note that in the standard cosmological scenario the WIMP freeze out temperature is $T_{fo} \simeq m_{\chi}/25$ [261].

In conclusion, this machinery allows us to compute the WIMP relic density, namely

$$\Omega_{DM} h^2 = \frac{\rho_{\chi}^0}{\rho_c^0} h^2 \simeq \frac{3 \cdot 10^{-27}}{\langle \sigma_{ann} v \rangle} \, \mathrm{cm}^3 \, \mathrm{s}^{-1}, \tag{9.6}$$

where ρ_{χ}^0 and ρ_c^0 are the present WIMP and critical density respectively. By recalling the observed value of $\Omega_{DM} h^2$ (9.1), one thus has that $\langle \sigma_{ann} v \rangle \simeq 3 \cdot 10^{-26} \mathrm{cm}^3 \, \mathrm{s}^{-1}$, which implies that we have obtained a cross section of weak strength for WIMPs. This scale of the annihilation cross section is what is expected in several BSM scenarios for a new particle with mass around the EW scale that interacts via the EW force. This coincidence is known as the *WIMP miracle* and has provided a very strong motivation for experimental WIMP searches.

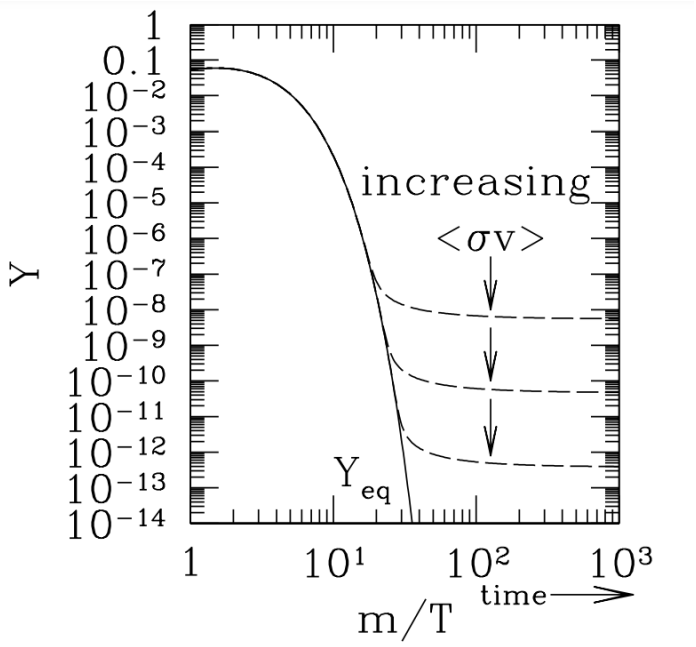

Figure 9.4: Typical evolution of the WIMP abundance in the early universe during freeze-out. Taken from [262].

9.5 How to detect Dark Matter?

Once convinced about the existence and the properties of DM, we can ask themselves which are the experimental strategies in order to detect it. This is a fundamental task, since measurements can in principle exclude theoretical models and candidates of DM which have been widely proposed in the past decades. For this reason, the search for DM is at present one of the most important experimental challenges for physics and can be distinguished in three distinct lines of research: Direct Detection, Indirect Detection and production at high-energy colliders. Let us explain the main ideas underlying these three experimental strategies, graphically illustrated in Figure 9.5.

9.5.1 Direct Detection of DM

The idea at the basis of Direct Detection (DD) strategies is the possibility to detect WIMP candidates through their scattering with nuclei in Earth-based experiments. Note that the same strategy can be implemented also for the detection of neutrinos through their elastic interaction with nuclei. For this reason, in fact, this kind of scattering constitutes a fundamental background for DD measurements, called *neutrino floor*, that cannot be eliminated because of the neutrino flux from the sky and that originates a signature that is indistinguishable from the one of a WIMP candidate. Very different techniques have been implemented over the time to detect the scattering of WIMPs on nuclei, namely scintillation light, which can be produced by de-excitation of nuclei, charge from ionization of atoms or phonons in bubble chambers. This is very challenging from the experimental point of view since, depending on the choice of the particular detection technique, a variety of target materials are employed in DD experiments. In the following Sections, we will analyse the impact of DD searches on two specific DM models.

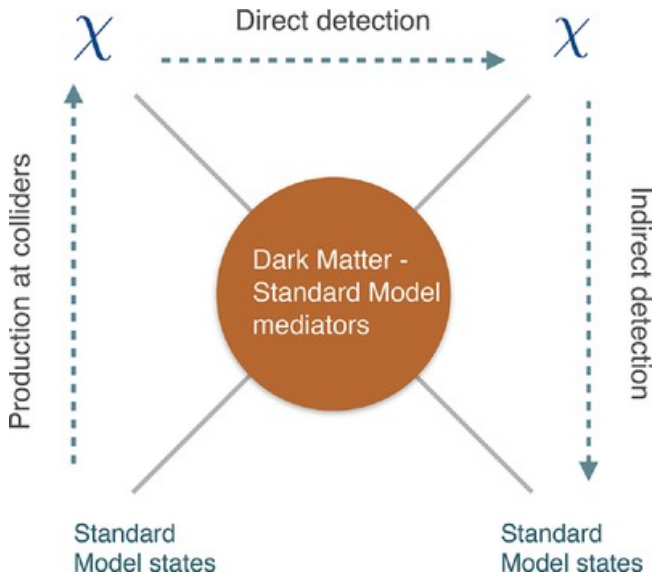

Figure 9.5: Schematic representation of the possible experimental strategies to detect DM particles. Taken from [263].

9.5.2 Indirect Detection of DM

Another intriguing possibility for DM discovery is offered by Indirect Detection (ID) techniques. As clear from Figure 9.5, the basic idea is to detect the products of annihilation processes involving DM particles, which can be in principle significant in our Universe. In other words, we should be able to detect an excess of SM particles above the standard astrophysical background and consequently address this issue towards the presence of DM annihilation processes.

Also in this case different experimental techniques can be implemented, namely we can look for different types od produced SM particles. The more attractive choice is constituted by the γ-rays, which can be emitted in different ways and thus produce very distinct spectral features. In this sense, photon observations can be primarily developed either with space telescopes and with ground-based Cherenkov detectors. We will see the impact of such kind of DM searches in the WIMP scenario. Note that other types of ID strategies can be complementary to γ-ray observations, namely the measurements of charged cosmic rays and/or neutrino telescopes.

9.5.3 Production of DM at colliders

The last possibility to detect DM is to directly produce it at colliders, given the interactions with the SM particles that each DM candidate has. Since by definition it is *dark*, such a particle is invisible to the detectors. Thus, the relevant signature that we can associate to DM is a large amount of missing momentum (or energy) when detecting one or more visible SM particles.

This kind of DM detection has to be considered complementary to DD and ID searches and is acquiring increasing interest in view of the realization of future high-energy colliders. Such machines, in fact, will be in principle able to exclude a broad class of models characterized by $\mathcal{O}$(TeV) mass scale for DM candidates, as for instance in the WIMPs case. For this reason, in the following Section we will study the discovery potential of WIMPs at a future high-energy lepton collider. Here we want to stress that this kind of study can be developed also at a high-energy hadron collider, in fact part of

the experimental program of FCC-hh will be devoted to DM production.

Chapter 10

A final word on WIMP Dark Matter

The possibility that DM is a new Weakly Interacting Massive Particle, thermally produced in the early Universe and freezing out through $2 \to 2$ annihilations into SM states, remains one of the main motivations for NP in the 10 GeV – 100 TeV range, as we have seen in the previous Chapter. A particularly interesting possibility within this framework, because of its minimality and predictive power, is that the DM is the lightest neutral component of one EW multiplet. In other words, we will add to the matter content of the SM the minimal number of new degrees of freedom, *i.e.* a fermionic or scalar n-plet of SU(2). We will consider firstly the real cases with odd n and zero hypercharge, since they automatically avoid strong constraints from direct detection searches, and then we will generalize the discussion to the complex cases. Note that the lightest particle in any such representation can be made stable by enforcing a symmetry acting on the DM only, with the exceptions of the multiplets for which such a symmetry arises accidentally in the renormalizable Lagrangian. However, we shall see that in general this can require additional assumptions about the completion of the theory at some high UV scale.

The predictive power of WIMP scenarios mainly relies in the fact that the only physical parameter to be determined is the mass of these new degrees of freedom. To achieve this goal, for any given n-plet, computing the EW annihilation cross-section in the early Universe allows to infer the WIMP cosmological abundance. By requiring it to match the measured value of the DM abundance today, $\Omega_{\rm DM}h^2 = 0.11933 \pm 0.00091$ [247], the mass of the n-plet can be univocally determined. These mass predictions are an essential input to assess if and how the future experimental program will be able to fully test the EW WIMP scenario. To be precise, note also that in the case of complex WIMPs, once the mass is fixed from the freeze-out predictions, the phenomenology of these degrees of freedom will depend essentially on two other parameters, as we will discuss in what follows.

For these reasons, in what follows we will firstly describe the EW WIMP paradigm and the main features of our freeze-out computation. Then, we will analyze the discovery potential of WIMPs at future experiments. To be more specific, on the one hand we will discuss the implications of our study for a future high-energy muon collider, while on the other hand we will re-examine the reach of DD and ID experiments in light of our findings.

My main contribution in this project concerns the study of Direct Detection searches. To be more specific, in both the real and the complex cases I have computed the cross sections of the scattering of DM with the nuclei and compared them with the reaches of present and future experiments. I have also contributed to the investigation of the discovery potential of WIMPs at muon colliders, through the study of the channels of production of one or two SM gauge bosons, as well as disappearing track searches. The details of all these computations can be found in the last three Sections of this Chapter.

10.1 Which WIMP?

Dark Matter spin	EW n-plet	M_χ (TeV)	$(\sigma v)^{J=0}_{\rm tot}/(\sigma v)^{J=0}_{\rm max}$	$\Lambda_{\rm Landau}/M_{\rm DM}$	$\Lambda_{\rm UV}/M_{\rm DM}$
Real scalar	3	2.53 ± 0.01	–	$2.4 \cdot 10^{37}$	$4 \cdot 10^{24}$*
	5	15.4 ± 0.7	0.002	$7 \cdot 10^{36}$	$3 \cdot 10^{24}$
	7	54.2 ± 3.1	0.022	$7.8 \cdot 10^{16}$	$2 \cdot 10^{24}$
	9	117.8 ± 15.4	0.088	$3 \cdot 10^{4}$	$2 \cdot 10^{24}$
	11	199 ± 42	0.25	62	$1 \cdot 10^{24}$
	13	338 ± 102	0.6	7.2	$2 \cdot 10^{24}$
Majorana fermion	3	2.86 ± 0.01	–	$2.4 \cdot 10^{37}$	$2 \cdot 10^{12}$*
	5	13.6 ± 0.8	0.003	$5.5 \cdot 10^{17}$	$3 \cdot 10^{12}$
	7	48.8 ± 3.3	0.019	$1.2 \cdot 10^{4}$	$1 \cdot 10^{8}$
	9	113 ± 15	0.07	41	$1 \cdot 10^{8}$
	11	202 ± 43	0.2	6	$1 \cdot 10^{8}$
	13	324.6 ± 94	0.5	2.6	$1 \cdot 10^{8}$

Table 10.1: Freeze-out mass predictions for WIMP DM in real EW multiplets with $Y = 0$. We provide a measure of how close the DM annihilation cross-section is to the unitarity bound for s-wave annihilation $(\sigma v)^{J=0}_{\rm max} = 4\pi/M^2_{\rm DM} v$. Approaching the unitarity bound, the error on the WIMP mass grows proportionally to the enhancement of the next-to-leading order (NLO) contributions estimated in Eq. (10.34). We derive the scale where EW gauge coupling will develop a Landau pole by integrating-in the WIMP multiplet at its freeze-out mass. The stability of both scalar and fermionic DM candidates can always be enforced by requiring a $\mathbb{Z}_2$ symmetry in the dark sector to forbid their decays. This symmetry forbids the scalar and fermionic 3-plets decay at renormalizable level as indicated by the *. The value of the UV cut-off $\Lambda_{\rm UV}$ gives an idea of the required *quality* for this symmetry to make DM stable and avoid stringent bounds on decaying DM ($\tau_{\rm DM} > 10^{28}$sec) [264]: a new physics scale lower than $\Lambda_{\rm UV}$ would require a $\mathbb{Z}_2$ to explain DM stability, while a cut-off higher than $\Lambda_{\rm UV}$ would make DM stability purely accidental.

We summarize here the logic of our WIMP classification, which is inspired by previous papers on the subject [265–269]. Requiring the neutral DM component to be embedded in a representation of the EW group imposes that $Q = T_3 + Y$, where $T_3 = {\rm diag}\left(\frac{n+1}{2} - i\right)$ with $i = 1, \ldots, n$, and Y is the hypercharge. At this level, we can distinguish two classes of WIMPs: *i*) real EW representations with $Y = 0$ and odd n; *ii*) complex EW representations with arbitrary n and $Y = \pm\left(\frac{n+1}{2} - i\right)$ for $i = 1, \ldots, n$. Within class *ii*), we can further distinguish two subclasses of complex WIMPs: *a*) complex representations $Y = 0$ and odd n; *b*) complex representation with $Y \neq 0$ with even n (odd n) for half-integer Y (integer Y). Note that the first subclass is a straightforward generalization of the models analyzed in [4] where the stability of the DM is guaranteed by an unbroken dark fermion number which can be gauged as was first done in Ref. [269].

10.1.1 Real WIMPs

Let us firstly focus on the first class of WIMPs, *i.e.* on class i), which is particularly interesting because the DM does not couple to the Z-boson at tree level, avoiding strong constraints from direct detection experiments. This choice brings to the EW multiplets listed in the first two columns of Table 10.1. At the renormalizable level, the extensions of the SM that we consider are

$$\mathcal{L}_{\rm s} = \frac{1}{2}\left(D_\mu \chi\right)^2 - \frac{1}{2}M_\chi^2\chi^2 - \frac{\lambda_H}{2}\chi^2|H|^2 - \frac{\lambda_\chi}{4}\chi^4\,, \tag{10.1}$$

$$\mathcal{L}_{\rm f} = \frac{1}{2}\chi\left(i\bar{\sigma}^\mu D_\mu - M_\chi\right)\chi\,, \tag{10.2}$$

for scalars and fermions, respectively, where $D_\mu = \partial_\mu - ig_2 W_\mu^a T_\chi^a$ is the covariant derivative, and T_χ^a are generators in the n-th representation of SU(2). The values of the masses of the WIMPs of interest are listed in Table 10.1 and we will explain precisely how they have been computed in what follows. Note also that the Lagrangian for the real scalar in Eq. (10.1) also admits quartic self-coupling and Higgs-portal interactions at the renormalizable level. As we will see, the latter is bounded from above by direct detection constraints and gives a negligible contribution to the annihilation cross-section.

The neutral component and the component with charge Q of the EW multiplet are splitted by radiative contributions from gauge boson loops. In the limit $m_W \ll M_{\rm DM}$ these contributions are non-zero and independent on M_χ. This fact can be understood by computing the Coulomb energy of a charged state at distance $r \gtrsim 1/m_W$ or the IR mismatch (regulated by m_W) between the self-energies of the charged and neutral states. The latter can be easily computed at 1-loop [270–272],

$$M_Q - M_0 \simeq \frac{Q^2\alpha_{\rm em}m_W}{2(1+\cos\theta_W)} = Q^2 \times (167 \pm 4)\ \text{MeV}\,, \tag{10.3}$$

with the uncertainty dominated by 2-loop contributions proportional to $\alpha_2^2 m_t/16\pi$. These have been explicitly computed in Ref.s [273, 274] giving a precise prediction for the lifetime of the singly-charged component, which decays to the neutral one mainly by emitting a charged pion with

$$c\tau_{\chi^+} \simeq \frac{120\ \text{mm}}{T(T+1)}\,, \tag{10.4}$$

where $2T+1 = n$. The suppression of the lifetime with the size of the EW multiplet can be understood in the $M_\chi \gg m_W$ limit where the mass splitting between the charged and neutral components is independent of n while the coupling to W is controlled by $\sqrt{T(T+1)/2}$. As we will discuss in what follows, the production of a singly charged DM component at colliders gives the unique opportunity of probing EW multiplets with $n = 3$ and $n = 5$ through disappearing tracks [265, 275–278].

Interestingly, the IR generated splitting from gauge boson loops is not modified substantially by UV contributions. The latter are generated only by dimension 7 (dimension 6) operators if the DM is a Majorana fermion (real scalar) and can be written as

$$\Delta\mathcal{L}_I \supset \frac{c_I}{\Lambda_{\rm UV}^{n_I}}\chi^a\chi^b(H^\dagger T^a H)(H^\dagger T^b H)\,, \tag{10.5}$$

with $n_I = 3, 2$ for $I = f, s$. This corresponds to a splitting $\Delta M_I \simeq c_I v^4/\Lambda_{\rm UV}^{n_I} M_\chi^{3-n_I}$ which is always negligible with respect to the residual error on the 2-loop splitting for $\Lambda_{\rm UV} \gtrsim 100$ TeV and $c_I \sim \mathcal{O}(1)$.

We now move to discuss DM stability. In the case of the EW 3-plet, the renormalizable operators $\chi H^\dagger H$ and χHL, for scalars and fermions, respectively, can induce fast DM decay. We assume these operators to be forbidden by a symmetry (e.g. a discrete $\mathbb{Z}_2$-symmetry) acting only on the

DM sector. For all the other n-plets with $n \geq 5$, instead, $\mathbb{Z}_2$-odd operators are accidentally absent at renormalizable level. Higher dimensional operators that break the $\mathbb{Z}_2$-symmetry are in general expected to be generated at the ultraviolet cut-off scale $\Lambda_{\rm UV}$. A lower bound on this energy scale is obtained by requiring the DM lifetime to be long enough to circumvent cosmological bounds [279,280] ($\tau_{\rm DM} \gtrsim 10^{19}$ sec) or astrophysical bounds on the decay products of decaying DM [264,281,282] ($\tau_{\rm DM} \gtrsim 10^{28}$ sec). We can then quantitatively measure the required *quality* of the $\mathbb{Z}_2$-symmetry by considering the ratio between the minimal $\Lambda_{\rm UV}$ allowed by the constraints and the WIMP freeze-out mass. By considering the operators of lowest dimension that can induce the decay of scalar and fermionic WIMPs for generic n, one can use a naive dimensional analysis to estimate $\Lambda_{\rm UV}$, assuming all the Wilson coefficients to be $\mathcal{O}(1)$, as given in Table 10.1 for all the relevant n-plets.

Requiring perturbativity of the EW gauge coupling above the WIMP thermal mass can provide an upper bound on the dimension of the SU(2) representation. Indeed, large SU(2) n-plets will make the EW gauge coupling run faster in the UV, eventually leading to a Landau pole. In Table 10.1 we provide the value of the scale $\Lambda_{\rm Landau}$ such that $g_2(\Lambda_{\rm Landau}) = 4\pi$. We integrate the RGE equations for the SM gauge couplings at 2-loops and integrate-in the n-plet at the WIMP thermal mass.[1] Comparing $\Lambda_{\rm Landau}$ and $\Lambda_{\rm UV}$, we see that the stability of the fermionic n-plets with $n \leq 5$ only depends on physics in a regime where the EW coupling is still perturbative. Instead, the stability of n-plets with $n > 5$ requires specifying a UV completion for the EW gauge group that does not give rise to the dangerous operators inducing the decay of scalar and fermionic WIMPs. In this sense, the Majorana 5-plet studied in Ref. [265] is special, because it can be made accidentally stable by raising the scale $\Lambda_{\rm UV}$, without any further assumption on the nature of the UV completion at $\Lambda_{\rm Landau}$. At this point, requiring $\Lambda_{\rm UV}/M_\chi \gtrsim 10$ to ensure perturbativity of the theory up to well above the WIMP mass would select $n \leq 9$ for fermions, and $n \leq 11$ for scalars. However, requiring a large hierarchy between $\Lambda_{\rm Landau}$ and M_χ is not necessary to ensure the calculability of thermal freeze-out, which depends only on EW processes at energies much below the DM mass. A more robust upper bound on the dimension of the SU(2) n-plets will be derived later by appropriately analyzing the s-wave unitarity of the annihilation cross-section. We anticipate here that this second bound will require $n \leq 13$ for both fermionic and scalar WIMPs.

10.1.2 Complex WIMPs

At this point, let us discuss the second class of WIMPs, *i.e.* the class *ii) b)*. Recall that we are referring to complex WIMPs with $Y \neq 0$, whose phenomenology differs substantially from the one with $Y = 0$. Here, we are going to focus the discussion only on the fermionic case for reasons of both space and clarity. This choice brings to the EW multiplets listed in the first two columns of Table 10.2. The discussion on the complex scalar WIMPs, instead, can be found in [12].

Now, the minimal Lagrangian for a fermionic complex WIMP with $Y \neq 0$ is:

$$\begin{aligned}
\mathcal{L}_{\rm D} &= \overline{\chi}\left(i\not{D} - M_\chi\right)\chi + \frac{y_0}{\Lambda_{UV}^{4Y-1}}\mathcal{O}_0 + \frac{y_+}{\Lambda_{UV}}\mathcal{O}_+ + h.c.\ , \\
\mathcal{O}_0 &= \frac{1}{2(4Y)!}\left(\overline{\chi}(T^a)^{2Y}\chi^c\right)\left[(H^{c\dagger})\frac{\sigma^a}{2}H\right]^{2Y}\ , \\
\mathcal{O}_+ &= -\overline{\chi}T^a\chi H^\dagger\frac{\sigma^a}{2}H\ ,
\end{aligned} \tag{10.6}$$

[1] Our results are compatible with the ones found in Ref. [283] (where χ is integrated-in at M_Z) given that $\Lambda_{\rm Landau}/M_{\rm DM}$ is approximately independent on $M_{\rm DM}$.

DM spin	n_Y	M_χ (TeV)	$\frac{\Lambda_{\rm Landau}}{M_\chi}$	$\frac{(\sigma v)^{J=0}_{\rm tot}}{(\sigma v)^{J=0}_{\rm max}}$	δm_0 [MeV]	$\frac{\Lambda^{\rm max}_{\rm UV}}{M_\chi}$	δm_{Q_M} [MeV]
DF	$2_{\frac{1}{2}}$	1.08 ± 0.02	$> M_{\rm Pl}$	-	0.22 - $2 \cdot 10^4$	10^7	4.8 - 10^4
	3_1	2.85 ± 0.14	$> M_{\rm Pl}$	-	0.22 - 40	60	312 - 1.6 $\cdot 10^4$
	$4_{\frac{1}{2}}$	4.8 ± 0.3	$\simeq M_{\rm Pl}$	0.001	0.21 - $3 \cdot 10^4$	$5 \cdot 10^6$	20 - 1.9 $\cdot 10^4$
	5_1	9.9 ± 0.7	$3 \cdot 10^6$	0.003	0.21 - 3	25	$10^3 - 2 \cdot 10^3$
	$6_{\frac{1}{2}}$	31.8 ± 5.2	$2 \cdot 10^4$	0.01	0.5 - $2 \cdot 10^4$	$4 \cdot 10^5$	100 - $2 \cdot 10^4$
	$8_{\frac{1}{2}}$	82 ± 8	15	0.05	0.84 - 10^4	10^5	440 - 10^4
	$10_{\frac{1}{2}}$	158 ± 12	3	0.16	1.2 - $8 \cdot 10^3$	6 $\cdot 10^4$	$1.1 \cdot 10^3$ - $9 \cdot 10^3$
	$12_{\frac{1}{2}}$	253 ± 20	2	0.45	1.6 - $6 \cdot 10^3$	4 $\cdot 10^4$	$2.3 \cdot 10^3$ - $7 \cdot 10^3$
CS	$2_{\frac{1}{2}}$	0.58 ± 0.01	$> M_{\rm Pl}$	-	4.9 - $1.4 \cdot 10^4$	-	4.2 - $7 \cdot 10^3$
	3_1	2.1 ± 0.1	$> M_{\rm Pl}$	-	3.7 - 500	120	75 - 1.3 $\cdot 10^4$
	$4_{\frac{1}{2}}$	4.98 ± 0.25	$> M_{\rm Pl}$	0.001	4.9 - $3 \cdot 10^4$	-	17 - 2 $\cdot 10^4$
	5_1	11.5 ± 0.8	$> M_{\rm Pl}$	0.004	3.7 - 10	20	650 - 3 $\cdot 10^3$
	$6_{\frac{1}{2}}$	32.7 ± 5.3	$\simeq 6 \cdot 10^{13}$	0.01	4.9 - $8 \cdot 10^4$	-	50 - $5 \cdot 10^4$
	$8_{\frac{1}{2}}$	84 ± 8	$2 \cdot 10^4$	0.05	4.9 - 6 $\cdot 10^4$	-	150 - $6 \cdot 10^4$
	$10_{\frac{1}{2}}$	162 ± 13	20	0.16	4.9 - $4 \cdot 10^4$	-	430 - $4 \cdot 10^4$
	$12_{\frac{1}{2}}$	263 ± 22	4	0.4	4.9 - $3 \cdot 10^4$	-	10^3 - $3 \cdot 10^4$

Table 10.2: Thermal masses of complex WIMPs with $Y \neq 0$, obtained including Sommerfeld enhancement and BSF, for Dirac Fermion (DF) and Complex Scalars (CS). The upper bound on n for even multiplets comes from the perturbative unitarity bound, as can be seen from the $(\sigma v)^{J=0}_{\rm tot}/(\sigma v)^{J=0}_{\rm max}$, where $(\sigma v)^{J=0}_{\rm max}$ is the maximal allowed annihilation cross section [284]. The loss of perturbativity is also signaled by the Landau pole $\Lambda_{\rm Landau}$ progressively approaching the DM mass. The upper bound on odd n with $Y = 1$ comes from the perturbativity of the higher dimensional operators generating δm_0 . For multiplets with $n > 5$ the largest UV cutoff $\Lambda^{\rm max}_{\rm UV}$ required to generate the minimal viable splitting is smaller than $10 M_{\rm DM}$. For each candidate we provide the allowed range for the mass splittings. The lower limit on δm_0 comes from strongest bound between direct detection and BBN as shown in Figure 10.1. The upper bound from the most stringent condition between DD constraint from PandaX-4T [285] and the perturbativity of the coupling of $\mathcal{O}_0$ in Eq. (10.6). Similarly, the lower limit on δm_{Q_M} comes from the BBN bound on the charged state decay rate, while the upper limit from the strongest limit between DD and the perturbativity of the coupling of $\mathcal{O}_+$ in Eq. (10.6).

where T^a is again a $\mathrm{SU}(2)_L$ generator in the DM representation. The main difference with respect to real WIMP case in Eq. (10.2) is that the renormalizable Lagrangian is no longer sufficient to make the DM model viable. In Eq. (10.6) we write the minimal amount of UV operators required to make the DM model viable. In principle, we can consider additional operators, obtained from the ones in Eq. (10.6) by adding a γ_5 inside the DM bilinear. However, one can demonstrate that these operators give subleading contributions both to the mass splittings, that we are going to define and discuss, and to the DD signals, that we will discuss at the end of this Chapter. Thus, in what follows we will neglect them.

The non-renormalizable operator $\mathcal{O}_0$ is required to remove the sizeable coupling to the Z boson of

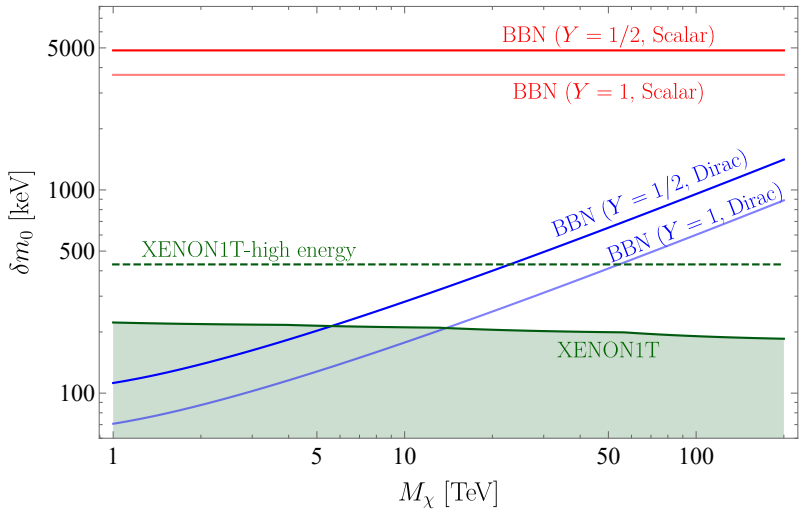

Figure 10.1: Summary of the lower bounds on the neutral mass splitting δm_0. The **dark green** shaded region is excluded by tree-level Z-exchange in Xenon1T [287] for both scalar and fermionic DM. The **dashed green** line shows what Xenon1T could probe by analyzing high recoil energy data. The **blue** and **red** lines are the BBN bounds on the splitting for fermionic and scalar DM respectively.

the neutral component χ_N of the complex EW multiplet

$$\mathcal{L}_Z = \frac{ieY}{\sin\theta_W \cos\theta_W} \overline{\chi}_N \not{Z} \chi_N \ . \tag{10.7}$$

This coupling would lead to an elastic cross section with nuclei already excluded by many orders of magnitude by present DD experiments [286]. After the EWSB, $\mathcal{O}_0$ induces a mixing between χ_N and χ_N^c. Replacing the Higgs with its VEV, $(H^{c\dagger})\frac{\sigma^a}{2}H$ is non-zero only if we pick $\sigma^a = \sigma^+$, so that the new (pseudo-Dirac) mass terms in the Lagrangian read

$$\begin{aligned} \mathcal{L}_m &= M_\chi \overline{\chi}_N \chi_N + \frac{\delta m_0}{4} \left[\overline{\chi}_N \chi_N^c + \overline{\chi^c}_N \chi_N\right], \\ \delta m_0 &= 4 y_0 c_{nY0} \Lambda_{\rm UV} \left(\frac{v}{\sqrt{2}\Lambda_{\rm UV}}\right)^{4Y} , \end{aligned} \tag{10.8}$$

where $c_{nYQ} = \frac{1}{2^{Y+1}(4Y)!} \prod_{j=-Y-|Q|}^{Y-1-|Q|} \sqrt{\frac{1}{2}\left(\frac{n+1}{2}+j\right)\left(\frac{n-1}{2}-j\right)}$ contains the normalization of $\mathcal{O}_0$ and the matrix elements of the generators. The mass eigenstates are Majorana fermions, χ_0 and $\chi_{\rm DM}$, with masses $M_0 = M_\chi + \delta m_0/2$ and $M_{\rm DM} = M_\chi - \delta m_0/2$, whose coupling to the Z boson is

$$\mathcal{L}_Z = \frac{ieY}{\sin\theta_W \cos\theta_W} \overline{\chi}_0 \not{Z} \chi_{\rm DM} \ . \tag{10.9}$$

The Z-mediated scattering of DM onto nucleons is no longer elastic and the process is kinematically forbidden if the kinetic energy of the DM-nucleus system in the center-of-mass frame is smaller than the mass splitting

$$\frac{1}{2}\mu v_{\rm rel}^2 < \delta m_0 \ , \quad \mu = \frac{M_{\rm DM} m_N}{M_{\rm DM} + m_N} \ , \tag{10.10}$$

where m_N is the mass of the nucleus, μ is the reduced mass and $v_{\rm rel}$ is DM-nucleus relative velocity. In particular, given the upper bound on the relative velocity $v_{\rm rel} < v_{\rm E} + v_{\rm esc}$, where $v_{\rm E} = 240$ km/sec is the Earth's velocity and $v_{\rm esc} = 600$ km/sec is the assumed escape velocity of DM in the Milky Way, the largest testable mass splitting is $\delta m_0^{\rm max} = 1/2\mu(v_{\rm E} + v_{\rm esc})^2$ which for Xenon nuclei gives $\delta m_0^{\rm max} \simeq 450$ keV. The splitting for a given recoil energy is

$$\delta m_0(E_R) = \sqrt{2 m_N E_R}(v_{\rm E} + v_{\rm esc}) - E_R \frac{m_N}{\mu} \ , \tag{10.11}$$

which explain why the maximal constrained splitting experimentally is $\delta m_0^{\rm max,exp} \simeq 240$ keV as shown in Fig. 10.1, given that Xenon1T [287] analyzed data only for $E_R < 40$ keV. Extending the range of Xenon1T to higher recoil energies would be enough to probe splitting up to $\delta m_0^{\rm max}$ as already noticed in Ref. [288, 289]. In principle, larger mass splittings can be reached using heavier recoil targets than xenon such as iodine in PICO-60 [290], tungsten in CRESST-II [291], $CaWO_4$ [292], $PbWO_4$ [293], ^{180}Ta [294], Hf [295] and Os [296]. However, these experiments currently do not have enough exposure to probe EW cross-sections.

A complementary bound on δm_0 comes from requiring that the decay $\chi_0 \to \chi_{\rm DM}$+SM happens well before BBN. The leading decay channels are $\chi_0 \to \chi_{\rm DM}\gamma$, $\chi_0 \to \chi_{\rm DM}\bar{\nu}\nu$ and $\chi_0 \to \chi_{\rm DM}\bar{e}e$ with decay widths

$$\Gamma_\gamma = \left(1 + \frac{1}{2}\log\left(\frac{m_W^2}{M_{\rm DM}^2}\right)\right)^2 \frac{Y^2 \alpha_2^2 \alpha_{\rm em}}{\pi^2} \frac{\delta m_0^3}{M_{\rm DM}^2} \ , \tag{10.12}$$

$$\Gamma_{\bar{\nu}\nu} \simeq 6\Gamma_{\bar{e}e} = \frac{G_F^2 \delta m_0^5 Y^2}{5\pi^3} \ . \tag{10.13}$$

The first process is induced by a dipole operator generated at 1-loop for fermionic DM as computed in [297]. The three body decays are instead induced at tree-level by the EW interactions both for fermionic and scalar DM. For fermionic DM, the dipole induced decay dominates the width in the mass range of interest. In order for these processes not to spoil BBN, we have to impose the following condition on the decay rate of χ_0:

$$\Gamma_{\chi_0} \equiv \Gamma_{\bar{\nu}\nu} + \Gamma_{\bar{e}e} + \Gamma_\gamma > \tau_{\rm BBN}^{-1} \ , \tag{10.14}$$

where $\tau_{\rm BBN}^{-1} = 6.58 \times 10^{-25}$ GeV. The lower bounds on the neutral mass splitting for fermions are shown in Fig. 10.1 together with those for scalars, which are explicitly computed in [12]. The main difference between scalars and fermions is that the former are typically more long lived due to the suppression of $\chi_0 \to \chi_{\rm DM}\gamma$. As a consequence, the BBN bounds are stronger for scalar WIMPs.

The operator $\mathcal{O}_+$ in Eq. (10.6) is necessary to make the DM the lightest state in the EW multiplet for all the n-plets where the hypercharge is not maximal. Recalling the discussion on real WIMPs, Eq. (10.3) can be generalized for non-zero hypercherge as [270–272]

$$\Delta M_Q^{\rm EW} = \delta_g \left(Q^2 + \frac{2YQ}{\cos\theta_W}\right) \ , \tag{10.15}$$

where $\delta_g = 167$ MeV and $Q = T_3 + Y$. This implies that negatively charged states with $Q = -Y$ are pushed to be lighter than the neutral ones by EW interactions. Notable exceptions are odd-n multiplets with $Y = 0$ and all the multiplets with maximal hypercharge $|Y_{\rm max}| = (n-1)/2$ where negatively charged states are not present. For these multiplets, having $y_+ = 0$ would be the minimal and phenomenologically viable choice.

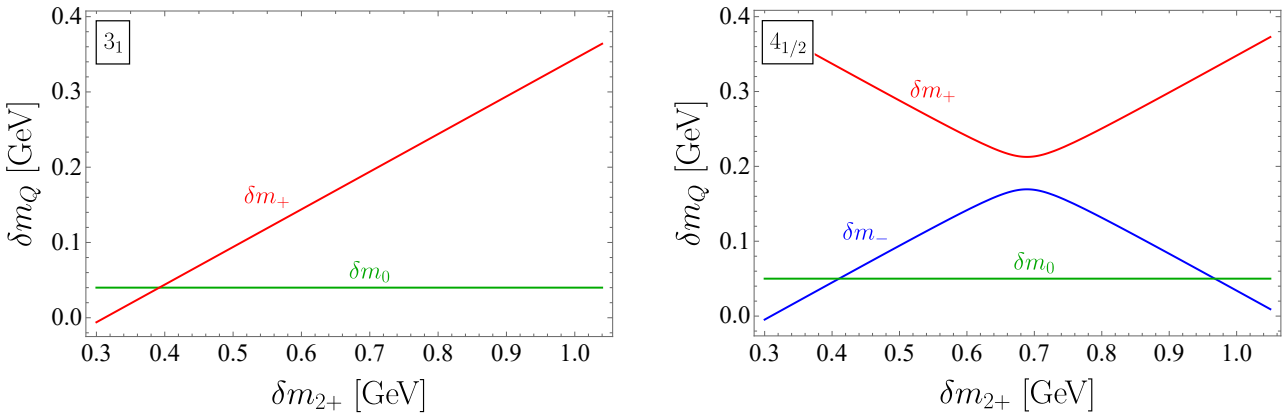

Figure 10.2: Mass splittings of 3_1 *(left)* and $4_{1/2}$ *(right)* as a function of δm_{2+}. In the 3_1 case, no mixing between the charged components of the multiplet can occur and δm_+ is a monotonic function of δm_{2+}. In the $4_{1/2}$ case, instead, because of the mixing induced by $\mathcal{O}_0$, the positively charged mass eigenstate χ_+ is always heavier than χ_-. The minimal splitting between them is of order δm_0.

Now, including the contribution of $\mathcal{O}_+$, the final splittings $\delta m_Q = M_Q - M_{\rm DM}$ between the DM and the charged components read

$$\delta m_Q = \frac{\delta m_0}{2} + \delta_g Q^2 + \text{sgn}(Q)\sqrt{\left(\frac{2Y\delta_g}{\cos\theta_W} - \frac{y_+ v^2}{4\Lambda_{\rm UV}}\right)^2 Q^2 + \frac{\delta m_0^2}{4}\frac{c_{nYQ}^2}{c_{nY0}^2}}\,, \tag{10.16}$$

where the presence of $\text{sgn}(Q)$ in Eq. (10.16) accounts for the presence of opposite charge states that are not related by charge conjugation, as implied by to the non-zero hypercharge of the considered WIMPs. Indeed, the second piece inside the square root comes from the mixing between χ_Q and χ^c_{-Q} induced by $\mathcal{O}_0$ and vanishes for $Q > (n-1)/2 - Y$.

The different charged-neutral mass splittings can all be written in terms of two independent splittings, which we choose to be δm_0 and δm_{Q_M}, where $Q_M \equiv Y + (n-1)/2$ is the largest electric charge in the multiplet. Since $c_{nYQ_M} = 0$, δm_{Q_M} is a monotonic function of y_+ and Eq. (10.16) can be inverted. In Fig. 10.2 we show as an example the mass splittings of 3_1 and $4_{1/2}$ as a function of δm_{2+}. In the former case, no mixing occur within the components of the multiplet and δm_+ is a monotonic function of δm_{2+}. For the $4_{1/2}$, instead, the mixing induced by $\mathcal{O}_0$ between the components with $Q = \pm 1$ makes the positively charged mass eigenstate χ_+ heavier than χ_-.

In this Chapter we will explore the parameter space spanned by δm_0 and δm_{Q_M}, fixing the thermal DM mass of every EW multiplet as shown in Table 10.2. Crucially, the operators inducing the splitting in Eq. (10.6) also generate new higgs-exchange contributions to the spin-independent scattering cross-section of DM on nucleons. Therefore, the current best upper limit on the DM elestic cross section onto nucleons set by PandaX-4T [285] translates into upper bounds on the neutral and charged splittings as reported in Table 10.2.

Charged-neutral splittings smaller than the EW one in Eq. (10.15) require a certain amount of fine-tuning between UV operators and the EW contribution. To quantify this we define the Fine Tuning (F.T.)

$$\text{F.T.} \equiv \max\left[\sum_I \frac{\text{d}\log\delta m_Q}{\text{d}\log\delta m_I}\right]\,, \tag{10.17}$$

where the index I runs over the three contributions in the definition of δm_Q in Eq. (10.16). Large values of F.T. imply a significant amount of cancellation between two or more parameters.

Let us now discuss the effects of UV contributions, as we have done for the real WIMP case. The EFT approach used to write Eq. (10.6) is meaningful only if the UV physics generating $\mathcal{O}_+$ and $\mathcal{O}_0$ is sufficiently decoupled from DM. When $\Lambda_{\rm UV}$ approaches the DM mass the cosmological evolution of the DM multiplet cannot be studied in isolation, since the heavy degrees of freedom populates the thermal bath at $T \simeq M_{\rm DM}$ and are likely to modify our freeze-out predictions. To avoid these difficulties we restrict ourselves to $\Lambda_{\rm UV} \geq 10 M_{\rm DM}$. This condition, together with the required inelastic splittings in Fig. 10.1, can be used to select the viable complex WIMPs. Starting from Eq. (10.8) and imposing $\delta m_0 > \delta m_0^{\rm min}$, we derive the viable window for $\Lambda_{\rm UV}$:

$$10 M_{\rm DM} < \Lambda_{\rm UV} \leq \left(\frac{4 y_0 c_{nY0} v^{4Y}}{2^{2Y} \delta m_0^{\rm min}} \right)^{\frac{1}{4Y-1}} . \tag{10.18}$$

We are now interested in estimating for which multiplets the viable window shrinks to zero. Setting $y_0 = (4\pi)^{4Y}$ in Eq. (10.18) (that is the largest value allowed by Naive Dimensional Analysis) we derive the values of n and Y having a non-zero cutoff window in Eq. (10.18). These are for both scalar and fermionic WIMPs $n_{1/2}$ multiplets with $n \leq 12$ together with the 3_1 and the 5_1 mupltiplets.

For what concerns the stability, the Lagrangian in Eq. (10.6) preserves the DM number and as a consequence the DM is automatically stable. Here we discuss whether the DM decays through gauge invariant interactions beyond those of Eq. (10.6) or can instead be accidentally stable. Throughout this discussion we not only require the DM lifetime to be long enough to circumvent cosmological bounds [279, 280] ($\tau_{\rm DM} \gtrsim 10^{19}$ sec), but also to satisfy the stronger astrophysical bounds on decaying DM [264, 281, 282] ($\tau_{\rm DM} \gtrsim 10^{28}$ sec).

For $2_{1/2}$ and 3_1 we can write renormalizable interactions $\overline{\chi^c} H e_R$ and $\overline{\chi} L^c H$ that break the DM number and lead to a fast DM decay. These EW multiplets require a DM number symmetry, for example a discrete $\mathbb{Z}_2$-symmetry acting only on the DM field to provide a viable DM candidate. For even multiplets with $Y = 1/2$ and $n > 2$ and for the 5_1 candidate, we can consider all the higher dimensional operators inducing DM decay, finding that we need at least $\Lambda_{\rm UV} > 10^{10} M_{\rm DM}$ for $\mathcal{O}(1)$ Wilson coefficients to preserve DM stability. This lower bound is incompatible with the upper bound on the UV physics scale required to generate the inelastic splitting δm_0. This result implies that DM stability requires the UV physics generating the neutral splitting in Eq. (10.8) to preserve DM number. As a result, none of the complex WIMPs with $Y \neq 0$ can be accidentally stable in the sense of Minimal Dark Matter [265].

10.2 WIMP cosmology: computation of freeze-out mass predictions

The determination of the DM thermal mass hinges on a careful computation of the DM annihilation cross-section in the non-relativistic regime. In particular, the potential generated by EW gauge boson exchange between DM pairs is attractive for isospins $I \lesssim \sqrt{2} n$ resulting into Bound State Formation (BSF) through the emission of an EW gauge boson in the final state. The energy of the emitted gauge boson is of the order of the Bound State (BS) binding energy $E_{B_I} \simeq \frac{\alpha_{\rm eff}^2 M_\chi}{4 n_B^2} - \alpha_{\rm eff} m_W$, where n_B is the BS energy level, $\alpha_{\rm eff}$ is the effective weak coupling defined in Eq. (10.27), and we neglected corrections of order m_W^2/M_χ^2. In the non-relativistic limit, and at leading order in gauge boson emission, the BSF process

$$\chi_i + \chi_j \to {\rm BS}_{i'j'} + V^a \tag{10.19}$$

is encoded in the effective dipole Hamiltonian described in Ref. [298, 299], which dictates the BS dynamics and it is written for completeness in Appendix E. In what follows, we will specialize the discussion on the real WIMP case, then we will highlight the main differences that hold in the case of complex DM candidates.

The BS dynamics relevant for DM freeze-out is well described by the unbroken phase of SU(2) so that the configuration of the DM pair can be decomposed into eigenstates of the isospin I of the pair

$$|\chi\chi\rangle_{II_z} = \mathcal{C}(II_z|ij)|\chi_i\chi_j\rangle, \;\; I_z \in \left[-\frac{I-1}{2}, \frac{I-1}{2}\right], \tag{10.20}$$

where $\mathcal{C}(II_z|ij)$ are the Clebsch-Gordan coefficients and I is the dimension of the isospin representation. Denoting with L and S the total angular momentum and the spin, the isospin-Lorentz structure of the dipole Hamiltonian enforces the following selection rules: *i*) $\Delta S = 0$ because the dipole Hamiltonian is spin-independent; *ii*) $|\Delta L| = 1$ because the dipole operator transform as a vector under rotations; *iii*) $|\Delta I| = 2$ because a single, G-parity odd weak boson is emitted.

Since we are dealing with real representations, spin-statistics imposes further restrictions on the allowed quantum numbers, depending on the fermionic or scalar nature of the wave function. In particular we have

$$(-1)^{L+S+\frac{I-1}{2}} = 1 \,, \tag{10.21}$$

which implies that for scalars $n_B s$ ($n_B p$) bound states, *i.e.* with $L = 0$ ($L = 1$), can exist only with even (odd) $\frac{I-1}{2}$, while for fermions odd (even) $\frac{I-1}{2}$ states with $L = 0$ are forced to have $S = 1$ ($S = 0$).

We are now ready to describe the system of coupled Boltzmann equations for the evolution of the number densities of DM and BS. Following [298], we will discuss how this coupled system can be reduced to a single equation for the DM number density with an effective annihilation cross-section. The Boltzmann equations for DM and BS read

$$z\frac{\mathrm{d}Y_{\rm DM}}{\mathrm{d}z} = -\frac{2s}{H}\langle\sigma_{\rm ann}v_{\rm rel}\rangle\left[Y_{\rm DM}^2 - (Y_{\rm DM}^{\rm eq})^2\right] - \frac{2s}{Hz}\sum_{B_I}\langle\sigma_{B_I}v_{\rm rel}\rangle\left[Y_{\rm DM}^2 - (Y_{\rm DM}^{\rm eq})^2\frac{Y_{B_I}}{Y_{B_I}^{\rm eq}}\right] \,, \tag{10.22a}$$

$$z\frac{\mathrm{d}Y_{B_I}}{\mathrm{d}z} = Y_{B_I}^{\rm eq}\left\{\frac{\langle\Gamma_{B_I,\rm break}\rangle}{H}\left[\frac{Y_{\rm DM}^2}{(Y_{\rm DM}^{\rm eq})^2} - \frac{Y_{B_I}}{Y_{B_I}^{\rm eq}}\right] + \frac{\langle\Gamma_{B_I,\rm ann}\rangle}{H}\left[1 - \frac{Y_{B_I}}{Y_{B_I}^{\rm eq}}\right] + \sum_{B_J}\frac{\langle\Gamma_{B_I\to B_J}\rangle}{H}\left[\frac{Y_{B_J}}{Y_{B_J}^{\rm eq}} - \frac{Y_{B_I}}{Y_{B_I}^{\rm eq}}\right]\right\} \,, \tag{10.22b}$$

where $B_{I,J,\ldots}$ labels the different bound states, $z = \frac{M_\chi}{T}$, s is the entropy density and $Y = \frac{n}{s}$ is the number density per co-moving volume.

The dynamics of a given BS B_I in the plasma is described by Eq. (10.22b) and depends on: *i*) its ionization rate $\langle\Gamma_{B_I,\rm break}\rangle$; *ii*) its annihilation rate into SM states $\langle\Gamma_{B_I,\rm ann}\rangle$; *iii*) its decay width into other bound states $\langle\Gamma_{B_I\to B_J}\rangle$. The ionization rate $\langle\Gamma_{B_I,\rm break}\rangle \equiv n_\gamma\langle\sigma_{I,\rm break}v_{\rm rel}\rangle$ encodes the probability of a photons from the plasma to break the BS B_I. Assuming thermal equilibrium, detailed balance relates the cross-section for the BS breaking $\langle\sigma_{I,\rm break}v_{\rm rel}\rangle$ to the BSF cross-section $\langle\sigma_{B_I}v_{\rm rel}\rangle$

$$\langle\Gamma_{B_I,\rm break}\rangle = \frac{g_\chi^2}{g_{B_I}}\frac{(M_\chi T)^{\frac{3}{2}}}{16\pi^{\frac{3}{2}}}e^{-\frac{E_{B_I}}{T}}\langle\sigma_{B_I}v_{\rm rel}\rangle \,, \tag{10.23}$$

where g_{B_I} and g_χ count the number of degrees of freedom of the bound state B_I and of the DM multiplet, respectively. If either the BS decay or the annihilation rate satisfies $\Gamma \gg H$, we can neglect the l.h.s. in Eq. (10.22b), obtaining algebraic relations between the DM and the BS yields.

Finally, by plugging these relations into Eq. (10.22a), we arrive at the final form of the DM Boltzmann equation

$$\frac{\mathrm{d}Y_{\rm DM}}{\mathrm{d}z} = -\frac{\langle\sigma_{\rm eff} v_{\rm rel}\rangle s}{Hz}(Y_{\rm DM}^2 - Y_{\rm DM}^{\rm eq,2}) \ , \tag{10.24}$$

where

$$\langle\sigma_{\rm eff} v_{\rm rel}\rangle \equiv S_{\rm ann}(z) + \sum_{B_J} S_{B_J}(z), \tag{10.25}$$

and we defined the effective cross-section as the sum of the direct annihilation processes, $S_{\rm ann}$, and the ones which go through BSF, S_{B_J}. In particular, $S_{\rm ann}$ can be written as

$$S_{\rm ann} = \sum_I \langle S_E^I \sigma_{\rm ann}^I v_{\rm rel}\rangle \ , \tag{10.26}$$

where $\sigma_{\rm ann}^I$ is the hard cross-section for a given isospin channel I, S_E^I is the Sommerfeld enhancement (SE) of the Born cross-section, and $v_{\rm rel}$ is the relative velocity of the two DM particles. In the limit of small relative velocity between the DM particles (but larger than m_W/M_χ), the SE factor can be approximated as

$$S_E^I \approx \frac{2\pi\alpha_{\rm eff}}{v_{\rm rel}} \ , \quad \text{where} \quad \alpha_{\rm eff} \equiv \frac{I^2 + 1 - 2n^2}{8}\alpha_2 \ . \tag{10.27}$$

The finite mass effects modify the behavior of the SE at $v_{\rm rel} \lesssim m_W/M_\chi$ and are included in our full computation (see Ref. [300] for explicit formulas). However, Eq. (10.27) will be enough to estimate the behavior of the SE at the temperatures most relevant for freeze-out.

Analogously, we can factorize the BSF processes as

$$S_{B_J} = \sum_{I,l} \langle S_E^I S_{B_J}^{I,l}\rangle R_{B_J} \ , \tag{10.28}$$

where $S_{B_J}^{I,l}$ is the "hard" BSF cross-section of the state B_J starting from a free state with angular momentum l and isospin I multiplied by the SE factor of that particular isospin channel as defined in Eq. (10.27). Explicit expressions for this can be found in Ref. [298, 299]. R_{B_J} gives instead the effective annihilation branching ratio into SM states which depends on the detailed BS dynamics (*i.e.* annihilation, ionization and decay). In particular, R_{B_J} approaches 1 once the temperature of the plasma drops below the binding energies of the bound states involved in the decay chains. In the case of a single BS, R_{B_J} takes a rather intuitive form

$$R_{B_J} = \frac{\langle\Gamma_{\rm ann}\rangle}{\langle\Gamma_{\rm ann}\rangle + \langle\Gamma_{\rm break}\rangle} \ , \tag{10.29}$$

which applies to $1s_I$ and $2s_I$ BS with $I \leq 5$. The latter, once formed, annihilate directly into pairs of SM vectors and fermions, with rates $\Gamma_{\rm ann} \simeq \alpha_{\rm eff}^5/n_B^2 M_\chi$. These BS together make up for more of the 50% of the BSF cross-section. Obviously, more complicated examples of BS dynamics can be developed for largest representations.

While the effect of BSF has already been computed for the fermionic 5-plet in Ref. [298], here we include it *for the first time* for all the real WIMP candidates with $n \geq 7$. For larger EW multiplets, we find the relative effect of BS dynamics on the total cross-section increases, as can be seen from Fig. 10.3. This is the consequence of two effects: *i*) the binding energy grows at large n, suppressing the ionization rate with respect to the annihilation one; *ii*) at larger n the number of attractive channels increases and thus the BS multiplicity per energy level grows linearly with n. For example,

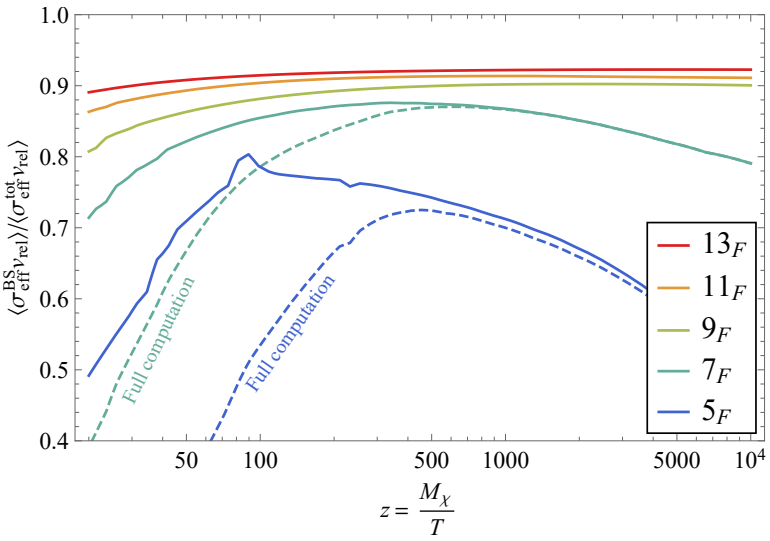

Figure 10.3: Effective cross-section for BSF normalized over the total annihilation cross-section as a function of $z = M_\chi/T$ assuming vanishing ionization rates, *i.e.* $R_{\rm BS} = 1$ (see Eq. (10.28) and below). The dashed lines for the real fermionic 5-plet (dark blue) and 7-plet (cyan) show the deviation of the real bound state dynamics from the approximation of vanishing ionization rates. For $n > 5$ the error due to the $R_{\rm BS} = 1$ is subdominant compared to the virtual and real effects at NLO in gauge boson emission.

for $n = 5$ the attractive channels have $I = 1, 3, 5$, for $n = 7$ BS with $I = 7, 9$ can also form. The relevance of these higher isospin channels was not recognized in [301], where only the $I = 1, 3$ channels were included, significantly underestimating the thermal mass already for $n = 7$. As we increase the dimension of the multiplet, the bound states become more tightly bounded and the effect of the ionization rate becomes smaller. This can be explicitly seen from Eq. (10.23) where the binding energy controls the Boltzmann suppression of the ionization rate. For this reason, we only account for the detailed BS dynamics for $n \leq 7$ while for $n > 7$ we set the annihilation branching ratios to 1. The final results can be found in Table 10.1.

For what concerns the uncertainties associated to our freeze-out mass predictions, we have estimated the error on the WIMP mass due to this approximation by comparing its effect on the thermal masses of 5-plet and the 7-plet against the full computation. We find a shift in mass $\Delta M_{DM} \simeq 5$ TeV for both $n = 5$ and $n = 7$ resulting in a smaller relative error for $n = 7$, as expected. We keep 5 TeV as an estimate of the error induced by this approximation for the larger multiplets. As we will discuss in what follows, the uncertainty for $n \geq 7$ will be anyhow dominated by the next-to-leading order (NLO) contributions to the SE which are not included here. Let us also comment on the theory uncertainty on the mass prediction for the 5-plet. This is dominated by the approximate treatment of EW symmetry breaking effects in computation of the BSF cross-sections. The SU(2)-symmetric approximation fails once the DM de Broglie wavelength becomes of the order of m_W (i.e. for $z \simeq 10^4$ for $n \geq 5$). After the EW phase transition, Coulomb and Yukawa potentials appear at the same time so that employing either the Coulomb or the Yukawa centrifugal correction to the SE (see Ref. [300]) overestimate and underestimate, respectively, the freeze out cross-section. This gives us a rough way of determining the theory uncertainty: *i*) to set the lower bound on the freeze-out mass we include BSF in $\sigma_{\rm eff}$ until $z = 10^4$ with the centrifugal correction coming from the Yukawa; *ii*) to set the upper bound we push the effect of BSF, neglecting the vector masses in the centrifugal correction,

to arbitrary large values of z. We observe that the abundance saturates already for $z \approx 10^5$. This procedure gives the uncertainty for the 5-plet in Table 10.1 which is different than the one quoted in Ref. [298], where the BS contribution was switched off at $z = 10^4$, underestimating the effect of BSF.

To conclude this Section, we discuss how this picture changes for complex WIMPs. First of all, in principle the UV mass splittings can affect the freeze-out computation, precisely in two ways: i) they directly contribute to the DM annihilation cross-section into Higgs bosons, ii) they generate a Higgs-mediated Yukawa potential, thus affecting the Sommerfeld enhancement. However, we expect that, for the numerical values of our interest, the splittings do not impact the freeze-out predictions contained in Table 10.2. To be more specific, although in principle the thermal mass becomes a function of δm_0 and δm_+, in order to compute the thermal masses we assume the minimal value allowed for δm_0, where the effect of the splitting is safely negligible, and account for the dependence on δm_+ in the theoretical uncertainty. Moreover, contrarily to the real WIMP case, there are different selection rules selecting the bound states allowed by symmetries. In the real case Eq. (10.21) has to be verified, while for complex WIMPs the bound states are of the form $\overline{\chi}\chi$, thus the selection rule (10.21) no longer applies. The BSF cross-section can be computed in the $SU(2)_L$ symmetric limit with good approximation and scales as

$$\sigma_{B_I} v_{\rm rel} \simeq \frac{E_{B_I} a_B}{M_{\rm DM} n^2} (\alpha_{2,\rm eff} S_E^{I\pm 2} + Y^2 \alpha_Y S_E^I) \ , \tag{10.30}$$

where the first and second term account for weak and hypercharge vector boson emission.

For what concerns the estimation the the theoretical uncertainties, also in this case neglecting BS ionizations is a good approximation for large EW multiplets. As for the real case, we estimate the error induced by this approximation at the 5 TeV level. Furthermore, in the symmetric limit the effect of the mass splittings generated after EWSB are not taken into account. In particular, they make the heavier components of the multiplet decouple earlier than the lighter ones, thus reducing the cross-section. In order to estimate the error due to this approximation, we compute the thermal mass first setting to zero σ_{B_I} for $T < \max \delta m_Q$ and then including BSF until the DM abundance saturates. These two effects are the dominant sources of error for $n \lesssim 8$.

10.3 The WIMP Unitarity Bound

We now analyze the constraint of perturbative unitarity on the annihilation cross-section, including bound state formation. The perturbative unitarity of the S-matrix sets an upper bound on the size of each partial wave contribution to the total annihilation cross-section [2]

$$(\sigma_{\rm eff} v_{\rm rel})^J \leq \frac{4\pi(2J+1)}{M_\chi^2 v_{\rm rel}} \ , \tag{10.31}$$

where $\vec{J} = \vec{L} + \vec{S}$ is the total angular momentum. The stronger inequality comes from the s-wave channel (i.e. $J = 0$) which can be written as

$$(\sigma_{\rm ann} v_{\rm rel}) + \sum_{B_J} f^0_{B_J} (\sigma_{B_J} v_{\rm rel}) \leq \frac{4\pi}{M_\chi^2 v_{\rm rel}} \ , \tag{10.32}$$

where $f^0_{B_i}$ selects the BS contributions that can be formed by $J = 0$ initial wave. As discussed in the previous Section, the BSF contribution is larger for complex WIMPs when compared with the real case due to the larger multiplicity of bound states that can be formed.

[2] This constraint was derived for e^+e^- annihilations in [302, 303] and then used for the first time in the DM context in [284]. It can be checked that this constraint is not modified in the presence of long range interactions [304].

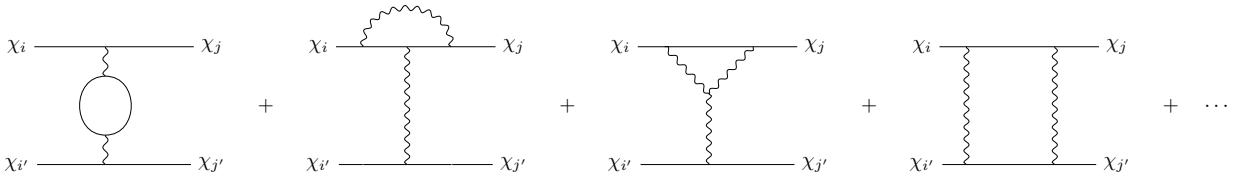

Figure 10.4: Examples of Feynman diagrams contributing at NLO to the non-relativistic potentials as estimated in Eq. (10.34).

For a scalar WIMP selecting the s-wave implies $L = 0$, and only BS in p-orbitals can contribute to the s-wave cross-section with $f^0_{\rm BS} = 1$. The spin statistics of the wave function in Eq. (10.21) forces these BS to have odd $(I-1)/2$. In practice, the s-wave unitarity bound for scalars is determined solely by the SE. For fermionic WIMP selecting the s-wave implies the same selection rules of the scalar when $S = 0$. Additional contributions arise from $S = 1$ s-orbital states, whose isospin must be odd due to Fermi statistics. In this case, the projection onto the $J = 0$ wave gives $f^0_{\rm BS} = \frac{1}{9}$. Solving the constraint in Eq. (10.32) we find that s-wave unitarity is violated for $n \geq 15$ for both fermion and scalar WIMPs. In both cases the s-wave cross-section is largely dominate by the SE. We checked that a similar constraint can be obtained by looking at the $p-$wave unitarity, where the cross-section is instead dominated by the formation of $1s$ BS.

The selection rules that regulates the BS dynamics derive from the dipole Hamiltonian which is written for completeness in Eq. (E.1). These selection rules are only broken by NLO contributions in gauge boson emission which can be estimated as

$$\frac{\Delta\sigma^{\rm NLO}_{\rm BSF}}{\sigma^{\rm LO}_{\rm BSF}} \sim \frac{\alpha^3_{\rm eff}}{64\pi} \,, \tag{10.33}$$

where the extra $\alpha^2_{\rm eff}$ correctly accounts for the phase space suppression in the limit of small velocities as detailed in Appendix E. As a result, the LO selection rules apply all the way till the breaking of perturbative unitarity.

Interestingly, the upper bound on n from perturbative unitarity derived from Eq. (10.32) is significantly stronger than the one derived from the perturbative unitarity of the Born cross-section which is violated for $n \geq 38$ (i.e. $\alpha_{\rm eff} \geq 4\pi$). This suggests that because of SE, the ratio between the NLO and the LO cross-section should appreciably deviate from the NDA scaling of the Born cross-section: $\sigma^{\rm NLO}_{\rm Born}/\sigma^{\rm LO}_{\rm Born} \sim \alpha_{\rm eff}/4\pi$. Estimating the NLO correction to the potentials controlling the SE we indeed get

$$\frac{\Delta V_{\rm NLO}}{V_{\rm LO}} \sim \frac{\alpha_{\rm eff}}{4\pi} \log\left(\frac{m_W\sqrt{z}}{M_\chi}\right) \,, \tag{10.34}$$

where the NLO potential is resumming ladder diagrams like the ones in Fig. 10.4, and where we substituted the de Broglie length $1/Mv_{\rm rel} \approx \sqrt{z}/M_\chi$ as the typical lenght scale for the annihilation process. Our estimate above matches the explicit NLO computation of the SE for the 3-plet in Ref. [305]. Requiring this correction to be $\lesssim 1$ across the freeze-out temperatures leads to a similar upper bound on n than the one inferred from perturbative unitarity.

We use the estimate above to assess the theory uncertainty on the WIMP thermal masses in Table 10.1. Indeed, Eq. (10.34) results in a correction to the Sommerfeld factor S_E, which affects both $S_{\rm ann}$ and S_{B_J} as introduced in Eq. (10.24). We find that neglecting the NLO contribution dominates

the DM mass theory uncertainty for $n \geq 7$. The uncertainty grows as we increase the dimensionality of the multiplet becoming as large as $\mathcal{O}(30\%)$ for $n = 13$.

At this point, following the logic of Section 9.5, we are interested in the possible experimental detections of the EW multiplets listed in Table 10.1. We will firstly focus our attention on this possibility at future high-energy lepton collider, then we will specialize the discussion on ID and DD searches.

10.4 WIMPs at high energy lepton colliders

We now look at the possible detection strategies for direct production of WIMPs at collider experiments. From the results in Table 10.1 one can immediately see that DM masses $\gtrsim 50$ TeV are required to achieve thermal freeze-out for EW multiplets with $n > 5$. Pair-production of these states would require center-of-mass energies exceeding 100 TeV, which are unlikely to be attained at any realistic future facility. On the other hand, multiplets with $n \leq 5$ have thermal masses in the few TeV range, potentially within the reach of present and future colliders.

Direct reach on these DM candidates at hadron colliders is limited by the absence of QCD interactions for the DM candidates, which can be produced only via EW interactions. As such the limits at the LHC (see e.g. [306]) are rather far from the interesting thermal mass targets and only a future pp collider may have the reach for some low-n candidates if collisions around 100 TeV can be attained [276, 307, 308]. Lepton colliders tend to have reach mainly through indirect effects, e.g. the modification of the angular distributions in simple $f\bar{f}$ production at center of mass energies below the threshold to produce the DM pair. The reach in this case is up to masses a factor a few above the center of mass energy [309, 310].

A very-high-energy lepton collider, such as a muon collider, would be the perfect machine to hunt for these WIMPs, due to its large center-of-mass energy, relatively clean collision environment, and the capability of pair-producing weakly interacting particles *up to kinematical threshold*. Here we consider in particular a future muon collider with center-of-mass energy of 10 TeV or more and the baseline integrated luminosity of [311]

$$\mathcal{L} \simeq 10 \text{ ab}^{-1} \cdot \left(\frac{\sqrt{s}}{10 \text{ TeV}} \right)^2 . \tag{10.35}$$

While such a machine is currently not feasible, various efforts to overcome the technological challenges are ongoing. Early developments on machine performances [312,313] found the luminosity Eq. (10.35) to be achievable for $\sqrt{s} \lesssim 6$ TeV, and further development to push it to larger energies is currently in progress.

We consider various search channels for both real and complex EW n-plets with $n \leq 5$, and determine the minimal center-of-mass energy and luminosity required to directly probe the freeze-out predictions. Firstly, we detail the prospects for the observation of DM as undetected carrier of momentum recoiling against one or more SM objects. We systematically study all the "mono-V" channels, where DM is recoiling against a SM gauge boson $V = \gamma, Z, W$. We also investigate double vector boson production, that we dub "di-V" channels, where requiring a second SM gauge boson in the final state could help ameliorating the sensitivity. Secondly, we study the reach of disappearing track searches – which are robust predictions of WIMPs in real EW representations – recasting the results of [277]. Notice that our study is in principle applicable both to high-energy $\mu^+\mu^-$ and e^+e^- colliders, even though soft QED radiation, beam-strahlung, and the presence of beam-induced backgrounds could affect the results in different ways.

Let us notice that, for what concerns the complex WIMP candidates, we will focus on the collider reach for the complex fermionic doublet ($2_{1/2}$) and the complex fermionic triplet (3_1) WIMPs, that are the lightest WIMPs and have the greater chance to be discoverable at $\sqrt{s} \leq 10$ TeV. Theoretically, these candidates are the most minimal complex WIMPs as they have maximal hypercharge and the neutral component is automatically the lightest one at the renormalizable level. The only required higher dimensional operator is $\mathcal{O}_0$ which generates the inelastic splitting in Eq. (10.8). In this sense, we will present collider results in the *minimal splitting scenario*, that is when the mass splittings are chosen to be the smallest possible allowed by the requirements of the previous Sections. We thus set $\delta m_0 = 250$ keV for both the complex doublet and the complex triplet WIMPs. Note also that, in this minimal setup, $2_{1/2}$ and 3_1 stand out as the only two multiplets where the DM is automatically the lightest state with a splitting with the $Q = 1$ state given by the pure EW splitting in Eq. (10.15) that is 354 MeV for $2_{1/2}$ and 542 MeV for 3_1.

The projections for direct production derived here have to be contrasted with similar studies in the context of future high energy proton machines [275, 276] (which are limited by the partial reconstruction of the collision kinematics) or electron-positron machines [314, 315] (which are limited by the moderate center-of-mass energy and hence more effective to hunt for lighter DM candidates). Complementary studies have also considered indirect probes of WIMPs at future high energy lepton colliders, focusing on the modifications of Drell-Yan processes [310]. Given the freeze-out masses of Table 10.1, EW n-plets with $n > 5$ are beyond the reach of any realistic future collider both *directly* and *indirectly*, even though a definitive statement about indirect observables would require further studies.

10.4.1 WIMPs as missing momentum

We perform a full study of the different channels to observe DM as undetected carrier of momentum. The generic strategy is to measure a hard SM particle or a set of particles X recoiling against a pair of invisible objects,

$$\ell^+\ell^- \to \chi^i\chi^j + X\,. \tag{10.36}$$

Notice that we treat all the components χ^i of the EW multiplet as invisible, assuming the soft decay products of the charged states to be undetected. Additional soft SM radiation is also implicit in Eq. (10.36). The prospects for the "mono-photon" topology at a future muon collider have been already studied in [278]. Here, we want to extend this analysis by enlarging the set of SM objects recoiling against the invisible DM multiplets.

Mono-V. We start by considering "mono-V" scattering processes where $V = \gamma, Z, W$ is a generic EW gauge boson that accompanies the production of χ states from the n-plet,

$$\text{mono-}\gamma\text{:} \qquad \ell^+\ell^- \to \chi^i\chi^{-i} + \gamma\,, \tag{10.37}$$

$$\text{mono-}Z\text{:} \qquad \ell^+\ell^- \to \chi^i\chi^{-i} + Z\,, \tag{10.38}$$

$$\text{mono-}W\text{:} \qquad \ell^+\ell^- \to \chi^i\chi^{-i\mp 1} + W^\pm\,. \tag{10.39}$$

The main contribution to all these processes comes from initial- and final-state radiation of a vector boson, which have sizeable rates because of the large weak charge of the DM multiplet and the weak charge of the beams.[3] We sum over all components of the multiplet χ^i, but the dominant

[3]The mono-Higgs signal has a much lower cross-section due to the suppression of initial- and final-state radiation. Furthermore, final-state radiation is model-dependent for scalar DM.

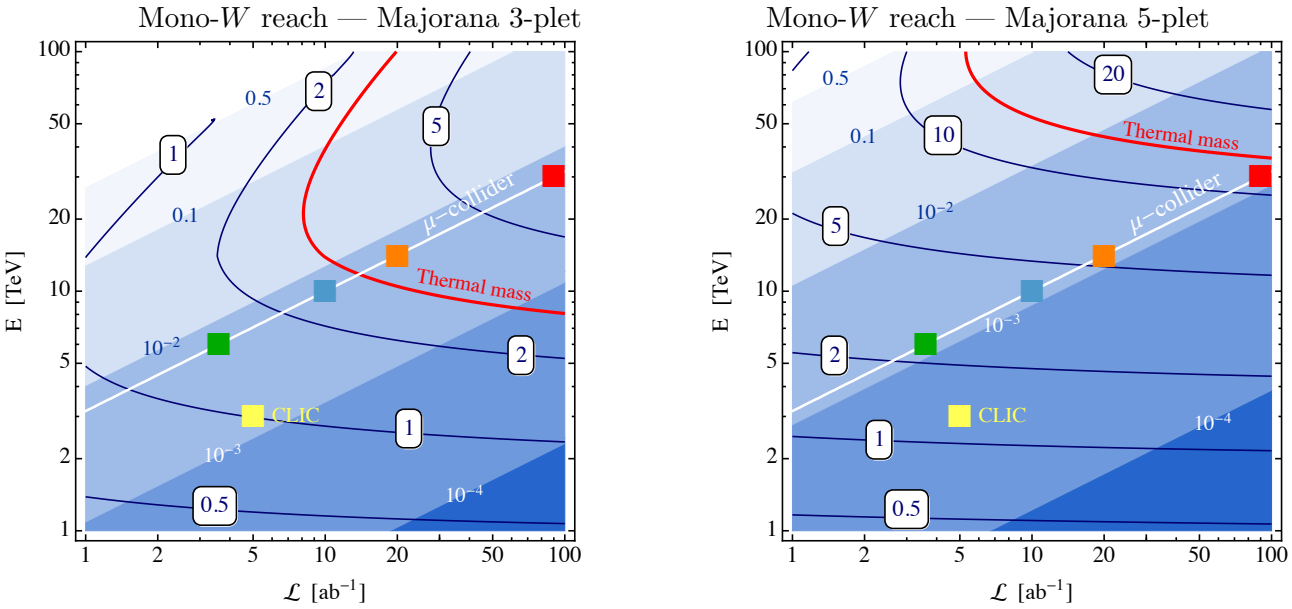

Figure 10.5: Reach from mono-W searches at a muon collider, as a function of collider center-of-mass energy $\sqrt{s}$ and integrated luminosity $\mathcal{L}$. The blue contours show the 95% C.L. reach on the WIMP mass; the prediction from thermal freeze-out is shown as a red line. The precision of the measurement is shown by the blue shadings. Systematic uncertainties are assumed to be negligible. The white line corresponds to the luminosity scaling Eq. (10.35), with various collider benchmarks shown as colored squares: $\sqrt{s} = 6$ TeV green, $\sqrt{s} = 10$ TeV blue, $\sqrt{s} = 14$ TeV orange and $\sqrt{s} = 30$ TeV red. The yellow square corresponds to the 3 TeV CLIC [316]. **Left:** Majorana 3-plet. **Right:** Majorana 5-plet.

signal corresponds to the production of the state with largest electric charge ($i = \pm n$), subsequently decaying into DM plus soft SM particles.

For each of these signals, the corresponding SM background is dominated by a single process,

$$\text{mono-}\gamma \text{ bkg:} \qquad \ell^+\ell^- \to \gamma\nu\bar{\nu}\,, \tag{10.40}$$

$$\text{mono-}Z \text{ bkg:} \qquad \ell^+\ell^- \to Z\nu\bar{\nu}\,, \tag{10.41}$$

$$\text{mono-}W \text{ bkg:} \qquad \ell^+\ell^- \to W^\mp\nu \;+\; \ell^\pm(\text{lost})\,, \tag{10.42}$$

where the missing transverse momentum is carried by neutrinos; the mono-W background also requires a lost charge along the beam.

We simulate signal and background events with MadGraph5_aMC@NLO [317, 318], for different DM mass hypotheses and different collider energies. The W and Z bosons are assumed to be reconstructed from all their visible decay products and are treated as single objects. We impose basic acceptance cuts on the rapidity and transverse momentum of the vectors, requiring $|\eta_V| < 2.5$ and $p_{\mathrm{T},V} > 10$ GeV. Other detector effects are neglected.

We then perform a cut-and-count analysis, estimating the significance of the signal as

$$\text{significance} = \frac{S}{\sqrt{S + B + \epsilon_{\text{sys}}^2\,(S^2 + B^2)}}\,, \tag{10.43}$$

where S, B are the numbers of physical signal and background events, and ϵ_{sys} parametrizes the systematic uncertainties. The signal is isolated from the background employing the kinematics of the

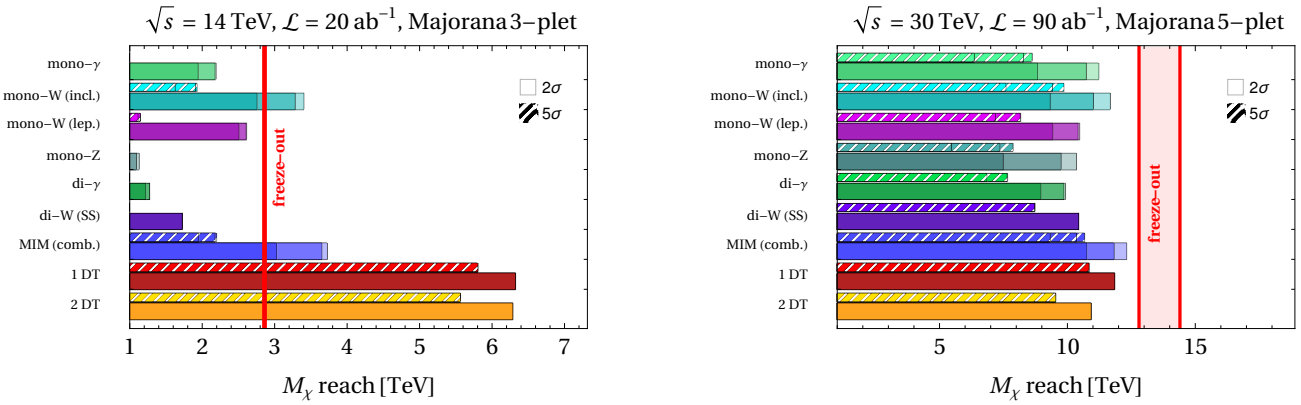

Figure 10.6: Different bars show the 2σ (solid wide) and 5σ (hatched thin) reach on the WIMP mass at a muon collider for different search channels. The first seven bars show the channels discussed in Sec. 10.4.1 where DM would appear as missing invariant mass (MIM) recoiling against one or more SM objects: mono-gamma, inclusive mono-W, leptonic mono-W, mono-Z, di-gamma, same sign di-W, and the combination of all these MIM channels (blue). The last two bars show the reach of disappearing tracks as discussed in Sec. 10.4.2, requiring at least 1 disappearing track (red), or at least 2 tracks (orange). All the results are shown assuming systematic uncertainties to be 0 (light), 1‰ (medium), or 1% (dark). The vertical red bands show the freeze-out prediction. **Left:** Majorana 3-plet for $\sqrt{s} = 14\,\text{TeV}$ and $\mathcal{L} = 20\,\text{ab}^{-1}$. **Right:** Majorana 5-plet for $\sqrt{s} = 30\,\text{TeV}$ and $\mathcal{L} = 90\,\text{ab}^{-1}$.

visible object, parametrized in terms of its transverse momentum $p_{\text{T},V}$, its pseudo-rapidity η_V, and the missing invariant mass (MIM) which is a function of the energy of the visible particle itself

$$\text{MIM} = \left(s + m_V^2 - 2\sqrt{s}E_V\right)^{1/2} . \tag{10.44}$$

We select events with $\text{MIM} \geq 2M_\chi$, $p_{\text{T},V} \geq p_{\text{T},V}^{\text{cut}}$, $|\eta_V| \leq \eta_V^{\text{cut}}$, where the p_T and η selection cuts are chosen to maximize the significance for each value of M_χ.

The background rates for mono-γ and mono-Z are very similar, with fiducial cross-sections of around 3 pb that depend weakly on the collider energy. As already pointed out in [278] for the mono-γ case, the optimal reach on M_χ is obtained for low signal-to-noise ratios – in other words, systematic uncertainties could be important. For this reason, we present results for different values of $\epsilon_{\text{sys}} = 0, 1‰, 1\%$. We point out that in presence of larger systematic uncertainties, the optimal selection cuts are stronger and lead to higher values of S/B.

The mono-W differs from the other two channels. The SM background is dominated by vector boson fusion (VBF) processes, that lead to forward leptons (lost along the beam pipe) and W bosons. The signal is instead made of events where the W is radiated from the initial or final states, leading to a more central distribution. The cut on $p_{\text{T},W}$ can efficiently suppress the VBF background, with a lesser impact on the signal compared to the mono-γ or mono-Z cases. As a consequence, we find that the mono-W search has the best sensitivity among the various mono-X channels. The 95% C.L. exclusion reach on M_χ is shown in Fig. 10.5 for instance for a Majorana 3-plet and 5-plet, as a function of collider center-of-mass energy $\sqrt{s}$ and luminosity $\mathcal{L}$. We also show the expected values of S/B for the excluded signal in absence of systematic errors, which are rather low also for the mono-W search.

Due to the presence of initial-state radiation, the W boson of the signal has a preference for being emitted in the forward (backward) direction, measured with respect to the flight direction of the ℓ^-

beam, if its charge is negative (positive). Since the charge of the W boson is potentially observable for leptonic decays, we can envisage a strategy to isolate the signal from the background using the full distribution in η_W (instead of its absolute value). We thus also perform an analysis of leptonic mono-W events, where we impose the additional cut $\eta_{W^\pm} \lessgtr 0$. We find the reach of this search to be weaker than the one of the inclusive mono-W because of the small leptonic branching ratio. However, the leptonic mono-W search possesses signal-free regions of the η_W distribution which would allow for an *in situ* calibration of the background from the data itself, leading to possible reduction of the systematic uncertainties.

Among all the channels considered, the only background that needs some careful treatment is the mono-W one. We split this background in two contributions. For pseudo-rapidities of the final state lost muon $\eta_\mu > \eta_{\rm match}$ (computed with respect to the direction of the initial state muon with the same charge), we compute the cross-section of the process $\gamma\mu^\mp \to W^\mp\nu$, using the improved Weizsäcker-Williams approximation [319]. For $2.5 < \eta_\mu < \eta_{\rm match}$, we compute the full hard process $\mu^-\mu^+ \to W^\mp\nu\ell^\pm$. The values used for $\eta_{\rm match}$ are $5.4, 6.2, 6.5, 7.0, 7.5$ for $\sqrt{s} = 3, 6, 10, 14, 30$ TeV, respectively. These values are such that the two background contributions are the same in the pseudorapidity region $(\eta_{\rm match}, \eta_{\rm match} + 0.2)$ for the lost muon.

Di-V. We now consider scattering processes with multiple emission of vector bosons, which have explicitly studied for real WIMPs. While generally being suppressed by higher powers of the gauge coupling constant, these processes can be enhanced for large center-of-mass energies, and for multiplets with large weak charge. They can therefore provide very useful handles to probe WIMPs in the regimes where the mono-V searches have very low signal-to-noise ratios. Of course, a too large rate for multiple boson radiation would indicate the breakdown of the perturbative expansion, requiring the resummation of large logarithms. We have checked that for the EW 3-plet and 5-plet, and for the energies under consideration here, the fixed-order computations are still accurate.

First, we consider the di-photon process

$$\ell^+\ell^- \to \chi^i\chi^{-i} + \gamma\gamma\,. \tag{10.45}$$

We apply the same acceptance cuts of the mono-γ analysis, and in addition we require a separation $\Delta R_{\gamma\gamma} > 0.4$ between the two photons. We employ the same event selection strategy of the mono-γ case, using as variables η_X, $p_{{\rm T},X}$, where X is the compound $\gamma\gamma$ system. Moreover, we require each photon to be as central as the $\gamma\gamma$ system itself. For the 5-plet, we find that the di-γ search can be stronger than the mono-γ in presence of large systematic uncertainties, where suppressing the SM background is more important. For the 3-plet, which has a smaller EW charge, the signal yield is too much affected by the requirement of a second emission to be competitive with the mono-V. In both cases, the values of S/B for the excluded di-γ signal are much larger than for the mono-γ signal, and systematic errors thus have a smaller impact.

Second, we consider the double W emission

$$\ell^+\ell^- \to \chi^i\chi^{-i\mp 2} + W^\pm W^\pm\,, \tag{10.46}$$

which holds a potentially very clean signature due to the two same-sign W bosons. We focus on leptonically decaying W bosons to ensure that their charge can be accurately tracked. A potential SM background consists in events with two lost charged particles, with the leading contribution being

$$\ell^+\ell^- \to W^-W^-W^+W^+\,, \tag{10.47}$$

where two W bosons of same sign are lost. This background is however negligible, as pairs of W bosons with opposite charge tend to be radiated from the same external leg and to be collinear: requiring

only one of two collinear W bosons to be within detector acceptance reduces the rate to negligible levels. The other possible background is given by events with a misidentified charge,

$$\ell^+\ell^- \to W^-W^+(\text{mistag})\ \nu\bar{\nu}\ , \tag{10.48a}$$
$$\ell^+\ell^- \to W^-W^+(\text{mistag})\ \ell^+\ell^-\ , \tag{10.48b}$$

where in the second case the charged final-state leptons are lost along the beam line. Requiring $p_{\text{T},WW} \gtrsim \sqrt{s}/10$ makes the process in Eq. (10.48b) subdominant with respect to the $\nu\bar{\nu}$ background Eq. (10.48a). On top of this p_T cut, we do not apply further selection cuts, and simply require the two W bosons to be within the geometrical acceptance of the detector, $|\eta_W| < 2.5$. As an estimate for the charge misidentification probability we take $\epsilon_{\text{misid}} = 10^{-3}$.

Due to the negligible background contamination, the same-sign di-W signal has a much higher signal-to-noise ratio than the mono-V channels and even than the di-photon signal, reaching up to $S/B \sim \mathcal{O}(1)$. This makes this channel very robust against systematic uncertainties, and particularly effective for large n-plets $n \geq 5$ at higher energies due to their large EW charge. This signature may be one of the most robust and convincing signal of $n = 5$ multiplets at colliders. Further sources of background and a proper characterization of the missing (transverse) momentum in this reaction depend on detector performances, as well as on the knowledge of the initial state of the collision to be used in the computation of kinematic variables.

For the real WIMPs, we summarize the results of all the mono-V and di-V signatures discussed above in Fig. 10.6, where we show the 95% C.L. exclusion on M_χ for real fermion 3-plets and 5-plets, together with the 5σ discovery potential, at two benchmark muon colliders. We also show the combined reach from all these missing mass channels. The bands with different shadings correspond to different systematic uncertainties. One can see that the inclusive mono-W yields the strongest exclusion for both the 3-plet and the 5-plet. The main effect of di-V searches is to reduce the impact of systematic uncertainties. A 14 TeV muon collider with the benchmark luminosity of Eq. (10.35) would be able to probe a thermally-produced Majorana 3-plet WIMP, while a center-of-mass energy of slightly above 30 TeV is needed to probe the thermal freeze-out mass with missing energy searches in the case of the 5-plet.

The same analysis can in principle be repeated also for scalar WIMPs. However, probing scalar WIMPs with typical missing mass searches is quite hard. This is due to multiple reasons: i) the scalar production cross-sections are roughly one order of magnitude smaller than for fermions with same n. A factor of 4 suppression comes from the lower number of degrees of freedom for scalar final states, while the remaining suppression comes from a velocity suppressed production cross-section compared to the fermionic case. One can see that the reach is a very slow function of the mass of the WIMP M_χ, thus a reduction of the signal cross-section implies a drastic change in the reach. ii) The scalar WIMPs have typically larger freeze-out masses compared to fermionic WIMPs with same EW charge n. All in all, scalar WIMPs give dimmer signals at colliders and are generically heavier than fermionic WIMP. It is thus not surprising that the results expected from collider searches of scalar WIMPs are far less exciting than those for fermions in Fig. 10.6.

Finally, we will extend this analysis to the complex $2_{1/2}$ and 3_1 WIMPs at the end of this Section.

10.4.2 Disappearing tracks

A second handle to tag the production of EW WIMPs at colliders is the detection of tracks from the charged states in the n-plet. In fact, the decay of $\chi^\pm \to \chi^0\pi^\pm$ has a lifetime of roughly $c\tau_{\chi^+} \simeq 48\ \text{cm}/(n^2-1)$, which is sufficiently long-lived to give rise, in the real case, to reconstructed tracks of

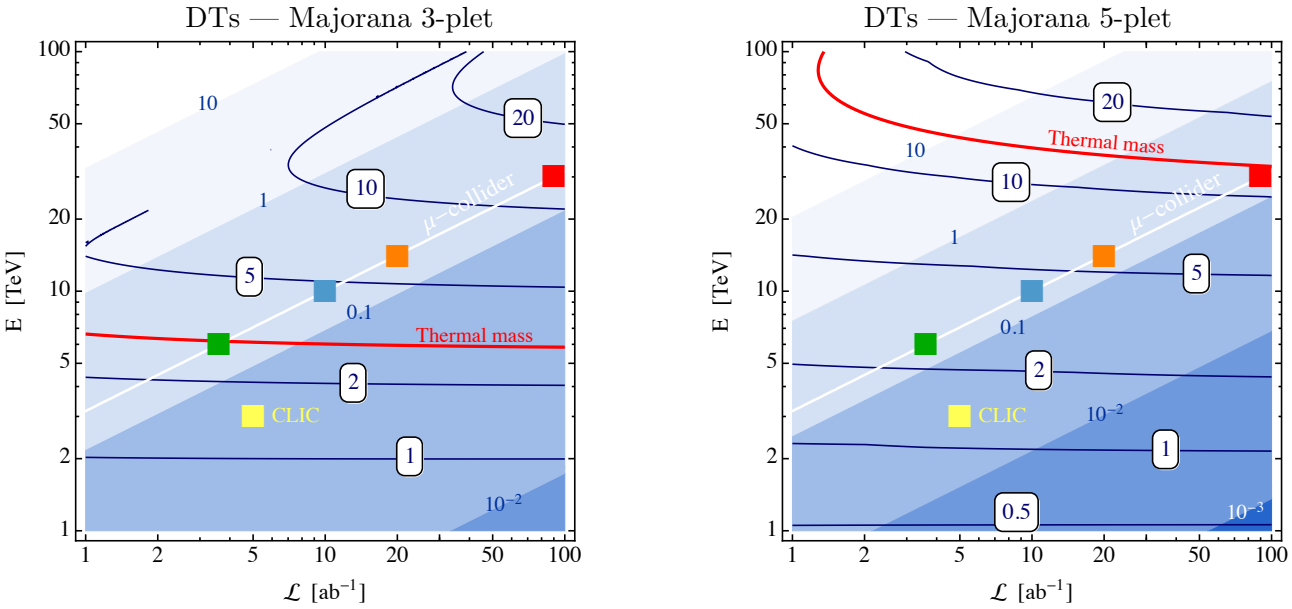

Figure 10.7: Same as Fig. 10.5, but for disappearing track searches in mono-γ events. **Left:** Majorana 3-plet. **Right:** Majorana 5-plet.

length $\mathcal{O}$(cm) for $n = 3, 5$ that can be observable at colliders (we posticipate the discussion for complex WIMPs in the following Subsection). The resulting tracks from these processes are somewhat too short for regular track reconstruction to work efficiently and they will show up as disappearing tracks (DTs), with missing hits in the outermost layers of the tracker and with little or no activity in the calorimeter and the muon chamber. States with higher electric charge in larger multiplets decay promptly to $\chi^{\pm}$, and eventually contribute to the number of disappearing tracks.

A full-detector level study has shown that a high energy lepton collider like CLIC at $\sqrt{s} = 3$ TeV can reconstruct them sufficiently well to separate them from other sources of look-alike short tracks [320, 321]. A recent study [322] has attempted a first evaluation of the performance of this type of search at a multi-TeV muon collider. A main source of worry and a main difference with respect to e^+e^- machines is the abundant number of tracker hits from underlying event activity due to the muon beam decay and to the resulting secondary particles from the interactions with the machine and detector materials. These hits can accidentally become a potentially severe source of background for searches aimed at highlighting the presence of short tracks of BSM origin. We do not enter in the details of these issues here, and simply follow the analysis of [322], which is based on a simulation of beam-induced background at 1.5 TeV, and recast their results for the EW 3-plet and the 5-plet. We remind that the background from decaying muons is expected to decrease at higher energies, making our estimate conservative in this sense.

We consider mono-photon events with disappearing tracks, and search for events compatible with a WIMP signal. Following [322], we distinguish two event-selection strategies to hunt for disappearing tracks: i) events with at least a disappearing track with $p_T > 300$ GeV and a hard photon with $E_\gamma > 25$ GeV; ii) events with a hard photon, and two disappearing tracks originating from the same point along the beam axis. To estimate the reach we work in the cut-and-count scheme as in Eq. (10.43), and ignore systematic uncertainties. Further details are summarized in Appendix F for completeness.

Focusing on real WIMPs, the result of our recast is shown in the last two columns of Fig. 10.6

for Majorana 3-plets and 5-plets at two benchmark colliders, and in Fig. 10.7 as a function of collider energy and luminosity. One can see that DTs are especially powerful in the case of the 3-plet, where the reach goes almost up to the kinematical threshold. In particular, an EW 3-plet WIMP of mass as predicted by thermal freeze-out can be discovered already at a 6 TeV muon collider as suggested in [278, 322]. For higher n-plets DT substantially loose exclusion power because the lifetimes of the $\chi^{\pm} \to \chi^0 \pi^{\pm}$ decay become shorter. For the 5-plet the DT reach is comparable to the combined reach of the MIM searches.

As discussed in more detail in the Appendix F, DT searches are particularly important to probe scalar WIMPs. It is remarkable that for real scalars the mass splitting between charged and neutral states in the n-plet is dominated by EW interactions. Indeed, no splitting term with the Higgs can be written at the quartic level, due to the antisymmetry of the SU(2) contraction. By hypercharge conservation, and assuming the scalar does not get any extra VEV, the leading terms contributing to the mass splitting are dimension 6 in the SM. Therefore the stub-track prediction is robust and does not depend on peculiar UV completions of the model. In conclusion, disappearing tracks might be the only direct signature of scalar WIMPs at collider experiments.

10.4.3 Results for the complex fermionic $2_{1/2}$ and 3_1 at muon collider

Let us finally repeat the aforementioned analyses for complex WIMPs, more specifically for the complex fermionic $2_{1/2}$ and 3_1 candidates. We stress again that, in what follows, we are working in a minimal splitting setup. In these cases, the expected signatures at future colliders depend very much on the lifetime of the charged states in the EW multiplet. This might decay back to the neutral DM either promptly or with a macroscopic lifetime on detector scales.

In the prompt case, the decay of the charged state will give rise to soft radiation which would be impossible to disentangle from the SM background and the DM signal will be characterized only by a large missing energy recoiling against EW radiation. This can be further disentangled from the SM background at lepton colliders thanks to the knowledge of the center of mass energy by looking for features in the MIM distribution. For complex candidates, we find that the MIM reach is dominated by the mono-W and the mono-γ channels. Despite the non-zero hypercharge enhancing the coupling to the Z, the mono-Z channel has a lower reach, similarly to what has been discussed for real WIMPs.

In the long lived case, depending on the decay length of the charged state it might be beneficial to look at DTs or to look at long lived charged tracks (CTs), that could be distinguished from the SM backgrounds by their energy losses in the material and by the measurement of their time of flight (see for example analogous searches performed by ATLAS and CMS at the LHC [323, 324]).

Here, we focus on the expected reach from DTs and MIM searches which are relevant for the $2_{1/2}$ and 3_1, fixing the splitting of the $Q = 1$ state with respect to the neutral one to be the one generated purely by EW corrections. In this minimal case, the rest frame lifetime of the charged state decaying back to the DM is $c\tau_+ = 6.6$ mm for the $2_{1/2}$ and $c\tau_+ = 0.7$ mm for the 3_1.

Our results for the combination of the MIM searches and the DT tracks search are given in Figures 10.8-10.9 for fixed thermal mass of the $2_{1/2}$ and similarly for the 3_1. As can be seen from these plots, the MIM search at $\sqrt{s} = 3$ TeV with the benchmark luminosity $\mathcal{L} = 1$ ab^{-1} is not sensitive to the $2_{1/2}$. A $\sqrt{s} = 6$ TeV collider with benchmark luminosity $\mathcal{L} = 4$ ab^{-1}, instead, is able to probe the complex doublet WIMP at 2σ C.L. In general the mono-W and mono-γ channels give comparable mass reach for the benchmark luminosity adopted here and the sensitivity of each channel has a specific behavior as a function of the luminosity and for different assumed systematics. We remark that in Figures 10.8-10.9 the reach deviates from a pure rescaling by $\sqrt{\mathcal{L}}$ because the selections, hence the result, have been optimized as a function of $\mathcal{L}$ when dealing with $\epsilon_{\rm sys} \neq 0$.

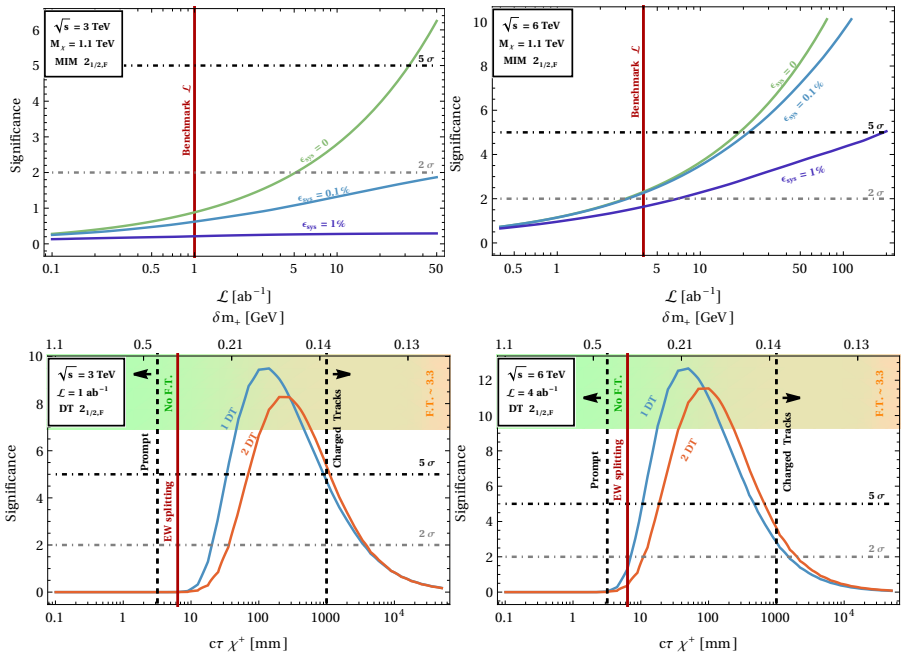

Figure 10.8: Collider reach for the $2_{1/2}$ of mass $M_\chi = 1.1$ TeV and $\sqrt{s} = 3$ TeV *(left)* and $\sqrt{s} = 6$ TeV *(right)*. Upper row: Combined reach for MIM as a function of the luminosity $\mathcal{L}$ for different values of the expected systematic uncertainties parametrized by $\epsilon_{\rm sys}$: 1% **(purple)**, 0.1% **(cyan)**, 0 **(green)**. The **red** lines show the benchmark luminosity following Eq. (10.35). Lower row: Reach of DT for varying lifetime of the charged track. The **red** vertical line shows the benchmark lifetime for EW splitting. The **blue** and **orange** curves correspond to the reach with 1 and 2 disappearing tracks. Fine-Tuning values computed on δm_+ following Eq. (10.17) are displayed as color code from green (no fine-tuning) to red (higher fine-tuning).

We also display results for the DT search as a function of the lifetime of the charge +1 state, that is in a 1-to-1 relation with the mass splitting δm_+. We see that a collider of $\sqrt{s} = 6$ TeV can probe the $2_{1/2}$ for charge-neutral splitting generated purely by EW interactions. A collider of $\sqrt{s} = 3$ TeV can probe a large portion of the allowed lifetimes for the charged tracks corresponding to non-zero UV contributions in Eq. (10.16).

We have similar results for the 3_1 at its thermal mass, which entails interesting results at 6 and 10 TeV center of mass energy machines. For the 10 TeV collider we find that MIM searches are effective probes of this WIMP candidate and can establish a bound at 95% CL with a small luminosity or give a discovery with the nominal luminosity. Mono-W and mono-γ perform similarly well and their combination is worth being done. The DT search cannot probe the EW splitting for the 3_1, however it can cover a large portion of allowed lifetimes in the non-minimal splitting case in which UV physics is contributing to the charged-neutral splitting.

Finally, it is important to notice that with an $\mathcal{O}(1)$ fine tuning of the UV contribution to the charged neutral splitting against the irreducible EW contribution the charged tracks could be extremely long-lived on detector scale for both the $2_{1/2}$ and 3_1. This observation motivates a detailed detector simulation of a muon collider environment to reliably estimate the expected reach in this channel. We will provide some estimates for the signal yield in the last Section.

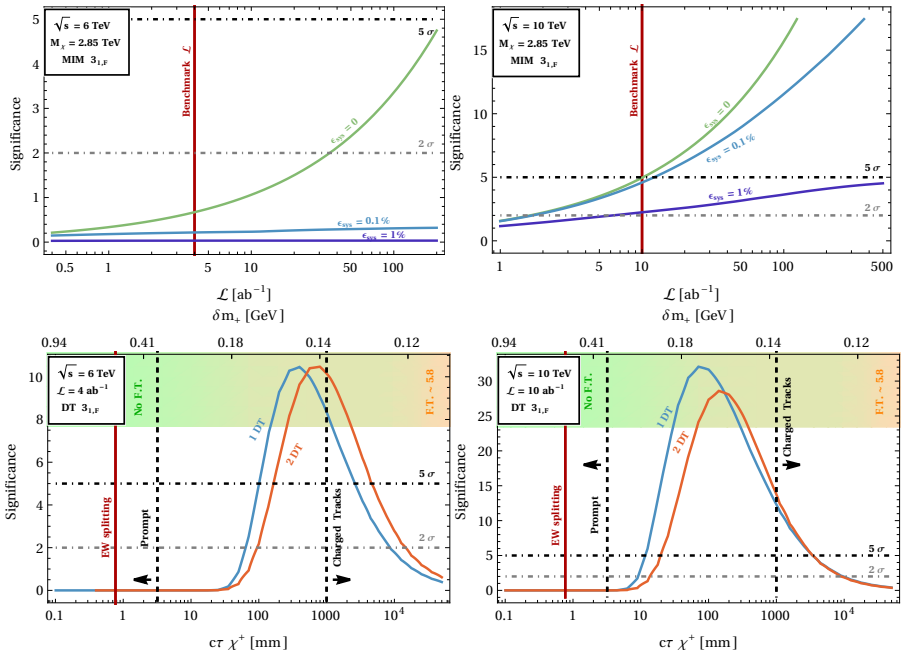

Figure 10.9: Same as for the Figure 10.8, but for the case of the 3_1 of mass $M_\chi = 2.85$ TeV and $\sqrt{s} = 6$ TeV *(left)* and $\sqrt{s} = 10$ TeV *(right)*.

10.5 WIMP direct and indirect detection

In this Section we briefly summarize the opportunities of the future experimental program in DD and ID searches, in light of the mass predictions derived in Tables 10.1 and 10.2.

10.5.1 Indirect Detection

The current and upcoming ground-based Cherenkov telescopes are in a very good position to probe heavy WIMP n-plets, which would be inaccessible otherwise. Indeed, these telescopes are designed to detect very high energy gamma-rays (i.e. $E_\gamma \gtrsim 100$ GeV) coming from different astrophysical objects and they are therefore sensitive to the gamma-ray signal from the annihilations of EW n-plets. The typical spectrum is characterized at very high energy by gamma-ray lines, peaking at the DM mass $E_\gamma \simeq M_\chi$, from the loop-induced annihilations into $\gamma\gamma$ and γZ. The cross-section in this channel is largely boosted by the SE (see e.g. [266, 326, 327]) and can raise above the gamma-ray continuum from the showering, hadronization and decays of the EW gauge bosons [328].

From the astrophysical point of view, the reach of high energy gamma lines searches depends very much on which portion of the sky the telescopes will be pointed at. In finding the optimal choice, a balance has to be found between the maximization of photon flux at Earth and the control over the systematical uncertainties. Two very well studied astrophysical targets are the Galactic Center (GC) [325, 329] and the Milky Way's dwarf Spheroidal galaxies (dSphs) [325]. In the GC, the uncertainties are dominated by the importance of the baryonic physics in the inner most region of the Milky Way which comes together with the poor knowledge of the DM distribution at the center of the Milky Way [330–333]. On the contrary, dSphs stands out as very clean environments to search for high energy γ-lines only residually affected by systematics related to the determination of their

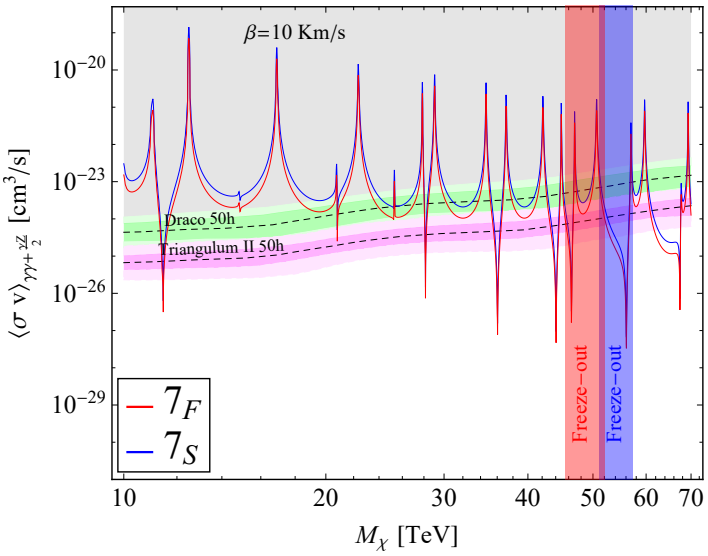

Figure 10.10: Expected CTA sensitivities (dashed black lines) with 68% and 95% CL intervals derived as in Ref. [325] assuming 50 hours observation time towards Draco (green) and Triangulum II (magenta). We show the SE annihilation cross-section into the channels that contribute to the monocromatic gamma line signal (i.e. $\gamma\gamma$ an γZ) for a real scalar 7-plet (blue) and a real fermionic 7-plet (red). The vertical bands show the predicted thermal masses for the scalar 7-plet (blue) and the fermionic 7-plet (red), where the theory uncertainty is dominated by the neglected NLO contributions (see Table 10.1).

astrophysical parameters in the presence of limited stellar tracers [334, 335].

Motivated by the above considerations, we show a preliminary analysis of ID signals coming from annihilations of the real WIMP 7-plet. We focus on the CTA prospects by considering 50h of observations time towards two dSph targets in the northern hemisphere: the classic dSph Draco and the ultra-faint one Triangulum II. Notice that the DM properties of Draco come from hundreds of stellar tracers, while those from Triangulum II are based on just 13 tracers, making the latter more speculative and subject to large systematics in the determination of the geometrical J-factor [336]. Hence, the reach of Draco should be taken as the baseline reach for CTA.

Our analysis is simplified because the signal shape we consider is essentially a single line at $E_\gamma \simeq M_\chi$. Consistently we take the CTA prospects derived in Ref. [325] for a pure line. We ignore the contributions of the continuum spectrum, the extra features of the spectral shape induced by the resummation of EW radiation and the contribution of the BSF to the photon flux. While neglecting BSF is justified if we focus on very high energy photons, a careful computation of the $\gamma + X$ cross-section, where X is any other final state, would be needed to precisely assess the experimental sensitivity [337]. In the last decade, many different groups have investigated the impact of large Sudakov logarithms and large collinear logarithms on the ID reach, focusing mainly on the case of the fermionic 3-plet [338–342, 342]. The inclusion of these effects has been shown to increase the reach of $\sim 20\%, 30\%$ for the 3-plet [325, 329, 343] and it is expected to be even more important for higher DM masses.

In Fig. 10.10 we overlay the SE annihilation cross-section for the 7-plets at $v = 10$ km/sec against the CTA experimental reaches. In order to compute the SE in this velocity regime, we took advantage

of the parametrization introduced in [327] and used the full expressions for the SE at leading order, including EW breaking effects. The SE saturate already at $v \simeq 10^{-3}, 10^{-2}$ far away from the resonances. As we can see, both a 50 hour observation of Triangulum II and of Draco have good chances to detect the high energy γ line in the 7-plet annihilation spectrum.

As we see from Fig. 10.10, given the strong mass-dependence of the features of the SE cross-section, a major source of theoretical uncertainty on the reach of ID is still the determination of the 7-plet thermal mass. Therefore, a full computation of the thermal relic mass including NLO effects is required together with a careful computation of the $\gamma+X$ cross-section along the lines of [338–342,342] to careful assess the ID reach for the 7-plet.

Independently on our current inability of making a conclusive statement because of the large theory uncertainties, it is clear that large n-plets are a perfect target for future Cherenkov telescopes which deserves further theoretical study. A complementary open phenomenological question is if the low energies gamma lines at $E_\gamma \simeq E_B$ associated to BSF can be actually disentangled from the continuum (see [298,344] for preliminary work in this direction). An analogous question can be asked for monocromatic neutrinos from BS annihilations.

10.5.2 Direct Detection

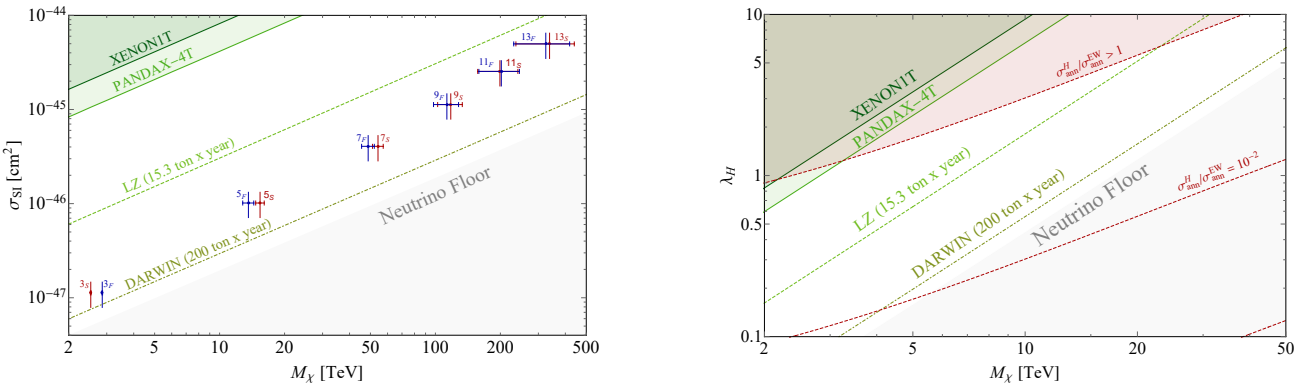

Figure 10.11: In dark green we show the present contraints from XENON-1T [345] and PandaX-4T [285], the green dashed line shows the reach of LZ [346] and the brown green dot-dashed line the ultimate reach of DARWIN [347]. The light gray region show the neutrino floor for 200 ton/year exposure derived in Ref. [348]. **Left:** Expected spin independent (SI) direct detection cross-section for Majorana n-plets (red) and for real scalar n-plets (blue) (assuming the Higgs portal coupling $\lambda_H = 0$). The vertical error bands correspond to LQCD uncertainties on the elastic cross-section in Eq. (10.50) while the horizontal error band comes from the theory determination of the WIMP freeze out mass. **Right:** Current and future reach on the Higgs portal quartic λ_H defined in Eq. (10.1) for scalar DM. In the shaded dark red region the quartic modifies the freeze-out cross-section by $\mathcal{O}(1)$ or more. The dashed red contours indicate smaller ratios of the Higgs-portal and the EW annihilation cross-sections.

In what follows, we finally investigate the discovery potential of both real and complex WIMPs at DD experiments. Note that, in the latter case, we will again work in a minimal splitting scenario, since in this case the spin independent (SI) scattering cross-section $\sigma_{\rm SI}$ can be computed by considering only EW loop diagrams. Generalizing what written at the beginning of the previous Section, this corresponds to set $\delta m_0 = 250$ keV for $n_{1/2}$ WIMPs with $n \leq 4$ as well as for the allowed n_1 WIMPs. For $n_{1/2}$ WIMPs with $n > 4$, instead, the BBN bound in Fig. 10.1 gives the minimal δm_0.

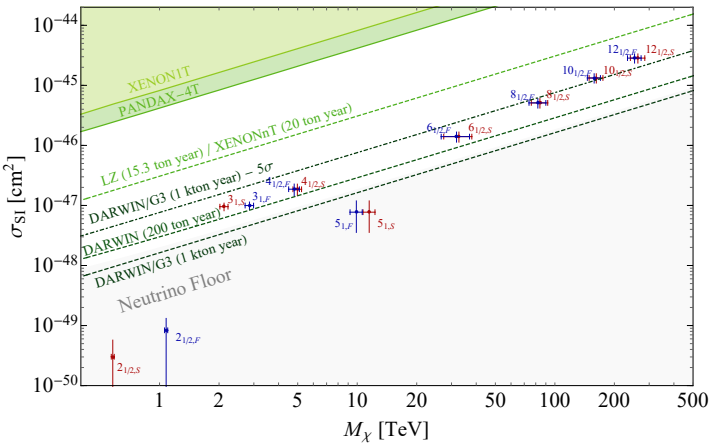

Figure 10.12: Expected SI cross-sections for complex WIMPs in the minimal splitting scenario. The **blue dots** correspond to Dirac WIMPs and the **red dots** to complex scalar WIMPs. The vertical and the horizontal error bands have the same meaning of Figure 10.11 (left). The **light green** shaded region is excluded by the present experimental contraints from XENON-1T [345] and PandaX-4T [285], the **green dashed** lines shows the expected 95% CL reach of LZ/Xenon-nT [346, 349] and DARWIN [8, 347].

Now, for the cases of our interest the elastic scattering of DM with the nuclei is induced by EW loop diagrams first computed in [350, 351]. After EW gauge bosons are integrated out, the structure of the UV effective Lagrangian describing the DM interactions reads

$$\mathcal{L}_{\rm eff}^{\rm SI} = \bar{\chi}\chi\left(f_q m_q \bar{q}q + f_G G_{\mu\nu}G^{\mu\nu}\right) + \frac{g_q}{M_\chi}\bar{\chi} i\partial^\mu\gamma^\nu\chi\mathcal{O}^q_{\mu\nu}\,,$$

where we focus on the DM SI interactions with quarks and gluons [352]. The quark twist-2 operator is defined as $\mathcal{O}^q_{\mu\nu} \equiv \frac{i}{2}\bar{q}\left(D_\mu\gamma_\nu + D_\nu\gamma_\mu - g_{\mu\nu}\not{D}/2\right)q$. The Wilson coefficients of the operators have been computed in Ref. [353] for arbitrary choices of $\{n, Y\}$ and at the leading order in $M_\chi/m_{W,h} \gg 1$ read

$$\begin{aligned}
f_q^{\rm EW} &\simeq -\frac{\pi\alpha_2^2}{16 m_h^2 m_W}\left[n^2 - 1 - \left(1.03 + 22(a_q^{V,2} - a_q^{A,2})\right)Y^2\right],\\
g_q^{\rm EW} &\simeq \frac{\pi\alpha_2^2}{24 m_W^3}\left[n^2 - 1 - \left(4 - 18.2(a_q^{V,2} + a_q^{A,2})\right)Y^2\right],\\
f_G^{\rm EW} &\simeq \frac{\alpha_s\alpha_2^2}{192 m_h^2 m_W}\left[\left(\sum_{q=c,b,t}\kappa_q + 2.6\right)(n^2-1) - \left(1.03\sum_{q=c,b,t}\kappa_q - 7.5\right)Y^2\right],
\end{aligned} \tag{10.49}$$

where m_h is the mass of the Higgs and $\kappa_c = 1.32$, $\kappa_b = 1.19$, $\kappa_t = 1$. Furthermore we have defined $a_q^V = T_{3q}/2 - Q_q s_w^2$, $a_q^A = -T_{3q}/2$ with c_w, s_w being the cosine and the sine of the Weinberg angle, respectively. Note that the terms proportional to Y correspond to the exchange of Z bosons inside the EW loops, in addition to the W ones.

Following Ref. [352], starting from the UV DM interactions we derive the IR interaction of DM with the nucleons. All in all, the SI elastic cross-section per nucleon in the limit $M_\chi \gg m_N$ reads

$$\sigma_{\rm SI}^{\rm EW} \simeq \frac{4}{\pi} m_N^4 |k_N^{\rm EW}|^2, \tag{10.50}$$

where m_N is the nucleon mass and $k_N^{\rm EW}$ is defined as

$$k_N^{\rm EW} = \sum_q f_q^{\rm EW} f_{Tq} + \frac{3}{4}(q(2)+\bar{q}(2)) g_q^{\rm EW} - \frac{8\pi}{9\alpha_s} f_{TG} f_G^{\rm EW} \,.$$

with the dimensionless nucleon form factors defined as $f_{Tq} = \langle N|m_q \bar{q} q|N\rangle/m_N$, $f_{TG} = 1 - \sum_q f_{Tq}$ with $q \in (u,d,s)$ and $\langle N(p)|\mathcal{O}^q_{\mu\nu}|N(p)\rangle = \frac{1}{m_N}(p_\mu p_\nu - \frac{1}{4} m_N^2 g_{\mu\nu})(q(2)+\bar{q}(2))$, where $q(2)$ and $\bar{q}(2)$ are the second moments of the parton distribution functions for a quark or antiquark in the nucleon taken from [353]. Notice that we choose a different set of values for the nucleon form factors with respect to previous studies [354] which explain the difference in our results. In particular, we take the FLAG 2021 average of the lattice computations in the case of $N_f = 2+1+1$ dynamical quarks [39,355,356]. Notice also that since $Y \neq 0$, the up and down quarks can give different contributions to the SI cross section in Eq. (10.50) for complex WIMPs. The ETM Collaboration [355] has computed the form factors in the case of degenerate light quarks so we take $f_{Tu} = f_{Td}$, ignoring possible differences between these two form factors.

By combining the previous expressions all together, namely Eq. (10.49) with Eq. (10.50), the parametric expression for $\sigma_{\rm SI}$ reads

$$\sigma_{\rm SI} \simeq 10^{-49}\ {\rm cm}^2 (n^2 - 1 - \xi\ Y^2)^2, \tag{10.51}$$

where $\xi = 16.6 \pm 1.3$. The error has been obtained by propagating the LQCD uncertainties on the elastic cross-section (10.50). This formula makes evident that large cancellations with respect to the natural size of the elastic cross section can take place when $Y \simeq \sqrt{(n^2-1)/\xi}$. In particular, for $n = 2$ the exact cancellation takes place at $Y \simeq 0.44 \pm 0.02$, which almost matches the exact hypercharge of the doublet. Similarly, the cancellation happens at $Y \simeq 1.2$ for $n = 5$.

Our results for the SI cross sections for each possible n-plet are shown in Figures 10.11 (left) and 10.12 for real and complex WIMPs, respectively. We obtain the vertical uncertainties on the SI cross-section predictions by propagating the LQCD uncertainties on the form factors. Furthermore, the horizontal bars represent the uncertainties coming from the computation of the thermal masses through the relic abundance. As shown in the plots, almost all the WIMPs lie in cross-sections above the Xenon neutrino floor, as computed in [348], and can be probed by a very large exposure experiment like DARWIN [347]. The only notable exceptions are the fermionic complex $2_{1/2}$ and 5_1 candidates. This issue, which is evident from Figure 10.12, can be understood through the previous discussion on Eq. (10.51).

For completeness, also spin dependent (SD) interactions of DM with the nuclei can be considered. They are again induced by EW loops

$$\mathcal{L}_{\rm eff}^{\rm SD} = d_q (\bar{\chi}\gamma^\mu \gamma_5 \chi)(\bar{q}\gamma_\mu\gamma_5 q), \tag{10.52}$$

where the Wilson coefficient has been computed in Ref. [353] for any choice of the $\{n, Y\}$ couple. However, although in some cases the predicted SD cross section can lead to a larger contribution compared to the SI one [353], for all the WIMPs it lies always well below the neutrino floor and it will be impossible to test even at future direct detection experiments.

Finally, let us comment on the new opportunities for DD that arise for real scalar DM. Here, a non-zero Higgs portal quartic in Eq. (10.2) leads to a new contribution to the SI DM scattering cross-section with the nuclei, which again in the $M_\chi \gg m_N$ limit reads

$$\sigma_{\rm SI}^{\rm H} = \frac{4}{\pi} m_N^4 |k_N^{\rm H}|^2 \ , \tag{10.53}$$

where

$$k_N^{\rm H} \simeq \frac{\lambda_H f_N}{4 m_h^2 M_\chi} \,, \tag{10.54}$$

with $f_N \simeq 0.31$ obtained from lattice QCD results (see [357] for a more detailed discussion on the real scalar triplet). In the right panel of Fig. 10.11 we show the regions of parameter-space where the Higgs-portal interaction can be tested in DD. The requirement of not significantly affecting the freeze-out dynamics bounds the annihilation cross-section induced by the Higgs portal to be smaller than the EW cross-section, $\sigma^H_{\rm ann}/\sigma^{\rm EW}_{\rm ann} \lesssim 1$, which results in an upper bound on the quartic coupling λ_H shown by the red shading in Fig. 10.11. An estimate for this bound can be obtained by comparing the hard annihilation cross-sections, and reads $\lambda_H^2 \lesssim (n^2-3)(n^2-1) g_2^4/8$. Interestingly, XENON1T and PANDAX-4T already exclude a large part of the region where the Higgs portal induces $\mathcal{O}(1)$ modifications of the freeze-out predictions, while LZ will completely exclude this possibility.

10.6 The non-minimal splitting scenario for complex WIMPs

Exploiting the freedom to change the spectrum given by the UV operators in Eq. 10.6, one can have significant changes in the phenomenology at both the muon collider and DD experiments, which we have described in the previous two Sections. We dedicate this last Section to explore the phenomenological consequences of releasing the minimal splitting assumption.

10.6.1 Direct detection

The Higgs portal operators in Eq. (10.6) generate upon EWSB a linear coupling of the DM to the Higgs boson of the form

$$\mathcal{L}_{D,h} = -\frac{\lambda_D v}{2\Lambda_{\rm UV}} \chi^2_{\rm DM} h \,. \tag{10.55}$$

This coupling mediates tree-level SI scattering processes of DM onto nuclei, therefore it can be constrained by DD experiments. As the mass splitting δm_0 has to be sufficiently large to suppress the scattering mediated by the Z boson, we find that the allowed parameter space for the non-renormalizable couplings is compact.

Following Ref. [358], we can integrate out the Higgs boson and write the couplings of the DM to the SM

$$\mathcal{L}^{\rm SI}_{\rm eff,h} = \frac{\lambda_D}{2 m_h^2 \Lambda_{\rm UV}} \chi^2 \left(m_q \bar{q} q - \frac{\alpha_s}{4\pi} G^a_{\mu\nu} G^{a\mu\nu} \right) , \tag{10.56}$$

so that the matrix elements f_q and f_G, defined in Eq. (10.49) for EW loops and required to compute $\sigma_{\rm SI}$, are simply given by

$$f_q = f_q^{\rm EW} + \frac{\lambda_D}{2 m_h^2 \Lambda_{\rm UV}} \,, \;\; f_G = f_G^{\rm EW} - \frac{\alpha_s}{8\pi} \frac{\lambda_D}{2 m_h^2 \Lambda_{\rm UV}} \,, \tag{10.57}$$

where $f_q^{\rm EW}$ and $f_G^{\rm EW}$ come exactly from Eq. (10.49). We can rewrite the coupling λ_D solely in terms of mass splitting as

$$\frac{\lambda_D}{\Lambda_{\rm UV}} = -\frac{2Y}{v^2} (\delta\mu_{Q_M} + n \delta\mu_0) \,, \tag{10.58}$$

where

$$\delta\mu_{Q_M} \equiv \frac{2\delta m_{Q_M} - \delta m_0 - 2\Delta M^{\rm EW}_{Q_M}}{2Q_M}, \quad \delta\mu_0 \equiv \frac{\delta m_0}{n}$$

and $\Delta M^{\rm EW}_{Q_M}$ is the gauge induced mass splitting in Eq. (10.15). Thus, replacing Eq. (10.58) into Eq. (10.50) allows us to translate the upper bound on $\sigma_{\rm SI}$ into an upper bound on δm_0 and δm_{Q_M}.

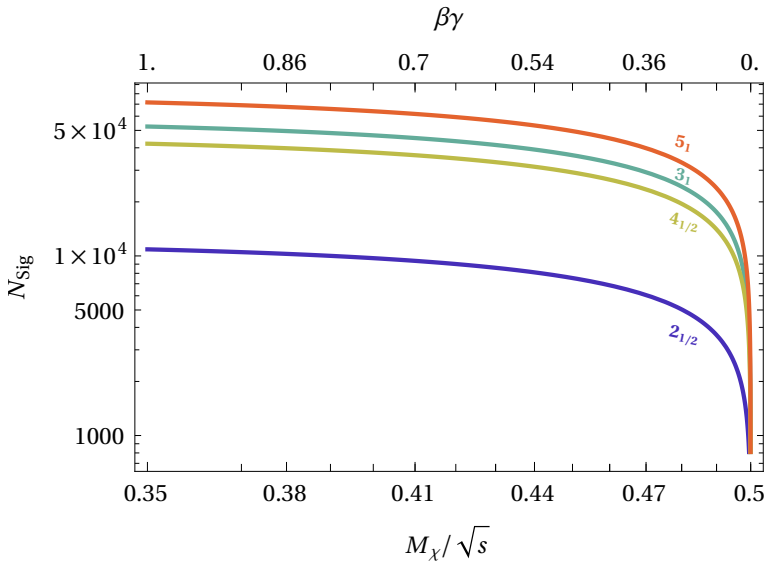

Figure 10.13: Signal yield of the charged tracks for the $2_{1/2}$, 3_1, $4_{1/2}$, 5_1.

10.6.2 Muon collider searches

The splittings $\delta m_0, \delta m_{Q_M}$ determine the lifetime of the charged components of the EW multiplet, which are pivotal to understand the viable collider signatures. In what follows we take as reference the detector geometry proposed in [277] and we classify the parameter space $(\delta m_0, \delta m_{Q_M})$ in various regions according to the lifetime $\tau_{\rm LCP}$ of the Longest Lived Charged Particle (LCP) of a given multiplet.

For $c\tau_{\rm LCP} > 1$ m the LCP gives long charged tracks with an average length roughly corresponding to the middle layer of the outer tracker. The SM background processes for this "long" track with anomalous properties strongly depends on the properties of the detector, therefore its study is outside the scope of this Thesis. We limit ourselves to estimate the number of expected signal events of charged χ pair production at a muon collider, as shown in Fig. 10.13. We highlight that this results approximately holds for generic $\sqrt{s}$ in the domain of tens of TeV of interest here, as long as Eq. 10.35 for the luminosity holds. In Fig. 10.13 we show the $\beta\gamma$ of the produced charged particle, which plays a crucial role to disentangle these special tracks from the SM background.

Our estimates for the CTs are based on the counting of the number of LCP produced. For the LCP we require $p_T > 200$ GeV, $|\eta_\chi| < 2$, inspired by LHC searches [324]. For the $2_{1/2}$ and 3_1 we include in our counting all charged particles production, assuming that χ^{2+} promptly decay to the long lived χ^+. For the $4_{1/2}$ and 5_1, which have more complicated spectra, we stick to the minimal splitting scenario for the estimate of the charged tracks yield, which corresponds to the minimal y_+ necessary to lift χ^- above $\chi_{\rm DM}$. In this spectrum configuration χ^- is the most natural and only candidate to make CTs, therefore we only consider this contribution in our result.[4]

Now, for 1 m $> c\tau_{\rm LCP} > 0.33$ cm the lightest charged WIMP gives, instead, a disappearing track signal, which has been introduced in the minimal splitting framework and it is further described in

[4]We neglect any possible contribution coming from χ^+ decaying into $\chi^{-,c}$, since in the region where mixing is relevant, the charged particles lifetimes are too short and are in the "stub tracks region", as shown in Fig. 10.14.

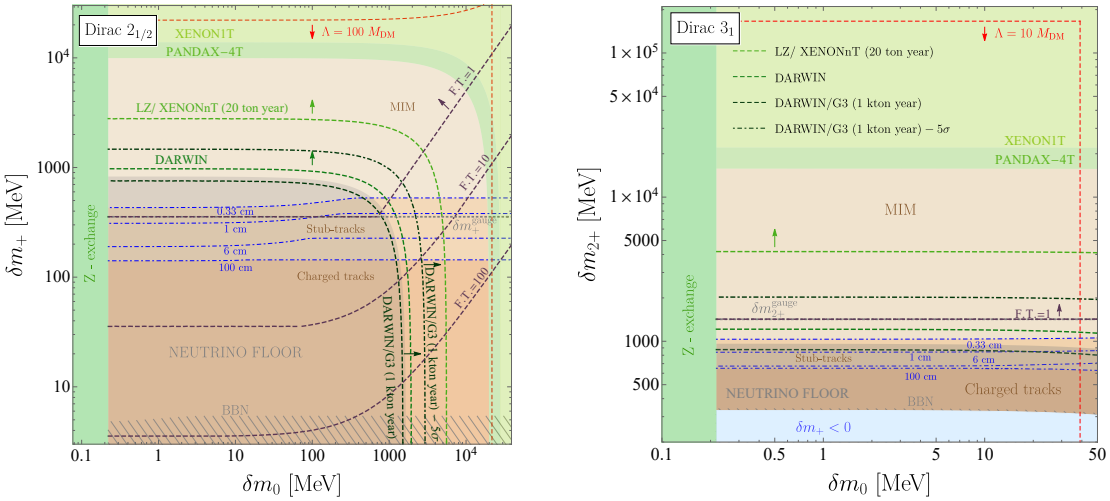

Figure 10.14: Direct Detection and collider signatures in the non-minimal splitting scenario in the plane δm_0 vs. δm_{Q_M} from the $2_{1/2}$ (*left*) and the 3_1 (*right*) . The **green** shaded regions are excluded by current DD constraints on inelastic DM (see Fig. 10.1). **Gray diagonally hatched** regions are excluded by BBN constraints on the longest lived unstable particle in the multiplet. Dashed green lines show prospects from future high exposure Xenon experiments: LZ, DARWIN and DARWIN/G3 (arrows pointing to the direction of the expected probed region). In the **gray shaded** region the direct detection signal falls below the so-called neutrino floor. **Blue** and **black** dashed lines show isocurves corresponding to different benchmark tracks lengths. Different hues of **brown** distinguish the regions suitable for charged track, stub tracks and missing mass searches. We show the pure gauge δm_{Q_M} as a dashed gray line for reference. **Red** dashed lines delimit the range of perturbative mass splitting at fixed $\Lambda_{\rm UV}/M_{\rm DM}$ ratio. **Purple** dashed lines show the contours of the fine-tuning among the different mass splittings as defined in Eq. (10.17). In particular, mass splittings above the line F.T.=1 are not fine tuned.

Appendix F.

Finally, for $c\tau_{\rm LCP} < 0.33$ cm the lightest charged WIMP decays promptly on collider scales and gives MIM signatures, such as the mono-W and mono-γ previously discussed. The choice for the threshold value to consider the signal as prompt corresponds to $c\tau/2$ of the CT for the $2_{1/2}$ WIMP in the minimal splitting scenario, which is a known benchmark where DT reconstruction starts to become challenging.

10.6.3 Two explicit examples: the Dirac $2_{1/2}$ and 3_1 WIMPs

At this point, let us examine in greater detail the parameter space spanned by δm_0 and δm_{Q_M} for the fermionic complex $2_{1/2}$ and 3_1 WIMPs, which have been explicitly described for both the muon collider and the DD searches in the minimal splitting scenario.

We recall that the $2_{1/2}$ and 3_1 are special WIMPs, since they are the only multiplets with maximal hypercharge compatible with our assumptions. In particular, for $2_{1/2}$ requiring $\delta m_{0,+} > 0$ automatically implies the neutral WIMP candidate is the lightest one. Perturbativity requires $\delta m_0 < 40$ MeV for the $n = 3_1$ WIMP. The narrower range of δm_0 for the 3_1 with respect to $2_{1/2}$ was expected from the higher dimensionality of $\mathcal{O}_0$ for $Y = 1$ as compared to $Y = 1/2$.

In Fig. 10.14 we show the constraints on the Dirac $2_{1/2}$ and 3_1 in the parameter space spanned by δm_0 and δm_{Q_M} coming from present DD experiments like Xenon1T and PANDAX-4T, as well as prospect from future high exposure Xenon experiments, *i.e.* LZ, XENONnT, DARWIN and DARWIN/G3. As we can see from Eq. (10.58), these bounds depend solely on the combination $\delta\mu \equiv 2\delta m_{Q_M} + (2Q_M - 1)\delta m_0$. In particular:

$$\sigma_{\rm SI} \approx 10^{-48}\ {\rm cm}^2 \begin{cases} \left(0.3 - \dfrac{\delta\mu}{1\ {\rm GeV}}\right)^2, & n = 2_{1/2}\ , \\ \left(0.2 + \dfrac{\delta\mu}{1\ {\rm GeV}}\right)^2, & n = 3_1\ . \end{cases} \tag{10.59}$$

In the region of low mass splitting for both $2_{1/2}$ and 3_1 the direct detection cross section lies below the neutrino floor. For $2_{1/2}$, Eq. (10.59) shows that large cancellations between EW loops and tree-level Higgs exchange occur around $\delta\mu \approx 300$ MeV, while for 3_1 the minimum $\sigma_{\rm SI}$ is obtained for $\delta\mu = 0$ and falls below the neutrino floor. To produce a direct detection cross section above the neutrino floor for the $2_{1/2}$ (3_1) we need $\delta\mu > 1.6$ GeV ($\delta\mu > 2.0$ GeV). PANDAX-4T already excludes mass splitting $\delta\mu < 20$ GeV ($\delta\mu < 30$ GeV) for the $2_{1/2}$ (3_1).

All in all, DD still leaves a large portion of parameter space unconstrained between the neutrino floor and the PANDAX-4T constraints. Remarkably, this region corresponds to mass splittings that do not corresponds to tuned adjustments of the three contributions to δm_0 and δm_+ that we have considered. Generic contribution from UV effects that modify the EW splitting are thus expected to populate this region currently not probed by DD experiment. The region of large splittings can be covered by large exposure Xenon experiments while the large portion of the parameter space lying below the neutrino floor should be taken as a major motivation for a future muon collider. For $2_{1/2}$ WIMP the neutrino floor region can be fully probed only via a combination of CTs, DTs and MIM searches that become relevant depending on the δm_+ value, as shown in Fig. 10.14. For the 3_1 WIMP DTs and CTs can exclude the entire neutrino floor region, while MIM and DT searches can be complementary to large exposure DD experiments to probe the rest of the parameter space.[5]

[5]While the plot in Fig. 10.14 show the possible regions in which DT can be reconstructed efficiently, they do not show if the reach is large enough to guarantee exclusion (or discovery) of the WIMP candidate. Recalling the discussion for the minimal splitting scenario, the general message is that for $\sqrt{s}$ sufficiently larger than twice the thermal DM mass DT searches will be powerful enough to probe the parameter space.

Chapter 11

Thermal decays of DM with LeptoQuarks

In this last Chapter we will investigate in detail another possible model of Dark Matter, based on its thermal decays. This scenario constitutes an important example of combined study of phenomenology of Dark Matter and Flavour Physics. In fact, the most important issue is the introduction of new interactions between DM and SM particles which are mediated by LeptoQuarks, whose general properties have been widely discussed in Chapter 8. This possibility is particularly interesting since it can in principle give a combined explanation to the observed DM abundance and to the anomalies observed in B-meson decays, with particular attention given to the $R(K)$, $R(K^*)$ ratios. In this sense, this model constitutes an important link between this Part and the previous ones of this Thesis.

In what follows, we will firstly describe the general ideas underlying this novel model. Then, we will write the generic form of the Boltzmann equations that describe these new DM interactions and study their features, deriving approximate solutions. Furthermore, we will discuss possible models that only involve one DM particle, then focusing on models where DM carries lepton number (e.g. a right-handed neutrino) and interacts with the SM via TeV-scale LQs (motivated by the flavour anomalies). Finally, we will study possible experimental signatures, with particular attention given to DD and ID searches.

My main contribution in this project concerns the computation of the decay widths of all the DM decays and the cross sections of all the thermal DM decays necessary for the implementation of the Boltzmann equations and for the study of freeze-out and freeze-in mechanisms. I have also contributed to the investigation of possible detection strategies at both Direct and Indirect detection experiments. All the details about these computations can be found in Sections 11.3, 11.5 and 11.6 of this Chapter.

11.1 The main motivations for Dark Matter and LeptoQuarks

The measured value of the DM energy density can in general be understood in terms of various hypothetical scattering processes occurring in the early universe. The most studied scenario considers $2 \leftrightarrow 0$ annihilation processes, where we count the number of DM-sector particles plus anti-particles in the initial and final state, without indicating the SM particles. Examples of such processes that change the number of DM (anti)particles by two units are

$$\mathrm{DM\,DM} \leftrightarrow \mathrm{SM\,SM}, \qquad \mathrm{DM\,DM} \leftrightarrow \mathrm{SM\,SM\,SM}. \tag{11.1}$$

A $\mathbb{Z}_2$ symmetry acting on the dark sector only usually justifies the presence of 2 DM (or, more generically, dark sector) particles and implies DM stability. These annihilations (or, more generically, co-annihilations) can lead to DM around the TeV scale as a freeze-out thermal relic, as we have seen for WIMPs in Chapter 9. A freeze-in non-thermal relic and other possibilities can also arise through the same interactions.

Processes more complicated than $2 \leftrightarrow 0$ received less attention: $2 \leftrightarrow 1$ scatterings, known as semi-annihilations, can arise in models where DM is stable, and behave similarly to annihilations (see [359–361] for recent references). $3 \leftrightarrow 2$ or $4 \leftrightarrow 2$ scatterings give qualitatively different behaviours sometimes dubbed 'cannibalistic DM' [362] or 'pandemic DM' [361], depending on the regime and on whether DM is in thermal equilibrium with the SM sector. These scatterings can reproduce the DM cosmological density for DM masses in the eV or MeV range, and can be justified by $\mathbb{Z}_3$ or higher symmetries.

Little attention has been received by the simplest possibility: $1 \leftrightarrow 0$ processes that could be dubbed 'decadent DM'. Examples of such transitions that change the DM number by one unit are

$$\mathrm{DM\,SM} \leftrightarrow \mathrm{SM\,SM}, \qquad \mathrm{DM} \leftrightarrow \mathrm{SM\,SM}, \qquad \mathrm{SM} \leftrightarrow \mathrm{DM\,SM}. \tag{11.2}$$

These processes arise in absence of a symmetry that forbids couplings between one DM particle and the SM sector. This is what can happen, for instance, in presence of interactions under which both DM and SM fields are charged, where imposing a symmetry that separates the dark sector from the SM might be not be a viable option. Prototypical examples of such a scenario include "sterile neutrino" DM, that can couple to leptons via a Higgs boson or a right-handed vector boson, or models where DM interacts with quarks via a LeptoQuark mediator. In both cases, the mediator carries a conserved SM charge and is allowed to couple to a DM-SM current. The possibility of DM coupled to LQs has been considered before [363–365], but usually in combination with an additional $\mathbb{Z}_2$ symmetry that forbids DM decay. Here we shall explore the *minimal* possibility that allows the mediator to simultaneously couple to DM-SM and pure SM currents.

Given that $1 \leftrightarrow 0$ processes are unavoidable in some theories, we show that, on the other hand, they can play a useful role in cosmology. Indeed, since DM needs to scatter on SM particles which are abundant in the primordial plasma, in order to reproduce the DM relic abundance these processes need a smaller cross section than that of the usual DM annihilations in Eq. (11.1), where DM needs instead to find a rare DM particle. We refer to the interactions in Eq. (11.2) as *"thermal decays"* because at finite temperature such transitions are conveniently described by Boltzmann equations with a thermal width Γ_T of DM. This terminology emphasises the obvious and potentially insurmountable problem: DM risks decaying too fast, since there is no separate dark sector with a conserved DM number. Interactions that lead to the thermal decays in Eq. (11.2) also lead to DM decays. To be quantitative:

- on one hand, the DM life-time $\tau_{\rm DM} = 1/\Gamma_{\rm DM}$ must surely be longer than the age of the Universe $\tau_{\rm DM} > T_U (\sim 10^{18}\,\mathrm{s})$. Many DM decay modes are more strongly constrained, requiring $\tau_{\rm DM} \gtrsim 10^{26}\,\mathrm{s}$ [366–368];
- on the other hand, thermal decays can give non-relativistic DM freeze-out[1] reproducing the cosmological DM abundance if their rate $\Gamma_{{\rm DM}T}$ is comparable to the Hubble rate H at temperatures around the DM mass M.

[1]Freeze-in needs a smaller $\Gamma_{{\rm DM}T}$. We do not consider relativistic DM freeze-out (analogous to neutrino decoupling), because the resulting DM abundance would be of order unity $Y_{\rm DM} \equiv n_{\rm DM}/s = 45\zeta(3) g_{\rm DM}/g_{\rm SM}(T_{\rm dec})\pi^4$ and thereby the DM cosmological abundance would be reproduced for warm DM with mass $M \approx 0.7\,\mathrm{eV}\, g_{\rm SM}(T_{\rm dec})/g_{\rm DM}$. To avoid problematic warm DM, the DM decoupling temperature $T_{\rm dec}$ must be mildly below the DM mass M. So we need a sizeable $\Gamma_{{\rm DM}T} \sim H$ at $T \sim M$.

As a result, the two requirements conflict easily and by many orders of magnitude: one needs

$$\Gamma_{\rm DM}/\Gamma_{\rm DM\mathit{T}} \lesssim 10^{-30}. \tag{11.3}$$

This gap by 30 orders of magnitude is such a strong constraint on possible models that this scenario is widely ignored. We nevertheless explore this possibility: while the simplest freeze-out picture in models with one DM particle is clearly ruled out, more complex possibilities with DM freeze-in or with multiple DM particles emerge and can lead to a peculiar phenomenology. We will investigate this issue at the end of this Chapter. A common feature of all viable models is the presence of some small coupling between DM and SM, which could be related to an underlying flavour structure.

11.2 The structure of Boltzmann equations for DM thermal decays

As usual, it is convenient to write the Boltzmann equation for $Y \equiv n/s$ in terms of $z = M/T$, where M is the DM mass, n is the DM number density, and s the total entropy. Including scatterings that involve two DM (the usual DM annihilations) and one DM (our thermal decays) the Boltzmann equation is

$$sHZz\frac{dY}{dz} = -2\gamma_{\rm ann}^{\rm eq}\left(\frac{Y^2}{Y_{\rm eq}^2}-1\right) - \gamma_{\rm dec}^{\rm eq}\left(\frac{Y}{Y_{\rm eq}}-1\right), \tag{11.4}$$

where the factor $Z = 1/(1+\frac{1}{3}\frac{d\ln g_{*s}}{d\ln T})$ can often be approximated as 1. In order to match the DM cosmological density, DM must freeze-out while non-relativistic, so that its thermal equilibrium abundance is Boltzmann suppressed, $n_i^{\rm eq} \simeq d_i(m_iT/2\pi)^{3/2}e^{-m_i/T}$, where d_i is the number of degrees of freedom for the particle i. The space-time density of scatterings $\gamma_i^{\rm eq}$ can thereby be simplified going to the non-relativistic limit. The initial state of the usual DM DM $\leftrightarrow$ SM SM annihilations becomes non-relativistic at low temperature. When considering more generic processes an unusual step is needed: identifying which side of the reaction becomes non-relativistic, namely the side that involves heavier particles. Defining as A, B the particles that can scatter at rest (they can be in the initial state or in the final state, depending on the kinematics of each process), the rate is approximated as

$$\gamma_i^{\rm eq} \overset{T\ll m}{\simeq} S n_A^{\rm eq} n_B^{\rm eq}\sigma_{i0} \qquad \text{where} \qquad \sigma_{i0} = \lim_{v\to 0}\langle\sigma_i v\rangle. \tag{11.5}$$

The initial-state symmetry factor S is only present when the non-relativistic particles are in the initial state. In the presence of multiple processes, the total $\gamma_i^{\rm eq}$ are computed by summing their rates. In the non-relativistic limit the Boltzmann equation becomes

$$\frac{dY}{dz} = -f_{\rm ann}(z)(Y^2 - Y_{\rm eq}^2) - f_{\rm dec}(z)\mathcal{B}(z)(Y - Y_{\rm eq}) \tag{11.6}$$

where we defined

$$f_i(z) \equiv \frac{s\sigma_{0i}}{HZz} \simeq \frac{\lambda_i}{z^2}\,, \qquad \lambda_i = M_{\rm Pl}M\sigma_{0i}\sqrt{\frac{\pi d_{\rm SM}}{45}}\,, \tag{11.7}$$

such that DM is in thermal equilibrium at $T \sim M$ if $\lambda_i \gg 1$. In the annihilation case, $\lambda_{\rm ann}$ is the usual dimension-less combination that helps obtaining approximate solutions in the limit $\lambda_{\rm ann} \gg 1$. The thermal scattering term contains an extra unusual but important factor $B(z)$, since it contains a Boltzmann suppression. Its non-relativistic approximation is

$$\mathcal{B} \equiv \frac{Y_A^{\rm eq}Y_B^{\rm eq}}{Y^{\rm eq}} \simeq \mathcal{R}\frac{d_{\rm DM}}{s}\left(\frac{MT}{2\pi}\right)^{3/2}\exp\left[-\frac{\Delta}{T}\right] \tag{11.8}$$

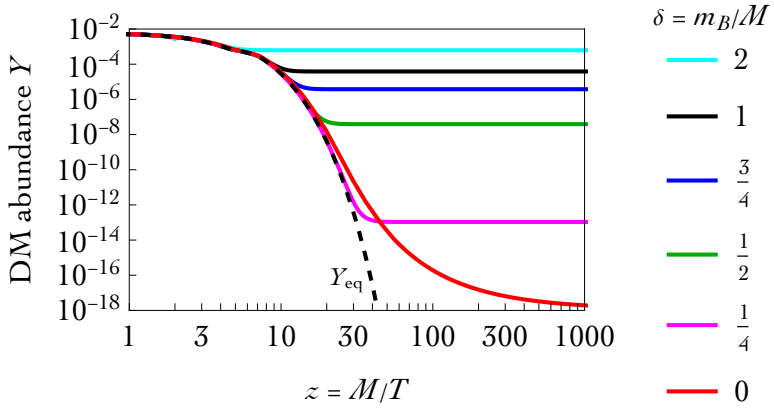

Figure 11.1: Evolution of the DM abundance $Y = n/s$ for thermal decays, assuming a heavier initial-state involving a SM particle with mass $m_B = \delta M$ and DM mass $M = 1\,\text{GeV}$. The case $\delta = 1$ corresponds to DM annihilations. For $\delta \neq 0$ we considered scatterings with heavier initial state, interaction strength $\lambda_{\rm dec} = 10^6$, degrees of freedom $d_{\rm DM} = 2$ and $d_{\rm B} = 4$. For $\delta = 0$ (red curve) we instead assumed $d_{\rm B} = 2$ and a smaller $\lambda_{\rm dec} = 10^4$: despite this it produces a lower DM relic abundance.

where

$$\mathcal{R} = \frac{d_A d_B}{d_{\rm DM}^2}\left(\frac{m_A m_B}{M^2}\right)^{3/2}, \qquad \Delta = m_A + m_B - M, \qquad \text{for heavier final state,} \tag{11.9}$$

$$\mathcal{R} = \frac{d_B}{d_{\rm DM}}\left(\frac{m_B}{M}\right)^{3/2}, \qquad \Delta = m_B, \qquad \text{for heavier initial state.} \tag{11.10}$$

The Δ factor that controls the exponential suppression is a combination of the masses M of DM, and m_A and m_B of the particles that become non-relativistic. The important observation is that, in general, $\Delta \neq M$. The DM mass M is the only relevant mass that controls how Boltzmann-suppressed the usual DM annihilations into light SM particles are.

One has $m_A = M$ and thereby $\Delta = m_B$ for processes where the initial state is heavier and hence non-relativistic. As we are considering $\text{DM}_A\,\text{SM}_B \leftrightarrow \text{SM}\,\text{SM}$ processes, Δ is the mass of the initial-state SM particle. If instead the final-state is heavier and hence non-relativistic, $\text{DM}\,\text{SM} \leftrightarrow \text{SM}_A\,\text{SM}_B$, Δ is given by a more complicated combination of masses.

In the presence of multiple process, the one with smallest Δ, i.e. least Boltzmann suppression, tends to dominate. The explicit expressions for Δ imply that the Boltzmann suppression is only avoided at the kinematical border where DM decay starts being kinematically allowed.

We see that the 'thermal decay' terms corresponds to an effective decay width $\Gamma_{{\rm DM}T} = B\sigma_{\rm dec0}$ that gets Boltzmann suppressed at low T. Indeed the rate of a true decay with width $\Gamma_{{\rm DM}T}$ would be $\gamma_{\rm dec} = \Gamma_{{\rm DM}T} n_1^{\rm eq} \text{K}_1(z)/\text{K}_2(z) \overset{z\gg 1}{\simeq} n_1^{\rm eq}\Gamma_{{\rm DM}T}$.

11.2.1 Approximate solution to the Boltzmann equations: freeze-out

The freeze-out abundance produced by DM annihilations or by thermal decays can be approximatively computed as follows. These processes reach thermal equilibrium if $\lambda_{\rm ann,dec} \gg 1$. Long before freeze-

out, *i.e.* at early $z \ll z_f$, we can expand Eq. (11.6) to first order in small $Y - Y_{\rm eq}$, finding for $\lambda_i \gg 1$

$$Y(z) - Y_{\rm eq} \overset{z\ll z_f}{\simeq} -\frac{z^2 Y'_{\rm eq}}{2\lambda_{\rm ann} Y_{\rm eq} + \lambda_{\rm dec}\mathcal{B}} = \frac{z(z-3/2)}{2\lambda_{\rm ann} + \lambda_{\rm dec}\mathcal{R}\, e^{z(1-\delta)}}, \tag{11.11}$$

where $\delta \equiv \Delta/M$ so that $\Delta/T = z\delta$. We see that $\delta < 1$ i.e. $\Delta < M$ enhances the effect of thermal decays compared to thermal annihilations. In general, the values of $\lambda_{\rm dec}/\lambda_{\rm ann}$ and of δ decide whether freeze-out is determined by annihilations or decays.

The final abundance is roughly approximated as $Y_\infty \sim Y_{\rm eq}(z_f)$ where the freeze-out temperature z_f is estimated imposing $Y - Y_{\rm eq} = cY_{\rm eq}$ with $c \approx 1$. In the usual case where only DM annihilations are present, namely when $\lambda_{\rm dec} = 0$, one gets the usual estimate for the freeze-out temperature $z_f \approx \ln\left(2d_{\rm SM}\lambda_{\rm ann}/z_f^2\right)$, and the usual freeze-out abundance $Y_\infty \sim z_f^2/2\lambda_{\rm ann}$. If instead only DM thermal decays are present, *i.e.* $\lambda_{\rm ann} = 0$, one gets

$$z_f \approx \frac{1}{2\delta} W\left[\frac{\delta}{\pi}\left(\frac{45c\lambda_{\rm dec}\mathcal{R}d_{\rm DM}}{4\pi^3 d_{\rm SM}}\right)^2\right], \tag{11.12}$$

where $\delta = \Delta/M$ and $W(x)$ is the 'product log' function, that solves $x = We^W$ and is roughly approximated by $\ln x$ as $x \to \infty$. The final DM abundance is approximated as[2]

$$Y_\infty \approx Y_{\rm eq}(z_f) \sim \lambda_{\rm dec}^{-1/\delta}, \tag{11.13}$$

showing that thermal decays need a smaller value of $\lambda \gg 1$ if $\delta < 1$, i.e. $\Delta < M$. Fig. 11.1 shows examples of numerical solutions to the Boltzmann equations for fixed interaction strength $\lambda_{\rm dec}$ and varying δ: we see that smaller δ leads to a lower DM final abundance in agreement with Eq. (11.13).

Note that thermal decays are maximally efficient for $\delta \to 0$. A look at kinematics shows that this limit corresponds to processes where DM scatters with a much lighter SM particle B, such as the photon. Thereby this case only arises near to the dangerous kinematical border where the phase space for DM decays starts opening up. In this case, the cancellation of IR divergences between real and virtual effects starts being relevant. In particular, we have that $\mathcal{B} = Y_B^{\rm eq}$ is constant (so that the non-relativistic limit used in previous approximation no longer holds), decoupling happens at $z_f \approx \sqrt{\lambda_{\rm dec} Y_B^{\rm eq}}$ (no longer log-suppressed) and the subsequent evolution is non-negligible leading to

$$Y_\infty \approx Y_{\rm eq}(z_f) e^{-\lambda_{\rm dec} Y_B^{\rm eq}/z_f} \approx \frac{45 d_{\rm DM} (\lambda_{\rm dec} Y_B^{\rm eq})^{3/4}}{2^{5/2}\pi^{7/2} d_{\rm SM}} e^{-2\sqrt{\lambda_{\rm dec} Y_B^{\rm eq}}}. \tag{11.14}$$

This case corresponds to the red line in Fig. 11.1.

Let us next discuss what these results mean in practice. We can approximate a non-relativistic cross section at $T \sim M$ as

$$\sigma_0 \approx g_{\rm SM}^p \begin{cases} g_{\rm DM}^2/4\pi M^2 & \text{dimension-4 interaction with coupling } g_{\rm DM} \\ G_{\rm DM}^2 M^2/4\pi & \text{dimension-6 interaction with coupling } G_{\rm DM} \end{cases} \tag{11.15}$$

where the interaction of DM with the SM sector is described by some dimension-4 interaction with dimension-less coupling $g_{\rm DM}$, or by some dimension-6 operator with coefficient $G_{\rm DM}$ with mass dimension -2. Depending on how many particles are involved in this DM interaction, extra couplings can be needed to obtain a cross-section, so that we add extra powers p of a generic SM coupling (such as e

[2]This expression is accurate up to order unity factors, as we neglected evolution at $z > z_f$.

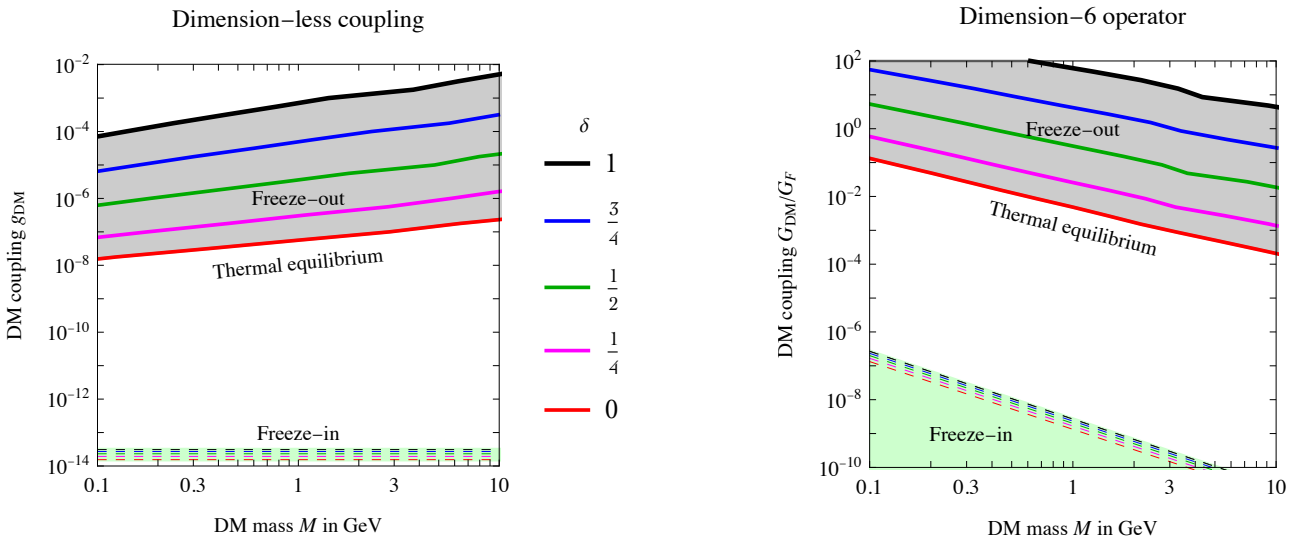

Figure 11.2: Values of the DM coupling to the SM needed to reproduce the DM cosmological abundance via thermal decays with exponent $\delta = \Delta/M$. The case $\delta = 1$ reproduces DM annihilations. We assume the cross section in Eq. (11.15) with coupling $g_{\rm SM} = 1$ and other specifications as in Fig. 11.1. **Left:** DM with a dimension-less coupling g_{DM} to the SM. **Right:** DM coupled via a dimension-6 operator with coefficient $G_{\rm DM}$. Its freeze-in estimate is the minimal contribution that arises if $T_{\rm RH} \sim M$.

or g_2 or f_π/m_π). Since its power is model-dependent, for the purpose of the present parametrisation we assume $g_{\rm SM} \sim 1$.

The condition $\lambda \gtrsim \lambda_{\rm min}$ translates into

$$g_{\rm DM} \gtrsim 10^{-9}\sqrt{\frac{\lambda_{\rm min} M}{\rm GeV}}, \qquad G_{\rm DM} \gtrsim 10^{-4} G_F \sqrt{\lambda_{\rm min}} \left(\frac{\rm GeV}{M}\right)^{3/2} \qquad \text{(thermal equilibrium)} \tag{11.16}$$

where G_F is the Fermi constant. Both annihilations and thermal decays need at least to reach thermal equilibrium, corresponding to $\lambda_{\rm min} \sim 1$. DM annihilations give the freeze-out abundance $Y_\infty \sim 1/\lambda_{\rm ann}$, so the cosmological DM abundance is reproduced for $\lambda \sim M/\,{\rm eV} \gg 1$, corresponding to

$$g_{\rm DM} \sim 10^{-4}\frac{M}{\rm GeV}, \qquad G_{\rm DM} \sim 10\, G_F \frac{\rm GeV}{M} \qquad \text{(DM annihilations)}. \tag{11.17}$$

For $\delta < 1$, DM thermal decays need DM couplings smaller than in Eq. (11.17), possibly down to the minimal value in Eq. (11.16) for $\lambda_{\rm min} \sim 1$, reached in the limit $\delta \ll 1$, *i.e.* $\Delta \ll M$ (where DM thermal decays become maximally efficient).

Fig. 11.2 shows the values of $g_{\rm DM}$ and $G_{\rm DM}$ needed to reproduce the DM relic abundance via freeze-out of thermal decays, assuming $g_{\rm SM} = 1$, considering different values of $0 \leq \delta \leq 1$ (solid curves). The needed values range between those characteristic freeze-out of DM annihilations ($\delta = 1$, Eq. (11.17) and black curves in Fig. 11.2) down to those needed to achieve thermal equilibrium ($\delta = 0$, Eq. (11.16) and red curves in Fig. 11.2).

11.2.2 Approximate solution to the Boltzmann equations: freeze-in

If DM couplings are so small that it never thermalized, one can instead assume a vanishing initial DM abundance (needless to say, this is a more questionable assumption than thermal equilibrium) and match the small amount of generated DM with the observed DM abundance.

The final DM abundance produced by freeze-in is obtained by setting $Y = 0$ in the right-handed side of Eq. (11.6). One gets

$$Y_\infty = \int_0^\infty \frac{dz}{z} \frac{\gamma_{\rm dec}^{\rm eq}}{Hs} \sim \max_T \frac{\gamma_{\rm dec}^{\rm eq}}{Hs} \sim \max_T \frac{\Gamma_{{\rm DM}T}}{H}. \tag{11.18}$$

The DM abundance suggested by cosmology, $Y_\infty \sim {\rm eV}/M$, is thereby reproduced for a comparably small value of $\Gamma_{{\rm DM}T}/H$. Unlike in the freeze-out case, replacing DM annihilations with DM thermal decays does not lead to significant changes in the dynamics. What changes is that the needed scattering can be partially mediated by SM couplings, that can have significant values $g_{\rm SM} \sim 1$. Freeze-in can be dominated at low $T \sim M$ or at high $T \gg M$ depending on the dimension of the interaction:

- If DM has a dimensionless coupling $g_{\rm DM}$, the rate $\gamma_{\rm dec}^{\rm eq} \sim g_{\rm SM}^2 g_{\rm DM}^2 T^4$ at $T \gg M$ gives a DM abundance Y_∞ dominated at $T \sim M$, $Y_\infty \sim g_{\rm SM}^2 g_{\rm DM}^2 M_{\rm Pl}/M$. This matches the cosmological DM abundance for

$$g_{\rm DM} g_{\rm SM} \sim \sqrt{T_0/M_{\rm Pl}} \sim 10^{-15} \qquad \text{(freeze-in of thermal decays)}. \tag{11.19}$$

  Precise order one factors depend on the process (such as a scattering or a decay, see [369] for examples). A general expression, valid up to these process-dependent order one factors, is obtained by inserting in Eq. (11.18) the universal non-relativistic limit

$$Y_\infty \approx \int_0^\infty dz\, f_{\rm dec} B Y_{\rm eq} = \lambda_{\rm dec} \frac{2025 d_{\rm DM}^2 R_B}{32\pi^7 d_{\rm SM}^2 (1+\delta)^2}. \tag{11.20}$$

  This is plotted in the left panel of Fig. 11.2 assuming the cross section in Eq. (11.15) with $g_{\rm SM} \sim 1$.

- If DM has a non-renormalizable interaction $G_{\rm DM}$, one has $\gamma_{\rm dec}^{\rm eq} \sim g_{\rm SM}^2 G_{\rm DM}^2 T^8$ so that DM production is dominated at $T \gg M$: the result depends on the full model. For example, the non-renormalizable operator could be produced by a mediator with mass $M_{\rm med}$ and renormalizable couplings. If the reheating temperature satisfies $T_{\rm RH} \gg M_{\rm med}$ the DM abundance is dominated at $T \sim M_{\rm med}$ and can be approximated in a way similar to Eq. (11.18). If $M \ll T_{\rm RH} \ll M_{\rm med}$ the DM abundance is dominated at $T \sim T_{\rm RH}$, $Y_\infty \sim g_{\rm SM}^2 G_{\rm DM}^2 M_{\rm Pl} T_{\rm RH}^3$. Eq. (11.18) provides the minimal contribution that arises at $T \sim M$ if $T_{\rm RH} \sim M$, plotted as upper bound in the right panel of Fig. 11.2.

11.3 DM with lepton number and freeze-in

We are looking for theories where DM number is significantly violated, but where, at the same time, DM is very long lived. Let us consider DM coupled to two SM particles with masses m_1 and m_2:

$$\text{DM SM}_1 \text{ SM}_2. \tag{11.21}$$

To avoid the most immediate danger, the tree-level decay ${\rm DM} \to {\rm SM}_1\, {\rm SM}_2$, we assume $M < m_1 + m_2$ so that this process is kinematically blocked. We also need to assume $M \sim m_{1,2}$, so that the SM particles take active part in DM decoupling. Finally, if the coupling (11.21) is large, it might be necessary to assume $M > |m_1 - m_2|$, to avoid potentially problematic decays of SM particles into DM.

Now, the next danger is represented by virtual decays such as ${\rm DM} \to {\rm SM}_1\, {\rm SM}_2^*$. The $\rm SM_2$ particle with mass m_2 and d_2 degrees of freedom is off-shell. Moreover, $\rm SM_2^*$ has quadri-momentum k_2 with

particle	life-time	mass	$\epsilon = \Gamma/m$	main decays
e	∞	0.511 MeV	0	stable
$p = duu$	$\gtrsim 10^{34}$ yr	938.3 MeV	$\lesssim 10^{-66}$	stable
$n = ddu$	880 s	939.6 MeV	$0.8\ 10^{-27}$	$pe\bar{\nu}$
μ	$2.2\,10^{-6}$ s	105.7 MeV	$2.8\ 10^{-18}$	$e\nu_\mu\bar{\nu}_e$
$K^- = s\bar{u}$	$1.2\,10^{-8}$ s	493.7 MeV	$1.1\ 10^{-16}$	$\mu\bar{\nu}_\mu, \pi^-\pi^0$
$\pi^- = d\bar{u}$	$2.6\,10^{-8}$ s	139.6 MeV	$1.8\ 10^{-16}$	$\mu\bar{\nu}_\mu$
$\Omega^- = sss$	$0.8\,10^{-10}$ s	1672 MeV	$4.8\,10^{-15}$	$\Lambda K^-, \Xi\pi$
$\Sigma^+ = uus$	$0.8\,10^{-10}$ s	1189 MeV	$6.9\,10^{-15}$	$p\pi^0, n\pi^+$

Table 11.1: SM particles with lowest narrowness $\epsilon = \Gamma/m$. One component out of multiplets is selected.

$x \equiv k_2^2/m_2^2 < 1$ and decays into lighter SM particles $\mathrm{SM}_{3,4,...}$ not directly coupled to DM. The DM decay width averaged over polarizations then is

$$\Gamma(\mathrm{DM} \to \mathrm{SM_1 SM_{3,4...}}) = \int \frac{\mathrm{dx}\sqrt{\mathrm{x}}}{(\mathrm{x}-1)^2}\,\Gamma(\mathrm{DM} \to \mathrm{SM_1 SM_2^*})\frac{\Gamma(\mathrm{SM_2^*} \to \mathrm{SM_{3,4,...}})}{\pi \mathrm{d_2 m_2}}. \tag{11.22}$$

The integral is dominated by the highest available $x_{\max} < 1$, so that some decay modes of SM_2 might be closed for SM_2^*. The off-shell decay width is thereby approximated as

$$\Gamma(\mathrm{DM} \to \mathrm{SM_1 SM_{3,4...}}) \approx \frac{\epsilon_2}{4\pi}\frac{\Gamma(\mathrm{DM} \to \mathrm{SM_1 SM_2^*})}{1-\mathrm{x_{max}}}, \qquad \epsilon_\mathrm{i} \equiv \mathrm{BR_i}\frac{\Gamma_\mathrm{i}}{\mathrm{m_i}}, \tag{11.23}$$

where Γ_i is the total decay width of SM_i, and BR_i (possibly equal to 1) its branching ratios into light enough particles (such as photons, neutrinos, electrons). Each SM_i particle has a value of ϵ_i, and its smallness is a figure-of-merit for coupling long-lived DM to SM particles. Table 11.1 lists the most narrow SM particles. All of them are lighter than about a GeV (heavier weak-scale SM particles decay too fast for our purposes), so DM too has to be similarly light. At sub-GeV energy, physics is described by baryons and mesons, rather than by quarks. In order to possibly reproduce the DM abundance via freeze-out, DM interactions cannot be suppressed by a scale much above the weak scale.

The electron and proton are stable in view of conservation of charge and baryon numbers. The other SM particles undergo weak decays suppressed by $(m/v)^4$ and possibly by phase space (the neutron) or by flavour (the K, Ω, Σ in Table 11.1). DM decays can be suppressed by $\epsilon \sim 10^{-15}$, far from the needed $\epsilon < 10^{-30}$. One dose of off-shell vaccine does not protect DM stability well enough.

However, two doses of the off-shell vaccine can give enough protection. Let us assume that DM is coupled to two SM particles as in Eq. (11.21) and its mass is $M < m_1, m_2$. Then doubly-virtual tree-level decays $\mathrm{DM} \to \mathrm{SM_1^* SM_2^*}$ are suppressed by $\epsilon_1\epsilon_2 \sim 10^{-30}$, corresponding to two weak interactions. An example in this sense is DM coupled to $\mu\pi$, see Fig. 11.3a.

Nevertheless, even if DM only directly couples to massive SM particles, so that its tree-level decay channels are suppressed, one-loop effects can give DM decays into light SM particles. DM that couples to a particle/anti-particle pair (such as $\pi^+\pi^-$) decays at one loop level into photons, $\mathrm{DM} \to \gamma\gamma$, with rate suppressed by a QED loop factor, $\epsilon \sim (e/4\pi)^4 \sim 10^{-5}$. This is far away from the needed 10^{-30} suppression. DM that couples to $\pi^\pm\ell^\mp$ decays as $\mathrm{DM} \to \nu\gamma$ at one loop level (see Fig. 11.3b), with rate suppressed by an electroweak loop factor, $\epsilon \sim (f_\pi/4\pi v)^4 \sim 10^{-18}$, but still below the needed 10^{-30}. Loop decays are present because this DM has lepton number, which is carried by nearly-massless neutrinos. Let us then discuss a minimal model that achieves the level of stability needed for freeze-in.

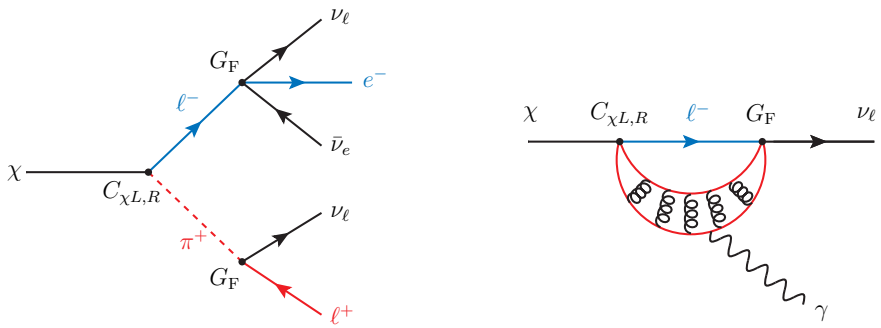

Figure 11.3: Decays of DM coupled to $\mu\pi$. **Left:** via off-shell μ and/or π. **Right:** at loop level. The $q\bar{q}$ quarks (in red) form QCD bound states, including pions.

11.3.1 Mediator models

We consider DM to be a fermion χ with no SM gauge interactions and lepton number $L = 1$. This corresponds to a sterile neutrino in presence of a Yukawa coupling χLH. This is a well-known allowed DM candidate if it has keV-scale mass: it can be cosmologically produced, compatibly with bounds on $\chi \to \nu\gamma$ decays [370], as freeze-in, via resonant oscillations or via the decay of an extra scalar.

We instead explore the possibility that the SM neutral lepton singlet χ has a heavier mass M and has gauge interactions in an appropriate extension of the SM. The natural possibilities allowed by group theory are the following:

- A $(\bar{\chi}\gamma_\mu \ell_R)\, W_R^\mu$ interaction in models where the right-handed W_R boson is part of an extra $\mathrm{SU}(2)_R$. The full couplings of the W_R mediator to fermions are

$$\mathcal{L}_{W_R} = \left(g_\chi^i\, \bar{\ell}_R^i \gamma_\mu \chi + g_R^{ij}\, \bar{u}_R^i \gamma_\mu d_R^j \right) W_R^\mu + \text{h.c.} \tag{11.24}$$

  where i, j are flavour indices. Integrating out the W_R generates

$$\mathcal{L}_{W_R}^{\rm eff} = -C_{\chi R} (\bar{\chi}\gamma^\mu \ell_R)(\bar{d}_R \gamma_\mu u_R) + \cdots \tag{11.25}$$

  with $C_{\chi R} = g_\chi g_R / M_{W_R}^2$.

- A $(\bar{u}_R \gamma_\mu \chi)\, U_1^\mu$ interaction with a vector leptoquark U_1^μ (see Table 8.1 for the corresponding quantum numbers), whose couplings to fermions are

$$\mathcal{L}_{\mathcal{U}} = \left(g_\chi^i\, \bar{u}_R^i \gamma^\mu \chi + g_R^{ij}\, \bar{d}_R^i \gamma^\mu \ell_R^j + g_L^{ij}\, \bar{Q}_L^i \gamma^\mu L_L^j \right) U_{1\mu} + \text{h.c.} \tag{11.26}$$

  We will discuss in what follows how a flavour structure can arise. Hereafter, we also drop the subscript 1 for simplicity, so that $\mathcal{U}^\mu \equiv U_1^\mu$. Note that the latter term in (11.26) has been considered as a possible interpretation of the flavour anomalies in decays of B mesons, adding interest to the possibility of obtaining DM in this context. Integrating out the leptoquark at tree level generates

$$\mathcal{L}_{\mathcal{U}}^{\rm eff} = -C_{\chi R} (\bar{\chi}\gamma^\mu \ell_R)(\bar{d}_R \gamma_\mu u_R) + 2 C_{\chi L} (\bar{\chi} L_L)(\bar{Q}_L u_R) - C_{LL} (\bar{s}_L \gamma^\mu b_L)(\bar{\mu}_L \gamma_\mu \mu_L) + \cdots \tag{11.27}$$

  with $C_{\chi R} = \frac{g_\chi g_R}{M_{\mathcal{U}}^2}$, $C_{\chi L} = \frac{g_\chi g_L}{M_{\mathcal{U}}^2}$, and $C_{LL} = \frac{g_L^{22} g_L^{32}}{M_{\mathcal{U}}^2}$, which reproduces the B-anomalies for $C_{LL} \approx -1.4\, V_{tb} V_{ts}^* \alpha_{\rm em} / 4\pi v^2 = 1.4/(36\,\text{TeV})^2$ [371].

- Alternatively, interactions can be mediated by a variety of scalar fields. An example is the already mentioned Yukawa coupling with a Higgs doublet, $H^c\bar{L}_L\chi$, in which case the DM can be identified with a right-handed neutrino [370]. Scalar leptoquarks, instead, can couple χ to SM quarks if they have suitable quantum numbers (see again Table 8.1 for this purpose). The only two possibilities that are able to induce a DM-SM^3 interaction are S_1 and $\tilde{R}_2$, with

$$\mathcal{L}_{S_1} = (g_\chi \bar{d}_R \chi + g_L \bar{Q}_L \varepsilon L_L^c + g_R \bar{u}_R e_R^c) S_1 + \text{h.c.}, \tag{11.28}$$

$$\mathcal{L}_{\tilde{R}_2} = (g_\chi \bar{Q}_L \chi + g_L \bar{d}_R L_L \varepsilon) \tilde{R}_2 + \text{h.c.} \tag{11.29}$$

The full list of possible DM couplings to one lepton and two quarks, all of which can be generated by the tree-level exchange of one of the previous mediators, is [372]

$$\begin{aligned} \mathcal{L}_{\rm DM}^{\rm eff} = &- C_{\chi R}(\bar{\chi}\gamma^\mu \ell_R)(\bar{d}_R \gamma_\mu u_R) + 2C_{\chi L}(\bar{\chi} L_L)(\bar{Q}_L u_R) \\ &- C'_{\chi L}(\bar{L}_L \chi)\varepsilon(\bar{Q}_L d_R) - C''_{\chi L}(\bar{Q}_L \chi)\varepsilon(\bar{L}_L d_R). \end{aligned} \tag{11.30}$$

We expect that the various operator coefficients satisfy $C_i \lesssim (\text{TeV})^{-2}$ because the charged or colored mediators that generate the effective interactions are generically constrained to be heavier than the TeV scale by collider bounds. We will sometimes collectively denote these couplings as $4G_{\rm DM}/\sqrt{2}$, including a normalization factor for ease of comparison with the Fermi constant G_F.

Below the QCD scale $\mathcal{L}_{\rm DM}^{\rm eff}$ becomes effective couplings to pions, $\chi\ell\pi$, and to heavier mesons (such as ρ and excited pions), as well as couplings to baryons, $\chi\ell\bar{p}n$. Heavier mesons give negligible effects in cosmology and are not subject to significant bounds, despite that kinematical space for their tree-level decays is open. The coupling to baryons can have more significant effects, since baryons remain as relics at $T \ll m_{p,n}$ thanks to the baryon asymmetry (DM couplings to quarks never lead to DM coupled to baryons but not to pions). Using chiral perturbation theory (see Appendix G) the coupling to pions is obtained substituting the quark terms in the effective operator Eq. (11.30) with pion terms with the same transformation properties:

$$\begin{aligned} \mathcal{L}_{\rm DM}^{\pi} \;=\; & \frac{C_{\chi R}}{\sqrt{2}}(\bar{\chi}\gamma^\mu \ell_R)\Big[f_\pi\, D_\mu \pi^+ + i(\pi^0 \partial_\mu \pi^+ - \pi^+ \partial_\mu \pi^0) + \cdots\Big] + \\ & -iC_{\chi L} f_\pi B_0 \Big[\sqrt{2}(\bar{\chi}\ell_L)\pi^+ + (\bar{\chi}\nu_L)\pi^0 + \cdots\Big] + \text{h.c.} \end{aligned} \tag{11.31}$$

where $f_\pi = 93\,\text{MeV}$, $B_0 \approx 22 f_\pi$ is the quark condensate, D is the gauge-covariant derivative and we will not need higher orders. We assumed DM couplings to right-handed quarks, but this information is lost in DM coupling to pions (the suppression is of order $f_\pi/\Lambda_{\rm QCD} \sim 1$). This will remove a suppression of weak loops.

11.3.2 DM decays (at loop and tree level)

We start discussing loop decays into massless particles, which are always kinematically allowed. The EW interactions couple pions to the charged lepton current (the SM Lagrangian is written in Eq. (G.2) in Appendix G). As a result leptonic DM with the interactions of Eq. (11.30) acquires at one loop a

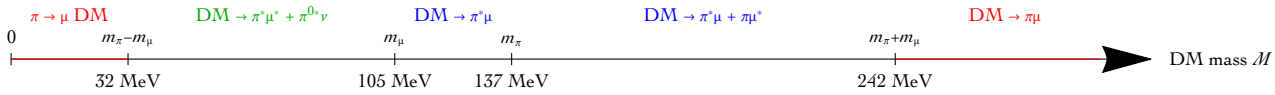

Figure 11.4: DM with lepton number coupled to $\mu\pi$: kinematical thresholds for most dangerous decays. A $*$ denotes a virtual particle, and thereby a Γ/M suppression. We here neglected the mass difference between charged and neutral pions.

negligible mass mixing between DM and neutrinos[3], and a mixed magnetic moment with neutrinos:[4]

$$\mathcal{L}_{\rm eff} = Ae(\bar{\chi}\sigma_{\mu\nu}\nu)F_{\mu\nu} \qquad \text{with} \qquad A \approx \frac{G_F\Lambda_{\rm QCD}^2}{(4\pi)^2}(m_\ell C_{\chi R} + \Lambda_{\rm QCD}C_{\chi L}). \tag{11.33}$$

A precise estimate is not possible, as the exact loop integral is dominated by momenta around the QCD scale where all resonances contribute. The resulting DM decay rates are

$$\Gamma(\mathrm{DM}\to\nu\gamma) = \frac{\mathrm{e^2A^2M^3}}{2\pi} \sim \frac{1}{4\,\mathrm{yr}}\frac{\mathrm{M^3}}{\mathrm{m_\pi^3}}\left(\frac{\mathrm{C_{\chi L}} + \mathrm{C_{\chi R}m_\ell/\Lambda_{QCD}}}{\mathrm{G_F}}\right)^2. \tag{11.34}$$

Let us now discuss tree-level decays. They can a) dominate over loop decays if DM $\to \ell\pi$ is kinematically open, or b) be comparable to loop decays if one of the two SM particles needs to be off-shell to kinematically open the decay, or c) be negligible compared to loop decays if both $\ell^*\pi^*$ need to be off-shell. Let us discuss in more detail the case of DM coupled to $\ell = \mu$ as a concrete example. Fig. 11.4 shows the main kinematical regimes. In the co-stability range, namely

$$34\,\mathrm{MeV} = m_\pi - m_\mu < M < m_\pi + m_\mu = 245\,\mathrm{MeV}, \tag{11.35}$$

all tree-level decays among χ, π, μ are closed. DM heavier than $m_\pi + m_\mu$ decays at tree level as $\chi \to \mu^\pm\pi^\mp$. One of these particles must be off shell if the DM mass M is in the range $m_\mu < M < m_\pi + m_\mu$, suppressing the DM tree-level decay rate by a $\epsilon_\mu, \epsilon_\pi \sim 10^{-17}$ factor. Furthermore, $\pi \to \mu^*\chi \to e\bar{\nu}_e\nu_\mu\chi$ decays are suppressed by $\epsilon_\mu \sim 10^{-16}$, and $\mu \to \pi^*\chi = e\bar{\nu}_e\chi$ decays by $\epsilon_\pi \sim 10^{-19}$. So the bounds $\mathrm{BR}(\pi \to \mu\chi) \lesssim 10^{-7}$ are easily satisfied. If $m_\pi - m_\mu < M < m_\mu$ (in green in Fig. 11.4), the tree-level $\chi \to \mu^*\pi^*$ decay rate is suppressed by $\epsilon_\pi\epsilon_\mu \sim 10^{-33}$ as both μ and π must be off-shell. However, in this case, loop decays dominate.

Now, Fig. 11.5 shows the life-time of DM coupled to left-handed (left panel) and right-handed (right panel) leptons ℓ and quarks. We fix a reference value for $C_{\chi R}$ and $C_{\chi L}$ equal to $4G_F/\sqrt{2}$. The solid curve in the left panel is the contribution from tree-level decays $\chi \to \nu_\ell\pi^0$. For $M < m_{\pi_0}$ this channel is kinematically closed and therefore the relevant contribution is into $\nu_\ell\gamma\gamma$ via the off-shell

[3] In the pion effective theory the mass mixing $\mu\,\chi\nu$ + h.c. is UV-divergent and estimated as

$$\mu \sim \frac{C_{\chi R}f_\pi^2 m_\ell g_2^2\Lambda_{\rm UV}^2}{(4\pi M_W)^2} \sim \mathrm{meV}\frac{m_\ell}{m_\mu}\frac{C_{\chi R}}{G_F}. \tag{11.32}$$

The UV cut-off has been estimated as $\Lambda_{\rm UV}^2 \sim M_W^2/(4\pi)^2$. Indeed, in the high-energy theory above the QCD and EW scales, the analogous effect is a log RG mixing between two dimension 6 operators: Eq. (11.30) at two loop induces $\chi LHH^\dagger H$, so $\mu \sim C_{\chi R}v^3 y_\ell y_u y_d g_2^2(4\pi)^4$. The extra $HH^\dagger$ and thereby $y_u y_d$ terms appear because, in the full theory, DM is coupled to right-handed quarks.

[4] Above the QCD and EW scales, the analogous effect is negligible: the dimension-6 operator of Eq. (11.30) induces at 2 loops the operator $(\bar{\chi}\sigma_{\mu\nu}LH)B^{\mu\nu}HH^\dagger$.

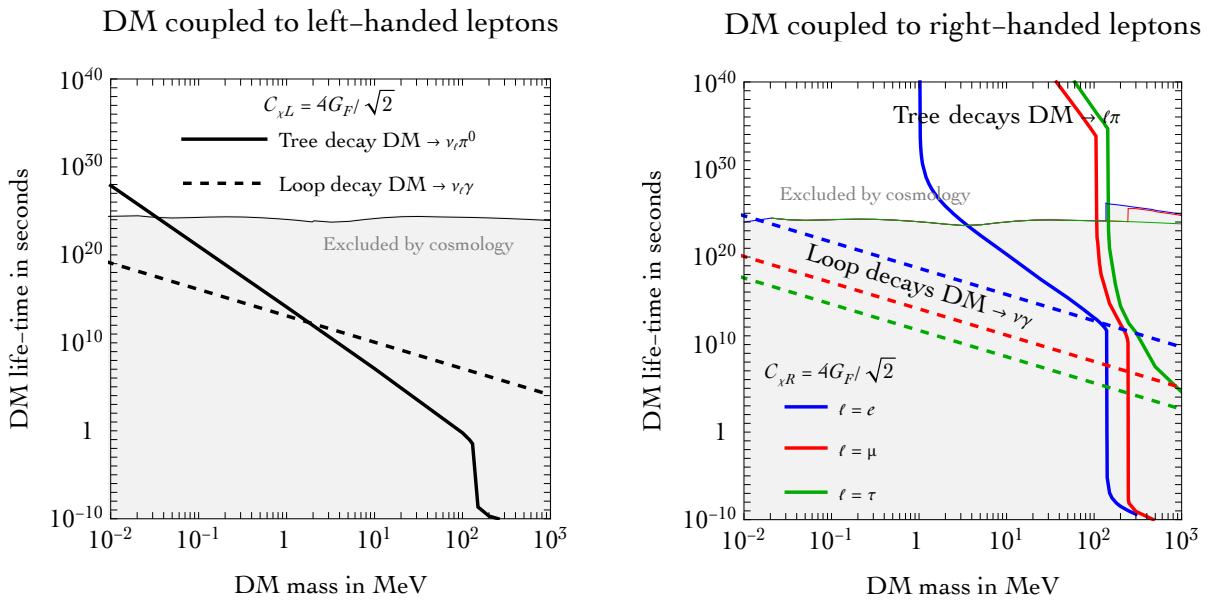

Figure 11.5: Life time of DM χ coupled to a lepton ℓ and to quarks. **Left**: DM coupled to left-handed leptons with coupling $C_{\chi L} = 4G_F/\sqrt{2}$. The dashed curve is the contribution from DM loop decays into $\nu_\ell\gamma$; the continuous curve is the contribution from tree-level decays into $\nu_\ell\pi^0 \to \nu_\ell\gamma\gamma$. **Right:** DM coupled to right-handed leptons with coupling $C_{\chi R} = 4G_F/\sqrt{2}$. Curves can be rescaled for different couplings taking into account that life-times scale as $1/C^2_{\chi L,\chi R}$, while the bounds from cosmological DM stability and from CMB do not depend on DM couplings, and are discussed in the text.

π_0. The dashed curve is the contribution from DM loop decays $\chi \to \nu_\ell\gamma$ which is independent on the lepton mass, as shown in Eq. (11.34), and is the dominant decay channel for $M < 2$ MeV. In the right-panel of the same figure, the solid curves indicate the contributions from tree-level decays, $\chi \to \ell\pi$. These predictions depend on the leptons (blue, red and green are for e, μ and τ respectively) and the different features are due to the kinematical thresholds as discussed in details above. The dashed curves show the contribution from DM loop decays into $\nu_\ell\gamma$, which depend on the lepton mass since we need a mass insertion to flip the chirality of the lepton (see Eq. 11.34). For a given lepton the loop decay is dominant at $M < m_\ell + m_\pi$ and therefore the co-stability regime is not important from the phenomenological point of view.

For life-times longer than the age of the Universe, limits from PLANCK and VOYAGER II apply. These bounds are shown as grey areas in the figure. For DM coupled to left-handed leptons, since there is always a neutrino that does not release energy into the plasma, we rescale the PLANCK bound for the channel DM $\to \gamma\gamma$ given in fig. 7 of [373]. In particular for $M > 2$ MeV we rescale the limit by a factor 2/3 (the final state is $\nu_\ell\gamma\gamma$ for both on- and off-shell π_0), while for lighter DM by a factor 1/2 since the loop decay into $\nu_\ell\gamma$ dominates. The bound is more complicated for DM coupled to right-handed leptons. For $M < m_\ell + m_\pi$ the dominant channel is into $\nu_\ell\gamma$, so we follow the same procedure described above. For $M > m_\ell + m_\pi$ the final state after the decay of the pion and lepton always involves a e^-e^+ pair with a given number of neutrinos (3, 5 and 7 for e, μ and τ respectively). We use the PLANCK and VOYAGER II limits given in [367, 368] for the decay channel $\chi \to e^+e^-$ rescaling them by a factor 2/5, 2/7 and 2/9 for e, μ and τ respectively. This is a good approximation for PLANCK, since the deposited energy matters, while for VOYAGER II this is a rough approximation

process	Boltzmann factor Δ
$\chi\ell^\pm \leftrightarrow \pi^\pm\gamma$	$\max(m_\ell, m_{\pi^\pm} - M)$
$\chi\gamma \leftrightarrow \ell^\pm\pi^\mp$	$m_\ell + m_{\pi^\pm} - M$
$\chi\pi^\pm \leftrightarrow \ell^\pm\gamma$	$m_{\pi^\pm}$
$\chi\pi^\pm \leftrightarrow \ell^\pm\pi^0$	$\max(m_{\pi^\pm}, m_\ell + m_{\pi^0} - M)$
$\chi\pi^0 \leftrightarrow \ell^\pm\pi^\mp$	$\max(m_{\pi^0}, m_\ell + m_{\pi^\pm} - M)$
$\chi\ell^\pm \leftrightarrow \pi^\pm\pi^0$	$\max(m_\ell, m_{\pi^0} + m_{\pi^\pm} - M)$
$\bar\chi\chi \leftrightarrow \ell^-\ell^+$	$\max(M, 2m_\ell - M)$
$\bar\chi\chi \leftrightarrow \pi^-\pi^+$	$\max(M, 2m_\pi - M)$

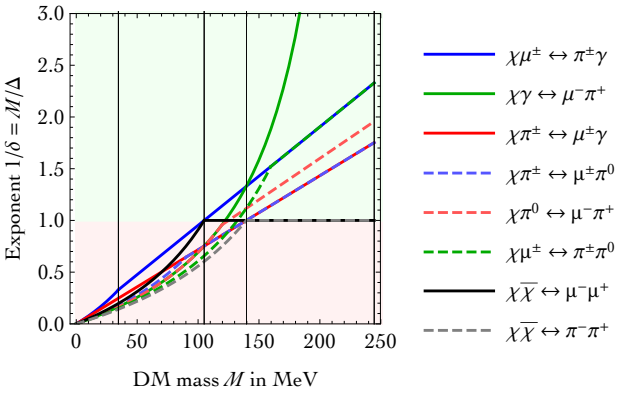

Figure 11.6: Assuming DM coupled to $\ell\pi$, we list the main processes that change by one unit the DM number. Their contribution to cosmological DM freeze-out is controlled by the exponent $\delta = \Delta/M$, plotted in the figure. Standard DM annihilations correspond to exponent $\delta = 1$, and more efficient scatterings correspond to $\delta < 1$.

given that the energy spectrum of the $e^\pm$ changes dramatically as we have a chain of multiple decays.

11.3.3 DM thermal decays

In the following discussion we will neglect scatterings that involve two DM particles, as their cross sections σ_2 arise at second order in the small new physics couplings C of Eq. (11.31). On the other hand, $2 \leftrightarrow 2$ scatterings that change DM number by one unit arise at first order, by combining the $C\,\chi\ell\pi$ interaction with either

- an electro-magnetic interaction with coupling $e \sim 0.3$, adding an extra γ to the process; or
- a strong interaction with coupling $\sim m_\pi/f_\pi \sim 1$ (see Eq. (11.31), the SM pion Lagrangian contains no π^3 interactions), adding an extra massive π to the process.

These processes have a larger cross section $\sigma_1 \gg \sigma_2$, that needs a much smaller critical value $\sigma_1 > \sigma_1^{\rm cr}$ to affect DM cosmological freeze-out, if their kinematical factors Δ that control the Boltzmann suppression are smaller than the DM mass M. The most important processes are shown in Fig. 11.6. It shows that some off-shell decays can be less Boltzmann suppressed than DM annihilations, but only when $M > m_\ell$, so that tree-level DM decays are not suppressed by two off-shell factors.

In conclusion, Fig. 11.7 shows the final result. In its left panel, we report the thermal decay rates as function of $z = M/T$: as expected the process with smallest δ ($\chi\gamma \leftrightarrow \pi\mu$ in the example) dominates at low temperature. The green curves in the right panel show the coupling needed to reproduce the cosmological DM abundance as freeze-out via thermal decays (one curve is the numerical result, one nearby curve is the analytic approximation). It shows that DM interactions to $\mu\pi$ needs to be a few order of magnitude stronger than weak interactions. As expected, freeze-out is excluded by too fast DM decays [367, 368] (red curve).

11.3.4 Collider bounds

Let us discuss collider bounds on the effective $(\bar\chi\gamma_\mu q)(\bar q\gamma^\mu\mu)$ interaction. We find that the strongest constraints are set by the ATLAS analysis in [374], which perform a search for a heavy charged boson

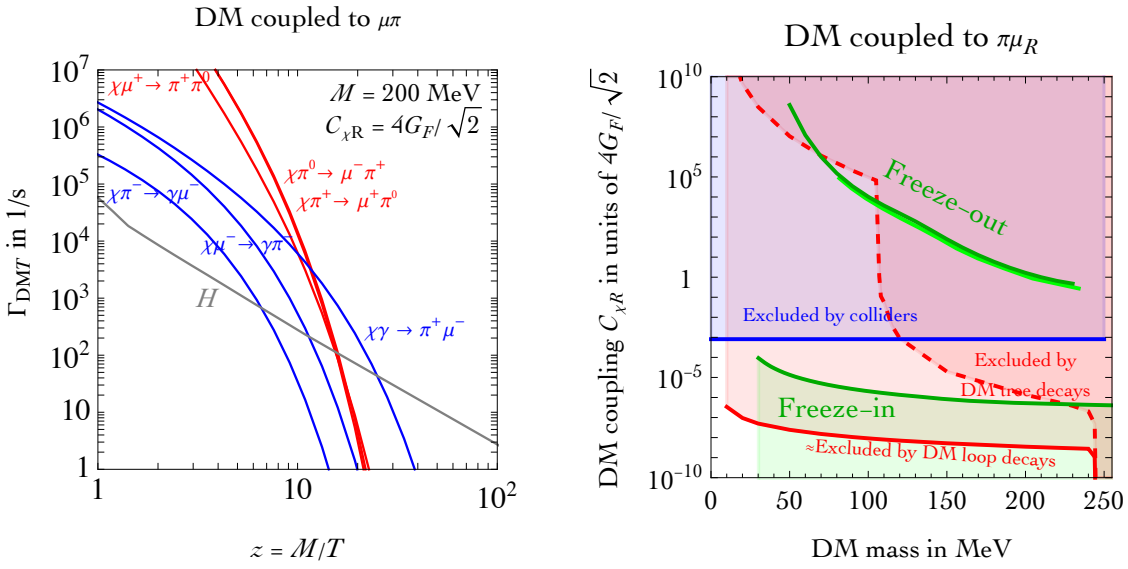

Figure 11.7: Dark Matter as a fermion coupled to $\mu^\pm\pi^\mp$. **Left**: rates of main thermal decays compared to the Hubble rate. As expected, $\chi\gamma \leftrightarrow \pi\mu$ dominates at $T \ll M$. **Right**: parameter space (mass, coupling). The red region is excluded by DM decays at tree (dashed) or loop (continuous) level, estimated as in Eq. (11.34). The blue region is excluded by collider data in any reasonable EW extension of the model. The DM abundance is reproduced thermally along the upper green curve, or as freeze-in below the lower green curve.

in events with a charged lepton and missing transverse momentum. In order to derive the bound, we have performed a recast of the ATLAS analysis. In particular, we have considered the reported bounds from the model-independent analysis in the muon channel, based on cuts on the variable m_T, defined as $m_T = [2p_T^\mu E_T^{\rm miss}(1-\cos\phi(\mu, E_T^{\rm miss}))]^{1/2}$. In order to identify the fiducial region, we have implemented the following cuts:

$$p_T^\mu > 55\,\text{GeV}\,, \qquad |\eta|_\mu < 2.5\,, \qquad E_T^{\rm miss} > 55\,\text{GeV}\,, \qquad m_T > 110\,\text{GeV}\,. \tag{11.36}$$

We thus considered the model where a LQ, with mass $M_{\rm med} \gg \sqrt{s}$, mediates the effective interaction in eq. (11.30), obtaining the constraint:

$$\frac{C_{\chi R}}{4G_F/\sqrt{2}} < 8.1\cdot 10^{-4}\,. \tag{11.37}$$

This result also excludes thermal freeze-out, and is plotted as a blue curve in Fig. (11.7). Calculations have been made with MadGraph [375].

11.3.5 DM relic abundance via freeze-in

As clear from Fig. (11.7), while freeze-out is excluded, freeze-in is allowed. Three different regimes are possible, depending on the highest reheating temperature $T_{\rm RH}$ attained by the SM plasma:

i) At $T \lesssim \Lambda_{\rm QCD}$, *i.e.* in the confined phase, DM interacts with pions according to Eq. (11.31). The dimension-5 interaction with right-handed leptons contributes to the DM freeze-in abundance

as $Y \sim e^2 C_{\chi R}^2 f_\pi^2 M_{\rm Pl} T$: the DM abundance is dominated by the maximal temperature $T_{\rm RH}$. The minimal amount of freeze-in (upper boundary of the green region in Fig. 11.7b) arises if $T_{\rm RH} \approx M$. This confined contribution alone allows to reproduce the DM abundance for $C_{\chi R} \sim \sqrt{T_0/M M_{\rm Pl}}/e f_\pi^{3/2} \sim 10^{-6} G_F$, nearly compatible with DM stability for $M < m_\pi + m_\mu$. For the renormalizable interaction with left-handed leptons, freeze-in happens around $T \sim M$, and the abundance $Y \sim e^2 C_{\chi L}^2 f_\pi^2 B_0^2 M_{\rm Pl}/M$ is independent of $T_{\rm RH}$. The pion description breaks down at $T \sim \Lambda_{\rm QCD}$ when the QCD phase transition happens.

ii) At temperatures above the QCD phase transition and below the mass of the mediator $M_{\rm med}$, namely in the region $\Lambda_{\rm QCD} \lesssim T \lesssim M_{\rm med}$, we have a higher $Y \sim C_{\chi R}^2 M_{\rm Pl} T^3$. This is again dominated by the highest temperature $T \lesssim \min(T_{\rm RH}, M_{\rm med})$, where $M_{\rm med} \lesssim C_{\chi R}^{-1/2}$.

iii) Finally, at temperatures above the mediator mass, DM has renormalizable interactions and freeze-in is dominated at $T \sim M_{\rm med}$. The dimension-less DM coupling to the mediator must be small, in order not to over-produce DM. Other interactions (such as gauge interactions with SM particles) can be large and keep the mediator in thermal equilibrium, so that the freeze-in DM abundance is produced by its decays. In Boltzmann approximation, the space-time density of mediator decays into DM is

$$\gamma_{\rm eq} = n_{\rm med}^{\rm eq} \frac{{\rm K}_1(M_{\rm med}/T)}{{\rm K}_2(M_{\rm med}/T)} \Gamma_{\rm dec} = \frac{d_{\rm med}}{2\pi^2} \Gamma_{\rm med} T M_{\rm med}^2 \, {\rm K}_1(M_{\rm med}/T), \tag{11.38}$$

where $\Gamma_{\rm med}$ is the mediator partial decay width into DM, and $d_{\rm med}$ is its number of degrees of freedom.[5] Inserting $\gamma_{\rm eq}$ in Eq. (11.18) gives

$$Y_\infty = \frac{405\sqrt{5} M_{\rm Pl} d_{\rm med} \Gamma_{\rm med}}{16 \pi^{9/2} d_{\rm SM}^{3/2} M_{\rm med}^2}. \tag{11.39}$$

If the mediator is the $\mathcal{U}$ leptoquark one has $\Gamma_{\rm med} = \frac{g_\chi^2 M_{\rm med}}{24\pi}$ and $d_{\rm med} = 18$, and the DM abundance is matched for

$$g_\chi \approx 2.2 \; 10^{-11} \sqrt{\frac{\rm GeV}{M} \frac{M_{\rm med}}{\rm TeV}} \, . \tag{11.40}$$

We remind that the coefficients C of the effective Lagrangian depend also on other couplings of the mediator. We now explore the possible flavour structure of these couplings, to see if some natural explanation can be found for the small size of g_χ.

11.4 Flavour expectations for DM couplings and the B anomalies

The fact that a leptoquark such as $\mathcal{U}_\mu$ could mediate at the same time the semi-leptonic interactions responsible for the B-physics anomalies, and the interactions responsible for DM freeze-in, although

[5] We can neglect scattering rates because suppressed by extra powers of couplings, such as g_2. At $T \gg M_{\rm med}$ the decay rate is suppressed by a Lorentz factor $T/M_{\rm med}$ compared to the scattering rates $\gamma_{\rm eq} \sim g_2^2 g_\chi^2 T^4$. This enhancement of scattering rates is not important for the final DM abundance, because it is dominated at $T \sim M_{\rm med}$. Furthermore this enhancement can be partially included as a NLO contribution to the decay rate, describing it as the thermal contribution to the mediator mass, $\delta M_{\rm med}^2 \sim g_2^2 T^2$. The thermal mass avoid an apparent IR-enhancement at $T \gg M_{\rm med}$ of t-channel scattering rates, that would anyhow cancel with loop corrections in a full NLO computation (KNL theorem, see [376,377] for a similar computation).

with couplings of different sizes, makes it interesting to speculate about a common origin of the two processes.

The B-physics anomalies can be explained, compatibly with other bounds from flavour and collider physics, in models where new physics couples dominantly to the third generation of fermions [246, 378–380]. Couplings to lighter generations of quarks and leptons then arise from the flavour rotations that diagonalize the Yukawa interactions, and are suppressed similarly to the masses and mixings of light fermions. This can applied to vector leptoquarks assuming that only 3rd-generation fermions are charged under an extended Pati-Salam group [381–383]. In the left-handed quark sector these rotations are of the order of the CKM matrix.

Given the tiny values of the coupling g_χ needed to reproduce the cosmological DM abundance via freeze-in, for DM masses in the MeV range, it is then natural to consider the DM χ as a right-handed neutral lepton of the first family. Other generations of χ, with larger couplings to SM, can be so heavy that they decay back fast to SM particles, without contributing to DM.

We parametrize the SM Yukawa couplings as

$$Y_u^{ij} \approx \epsilon_{Q_i}\epsilon_{u_j}, \qquad Y_d^{ij} \approx \epsilon_{Q_i}\epsilon_{d_j}, \qquad Y_e^{ij} \approx \epsilon_{L_i}\epsilon_{e_j}, \tag{11.41}$$

where ϵ_{f_i} are small parameters carrying the flavour suppression of the couplings to the i-th family of $f = \{Q, u, d, L, e\}$, and the relations hold up to $\mathcal{O}(1)$ factors. Here and in subsequent estimates we also ignore an overall coupling, assumed to be of order one. Such a pattern of Yukawa couplings is easily obtained in Froggatt-Nielsen scenarios [384], or in models with partial composite fermions [385–387]. More stringent relations between the ϵ_f^i can be obtained in models with a larger flavour symmetry, such as Minimal Flavour Violation [133, 388, 389] or U(2) models [135, 390], as mentioned in Chapter 6.

The values of $\epsilon_{Q,u,d}$ can be estimated from the CKM mixings and the quark masses. Indeed,

$$V_{\rm CKM}^{ij} \approx \epsilon_{Q_i}/\epsilon_{Q_j}, \qquad \epsilon_{Q_i}\epsilon_{u_i} \approx (y_u, y_c, y_t), \qquad \epsilon_{Q_i}\epsilon_{d_i} \approx (y_d, y_s, y_b), \tag{11.42}$$

from which one gets

$$\epsilon_Q \sim (\lambda^3, \lambda^2, 1)\,\eta_q, \qquad \epsilon_u \sim (\lambda^4, \lambda, 1)\,\eta_q^{-1}, \qquad \epsilon_d \sim (\lambda^4, \lambda^3, \lambda^2)\,\eta_q^{-1}, \tag{11.43}$$

where $\lambda \sim 0.2$ is the Cabibbo angle, and η_q is an overall $\mathcal{O}(1)$ parameter. The parameters in the lepton sector can not be estimated as easily at this level, since the neutrino mixings are not necessarily directly related to the Yukawa couplings.

We can now make the assumption that the flavour structure of the new physics couplings is determined by the same flavour parameters that control the SM Yukawas. Let us focus on the case of the vector leptoquark $\mathcal{U} \sim (3,1)_{2/3}$ for definiteness. The couplings of $\mathcal{U}$ to fermions are defined in Eq. (11.26). In terms of the flavour spurions ϵ those couplings read

$$g_L^{ij} \approx \epsilon_{Q_i}\epsilon_{L_j}, \qquad g_R^{ij} \approx \epsilon_{d_i}\epsilon_{e_j}, \qquad g_\chi^i \approx \epsilon_{u_i}\epsilon_\chi, \tag{11.44}$$

where we have introduced an additional (small) parameter ϵ_χ that controls the DM couplings.

The exchange of a vector leptoquark contributes to semi-leptonic left-handed interactions via the couplings g_L. These couplings can thus be partially determined by fitting the $b \to s\ell\ell$ anomalies [246]. The contribution to the Wilson coefficient of the semi-leptonic operator $(\bar{b}_L\gamma^\mu s_L)(\bar{\mu}_L\gamma_\mu\mu_L)$ reads

$$\Delta C_9^\mu = -\Delta C_{10}^\mu = \frac{g_L^{32} g_L^{22}}{M_{\mathcal{U}}^2} \approx V_{tb}^* V_{ts} \frac{\eta_q^2 \epsilon_{L_2}\epsilon_{L_2}}{M_{\mathcal{U}}^2}, \tag{11.45}$$

which fits the observed deviations if $(\epsilon_{L_2})^2\eta_Q^2/M_{\mathcal{U}}^2 \approx (6\,\text{TeV})^{-2}$. For $M_{\mathcal{U}} \approx$ TeV the muon couplings can be $\epsilon_{L_2} \sim \mathcal{O}(0.1)$. The first-generation coupling is required to be small, $\epsilon_{L_1} \ll \epsilon_{L_2}$, in order to suppress new physics effects in $b \to se^+e^-$. The right-handed couplings ϵ_e are then related to the charged lepton Yukawa couplings, $\epsilon_{L_i}\epsilon_{e_j} \sim (y_e, y_\mu, y_\tau)$, and one has

$$\epsilon_{e_1} \gtrsim 10^{-4}, \qquad \epsilon_{e_2} \sim \text{few} \times 10^{-3}, \qquad \epsilon_{e_3} \sim 10^{-2}, \tag{11.46}$$

where we assumed $\epsilon_{L_1} \lesssim \mathcal{O}(10^{-2})$ (an order of magnitude smaller than the muon coupling) and $\epsilon_{L_3} \sim 1$.

Notice that all the right-handed mixings $\epsilon_{u,d,e}$ estimated above are smaller than the left-handed ones $\epsilon_{Q,L}$ (except for the case of the electron where no hint on the size of ϵ_{L_1} exists). In particular, this is consistent with the observation of sizable LQ-induced effects in left-handed currents, but the absence of large right-handed currents.

Finally, reproducing the cosmological DM abundance via freeze-in as in Eq. (11.40) fixes the LQ coupling to DM, and in turn $\epsilon_\chi \sim g_\chi/\epsilon_u$. Two limiting scenarios can be envisaged, depending on which up-quark flavour couples dominantly to DM. If the dominant decay is with the top quark, given the hierarchy of Eq. (11.43), for $M \gtrsim 10\,\text{keV}$ and $M_{\mathcal{U}} \sim$ TeV one needs $\epsilon_\chi \lesssim 10^{-8}$, much smaller than the corresponding electron spurion. If instead χ couples dominantly to the first family of quarks, due to the additional ϵ_{u_1} suppression one gets $\epsilon_\chi \sim 10^{-5}$, which is comparable to the analogous factor for electrons. The latter scenario could be motivated if χ is identified with the first-family member of a flavour triplet of right-handed neutrinos χ^i: in this case its dominant coupling can be to other first-family fermions if flavour violation is suppressed in the right-handed sector, as is the case for instance in MFV or $U(2)$ models.

We finally discuss why the Higgs doublet H, unlike the leptoquark $\mathcal{U}$, cannot generate DM via freeze-in. The Higgs doublet too can couple to DM as

$$y_\chi^i\, H^* \bar{L}_L^i \chi \tag{11.47}$$

where we estimate the Yukawa coupling as $y_\chi^i \approx \epsilon_\chi \epsilon_{L,i}$. Thus Higgs decays $h \to \nu_L \chi$ can in principle contribute to DM freeze-in production. However DM dominantly produced in this way is excluded, because Eq. (11.47) implies a too large mixing of DM with neutrinos, $\theta_i \approx y_\chi^i v/M_\chi$. This is problematic because it gives a contribution to neutrino masses and, more importantly, because it contributes to DM decays as

$$\Gamma(\chi \to \nu_i \gamma) = \frac{9\alpha G_F^2 M^5}{256\pi^4}\theta_i^2 \approx \frac{1}{10^{25}\,\text{sec}}\left(\frac{y_\chi^i}{10^{-10}}\right)^2\left(\frac{M}{\text{keV}}\right)^3. \tag{11.48}$$

Higgs freeze-in instead needs a Yukawa coupling $y_\chi \approx 7 \times 10^{-8}\sqrt{\text{keV}/M}$, which is slightly larger for masses $M \gtrsim$ few eV. In fact, ad-hoc scalar coupled to two DM particles was introduced in [391] to achieve freeze-in: we have shown that this role can be played by the vector leptoquark motivated by flavour anomalies, as its $\mathcal{U}u\chi$ couplings do not directly induce DM decay.

In any case, we need to assume that y_χ is small enough so that Eq. (11.48) is satisfied and the Higgs plays no role in freeze-in. In this case, the corrections to neutrino masses do not exceed the experimental values and do not impose further constraints. We point out that the required Yukawa coupling is smaller than the naive expectation $y_\chi \approx \epsilon_\chi \epsilon_L$ even in the case where flavour violation is suppressed in the lepton sector and the dominant coupling is to electrons. The need for small mixings between left- and right-handed neutrinos is a common issue in models where the leptoquarks arise from partial unification at the TeV scale, and most likely requires a more complex neutrino sector [382,383].

11.5 Direct Detection signals

DD experiments are sensitive to DM scattering with light degrees of freedom such as light quarks, gluons and electrons. We consider DM that interacts with SM leptons and quarks as described by Eq. (11.30), and in particular on the first two 4-fermion interactions. After matching the interaction Lagrangian to the nucleon level, DM charged- and neutral-current interactions with nucleons arise. We now briefly discuss the novel signatures in DD and ID searches of DM induced by these interactions. We anticipate that, although these signatures are potentially interesting, the effective scale of the dimension 6 operators in Eq. (11.30) must be large to avoid bounds from DM decay as shown in Fig. 11.5. Therefore, one generally expects the signals to be much below the experimental sensitivities — with a few notable exceptions that we discuss.

Concerning charged currents, the leading order amplitudes are obtained from the (axial) vector interaction with right-handed leptons

$$C_{\chi R}(\bar{\chi}\gamma_\mu e_R)\left(\bar{n}\gamma^\mu \frac{1+g_A\gamma_5}{2}p\right), \tag{11.49}$$

where $g_A \approx 1.27$ [392], and the scalar interaction with left-handed leptons $(\bar{\chi}e_L)\,(\bar{n}p)$, with a coefficient proportional to $C_{\chi L}$. Both these interactions lead to a DM-induced β decay. At the nuclear level, the relevant process is the β^- transition $\mathrm{DM} + {}^A_Z\mathcal{N} \to e^- + {}^A_{Z+1}\mathcal{N}$, which is energetically possible if the DM mass is larger than the capture threshold $Q + m_e$, where $Q = m_{A,Z+1} - m_{A,Z}$ is the mass difference of the two nuclei. Following [393] the thermally averaged cross section arising from the charged current operator is

$$\langle\sigma v\rangle = \frac{C^2_{\chi L(R)} M^2}{16\pi} f(E_R) \tag{11.50}$$

where $f(E_R)$ is a function of the detected energy that encapsulates the nuclear details of the β^- transition. For light DM particles with kinetic energies much less than $\delta = M - (m_e + Q)$, the spectrum of recoiling electrons exhibits a peak at $E_R \approx \delta$. The left panel of Fig. 11.8 compares the estimated sensitivities of current direct detection experiments, taken from [393], with bounds from DM decays and from colliders.

One could wonder whether there is a possibility to explain the anomalous counting rate of electromagnetic recoils in the XENON1T detector peaked around 3 keV [394]. Considering Xenon as target, the process $\mathrm{DM} + {}^A_{54}\mathrm{Xe} \to e^- {}^A_{55}\mathrm{Cs}$ can have capture thresholds as low as a few hundreds keV: in particular, the ${}^{131}_{54}$Xe isotope has an abundance of about 21% and a capture threshold of only 355 keV [395]. One therefore can have a signal peaked at $E_R \approx 3\,\mathrm{keV}$ if the DM mass is $M \approx (m_e+Q)+E_R \approx 358\,\mathrm{keV}$. This needs some tuning among the electron and DM masses, and a slightly larger M would give a peak in the few hundreds of keV range. We show the best fit to the XENON1T data in the right panel of Fig. 11.8, obtained using the rate reported in [393]. Assuming local DM density $\rho_\odot = 0.4\,\mathrm{GeV/\,cm^3}$, the anomaly can be fitted for values of the DM coupling $C_{\chi R} \approx 1/(1.7\,\mathrm{TeV})^2$. For this value of the coupling to right-handed electrons, the loop-induced decay rate into $\nu_e\gamma$ gives a DM life-time $\tau \approx 10^{24}\,\mathrm{s}$, around the experimental bound from PLANCK, as shown in the left panel of Fig. 11.8. However, collider searches in the lepton plus missing energy final state constrain $C_{\chi R}$ to be a factor three smaller and rule out this possibility. A similar coupling to left-handed electrons is instead largely excluded by DM decays. The XENON signal can thus not be explained in our framework, but future experiments will have the sensitivity to probe a parameter space relevant for DM freeze-in via coupling to right-handed leptons, provided that the reheating temperature is low, namely $T_{\mathrm{RH}} \sim \Lambda_{\mathrm{QCD}}$.

Furthermore a novel specific signature from the ${}^{136}_{55}$Cs decay arises. Indeed, following the analysis done in [395] for solar neutrino capture in LXe, one could detect DM with lepton number by using a

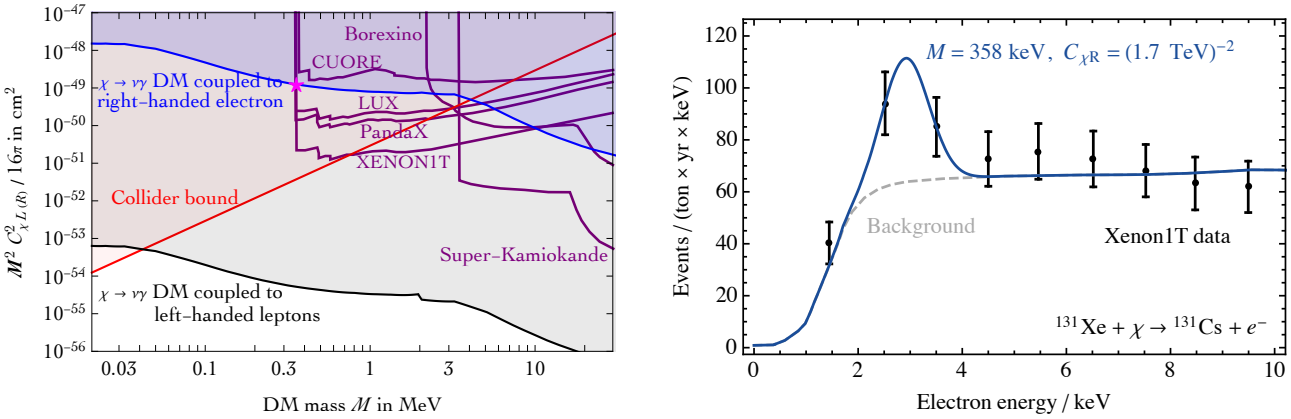

Figure 11.8: **Left:** Estimated experimental sensitivities for the DM absorption cross section (from [393]), compared to the indirect detection bound on DM life-time (these are stronger than in [393], where the dominant QCD contribution to $\chi \to \nu\gamma$ was not considered) and to collider bounds (red line). The magenta star shows the parameters that can fit the XENON1T excess. **Right:** Best fit to the XENON1T electron-recoil data from DM absorption on ^{131}Xe.

delayed coincidence signature from long-lived states of $^{136}_{55}$Cs.

Concerning neutral currents, DM couplings to left-handed leptons induce an interaction with nucleons $\mathcal{N}$ described at leading order by the scalar operators

$$(\bar{\chi}\nu_L)(\bar{n}n) \qquad \text{and} \qquad (\bar{\chi}\nu_L)(\bar{p}p). \tag{11.51}$$

This is spin-independent and leads to a sort of exothermic DM-nucleus collision DM $\mathcal{N} \to \nu\,\mathcal{N}$ with mass splitting $\delta = M - m_\nu \simeq M$. For light DM particles with kinetic energies much less than the splitting, exothermic spectra exhibit a peak at nuclear recoil energy $E_{\rm R} = \delta\, M/(2m_{\mathcal{N}}) \approx M^2/(2m_{\mathcal{N}})$, where $m_{\mathcal{N}}$ is the mass of the target nucleus. Hence, for Xenon target we expect detectable nuclear recoil in the keV range when the DM mass is around 20 MeV. It is worth noticing that the window of DM masses probed in such scenario is much smaller than the one achieved with standard DM-nucleus collisions. However, the spectrum is analogous to the one of exothermic collisions and therefore we cannot discriminate further among them.

DM absorption signals have been studied previously in [393]. However, when discussing neutral currents these authors considered a $(\bar{\chi}\nu_R)(\bar{q}q)$ effective interaction involving ν_R (rather than ν_L or ℓ) in order to avoid too fast DM decay $\chi \to \nu_R\gamma$. Since ν_R has no SM gauge interactions their signals are equivalent to those of inelastic DM with two states χ, χ' and a $(\bar{\chi}\chi')(\bar{q}q)$ interaction. When discussing charged currents [393] considers our same $(\bar{\chi}\ell)(\bar{d}u)$ interaction, but does not include the DM decay channel $\chi \to \nu\gamma$ mediated by QCD states at one loop. We report in the left panel of Fig. 11.8 the projected constraints for the DM-induced β^- signals taken from [393]. One can see that, while DM coupled to right-handed electrons can give observable signals in various experiments, for DM coupled to left-handed leptons the signals compatible with DM life-time are always below the experimental sensitivity.

11.6 Indirect Detection signals and the 3.5 keV anomaly

DM decays provide ID signals: the constraints on tree-level and loop-induced DM decay from PLANCK and VOYAGER have already been discussed in Subsection 11.3.2. As these constraints can be saturated,

signals from DM decays are detectable.

In particular, the unidentified X-ray emission line claimed at 3.5 keV [396, 397] could be due to DM with mass $M \approx 7\,\text{keV}$ decaying as $\chi \to \nu_\ell \gamma$ with rate $\Gamma \approx 1.4\ 10^{-28}/\,\text{s}$ (see e.g. fig. 13 of [396]). In the considered models the needed DM life-time is obtained for

$$C_{\chi L} \approx 10^{-4} \frac{4G_F}{\sqrt{2}} \qquad \text{or} \qquad C_{\chi R} \approx \frac{4G_F}{\sqrt{2}} \begin{cases} 6\ 10^{-2} & \text{DM coupled to } \ell = e \\ 3\ 10^{-4} & \text{DM coupled to } \ell = \mu \\ 2\ 10^{-5} & \text{DM coupled to } \ell = \tau \end{cases} . \tag{11.52}$$

For such values of the couplings the relic DM abundance can be reproduced via the freeze-in mechanism with a low reheating temperature $T_{\rm RH} \sim \Lambda_{\rm QCD}$, see fig. 11.7. This is a non-trivial result, as other models where DM is a sterile neutrino can fit the 3.5 keV line, but its relic abundance cannot be obtained via freeze-in as non-resonant oscillations: extra mechanisms are needed, such as decays $S \to \chi\,\chi$ of an ad-hoc scalar S [391]. In our model on the other hand the leptoquark motivated by flavour anomalies plays a similar role, decaying into one DM particle and one SM particle.

Concerning scatterings that could induce a gamma-ray signal, the only relevant interactions are those that change the DM number by one. Indeed the pair-annihilation of DM particles is extremely suppressed within the freeze-in production mechanism, namely as $\langle \sigma_{\rm ann} v \rangle \propto g_\chi^4$, and the g_χ coupling is very small.

We thereby focus on further indirect detection gamma-rays signals coming from DM decay and from scatterings that change DM number by one unit. A possible way to get a signal is to change the DM number by one via the scatterings with highly energetic Galactic Cosmic-Ray (CR) electrons and protons. The relevant primary channels are $\chi e^+ \to \bar{d} u$ and $\chi \bar{p} \to \bar{n} e$ and the corresponding charge conjugates. The spatial morphology of the induced gamma-ray signal is non-conventional and is enhanced in regions with high density of baryons and DM. As a consequence dwarf galaxies, which are usually considered as the cleanest laboratories in indirect detection (see the discussion in Subsection 10.5.1), are not the best place to look for gamma-rays signals from DM with lepton number. The energy spectrum is similar to the one from standard pair-annihilation with the difference that the total energy is not $4M^2$ but $(M + E_{\rm CR})^2$ with $E_{\rm CR}$ the energy of Galactic CR. The cross section of highly energetic Galactic CR electrons and protons scattering off non-relativistic DM is

$$\sigma \approx C_{\chi L(R)}^2 \, (M + E_{e,p})^2 = 5.3 \times 10^{-10}\,\text{pb} \left(\frac{C_{\chi L(R)}}{10^{-4} G_F} \right)^2 \left(\frac{M + E_{e,p}}{\text{GeV}} \right)^2 . \tag{11.53}$$

The highest $C_{\chi L(R)} \sim 10^{-4} G_F$ allowed by DM stability and consistent with the freeze-in mechanism with low reheating temperature $T_{\rm RH} \sim \Lambda_{\rm QCD}$ is obtained for very light DM. Hence we predict $\sigma \lesssim 10^{-9}\text{pb}\,(E_{e,p}/\text{GeV})^2$, which gives a flux too low to be detected by any indirect detection experiments.

11.7 Flavour models with multiple DM and freeze-out

Throughout this Chapter we considered minimal models with only one DM particle and we could not reproduce its cosmological abundance from freeze-out via thermal decays, compatibly with bounds on the DM lifetime, $\tau \gtrsim 10^{26}$ s, although we found viable models assuming DM freeze-in. Let us now briefly show how these bounds on the DM lifetime can be easily satisfied in the presence of two or more DM states χ_i. Note that this is to be contrasted to the DM models in which a cosmologically short-lived state freezes out due to pair annihilations and later decays to one or more SM states plus a cosmologically long-lived (so-called super-WIMP) DM state, discussed for instance in [398, 399]. In this case, in fact, DM decays are slower than the Hubble time and play no role in fixing the initial

DM freeze-out abundance. On the contrary, they only enter later reducing it by the ratio of the two masses in the dark sector. This "freeze-out and decay" scenario can be extended to freeze-out via thermal decays, but it contains out-of-equilibrium elements. For this reason, we prefer here to focus on strict freeze-out scenario.

There can be precise flavour considerations that justify the possibility of multiple DM states and the extension of our model to two or more DM states χ_i. For example, in the models with extra vectors such as Eq. (11.26) one would naturally expect three generations of DM singlets $\chi_{1,2,3}$. To keep the discussion simple and general, we can summarize the results about the decay rate of one DM particle as

$$\Gamma_{\rm DM} \sim \epsilon_{\rm SM}\epsilon_{\rm DM} M \qquad \text{where} \qquad \epsilon_{\rm DM} \sim C^2 M^4, \qquad \epsilon_{\rm SM} \sim \frac{G_F^2 M^4}{(4\pi)^4}. \tag{11.54}$$

$\epsilon_{\rm SM} \sim 10^{-18}$ is a typical electroweak loop factor at the DM mass $M \lesssim$ GeV. If $C \sim G_F$, as needed to have thermal freeze-out at $M \sim$ GeV, the two ϵ suppression do not give a stable enough DM (while freeze-in needs $C \ll G_F$, improving DM stability).

Stable enough DM is obtained, instead, in the presence of two states, χ_1 and χ_2, with mass $M_{1,2} \lesssim$ GeV (arising, for example, as $m_\ell + m_\pi$) and effective interactions of the type

$$C_{\rm DM_1}(\bar\chi_1 \ell)(\bar d u) + C_{\rm DM_2}(\bar\chi_2 \ell)(\bar d u) + C_{\rm DM_{12}}(\bar\chi_1 \chi_2)(\bar q q). \tag{11.55}$$

Notice that we have not imposed any $\mathbb{Z}_2$ symmetry that keeps the dark sector separated from the SM sector. We next assume that $C_{\rm DM_1}$ is negligibly small, and that masses $M_1 < M_2$ are in the range such that $\chi_2 \to \ell\pi$ decays are kinematically closed, while $\chi_2 \to \chi_1 \pi^0$ decays are kinematically open (we make this latter assumption just for simplicity, as we could relax it and use $\chi_2 \to \chi_1 \gamma\gamma$ decays). Then the decay widths are

$$\Gamma_{\rm DM_2} \sim \epsilon_{\rm DM_2} M_2, \qquad \Gamma_{\rm DM_1} \sim \epsilon_{\rm DM_{12}} \frac{\Gamma^*_{\rm DM_2}}{M_2} M_1 \sim \epsilon_{\rm SM}\epsilon_{\rm DM_2}\epsilon_{\rm DM_{12}} M_1 \tag{11.56}$$

where $\epsilon_{\rm DM_{12}} \sim C^2_{\rm DM_{12}} M^4_{1,2}$. The smallness of $C_{\rm DM_1}$, at a level that saturates the decay width $\Gamma_{\rm DM_1}$ above, could be motivated by flavour considerations (for instance a very precise flavour alignment in the right-handed lepton sector, if χ carry lepton flavour number). Quantum effects respect this requirement. Assuming now that $C_{\rm DM_2} \sim C_{\rm DM_{12}} \sim G_F$ or even larger depending on the masses, we have, at the same time:

i) Very long lived χ_1 DM, that satisfies bounds on the DM life-time;

ii) Cosmologically fast decays of χ_2, so that it does not pose cosmological problems;

iii) Thermal freeze-out via $\chi_1 \leftrightarrow \chi_2 \leftrightarrow$ SM scatterings at finite temperature.

Although not necessary, DM stability can be improved by an extra $\epsilon_{\rm DM_{23}}$ factor adding a third generation χ_3 and repeating the above structure: each mediation step can give one extra ϵ suppression at zero temperature, while rates at finite temperature can reach thermal equilibrium, $\Gamma \sim H$ at $T \sim M$, if $C_{\rm DM} \sim G_F$.

Chapter 12

Conclusions

Flavour Physics has been and continues to be a fundamental guideline for research activities in theoretical particle physics. At present, the tensions in the exclusive and inclusive determinations of the CKM matrix elements $|V_{cb}|$ and (although more slightly) $|V_{ub}|$ and the discrepancies between the theoretical expectations and the measurements of the $R(D^{(*)})$ and the $R(K^{(*)})$ ratios have clearly indicated a possible path to look for effects of New Physics. In fact, two are the possibilities in order to solve these *anomalies*. On the one hand, one can review the theoretical computations within the SM and compute the flavour observables without introducing any kind of approximation. This can bring us to an appropriate and truthful estimation of the mean values and (especially) the uncertainties of such quantities, thus reducing the aforementioned tensions. On the other hand, one can state that there is New Physics that can explain these discrepancies, pointing towards the existence of BSM effects affecting B-physics.

This PhD thesis tries first of all to explore both these paths, by giving an overall picture of the state-of-the-art of the $\Delta B = 1$ transitions and novel improvements.

In Part I we have focused our attention on the semileptonic charged-current B decays, with particular attention given to the $B \to D^{(*)}\ell\nu$ transitions. These processes have received increasing attention in the recent years since they give the possibility of both determining an exclusive estimate of the CKM matrix element $|V_{cb}|$ and testing LFU through the determination of the $R(D^{(*)})$ ratios. Since these decays occur at tree-level through the exchange of a W-boson, when computing their differential decay widths one has to properly take into account the hadronic matrix element. It is expressed in terms of complicated functions of the quadratic transferred momentum, *i.e.* the Form Factors, which encode all the informations about the strong dynamics of quarks. Our proposal to analyse the FFs and, more in general, the semileptonic charged-current B decays brings to new determinations of the exclusive value of $|V_{cb}|$ and the ratio $R(D^*)$ which are compatible at the 1σ level with the corresponding inclusive value and at the $\sim 1.5\sigma$ level with the corresponding average of measurements, respectively. Let us summarize this in detail.

In Chapter 3 we have introduced a novel method to describe the FFs in the whole kinematical range, starting from the available LQCD computations of the same quantities at high momentum transfer. This is the *Dispersive Matrix Method*. In these summary remarks, I think that it is important to recall and highlight its main and most important properties. As we have seen, it is entirely based on first principles, namely unitarity, analiticity and crossing-symmetry, and uses only non-perturbative inputs, *i.e.* the LQCD evaluation of 2- and 3-point Euclidean correlators. It is completely model-independent, since it is independent of any assumption on the functional dependence of the FFs on the momentum

transfer. Furthermore, it allows us to keep theoretical calculations and experimental data separated. Finally, it is also universal, in other words it can be applied to any exclusive semileptonic decays of mesons and baryons. The DMM constitutes an important theoretical improvement in the descritpion of the hadronic FFs since, contrarily to the well-known CLN, BCL and BGL parametrizations, it does not rely on any power series expansion of the FFs and on any perturbative input. Moreover, it does not use any approximate symmetry, such as Heavy Quark Effective Theory.

In Chapters 4 and 5 we have applied for the first time the DMM to semileptonic charged-current B decays. We have started by taking into consideration the $B \to D^{(*)}\ell\nu$ transitions. Our main result is that *for the first time* we have obtained both an exclusive estimate of $|V_{cb}|$ from the $B \to D^*$ channel which is compatible with the inclusive value and a theoretical expectation of $R(D^*)$ which is compatible with the corresponding experimental average by the HFLAV Collaboration. This result can be attributed both to the use of the DMM and to the avoiding of a mixing between the LQCD computations of the FFs and experimental measurements of the differential decay widths. Given the universality of the DMM, we have extended our study also to the $B_s \to D_s^{(*)}\ell\nu$, the $B \to \pi\ell\nu$ and the $B_s \to K\ell\nu$ decays. On the one hand, the first ones are particularly relevant since they allow both to obtain further exclusive estimates of $|V_{cb}|$ and to test possible $SU(3)_F$ symmetry breaking effects affecting semileptonic B decays. On the other hand, the other ones give the opportunity to obtain new exclusive estimates of $|V_{ub}|$. For what concerns our final determinations of the CKM matrix elements, we have discussed the compatibility of the DMM determinations of $\{|V_{cb}|, |V_{ub}|\}$ with the ones coming from the last UTfit analysis 2022. This is very important since the UTfit predictions are based on the Unitarity Triangle Analysis, which determines precisely the SM parameters of the flavour sector in a way that is completely independent of the LQCD and experimental data explicitly studied in Chapters 4 and 5 and is thus an important test of the reliability of our DMM estimates. The final result is that both the DMM and the UTfit studies point towards a value of $|V_{cb}|$ which is higher with respect to the FLAG exclusive estimate [39] and, at the same time, compatible with the inclusive determination [30].

In Part II we have enlarged the discussion to the Beyond the Standard Model approach to Flavour Physics. There are, in fact, several experimental evidences and theoretical arguments that point towards the existence of an extension of the SM, which can be considered at all the effects as an infrared theory valid only at low energies. Nevertheless, a correct and precise estimation of the SM parameters is fundamental in order to develop NP studied since, as repeated more times throughout this Thesis, the more precise are the theoretical estimates of these parameters, the more strongest will be the bounds on New Physics. This is the fundamental issue that links Part I and Part II to each other.

In Chapter 6 we have firstly discussed the Effective Field Theory approach to Flavour Physics. The EFT is particularly useful in order to study possible New Physics effects affecting low-energy processes, such as the $\Delta B = 1$ and $\Delta B = 2$ transitions, in a completely model-independent way. In this sense, as stated before, Flavour Physics offers several hints of existence of Beyond the Standard Model degrees of freedom. One of the major examples is offered, for instance, by the flavour anomalies in semileptonic $b \to c$ and $b \to s$ transitions. We have reviewed the EFT framework, and have also noted that the approach to New Physics can be built up also starting from considerations of symmetry, whose best examples are without any doubt offered by the Minimal Flavour Violation and the $U(2)^3$ frameworks.

In Chapters 7 and 8 we have then focused the discussion on two explicit BSM models, *i.e.* the Composite Higgs and the LeptoQuark scenarios, respectively. In the former case, we have firstly reviewed the theoretical properties underlying the CH models. Then, we have developed an original

application, *i.e.* we have determined new bounds on the masses of the fermion modes (that naturally arise in CH scenarios) by considering the expected improvement in precision at future experiments, namely LHCb Upgrade II and Belle II. The final result is that the combination of the bounds coming from low-energy processes point towards a $O(10\,\text{TeV})$ mass of these new heavy degrees of freedom. In the latter case, we have reviewed the main properties of the LQ scenarios together with possible UV completions of such theories, in view of their application in the last Part. We have also reviewed the results of the application of a simplified U_1^μ model to explain the flavour anomalies, as presented by the authors of [193].

One other example of the main challenges of theoretical physics is, at present, trying to explain the origin of the Dark Matter abundance in our Universe. This is the topic of the last Part of this Thesis, namely the Part III. While the existence of DM is ensured by several cosmological and astrophysical probes, the understanding of the nature of DM is unclear. As discussed in Chapter 9, a huge effort has been and is still being developed from the experimental point of view in order to detect possible DM candidates. In this sense, there are basically three standard ways to look for DM particles, *i.e.* direct detection searches, indirect detection ones and finally direct production at colliders. The study of DM phenomenology can be connected to a BSM approach to Flavour Physics. At present, in fact, several papers in literature try to find combined explainations of both the DM abundance and some of the anomalies coming from the flavour sector, for example the $R(K^{(*)})$ ones. This is exactly what have been developed in one of the two DM models presented in this Thesis, namely the one with LeptoQuark mediators.

To be more specific, in Chapter 10 we have widely discussed and described the WIMP scenario. In the spirit of Minimal Dark Matter models, we have added the minimal amount of new degrees of freedom to the matter content of the SM, *i.e.* a new EW multiplet of $SU(2)_L$. For the first time, we have computed the thermal masses of all the multiplets allowed by the unitarity and computability criterions, taking into consideration the effects of the Sommerfeld enhancement and of the formation of bound states. While these effects have been previously computed in specific cases, a general treatment was still lacking. We have then critically investigated the discovery potential of such new heavy particles both at future muon colliders and at (in)direct detection experiments. Our conclusions are that all the multiplets are detectable by future large exposure DD experiments, as DARWIN, with the notable exception of the complex $2_{1/2}$ candidate. This exception constitutes an important motivation for the realization of a future muon collider since the complex doublet can be excluded by this machine with a center of mass energy equal to 6 TeV. Muon collider with higher energies will be also able to test larger EW multiplets, with masses close to the kinematical threshold, in various channels such as single gauge boson emission (mono-X) or disappearing tracks. The indirect searches are complementary to the aforementioned ways to detect DM, to be more specific they offer a parallel opportunity to detect the heaviest multiplets. As an example, we have discussed the case of the real 7-plet at future Cherenkov telescopes, like CTA.

Finally, in Chapter 11 we have introduced a new model of Dark Matter, *i.e.* the one based on its thermal decays. This model is innovative with respect to the usual scenario since it hypotheses interactions between DM and SM particles in which the DM number changes only by one unit. Very strong bounds come from the fact that Dark Matter is not stable, which in turn requires its couplings to be small. This scenario can be realized by introducing a vector LeptoQuark as a mediator of these interactions. Our final result is that this class of models is able to provide a DM candidate which is long-lived enough, and reproduce its cosmological abundance if the DM undergoes freeze-in. In this case, it is possible to explain at the same time the observed abundance of Dark Matter and the $R(K^{(*)})$ anomalies by means of a LeptoQuark exchange. To achieve this goal, one has to introduce a

specific flavour structure. Instead, DM freeze-out is not compatible with the bounds from DM decays. These conclusions can be relaxed in presence of multiple DM states, which can be motivated by flavour considerations. In this case, the DM abundance can be reproduced also through the freeze-out mechanism.

The future will reserve important novelties for both Flavour Physics and Dark Matter phenomenology, since lots of experimental data are going to come out in the next years. In the first case, new important measurements of the flavour observables will be published by both the LHCb and the Belle II Collaborations. They will give a new insight on the theoretical analyses of low-energy processes in flavour physics, either pointing towards the existence of New Physics in these transitions, or not. One fundamental question is whether or not Beyond the SM effects are required in order to explain the $R(D^{(*)})$ and the $R(K^{(*)})$ anomalies. In the second case, new (in)direct detection experiments as well as new colliders will be activated in the next decades, both closing finally the window for some DM models and opening it for others. This will give a new insight on the scenarios that are effectively admitted by the data and that can be further investigated, maybe in connection with flavour physics. So, to conclude, in order to find some answers to fundamental questions of theoretical physics, there is only one way, *i.e.* to ameliorate at the same time the precision of both the theoretical predictions and the measurements. Only this possibility will allow us to better investigate NP effects affecting Flavour Physics in the next years.

Acknowledgements

First of all, I want to thank with all my heart my "Pisan" mentor Dario Buttazzo and my "Roman" mentors Guido Martinelli and Silvano Simula. I am very grateful to Dario for having carefully supervised this Thesis work and for having taught me a lot of new physics that was completely obscure to me before the beginning of our research activity and collaboration. I thank him for having helped me in many delicate situations, in particular the calls for the PostDocs (in which case his help has been without any doubt fundamental), while always being helpful and patient. I want also to thank him for having managed to remedy a lack of points of reference inside the phenomenology group of Scuola Normale Superiore during the last year, at least this is my personal opinion. I infinitely thank Guido and Silvano for the constant interaction and collaboration that we have carried out during these years. I have grown and matured a lot after all the scientific discussions we had and all the battles we faced to defend our points of view. I have learnt a lot of physics that has strenghtened the skills acquired during the Master Thesis. This collaboration has been very special not only from a scientific point of view, but also from a human one. I had a lot of fun with them also in the most delicate situations arised during our research. Last but not the least, they both have helped me to not fall down during one of the most difficult moments of my life, and I will always remember it.

I thank all the other professors and researchers with which I have had the opportunity to interact during these four years, in particular Paolo Panci, Diego Redigolo, Roberto Franceschini, Alessandro Strumia, Enrico Trincherini, Benedetta Belfatto and Ryoutaro Watanabe from the "Pisan" side and Luca Silvestrini, Marcella Bona, Roberto Contino, Vittorio Lubicz and Mauro Valli from the "Roman" one.

I am very grateful to my friends and colleagues Salvatore Bottaro and Marco Costa, with whom I managed to collaborate both during and after the COVID pandemics and with which we have shared and enjoyed a lot of time in particular during the last year. Let me thank also Sonali Verma, Manuel Naviglio and all the other colleagues and friends in Pisa.

Let me thank my Roman Master colleagues, in particular Gianmarco Perrupato and Riccardo Verratti, with which we continued to interact in particular during the most difficult period of the COVID pandemics and with which we have always had very interesting physics discussion, going beyond the arguments contained in this Thesis.

In conclusion, a big thanks to all the members of my family and to all the most important friends of my life for having never stopped to sustain me, especially in the most difficult times.

Appendix A

Details on the polarization functions

In this Appendix we will show how to compute the two-particle and the one-particle contributions to the imaginary parts of the polarization functions, respectively. To achieve this goal, one has to consider all the possible two-particle and one-particle intermediate hadronic states that occur in the completeness sum in Eq. (3.24).

Let us start with the two-particle contributions. To be as generic as possible, we are going to show all the two-particle states composed by a $B^{(*)}$-meson and a $D^{(*)}$-meson, although the B^* case has not been considered in the main text given the phenomenological applications of the DM method to semileptonic charged-current B decays. The matrix elements of interest can be thus classified as:

- vector current matrix elements

$$\begin{aligned}
\sqrt{m_B m_D}\langle D(p_D)|V^\mu|\bar{B}(p_B)\rangle &= f_+(p_B+p_D)^\mu + f_-(p_B-p_D)^\mu\,;\\
\sqrt{m_B m_{D^*}}\langle D^*(p_D,\epsilon_D)|V^\mu|\bar{B}(p_B)\rangle &= i f_V \epsilon^{\mu\nu\alpha\beta}\epsilon^*_{D\nu}p_{D\alpha}p_{B\beta}\,;\\
\sqrt{m_{B^*} m_D}\langle D(p_D)|V^\mu|\bar{B}^*(p_B,\epsilon_B)\rangle &= i f_{\bar{V}} \epsilon^{\mu\nu\alpha\beta}\epsilon_{B\nu}p_{D\alpha}p_{B\beta}\,;\\
\sqrt{m_{B^*} m_{D^*}}\langle D^*(p_D,\epsilon_D)|V^\mu|\bar{B}^*(p_B,\epsilon_B)\rangle &= -[f_1(p_B+p_D)^\mu + f_2(p_B-p_D)^\mu]\,(\epsilon^*_D\cdot\epsilon_B)\\
&\times\ +f_3(\epsilon^*_D\cdot p_B)\epsilon^\mu_B + f_4(\epsilon_B\cdot p_D)\epsilon^{*\mu}_D\\
&-\ [f_5 p^\mu_B + f_6 p^\mu_D](\epsilon^*_D\cdot p_B)(\epsilon_B\cdot p_D)\,;
\end{aligned} \tag{A.1}$$

- axial current matrix elements

$$\begin{aligned}
\sqrt{m_B m_{D^*}}\langle D^*(p_D,\epsilon_D)|A^\mu|\bar{B}(p_B)\rangle &= f_{A_1}\epsilon^{*\mu}_D - [f_{A_2}p^\mu_B + f_{A_3}p^\mu_D](\epsilon^*_D\cdot p_B)\,;\\
\sqrt{m_{B^*} m_D}\langle D(p_D)|A^\mu|\bar{B}^*(p_B,\epsilon_B)\rangle &= f_{\bar{A}_1}\epsilon^\mu_B - [f_{\bar{A}_2}p^\mu_B + f_{\bar{A}_3}p^\mu_D](\epsilon_B\cdot p_D)\,;\\
\sqrt{m_{B^*} m_{D^*}}\langle D^*(p_D,\epsilon_D)|A^\mu|\bar{B}^*(p_B,\epsilon_B)\rangle &= i\epsilon^{\mu\nu\alpha\beta}\{[f_7(p_B+p_D)_\nu\\
&+\ f_8(p_B-p_D)_\nu]\epsilon_{B\alpha}\epsilon^*_{D\beta} + [f_9(\epsilon^*_D\cdot p_B)\epsilon_{B\nu}\\
&+\ f_{10}(\epsilon_B\cdot p_D)\epsilon^*_{D\nu}]p_{D\alpha}p_{B\beta}\}\,,
\end{aligned} \tag{A.2}$$

Note that the first two matrix elements of Eq. (A.1) and the first one of Eq. (A.2) are precisely the hadronic matrix elements discussed in Chapter 3. Moreover, the normalisation of the states differs from the Feynman one by a factor equal to the square root of the meson mass, $|p_M\rangle_{\text{Feynman}} = \sqrt{M_M}\,|p_M\rangle$, because this is more convenient in the framework of the HQET. In fact, in Ref. [66] Caprini, Lellouch and Neubert introduced the quantities h_i, which are linear combinations of the FFs f_i previously defined, expressed as functions of the recoil variable w rather than of q^2 (the index i labels a generic FF). The h_i describe the decompositions (A.1)-(A.2) in terms of the meson 4-velocities instead of the meson 4-momenta, according to the following classification:

- scalar FFs

$$\begin{aligned} S_1^{BD} &= h_+ - \frac{1+r}{1-r}\frac{w-1}{w+1}h_-; \\ S_2^{B^*D^*} &= h_1 - \frac{1+r}{1-r}\frac{w-1}{w+1}h_2\,; \\ S_3^{B^*D^*} &= w\left[h_1 - \frac{1+r}{1-r}\frac{w-1}{w+1}h_2\right] \\ &+ \frac{w-1}{1-r}\left[rh_3 - h_4 + (1-wr)h_5 + (w-r)h_6\right]\,; \end{aligned} \tag{A.3}$$

- vector FFs

$$\begin{aligned} V_1^{BD} &= h_+ - \frac{1-r}{1+r}h_-; \\ V_2^{B^*D^*} &= h_1 - \frac{1-r}{1+r}h_2\,; \\ V_3^{B^*D^*} &= w\left[h_1 - \frac{1-r}{1+r}h_2\right] \\ &+ \frac{1}{1+r}\left[(1-wr)h_3 + (r-w)h_4 + (w^2-1)(rh_5+h_6)\right] \\ V_4^{BD^*} &= h_V; \\ V_5^{B^*D} &= h_{\bar{V}}\,; \\ V_6^{B^*D^*} &= h_3,; \\ V_7^{B^*D^*} &= h_4\,; \end{aligned} \tag{A.4}$$

- pseudoscalar FFs

$$\begin{aligned} P_1^{BD^*} &= \frac{1}{1+r}[(w+1)h_{A_1} - (1-rw)h_{A_2} - (w-r)h_{A_3}]\,; \\ P_2^{B^*D} &= \frac{1}{1+r}[r(w+1)h_{\bar{A}_1} - (r-w)h_{\bar{A}_2} - (rw-1)h_{\bar{A}_3}]\,; \\ P_3^{B^*D^*} &= h_7 - \frac{1-r}{1+r}h_8\,; \end{aligned} \tag{A.5}$$

- axial FFs

$$\begin{aligned} A_1^{BD^*} &= h_{A_1}; \\ A_2^{B^*D} &= h_{\bar{A}_1}\,; \\ A_3^{B^*D^*} &= h_7 - \frac{w-1}{w+1}h_8 + (w-1)h_{10}\,; \\ A_4^{B^*D^*} &= h_7 + \frac{w-1}{w+1}h_8 + (w-1)h_9\,; \\ A_5^{BD^*} &= \frac{1}{1-r}[(w-r)h_{A_1} - (w-1)(rh_{A_2} + h_{A_3})]\,; \\ A_6^{B^*D} &= \frac{1}{1-r}[(1-wr)h_{\bar{A}_1} + (w-1)(h_{\bar{A}_2} + rh_{\bar{A}_3})]\,; \\ A_7^{B^*D^*} &= h_7 - \frac{1+r}{1-r}\frac{w-1}{w+1}h_8\,. \end{aligned} \tag{A.6}$$

The last classification of the FFs allows to separate different values of spin and parity quantum numbers from each other. For simplicity, all scalar, pseudoscalar, vector and axial quantities have been presented indicating initial and final states as superscripts, so that we can easily remember to which process each FF refers to. At this point, a direct computation shows that the two-particle contribution to the polarization functions can be expressed in terms of the FFs as:

- scalar channel

$$q^2\,\mathrm{Im}\Pi_{0^+,2p}\left[w(q^2)\right] = \frac{m_{B^{(*)}}m_{D^{(*)}}}{8\pi}\sum_{i=1}^{3}(1+\delta_{i2})\frac{(w^2-1)^{1/2}(w+1)^2}{4}\frac{(\beta_i^2-1)|S_i|^2}{(\beta_i^2-\frac{w+1}{2})^2}\,, \tag{A.7}$$

- vector channel

$$\begin{aligned} q^2\,\mathrm{Im}\Pi_{1^-,2p}\left[w(q^2)\right] = \frac{m_{B^{(*)}}m_{D^{(*)}}}{96\pi}\Bigg[&\sum_{i=1}^{3}(1+\delta_{i2})(w^2-1)^{3/2}\frac{\beta_i^2|V_i|^2}{(\beta_i^2-\frac{w+1}{2})^2} \\ &+\sum_{i=4}^{7}(w^2-1)^{3/2}\frac{2|V_i|^2}{(\beta_i^2-\frac{w+1}{2})}\Bigg]\,, \end{aligned} \tag{A.8}$$

- pseudoscalar channel

$$q^2\,\mathrm{Im}\Pi_{0^-,2p}\left[w(q^2)\right] = \frac{m_{B^{(*)}}m_{D^{(*)}}}{32\pi}\sum_{i=1}^{3}(1+\delta_{i3})(w^2-1)^{3/2}\frac{\beta_i^2|P_i|^2}{(\beta_i^2-\frac{w+1}{2})^2}\,, \tag{A.9}$$

- axial channel

$$\begin{aligned} q^2\,\mathrm{Im}\Pi_{1^+,2p}\left[w(q^2)\right] = \frac{m_{B^{(*)}}m_{D^{(*)}}}{24\pi}\Bigg[&\sum_{i=1}^{4}(w^2-1)^{1/2}\frac{(w+1)^2}{4}\frac{2|A_i|^2}{(\beta_i^2-\frac{w+1}{2})} \\ &+\sum_{i=5}^{7}(w^2-1)^{1/2}\frac{(w+1)^2}{4}(1+\delta_{i7})\frac{(\beta_i^2-1)|A_i|^2}{(\beta_i^2-\frac{w+1}{2})^2}\Bigg]\,, \end{aligned} \tag{A.10}$$

where the quantity β_i is defined as

$$\beta_i = \frac{m_{B^{(*)}}+m_{D^{(*)}}}{2\sqrt{m_{B^{(*)}}m_{D^{(*)}}}}. \tag{A.11}$$

Note that the above expressions hold for a single two-particle $B^{(*)}$-$D^{(*)}$ intermediate state. If there are several, essentially degenerate, such states, differing for example by the replacement of an up with a down quark (such as B^- - $\bar{D}^0$ with B^0 - D^-), then we have to sum up their contributions to $\mathrm{Im}\Pi_{J^P,2p}$.

Let us pass now to the one-particle contribution of mesons to the imaginary part of the polarization functions. In the case of the vector B_c^* and of the pseudoscalar B_c mesons the one-particle current matrix elements are defined as

$$\begin{aligned} \langle 0|\,A^\mu\,|B_c\rangle &= f_{B_c}\,p_{B_c}^\mu, \\ \langle 0|\,V^\mu\,|B_c^*,\lambda\rangle &= f_{B_c^*}M_{B_c^*}\epsilon_\lambda^\mu(p_{B_c^*}) \qquad (\lambda=1,2,3) \end{aligned} \tag{A.12}$$

with $f_{B_c^{(*)}}$ being the decay constants of the aforementioned mesons, $M_{B_c^{(*)}}$ their masses, λ the B_c^* polarization and ϵ_λ the corresponding polarization vector. The one-particle contributions to the polarization functions are then given by

$$q^2\,\mathrm{Im}\Pi_{0^-,1p}(q^2) = \pi\delta(q^2-M_{B_c}^2)\,f_{B_c}^2M_{B_c}^2\,,$$

$$q^2\,\mathrm{Im}\Pi_{1^-,1p}(q^2) = \pi\delta(q^2 - M^2_{B_c^*})\, f^2_{B_c^*} M^2_{B_c^*}\,. \tag{A.13}$$

The generalization to possible one-particle states below the annihilation threshold in the scalar and axial-vector channels is straightforward.

Appendix B

The BGL, BCL and CLN parametrizations of the FFs

In this Appendix we will briefly review the main properties underlying the well-known BGL, BCL and CLN parametrizations of the hadronic FFs.

B.1 The BGL parametrization

The parametrization introduced by Boyd, Grinstein and Lebed [61–63] relies on the same first principles, namely unitarity and analiticity of the FFs, that are at the basis of the Dispersive Matrix method. However, it is based on a power series expansion of the FFs in terms of the conformal variable z introduced in the Eq. (3.33).

To be more specific, let us go back to Eq.(3.34). The important property of the quantity $\tilde{\Phi}(t,t_0)P(t)f(t)$ is that it does not have any kinematical and sub-threshold singularity. Thus, we can expand $\tilde{\Phi}(t,t_0)P(t)f(t)$ in a set of *orthonormal functions*, which are proportional to powers of $z(t,t_0)$. The consequence of this strategy is that we can express $f(t)$ in the semileptonic region as

$$f(t) = \frac{1}{P(t)\phi(t,t_0)} \sum_{n=0}^{\infty} a_n z(t,t_0)^n, \tag{B.1}$$

where the BGL coefficients a_n have to satisfy, by construction, the unitarity condition

$$\sum_{n=0}^{\infty} |a_n|^2 \leq 1. \tag{B.2}$$

From a practical point of view, when fitting the shape of the FFs with appropriate LQCD/experimental data, the series present in Eq.(B.1) has to be truncated. This is an important difference with respect to the Dispersive Matrix method, which instead is independent of any truncation of the power series expansion and, in fact, it is equivalent to the results of all possible BGL fits which satisfy unitarity and at the same time reproduce exactly the input data.

In the Eq. (B.1) we find the same basic ingredients that we have introduced for the Dispersive Matrix approach. The first one is the kinematical function $\phi(t,t_0)$, which has a very similar structure

to Eqs. (3.45) and (4.8). In fact, one can demonstrate that these functions have the general form [63]

$$\begin{aligned}\phi(t,t_0) = &\sqrt{\frac{n_I}{K\pi\chi}}\left(\frac{t_+ - t}{t_+ - t_0}\right)^{1/4}\left(\sqrt{t_+ - t} + \sqrt{t_+ - t_0}\right), \\ &\times (t_+ - t)^{a/4}\left(\frac{t_+ - t}{t_+ - t_-}\right)^{b/2}\left(\frac{t_+ - t}{t_+}\right)^{-(c+3)},\end{aligned} \tag{B.3}$$

where the coefficients K, a, b and c are integers that depend on the particular FF (see Table B.1 for their values in semileptonic $B \to D, D^*$ decays) and n_I is a Clebsh-Gordan factor. Note that in BGL parametrization the susceptibility χ appears explicitly in the definition of the kinematical function ϕ, contrarily to what happens in the Dispersive Matrix approach. Finally, Eq. (B.3) can be re-expressed in terms of the conformal variable z by recalling the transformation (3.33).

Table B.1: Values of the integers present in Eq.(B.3). The first two form factors enter semileptonic $B \to D$ decays, while the other four concern $B \to D^*$ ones.

Form factor	K	a	b	c
f_+	48	3	3	2
f_0	16	1	1	1
f	24	1	1	1
g	96	3	3	1
$\mathcal{F}_1$	48	1	1	2
P_1	64	3	3	1

The second ingredient present in Eq.(B.3) is the Blaschke factor, whose general form is

$$P(z) = \prod_{P=1}^{n} \frac{z - z_P}{1 - z z_P} \tag{B.4}$$

where we have also introduced the quantities

$$z_P = \frac{\sqrt{t_+ - m_P^2} - \sqrt{t_+ - t_-}}{\sqrt{t_+ + m_P^2} - \sqrt{t_+ - t_-}}.$$

These functions allow us to eliminate all the singularities caused by the pole states, whose masses have been denoted with m_P in the previous Equations and whose spin-parity quantum numbers have to be the same ones of the form factor we are taking into consideration. Note that the terms in Eq. (B.4) are completely equivalent to the ones introduced in Eq. (5.6) for the implementation of the Dispersive Matrix method.

B.2 BCL parametrization

The parametrization introduced by Bourrely, Caprini and Lellouch [64] is quite similar to the BGL one. This parametrization is often used to describe semileptonic $B \to \pi$ decays, thus we are going to

specialize the discussion on the FFs $f^{\pi}_{+,0}(q^2)$ studied in Chapter 4. According to BCL, we can express these FFs as

$$f^{\pi}_{+}(z) = \frac{1}{1-q^2/m^2_{B^*}} \sum_{n=0}^{N_z-1} a_k \left[z^n - (-1)^{n-N_z} \frac{n}{N_z} z^{N_z} \right], \tag{B.5}$$

$$f^{\pi}_{0}(z) = \sum_{n=0}^{N_z-1} b_k z^k. \tag{B.6}$$

The first term in Eq. (B.5) is the analogous of the Blaschke factor, which takes into account the effect of the B^*-pole. Also in the BCL case, we have to truncate the series in Eqs. (B.5)-(B.6) when fitting the available LQCD/experimental data. We want to highlight again that this problem is completely absent in the Dispersive Matrix study of the FFs since, in that case, the DM bands of the FFs are completely equivalent to the results of all the possible BCL fits which satisfy unitarity and at the same time reproduce exactly the input data.

Another important task is the unitarity constraint that the BCL coefficients have to satisfy, *i.e.*

$$\sum_{i,j=0}^{N_z} B^{+}_{mn} a_m a_n \leq 1, \quad \sum_{i,j=0}^{N_z} B^{0}_{mn} b_m b_n \leq 1 \tag{B.7}$$

for the 1^- and the 0^+ channels, respectively. For numerical values of the $B^{\{+,0\}}_{mn}$ coefficients, see [64, 107, 108]. Note that in these papers the authors use a perturbative evaluation of the 1^- susceptibility in order to derive these numbers, *i.e.* $\chi_{1^-} \cdot 10^4 \simeq 5\,\mathrm{GeV}^{-2}$ [64], which is compatible with our non-perturbative determination $\chi^{np}_{1^-} \cdot 10^4 = 4.45(1.16)\,\mathrm{GeV}^{-2}$, that will be presented in Appendix D.

B.3 CLN parametrization

The last possibility that we will finally investigate is the parametrization proposed by Caprini, Lellouch and Neubert [65,66]. The main feature of this method is the usage of the Heavy Quark Effective Theory (HQET) in order to derive useful relations between the hadronic FFs.

By defining the function (here the subscript j refers to a particular spin-parity channel)

$$\tilde{f}_j(z) \equiv \tilde{\Phi}_j(t,t_0) P_j(t) F_j(t), \tag{B.8}$$

which is analytic inside the unitary disc, and recalling again Eq.(3.34), we have that

$$\frac{1}{2\pi} \int_0^{2\pi} d\theta \sum_j |\tilde{f}_j(e^{i\theta})|^2 \leq 1, \tag{B.9}$$

where we have put $z = e^{i\theta}$. We can then expand the functions $\tilde{f}_j(z)$ present in Eq.(B.9) so that

$$\sum_j \sum_{n=0}^{\infty} |\frac{1}{n!} \tilde{f}^{(n)}_j(0)|^2 \leq 1, \tag{B.10}$$

where $\tilde{f}^{(n)}_j(0)$ indicates the n-th derivative of $\tilde{f}_j(z)$ with respect to the variable z, then evaluated at $z = 0$.

At this point, one can relate the derivatives of the form factors at $z = 0$ to the ones computed with respect to the recoil variable w and then evaluated at $w = w_0$, where w_0 satisfies the relation $z(w_0) = 0$. To this end, one can easily show from Eqs. (3.11) and (3.37) that

$$z = \frac{\sqrt{w+1} - \sqrt{2}}{\sqrt{w+1} + \sqrt{2}}, \tag{B.11}$$

or equivalently, by inverting the Eq. (B.11),

$$w(z) = 2\left(\frac{1+z}{1-z}\right)^2 - 1. \tag{B.12}$$

It is straightforward that $w_0 = 1$. By way of example, let us take into consideration the FF $V_1(w)$ (that has been defined in Appendix A), then we get

$$\begin{aligned}
\partial_z V_1(w(z))|_{z=0} &= -8\rho_1^2 V_1(1), \\
\partial_z^2 V_1(w(z))|_{z=0} &= (128c_1 - 32\rho_1^2) V_1(1), \\
\partial_z^3 V_1(w(z))|_{z=0} &= (3072d_1 + 1536c_1 - 144\rho_1^2) V_1(1),
\end{aligned}$$

The parameters ρ_1^2, c_1 and d_1 entering the previous expressions are defined by the expansion

$$V_1(w) = V_1(1)\left[1 - \rho_1^2(w-1) + c_1(w-1)^2 + d_1(w-1)^3 + \ldots\right]. \tag{B.13}$$

At this point, we note that in the HQET all the FFs $F_j(w)$ become identically equal to the Isgur-Wise function $\xi(w)$ [400] in the semileptonic region. In order to incorporate corrections to that limit Caprini, Lellouch and Neubert choose the form factor $V_1(w)$ as a reference and express the expansion parameters of all the other form factors in terms of the expansion parameters ρ_1^2, c_1 and d_1 that we have just defined. Their choice is motivated by the fact that $V_1(w)$ is the physical form factor which describes the semileptonic decay $B \to D\ell\nu$. Hence, we can write the ratios $R_j(w)$ as

$$R_j(w) \equiv \frac{F_j(w)}{V_1(w)} = A_j\left[1 + B_j(w-1) + C_j(w-1)^2 + D_j(w-1)^3 + \ldots\right], \tag{B.14}$$

where the expansion parameters A_j, B_j, C_j and D_j are computed by including the leading perturbative and $1/m_b$ corrections, where m_b is the bottom mass (see Figure B.1.). Now, for phenomenological applications it is necessary to compute the zero-recoil expansions of the ratios $R_j(w)$. To achieve this goal, Caprini, Lellouch and Neubert have studied the behaviour of the inequality (B.10) for the form factor $V_1(w)$ after the inclusion of firstly two and secondly three derivatives. They also express $V_1(w(z))$ as a power series in z (rather than in $(w-1)$) in order to improve the convergence rate of the series. The result of this analysis is that the relation (B.13) becomes

$$\frac{V_1(w(z))}{V_1(1)} \approx 1 - 8\rho_1^2 z + (51\rho_1^2 - 10)z^2 - (252\rho_1^2 - 84)z^3, \tag{B.15}$$

where the authors do not include higher-order terms as they are confident that the third-order results provide an adequate representation of the form factor over the entire kinematical region accessible in semileptonic decays.

F_j	A_j	B_j	C_j	D_j
S_1	1.0208	−0.0436	0.0201	−0.0105
S_2	1.0208	−0.0749	−0.0846	0.0418
S_3	1.0208	0.0710	−0.1903	0.0947
P_1	1.2089	−0.2164	0.0026	−0.0007
P_2	0.8938	−0.0949	0.0034	−0.0009
P_3	1.0544	−0.2490	0.0030	−0.0008
V_1	1	0	0	0
V_2	1.0894	−0.2251	0.0000	0.0000
V_3	1.1777	−0.2651	0.0000	0.0000
V_4	1.2351	−0.1492	−0.0012	0.0003
V_5	1.0399	−0.0440	−0.0014	0.0004
V_6	1.5808	−0.1835	−0.0009	0.0003
V_7	1.3856	−0.1821	−0.0011	0.0003
A_1	0.9656	−0.0704	−0.0580	0.0276
A_2	0.9656	−0.0280	−0.0074	0.0023
A_3	0.9656	−0.0629	−0.0969	0.0470
A_4	0.9656	−0.0009	−0.1475	0.0723
A_5	0.9656	0.3488	−0.2944	0.1456
A_6	0.9656	−0.2548	0.0978	−0.0504
A_7	0.9656	−0.0528	−0.0942	0.0455

Figure B.1: Updated values of the coefficients of the expansion of the ratio $R_j(w)$ in powers of $(w-1)$. Taken from [69].

Appendix C

Determinants and inequalities in the DM method

In this appendix we give some formulae which are useful to simplify the numerical calculation of the determinants of the matrix $\mathbf{M}$ and of the minors $\mathbf{M}^{(i,j)}$ discussed in Chapter 3. We consider explicitly the case of real matrices only, because in practice this is the standard case. The generalization to complex matrices is straightforward. We will also make use of the explicit expressions (3.42) of the inner products.

Let us start from the calculation of the determinant of the $N \times N$ matrix corresponding to the inner products $\langle g_{t_i} | g_{t_j} \rangle = 1/(1 - z_i z_j)$, where $z_i \equiv z(t_i, t_-)$ are assumed to be real numbers satisfying the conditions $z_i \neq z_j$ and $|z_i| < 1$ with $i, j = 1, 2, ...N$. Thus, we want to calculate the determinant of the following matrix

$$G \equiv \begin{pmatrix} \frac{1}{1-z_1^2} & \frac{1}{1-z_1 z_2} & \cdots & \frac{1}{1-z_1 z_N} \\ \frac{1}{1-z_2 z_1} & \frac{1}{1-z_2^2} & \cdots & \frac{1}{1-z_2 z_N} \\ \cdots & \cdots & \cdots & \cdots \\ \frac{1}{1-z_N z_1} & \frac{1}{1-z_N z_2} & \cdots & \frac{1}{1-z_N^2} \end{pmatrix} . \tag{C.1}$$

A simple evaluation by induction shows that

$$G^N(z_1, z_2, ...z_N) \equiv \det[G] = \frac{1}{\prod_{i=1}^N (1 - z_i^2)} \left(\prod_{i<j=1}^N \frac{z_i - z_j}{1 - z_i z_j} \right)^2 , \tag{C.2}$$

where, in the case $N = 1$ it is understood that $\prod_{i<j=1}^N (...) \to 1$.

The matrix of which we want to calculate the determinant is given by Eq. (3.43), namely it has the form

$$\mathbf{M} \equiv \begin{pmatrix} \chi & \phi f & \phi_1 f_1 & \phi_2 f_2 & ... & \phi_N f_N \\ \phi f & \frac{1}{1-z_0^2} & \frac{1}{1-z_0 z_1} & \frac{1}{1-z_0 z_2} & ... & \frac{1}{1-z_0 z_N} \\ \phi_1 f_1 & \frac{1}{1-z_1 z_0} & \frac{1}{1-z_1^2} & \frac{1}{1-z_1 z_2} & ... & \frac{1}{1-z_1 z_N} \\ \phi_2 f_2 & \frac{1}{1-z_2 z_0} & \frac{1}{1-z_2 z_1} & \frac{1}{1-z_2^2} & ... & \frac{1}{1-z_2 z_N} \\ ... & ... & ... & ... & ... & ... \\ \phi_N f_N & \frac{1}{1-z_N z_0} & \frac{1}{1-z_N z_1} & \frac{1}{1-z_N z_2} & ... & \frac{1}{1-z_N^2} \end{pmatrix} , \tag{C.3}$$

where χ is the susceptibility that bounds the inner product $\langle \phi f | \phi f \rangle$ and, we remind, $\phi_i f_i$ corresponds to the scalar product $\langle \phi f | g_{t_i} \rangle$ for the known values of the FF $f_i = f(z_i)$, whereas ϕf is the scalar product $\langle \phi f | g_t \rangle$ of the FF $f(z(t))$ that we want to constrain. In order to use a compact notation let us indicate the values of the conformal variable z and of $\phi(z)f(z)$ as z_0 and $\phi_0 f_0$, respectively, so that in what follow the index i may run from 0 to N.

A simple evaluation by induction, as before, yields

$$\begin{aligned} \det[\mathbf{M}] &= G^{(N+1)}(z_0, z_1, z_2, ...z_N) \left[\chi - \sum_{i=0}^{N} \phi_i^2 f_i^2 (1 - z_i^2) \left(\prod_{m \neq i = 0}^{N} \frac{1 - z_i z_m}{z_i - z_m} \right)^2 \right. \\ &+ \left. 2 \sum_{i<j=0}^{N} \phi_i f_i \phi_j f_j \frac{(1 - z_i^2)(1 - z_j^2)(1 - z_i z_j)}{(z_i - z_j)^2} \left(\prod_{m \neq (i,j) = 0}^{N} \frac{1 - z_i z_m}{z_i - z_m} \frac{1 - z_j z_m}{z_j - z_m} \right) \right] , \end{aligned} \tag{C.4}$$

where

$$G^{(N+1)}(z, z_1, z_2, ...z_N) = \frac{1}{1 - z^2} \left(\prod_{i=1}^{N} \frac{z - z_i}{1 - z z_i} \right)^2 G^{(N)}(z_1, z_2, ...z_N) \ . \tag{C.5}$$

The unitarity bounds for the (unknown) form factor f_0 result from the condition

$$\det[\mathbf{M}] = \alpha \phi_0^2 \left[-f_0^2 + 2\overline{\beta} f_0 - \overline{\beta}^2 + \overline{\gamma} \right] \geq 0 \ , \tag{C.6}$$

which implies[1]

$$\overline{\beta} - \sqrt{\overline{\gamma}} \leq f_0 \leq \overline{\beta} + \sqrt{\overline{\gamma}} \ , \tag{C.7}$$

where (after some algebraic manipulations)

$$\alpha \equiv G^{(N)}(z_1, z_2, ...z_N) \geq 0 \ , \tag{C.8}$$

$$\overline{\beta} = \frac{1}{\phi_0 d_0} \sum_{j=1}^{N} f_j \phi_j d_j \frac{1 - z_j^2}{z_0 - z_j} \ , \tag{C.9}$$

$$\overline{\gamma} = \frac{1}{1 - z_0^2} \frac{1}{\phi_0^2 d_0^2} (\chi - \overline{\chi}) \ , \tag{C.10}$$

$$\overline{\chi} = \sum_{i,j=1}^{N} f_i f_j \phi_i d_i \phi_j d_j \frac{(1 - z_i^2)(1 - z_j^2)}{1 - z_i z_j} \ , \tag{C.11}$$

with

$$d_0 \equiv \prod_{m=1}^{N} \frac{1 - z_0 z_m}{z_0 - z_m} \ , \tag{C.12}$$

$$d_j \equiv \prod_{m \neq j = 1}^{N} \frac{1 - z_j z_m}{z_j - z_m} \ . \tag{C.13}$$

[1]The relations of the coefficients $\overline{\beta}$ and $\overline{\gamma}$ with β and γ, defined in Eq. (3.50), are: $\overline{\beta} = -\beta/(\alpha\phi_0)$ and $\overline{\gamma} = (\beta^2 + \alpha\gamma)/(\alpha\phi_0)^2 = \Delta_1\Delta_2/(\alpha\phi_0)^2$.

Unitarity is satisfied only when $\overline{\gamma} \geq 0$, which implies $\chi \geq \overline{\chi}$. Note that d_0 and ϕ_0 depend on z_0, while the quantities d_j and ϕ_j with $j = 1, 2, ...N$ do not. Thus, the values of $\overline{\beta}$ and $\overline{\gamma}$ depend on z_0, while the value of $\overline{\chi}$ does not depend on z_0 and it depends only on the set of input data. Consequently, the unitarity condition $\chi \geq \overline{\chi}$ does not depend on z_0.

Note that:

- When z_0 goes toward one of the known values z_j, let's say $z_0 \to z_{j^*}$, one has $d_0 \to d_{j^*}(1 - z_{j^*}^2)/(z_0 - z_{j^*})[1 + \mathcal{O}(z_0 - z_{j^*})]$, so that one gets (as expected)

$$\overline{\beta} \;\to\; f_{j^*} \;, \tag{C.14}$$

$$\overline{\gamma} \;\to\; 0 \;. \tag{C.15}$$

- By expanding the factor $1/(1 - z_i z_j)$ in Eq. (C.11) for $|z_i| < 1$ one has

$$\overline{\chi} = \sum_{k=0}^{\infty} \left[\sum_{i=1}^{N} f_i \phi_i d_i (1 - z_i^2) z_i^k \right]^2 \;, \tag{C.16}$$

  which implies $\overline{\chi} \geq 0$.

- Since in terms of the squared 4-momentum transfer t the variable z_0 is given by

$$z_0 = \frac{\sqrt{t_+ - t} - \sqrt{t_+ - t_-}}{\sqrt{t_+ - t} + \sqrt{t_+ - t_-}} \tag{C.17}$$

  the annihilation threshold $t = t_+$ corresponds to $z_0 = -1$, while $t \to -\infty$ corresponds to $z_0 = 1$. From Eq. (C.10) it follows that unitarity may have no predictive power (i.e. $\overline{\gamma} \to \infty$) both at the annihilation threshold t_+ and for $t \to -\infty$.

Appendix D

Non-perturbative computation of the susceptibilities

In this Appendix we discuss the theoretical idea underlying the non-perturbative computation of the two-point correlation functions, namely the susceptibilities χ, that have been used as inputs of the Dispersive Matrix approach (see Eq. (3.40)). Note that many of the definitions and formulae introduced here have been used on the lattice to compute the HVP function of two electromagnetic currents [401] and its isospin-breaking corrections [402] contributing to the muon $g-2$. For all the details about the implementation and the numerical results of these computations on the lattice, see [2].

D.1 Basic definitions

We compute the correlation functions at the Euclidean four-momentum $Q \equiv (Q_0, \vec{Q})$, given in terms of the Minkowskian momentum $q \equiv (q_0, \vec{q})$ by the relations $Q_0 = iq_0$ and $\vec{Q} = \vec{q}$. With this choice $Q^2 = -q^2$. Furthermore, we perform a Wick rotation on the coordinates, so that we pass from the Minkoskian coordinates $x_M = (\tau, \vec{x})$ to the Euclidean ones $x = (t, \vec{x})$, with $t = i\,\tau$. The vector and axial HVP tensors take the form

$$\begin{aligned}
\Pi_V^{\mu\nu}(Q) &= \int d^4x e^{-iQ\cdot x} \langle 0| T\{V_E^{\mu\dagger}(x) V_E^{\nu}(0)\} |0\rangle \\
&= (-Q^\mu Q^\nu + \delta^{\mu\nu} Q^2)\Pi_{1^-}(Q^2) - Q^\mu Q^\nu \Pi_{0^+}(Q^2)\,, \qquad \text{(D.1)} \\
\Pi_A^{\mu\nu}(Q) &= \int d^4x e^{-iQ\cdot x} \langle 0| T\{A_E^{\mu\dagger}(x) A_E^{\nu}(0)\} |0\rangle \\
&= (-Q^\mu Q^\nu + \delta^{\mu\nu} Q^2)\Pi_{1^+}(Q^2) - Q^\mu Q^\nu \Pi_{0^-}(Q^2)\,,
\end{aligned}$$

where we have introduced the currents

$$V_E^\mu = \bar{c}\gamma_E^\mu b, \quad A^\mu = \bar{c}\gamma_E^\mu \gamma_E^5 b\,. \qquad \text{(D.2)}$$

defined in terms of Hermitian, Euclidean Dirac matrices satisfying the anticommutation relations

$$\{\gamma_E^\mu, \gamma_E^\nu\} = 2\delta^{\mu\nu}\,. \qquad \text{(D.3)}$$

In the following we will omit the explicit subscript E in the definition of the Euclidean currents and γ-matrices.

A convenient choice is to work with the momentum $Q = (Q^0, \vec{0})$ so that

$$\begin{aligned} Q^2\Pi_{0^+}(Q^2) &= -\int_{-\infty}^{\infty} dt'\, e^{-iQt'} C_{0^+}(t')\,, \\ Q^2\Pi_{1^-}(Q^2) &= -\int_{-\infty}^{\infty} dt'\, e^{-iQt'} C_{1^-}(t')\,, \\ Q^2\Pi_{0^-}(Q^2) &= -\int_{-\infty}^{\infty} dt'\, e^{-iQt'} C_{0^-}(t')\,, \\ Q^2\Pi_{1^+}(Q^2) &= -\int_{-\infty}^{\infty} dt'\, e^{-iQt'} C_{1^+}(t')\,, \end{aligned} \tag{D.4}$$

where the explicit expressions of the various correlators computed at the time distance t are

$$\begin{aligned} C_{0^+}(t) &= \int d^3\vec{x}\ \langle 0|\, T\{\bar{b}(t,\vec{x})\gamma_0 c(t,\vec{x})\bar{c}(0)\gamma_0 b(0)\}\,|0\rangle\ , \\ C_{1^-}(t) &= \frac{1}{3}\sum_{i=1}^{3}\int d^3\vec{x}\ \langle 0|\, T\{\bar{b}(t,\vec{x})\gamma_i c(t,\vec{x})\bar{c}(0)\gamma_i b(0)\}\,|0\rangle\ , \\ C_{0^-}(t) &= \int d^3\vec{x}\ \langle 0|\, T\{\bar{b}(t,\vec{x})\gamma_0\gamma_5 c(t,\vec{x})\bar{c}(0)\gamma_0\gamma_5 b(0)\}\,|0\rangle\ , \\ C_{1^+}(t) &= \frac{1}{3}\sum_{i=1}^{3}\int d^3\vec{x}\ \langle 0|\, T\{\bar{b}(t,\vec{x})\gamma_i\gamma_5 c(t,\vec{x})\bar{c}(0)\gamma_i\gamma_5 b(0)\}\,|0\rangle\ . \end{aligned} \tag{D.5}$$

By recalling the definition of the spherical Bessel functions

$$j_0(z) = \frac{\sin(z)}{z}\ , \qquad j_1(z) = \frac{\sin(z)}{z^2} - \frac{\cos(z)}{z} \tag{D.6}$$

and given that

$$\frac{\partial}{\partial Q^2}\cos(Qt) = -\frac{t^2}{2} j_0(Qt), \tag{D.7}$$

we get

$$\begin{aligned} \chi_{0^+}(Q^2) &= \int_0^{\infty} dt'\, t'^{\,2} j_0(Qt') C_{0^+}(t')\,, \\ \chi_{1^-}(Q^2) &= \frac{1}{4}\int_0^{\infty} dt'\, t'^{\,4} \frac{j_1(Qt')}{Qt} C_{1^-}(t')\,, \\ \chi_{0^-}(Q^2) &= \int_0^{\infty} dt'\, t'^{\,2} j_0(Qt') C_{0^-}(t')\,, \\ \chi_{1^+}(Q^2) &= \frac{1}{4}\int_0^{\infty} dt'\, t'^{\,4} \frac{j_1(Qt')}{Qt'} C_{1^+}(t')\,. \end{aligned} \tag{D.8}$$

In this Thesis we will always take $Q^2 = 0$. In this case $j_0(0) = 1$ and $\lim_{x\to 0} j_1(x)/x = 1/3$, so that the derivatives of the longitudinal and transverse polarization functions are equal to the second and the fourth moments of the longitudinal and transverse Euclidean correlators, respectively. We point out again that, by using the two-point correlation functions determined non-perturbatively, we may constrain the form factors also at $Q^2 \neq 0$.

Some relations, which are particularly useful in the analysis of the numerical results, can be derived using the Ward Identities (WIs) that the vector and axial vector quark currents satisfy

$$\begin{aligned} \partial_\mu \bar{b}(x)\gamma_\mu c(x) &= (m_b - m_c)\bar{b}(x)c(x)\,, \\ \partial_\mu \bar{b}(x)\gamma_\mu\gamma_5 c(x) &= (m_b + m_c)\bar{b}(x)\gamma_5 c(x)\,, \end{aligned} \tag{D.9}$$

where m_b and m_c are the (bare) masses of the bottom and charm quarks respectively. Hence, by defining two further (Euclidean) polarization functions connected to the scalar and the pseudoscalar currents, namely

$$\begin{aligned} \Pi_S(Q^2) &\equiv \int d^4x\, e^{-iQ\cdot x}\, \langle 0|\, T\{\bar{b}(x)c(x)\bar{c}(0)b(0)\}\,|0\rangle\ , \\ \Pi_P(Q^2) &\equiv \int d^4x\, e^{-iQ\cdot x}\, \langle 0|\, T\{\bar{b}(x)\gamma_5 c(x)\bar{c}(0)\gamma_5 b(0)\}\,|0\rangle\ , \end{aligned} \tag{D.10}$$

the WIs imply that

$$\begin{aligned} Q_\mu Q_\nu \Pi^V_{\mu\nu}(Q) &= (m_b - m_c)^2\ \Pi_S(Q^2)\,, \\ Q_\mu Q_\nu \Pi^A_{\mu\nu}(Q) &= (m_b + m_c)^2\ \Pi_P(Q^2)\,, \end{aligned} \tag{D.11}$$

from which we obtain

$$\begin{aligned} -Q^4\Pi_{0^+}(Q^2) &= (m_b - m_c)^2\Pi_S(Q^2)\,, \\ -Q^4\Pi_{0^-}(Q^2) &= (m_b + m_c)^2\Pi_P(Q^2)\,. \end{aligned} \tag{D.12}$$

Moreover, by performing a double derivative with respect to Q^2 we get

$$\begin{aligned} \left(-2\frac{\partial}{\partial Q^2} - Q^2\frac{\partial^2}{\partial^2 Q^2}\right)[Q^2\Pi_{0^+}(Q^2)] &= (m_b - m_c)^2\frac{\partial^2}{\partial^2 Q^2}\Pi_S(Q^2)\,, \\ \left(-2\frac{\partial}{\partial Q^2} - Q^2\frac{\partial^2}{\partial^2 Q^2}\right)[Q^2\Pi_{0^-}(Q^2)] &= (m_b + m_c)^2\frac{\partial^2}{\partial^2 Q^2}\Pi_P(Q^2)\,. \end{aligned} \tag{D.13}$$

At this point, we can define the scalar and pseudoscalar analogues of Eqs. (D.5):

$$\begin{aligned} \chi_S(Q^2) &= -\frac{1}{2}\left(\frac{\partial^2}{\partial^2 Q^2}\right)\Pi_S(Q^2) = \frac{1}{4}\int_0^\infty dt'\, t'^4\ \frac{j_1(Qt')}{Qt'}C_S(t'), \\ \chi_P(Q^2) &= -\frac{1}{2}\left(\frac{\partial^2}{\partial^2 Q^2}\right)\Pi_P(Q^2) = \frac{1}{4}\int_0^\infty dt'\, t'^4\ \frac{j_1(Qt')}{Qt'}C_P(t'), \end{aligned} \tag{D.14}$$

where the scalar and pseudoscalar Euclidean correlators are defined as

$$\begin{aligned} C_S(t) &= \int d^3\vec{x}\ \langle 0|\, T\{\bar{b}(t,\vec{x})c(t,\vec{x})\bar{c}(0)b(0)\}\,|0\rangle\,, \\ C_P(t) &= \int d^3\vec{x}\ \langle 0|\, T\{\bar{b}(t,\vec{x})\gamma_5 c(t,\vec{x})\bar{c}(0)\gamma_5 b(0)\}\,|0\rangle\ . \end{aligned} \tag{D.15}$$

The WIs offer thus the possibility to express the derivatives of vector longitudinal and axial longitudinal polarization functions in a different way, namely

$$\chi_{0^+}(Q^2) = (m_b - m_c)^2\chi_S(Q^2) - \frac{1}{2}Q^2\frac{\partial}{\partial Q^2}\chi_{0^+}(Q^2)$$

$$= \frac{1}{4}\int_0^\infty dt'\, t'^4\, \frac{j_1(Qt')}{Qt'}\left[(m_b-m_c)^2 C_S(t') + Q^2 C_{0^+}(t')\right] \tag{D.16}$$

$$\chi_{0^-}(Q^2) = (m_b+m_c)^2\chi_P(Q^2) - \frac{1}{2}Q^2\frac{\partial}{\partial Q^2}\chi_{0^-}(Q^2)$$

$$= \frac{1}{4}\int_0^\infty dt'\, t'^4\, \frac{j_1(Qt')}{Qt'}\left[(m_b+m_c)^2 C_P(t') + Q^2 C_{0^-}(t')\right] .$$

Thus, when setting $Q^2 = 0$, we can compute the derivatives of the longitudinal vector and axial-vector polarization functions directly through the fourth moments of the scalar and pseudoscalar correlators, respectively. The advantage of the above procedure based on the WIs will be clarified in what follows.

D.2 HVP tensors in perturbation theory and lattice artefacts

When computing the quantities (D.8) and (D.16) on the lattice, one has to deal with discretization terms that vanish in the continuum limit, namely when the lattice spacing $a \to 0$. These discretization effects enter both in the expressions of the WIs on the lattice [403] and in the non-perturbative computation of the T-products. As it will be clear in the following discussion, we propose to reduce such discretisation errors by using a combination of non-perturbative and perturbative subtractions which were found very effective in the past. We are going to examine this idea in detail, by illustrating the main ideas for the *perturbative calculation of the polarization functions*. Although, in what follows, we will consider lattice QCD in the Twisted Mass Fermion (TMF) regularisation, the main arguments of our discussion are general and can be applied to any lattice regularisation of the theory. One peculiarity, which is however common to other regularisations, is the on-shell $O(a)$ improvement of the physical particle spectrum and of the matrix elements of local bilinear operators. Thus the lattice artefacts for physical quantities related to these matrix elements are of $O(a^2)$.

In lattice simulations performed at finite lattice spacing one can attempt to obtain the physical results either by extrapolating the lattice quantities to the continuum or by reducing the discretisation effects by a subtraction procedure based on perturbation theory. A combination of the two strategies is indeed the most effective one. To this end, a specific perturbative approach can be implemented at one-loop (or higher-loops) order by computing for a given quantity, say the polarization function or its derivatives, the corresponding Feynman diagrams, at finite lattice spacing.

Recalling the definitions of $\Pi^{\mu\nu}_{V,A}$ given in Eq. (D.1), we analyse the structure of a twisted fermions loop, the graphical representation of which, at lowest order, corresponds to the first Feynman diagram on the left in Fig. D.1.

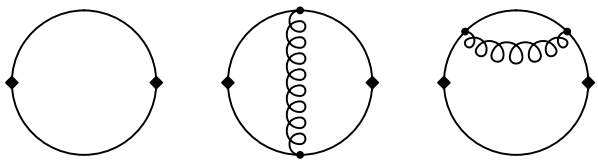

Figure D.1: *One- and two-loop Feynman diagrams for the polarization function. The crosses represent the bilinear operators and the curly line the gluon propagator.*

Given the on-shell $O(a)$ improvement of the vector current correlators at physical distances we focus on the impact of contributions to the Fourier sum from small and zero distance. Formally, we

are interested in the expansion of the generic polarization function $\Pi(Q^2) \equiv \Pi_{0^\pm,1^\mp}(Q^2)$

$$\Pi(Q^2) = \sum_{k\geq -6} C_k a^k \tag{D.17}$$

where one can show that $C_1 = 0$ with maximally TMF. Let us discuss as an example the case of the vector current. In this case, the coefficients of the expansion can be derived from the generic form of the lattice polarization tensor using the symmetries of the lattice action [404]

$$\begin{aligned}\Pi_V^{\mu\nu}(Q^2) &= \Pi_{V\,\mathrm{con}}^{\mu\nu}(Q^2) + \left(\frac{Z_1}{a^2} + \tilde{Z}_1\langle -S_6 + \frac{1}{2}S_5^2\rangle_0\right)\,\delta^{\mu\nu} + Z^+_{\mu^2}\,\left(\mu_1^2+\mu_2^2\right)\,\delta^{\mu\nu} + Z^-_{\mu^2}\,\left(\mu_1^2-\mu_2^2\right)\,\delta^{\mu\nu} \\ &\quad + \left(Z_{Q^2}Q^2\,\delta^{\mu\nu} + Z_{QQ}\,Q^\mu Q^\nu\right) + O(a^2,\ \text{operators of higher dimension})\,,\end{aligned} \tag{D.18}$$

where $\Pi_{V\,\mathrm{con}}(Q^2)$ is the continuum polarization tensor, S_5 and S_6 are defined by the expansion of the lattice action close to the continuum limit

$$S_{eff} = S_4 + a\,S_5 + a^2\,S_6 + a^2\,S_7 + \dots\,, \tag{D.19}$$

where $S_k = \int d^4x\,\mathcal{L}_k$ with the terms $\mathcal{L}_k$ containing linear combinations of fields with mass dimension k, and $\langle\dots\rangle_0$ stands for vacuum expectation value of some combination of operators, either local, e.g. $\langle S_6\rangle_0$, or non local, $\langle S_5^2\rangle_0$. We will indicate explicitly the dependence of $\Pi^{\mu\nu}(Q^2)$ or of the χ's on the quark masses only when it will be necessary for the discussion of the results.

Luckily enough all the divergent or mass dependent lattice artefacts in the first line of Eq. (D.18) disappear when we apply the derivative with respect to Q^2 to obtain the susceptibilities χ's, see Eqs. (3.28). There are however terms of $O(a^0)$ which remain and that, in some cases, can even make the longitudinal polarization function different form zero even with degenerate quark masses $\mu_1 = \mu_2$. Besides these terms there are discretisation errors of $O(a^2)$ or higher which remain. The strategy to reduce their effect is that widely used in literature, see for example Ref. [405]. In our case it is even simpler since the quantities that we consider, namely the χ's, are finite in perturbation theory. Let us call $\chi_{\mathrm{LAT}}(Q^2,a)$ the generic susceptibility computed non perturbatively on the lattice, $\chi(Q^2,a)$ the corresponding susceptibility computed in lattice perturbation theory, $\tilde{\chi}(Q^2)$ the expression resulting from $\chi(Q^2,a)$ by neglecting all contributions which vanish for $a\to 0$, $\lim_{a\to 0}\chi(Q^2,a) \to \tilde{\chi}(Q^2)$, $\chi_{\mathrm{con}}(Q^2)$ the susceptibility computed perturbatively in the continuum theory. We introduce the following quantities

$$\Delta_{1\chi}(Q^2,a) = \chi(Q^2,a) - \tilde{\chi}(Q^2)\,, \qquad \Delta_{2\chi}(Q^2) = \tilde{\chi}(Q^2) - \chi_{\mathrm{con}}(Q^2)\,, \tag{D.20}$$

where $\Delta_{1\chi}(Q^2,a)$ represents the discretisation errors that we want to subtract, and $\Delta_{2\chi}(Q^2,a)$ the finite terms which are different in the continuum with respect to the lattice case. In order to extract the subtracted susceptibility we construct then the combination

$$\chi_s(Q^2,a) = \chi_{\mathrm{LAT}}(Q^2,a) - \Delta_{1\chi}(Q^2,a) - \Delta_{2\chi}(Q^2) = \chi_{\mathrm{LAT}}(Q^2,a) - \chi(Q^2,a) + \chi_{\mathrm{con}}(Q^2,\mu)\,. \tag{D.21}$$

Thus, up to a certain order in perturbation theory and up to non perturbative effects, $\chi_s(Q^2,a)$ reduces to the continuum result without discretisation errors. As we will show in a moment, if one uses the one-loop perturbative calculations, the discretisation error then reduces to $O(\alpha_s a^2)$.

D.3 An instructive example: the vector current polarization tensor at one loop

In order to illustrate the procedure followed to reduce the discretisation errors, as an instructive example we discuss in details the one-loop perturbative calculation of the vector current polarization tensor and of the corresponding susceptibilities.

At lowest order in perturbation theory, by calling k the internal momentum, we may easily compute the correlator of two local vector currents on the lattice

$$\Pi_V^{\mu\nu}(Q,a) = \int_{-\pi/a}^{+\pi/a} \frac{d^4k}{(2\pi)^4} \,\mathrm{Tr}\left[\gamma^\mu G_1(k+\frac{Q}{2})\gamma^\nu G_2(k-\frac{Q}{2})\right], \tag{D.22}$$

where the integration interval represents the first Brillouin zone. Here $G_{i=1,2}$ indicates the tree-level Wilson twisted-mass propagator, namely

$$G_i(p) = \frac{-i\gamma_\mu \mathring{p}_\mu + \mathcal{M}_i(p) - i\mu_{q,i}\gamma_5\tau^3}{\mathring{p}^2 + \mathcal{M}_i^2(p) + \mu_{q,i}^2}, \qquad i=1,2 \tag{D.23}$$

where we have defined on the lattice

$$\mathring{p}_\mu \equiv \frac{1}{a}\sin(ap_\mu), \qquad \mathcal{M}_i(p) \equiv m_i + \frac{r_i}{2}a\hat{p}_\mu^2, \qquad \hat{p} \equiv \frac{2}{a}\sin\Big(\frac{ap_\mu}{2}\Big). \tag{D.24}$$

In order to make the calculation it is convenient to define the dimensionless quantities

$$\rho_\mu \equiv p_\mu a, \quad \tilde{m} \equiv ma, \quad \tilde{\mu} \equiv \mu a\,, \tag{D.25}$$

and express Eq.(D.23) as

$$G_i(\rho) = a\,\frac{-i\gamma_\mu \mathring{\rho}_\mu + \mathcal{M}_i(\rho) - i\tilde{\mu}_{q,i}\gamma_5\tau^3}{\mathring{\rho}^2 + \mathcal{M}_i^2(\rho) + \tilde{\mu}_{q,i}^2}, \qquad i=1,2\,. \tag{D.26}$$

Taking into account the change of the integration variables, we have that

$$\Pi_V^{\mu\nu}(Q,a) = \frac{1}{a^2}\,\mathcal{P}_V^{\mu\nu}(Qa) = \frac{1}{a^2}\int_{-\pi}^{+\pi} \frac{d^4\rho}{(2\pi)^4} \,\mathrm{Tr}\left[\gamma^\mu G_1(\rho+\frac{Qa}{2})\gamma^\nu G_2(\rho-\frac{Qa}{2})\right], \tag{D.27}$$

where $\mathcal{P}_V^{\mu\nu}(Qa)$ is a dimensionless quantity which can only depend on dimensionless quantities (Qa, m_1a, m_2a, ...). At this point we may obtain the χ's by applying the appropriate derivatives with respect to Q_μ to the expression given in Eq. (D.27). Note that any derivative with respect to Q_μ we make to obtain the χ's implies the appearance of a factor a in front of the r.h.s. of Eq. (D.27), since the integral only depends on the product Qa. A particularly convenient choice of Q in the evaluation of the lattice integral (D.27) is $Q = (Q_0, \vec{0})$, $Q^2 = Q_0^2$, $\partial/\partial Q^2 = 1/(2Q_0)\partial/\partial Q_0$, see Eqs. (D.4)–(D.8). When we want to obtain the continuum expression (at this order we do not need to define the renormalisation scheme since everything is finite) it is enough to take the limit $a \to 0$ in the integrand (D.22) and apply to $\mathcal{P}_V^{\mu\nu}(Qa)$ the derivatives with respect to Q_0.

Let us discuss the case of the susceptibilities at $Q=0$, that in this Thesis are used as inputs of the Dispersive Matrix approach. In this case, in the continuum, one obtains

$$\left(m_2^2\,\chi_{1^-}(Q^2=0)\right)_{\rm con} \;=\; \frac{N_c}{96\pi^2\,(1-u^2)^5}\,\left\{\left(1-u^2\right)\left(3+4u-21u^2+40u^3-21u^4+4u^5+3u^6\right)\right.$$

$$+12u^3\left(2-3u+2u^2\right)\log\left[u^2\right]\Big\} \tag{D.28}$$

$$\left(\chi_{0^+}(Q^2=0)\right)_{\rm con} = \frac{N_c}{24\pi^2\left(1-u^2\right)^3}\left\{\left(1-u^2\right)\left(1-4u+u^2\right)\left(1+u+u^2\right)-6u^3\log\left[u^2\right]\right\},$$

where N_c is the number of colours and the quantities on the l.h.s. being dimensionless can only depend on the ratio $u \equiv m_1/m_2$. In what follows m_2 will always denote the heavier of the two valence quarks in the decaying meson, namely the b quark for $B \to D^{(*)}$ decays. Note that in the limit $m_1 \to m_2$ (i.e. $u \to 1$) the longitudinal susceptibility $\chi_{0^+}(Q^2)$ vanishes because the currents are conserved in this limit. Also on the lattice, as $a \to 0$, the χ's can only depend on u and thus, in perturbation theory we expect

$$\begin{aligned}\left(m_2^2\,\chi_{1^-}(Q^2=0,a)\right)_{\rm LAT} &= \left(m_2^2\,\chi_{1^-}(Q^2=0)\right)_{\rm con} + a^2m_2^2\,\delta\chi'_{1^-}(u,a^2m_2^2)\,,\\ \left(\chi_{0^+}(Q^2=0,a)\right)_{\rm LAT} &= \left(\chi_{0^+}(Q^2=0)\right)_{\rm con} + \delta\chi_{0^+}(u) + a^2m_2^2\,\delta\chi'_{0^+}(u,a^2m_2^2)\,,\end{aligned} \tag{D.29}$$

where the quantities $\delta\chi_i^{(\prime)}$ can be eliminated in perturbation theory following the scheme described in Eq. (D.21). The lattice susceptibilities $\left(m_2^2\,\chi_{1^-}(Q^2=0,a)\right)_{\rm LAT}$ and $\left(\chi_{0^+}(Q^2=0,a)\right)_{\rm LAT}$ are obtained by applying the appropriate derivatives with respect to Q_0 to the expression in Eq. (D.27) and putting $Q_0 = 0$. The four dimensional integral can be performed numerically without difficulties. Note also that, since we are able to compute the polarization tensor non perturbatively, in principle we are also able to enforce the unitarity constraints on the FFs at $Q^2 \neq 0$, although it goes beyond the goals of this Thesis.

The advantage of the WIs (D.16) is now clear from Eq. (D.29). When we compute the vector (or axial) longitudinal polarization functions through their definitions (3.28), namely computing only one derivative with respect to q^2 of the corresponding polarization functions, we will find *by construction* some $O(a^0)$ discretization effects, namely $\delta\chi_{0^+}$ (or $\delta\chi_{0^-}$). This is not true when performing two derivatives with respect to q^2 of the polarization functions, which can be done by considering the WIs in Eq. (D.16).

	Perturbative	Non-perturbative
$\chi_{0^+}^{b\to c}[10^{-3}]$	6.204	7.58 ± 0.59
$\chi_{0^-}^{b\to c}[10^{-3}]$	19.4	21.9 ± 1.9
$\chi_{1^-}^{b\to c}[10^{-4}\ \mathrm{GeV}^{-2}]$	5.131	5.84 ± 0.44
$\chi_{1^+}^{b\to c}[10^{-4}\ \mathrm{GeV}^{-2}]$	3.89	4.69 ± 0.30

Table D.1: *Values of the susceptibilities adopted for the Dispersive Matrix method for the $b \to c$ quark transitions. We compare the perturbative estimates [50, 69] with our non-perturbative results. Note that, in the former case, the uncertainties are completely negligible.*

D.4 Non-perturbative numerical values of the susceptibilities

After having explained the theoretical ideas underlying the non-perturbative computation of the susceptibilities χs, let us show the final results of the simulations on the lattice.

For the $b \to c$ quark currents, these values are contained in the last column of Table D.1, which are the values used for the phenomenological applications discussed in Chapters 4 and 5. In the Table we show also for comparison the perturbative estimates computed in [50,69]. We note that the differences

are negligible for the 1^- and 0^- channels, *i.e.* $\sim 4\%$ and $\sim 7\%$ respectively, while are slightly larger in the 0^+ and 1^+ channels, namely both $\sim 20\%$.

For the $b \to u$ quark currents, no recent perturbative estimates have been published in literature, thus we show directly the results of our non-perturbative computation, *i.e.*

$$\chi_{0^+}^{b\to u} = (2.04 \pm 0.20) \cdot 10^{-2} \,, \tag{D.30}$$

$$\chi_{1^-}^{b\to u} = (4.45 \pm 1.16) \cdot 10^{-4} \text{ GeV}^{-2} \,, \tag{D.31}$$

where we show only the 0^+ and the 1^- since they are the only ones relevant for the phenomenological applications discussed in Chapter 4.

Appendix E

Some details about Bound States Dynamics for WIMP DM

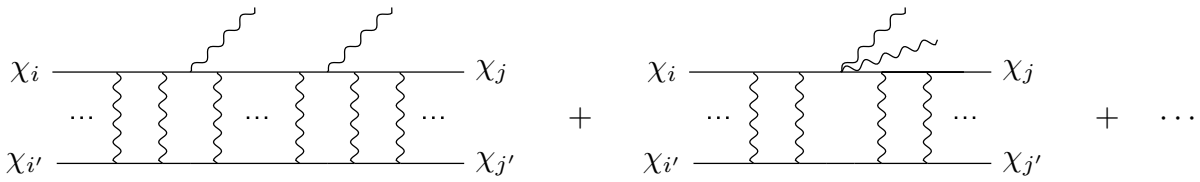

Figure E.1: Examples of diagrams controlling the BS effective Hamiltonian at next-to-leading order in gauge boson emission. The first diagram corresponds to the second order Born approximation for the dipole operators in Eq. (E.1). The second diagram, instead, is obtained from the $\mathcal{O}(A^2)$ terms in the interaction Hamiltonian, at leading order in the Born approximation.

In this Appendix we discuss the details of the dynamics of Bound State Formation (BSF). To be more specific, we will show the general features of BSF at leading order (LO) in gauge boson emission and at next-to-leading order (NLO) in gauge boson emission.

At LO, bound states form through the emission of a single vector boson V^a: $\chi_i + \chi_j \to \mathrm{BS}_{i'j'} + V^a$. The non-relativistic limit of the amplitude can be recast in the form of an effective interaction Hamiltonian, such that the full amplitude can be obtained from its matrix element with the wave function of the initial and final two-particle states (reconstructed from the resummation of the ladder diagrams). The leading order contribution to this effective hamiltonian comes in the form of electric dipole interaction terms [298, 299]:

$$\mathscr{H}_I^{\mathrm{LO}} = -\frac{g_2}{M_\chi}\left(\vec{A}^a(\vec{x}_1)\cdot\vec{p}_1 T^a_{i'i}\delta_{j'j} + \vec{A}^a(\vec{x}_2)\cdot\vec{p}_2\overline{T}^a_{j'j}\delta_{i'i}\right) + g_2\alpha_2\left(\vec{A}^a(0)\cdot\hat{r}e^{-M_a r}\right)T^b_{i'i}\overline{T}^c_{j'j}f^{abc}\ , \quad \text{(E.1)}$$

where the first to terms are a simple generalization of the standard QED dipole interaction while the last one is a purely non-abelian term which arises from vector boson emission from a vector line.

The computation of the transition amplitudes from Eq. (E.1) simplifies if we assume the $\mathrm{SU}(2)_L$-invariant limit. This approximation applies when the DM de Broglie wavelength is much smaller

than the range of the Yukawa interaction $1/m_W$ and therefore for $z \leq (M_\chi/m_W)^2$. In this regime the Yukawa potential is well approximated by the Coulomb one which turns out to be a good approximation to describe WIMP freeze-out. The BS dynamics can then be understood by using isospin selection rules while the main consequence of having finite vector masses is to provide an energy threshold to the emission of a single massive boson in the formation or the decay of a BS.

Since $\alpha_{\rm eff} \sim n^2$, increasing the dimensionality of the DM multiplet enhances NLO processes in gauge boson emission such as $\chi_i + \chi_j \to {\rm BS}_{i'j'} + V^a + V^b$. These could be in principle relevant for both the computation of the thermal mass and the saturation of the perturbative unitarity bound. The main NLO contributions to BSF come from diagrams like the ones in Fig. E.1 and are essentially of two types: i) the first diagram is essentially the second order Born approximation of the LO Hamiltonian, with the intermediate state being a free one or a BS; ii) the second diagram, where the two emitted vectors come from the same vertex, is generated by the effective Hamiltonian at order $\mathcal{O}(A^2)$. The latter contains terms of the form

$$\mathscr{H}_I^{\rm NLO} \supset \frac{g_2^2}{2M_\chi} T^a T^b \left[\vec{A}^a \cdot \vec{A}^b + \frac{(\vec{p}\cdot\vec{A}^a)(\vec{p}\cdot\vec{A}^b)}{M_\chi^2} \right], \tag{E.2}$$

where we focus here on the abelian part of the hamiltonian. From Eqs. (E.1)-(E.2) we can estimate the contribution to the double emission BSF cross-section as:

$$\sigma_{\rm BSF}^{\rm LO} v_{\rm rel} \simeq \frac{2\pi\alpha_{\rm eff}}{M_\chi^3}\Delta E, \qquad \sigma_{\rm BSF}^{\rm NLO} v_{\rm rel} \simeq \frac{g_\chi^2}{8M_\chi^2 v_{\rm rel}} \left(\frac{\Delta E}{M_\chi}\right)^3 , \tag{E.3}$$

where $g_\chi = 1$ for Majorana fermions ($g_\chi = 2$ for real scalars). In the LO estimate, a factor $\frac{2}{\alpha_{\rm eff} M_\chi}\frac{2\pi\alpha_{\rm eff}}{v_{\rm rel}}$ comes from the overlap integral while a factor $\frac{\Delta E}{8\pi}$ from the two-body phase space. Similarly, in the NLO estimate a factor $\frac{1}{2}\frac{\Delta E^3}{256\pi^3}$ comes from the 3-body phase space, taking into account the two identical final vectors, and $\left(\frac{2}{\alpha_{\rm eff} M_\chi}\right)^3 \frac{2\pi\alpha_{\rm eff}}{v_{\rm rel}}$ from the overlap integrals between the wave functions. From the above formula one can derive the scaling of the NLO corrections in Eq. (10.33).

Now, we are looking for the contributions from second order Born expansion, whose general expression is

$$(\sigma v_{\rm rel})_{2V} = \frac{2^6\alpha_2^2}{3^3\pi M_\chi^4} \int {\rm d}\omega \omega (E_n - \omega) \left| \mathcal{C}_{\rm BS} + \mathcal{C}_{\rm free} \right|^2 , \tag{E.4}$$

where we defined

$$\mathcal{C}_{\rm BS} = \sum_m \left(\frac{1}{E_n - E_m - \omega + i\Gamma_{{\rm dec},m}} + \frac{1}{\omega - E_m + i\Gamma_{{\rm dec},m}} \right) \mathcal{I}_{\vec{q}m}\mathcal{I}_{mn} , \tag{E.5a}$$

$$\mathcal{C}_{\rm free} = \int \frac{{\rm d}^3k}{(2\pi)^3} \left(\frac{1}{E_n - \omega + \frac{k^2}{M_\chi} + i\epsilon} + \frac{1}{\omega - \frac{q^2}{M_\chi} + \frac{k^2}{M_\chi} + i\epsilon} \right) \mathcal{I}_{\vec{q}\vec{k}}\mathcal{I}_{\vec{k}f} , \tag{E.5b}$$

with $\mathcal{I}_{if}$ being the overlap integrals between the states i and f, the index m running over all intermediate BS and the k-integral running over all the intermediate scattering states. Starting from $\mathcal{C}_{\rm BS}$, the intermediate BS are rather narrow resonances because

$$\Gamma_{\rm dec} \sim \alpha_{\rm eff}^3 E_B \ll E_B , \tag{E.6}$$

where E_B is a typical binding energy. This quick estimate, supported by the full numerical computation, suggests that $\mathcal{C}_{\rm BS}$ contribution is fully captured in the Narrow Width Approximation (NWA)

for the intermediate BS. Therefore, neglecting the interference terms, one gets

$$(\sigma v_{\rm rel})_{2V} = \sum_m (\sigma v_{\rm rel})_{1V,m} {\rm BR}_{m\to n}. \tag{E.7}$$

To estimate the contribution from $\mathcal{C}_{\rm free}$ we need to estimate $\mathcal{I}_{\vec{q}\vec{k}}$ which encodes the contribution from intermediate continuum states. For simplicity, we stick to the abelian contribution which reads

$$\mathcal{I}_{\vec{q}\vec{k}} = \int r^2 {\rm d}r R_{\vec{k},1} \partial_r R_{\vec{q},0} \ . \tag{E.8}$$

The integral above can be split into small and large r regions, roughly separated by the Bohr radius $a_0 = \frac{1}{\alpha_{\rm eff} M_\chi}$, *i.e.*

$$\begin{aligned} \mathcal{I}_{\vec{q}\vec{k}} &= \int_0^{a_0} r^2 {\rm d}r R_{\vec{k},1} \partial_r R_{\vec{q},0} + \int_{a_0}^{\infty} r^2 {\rm d}r R_{\vec{k},1} \partial_r R_{\vec{q},0} \\ &\sim \frac{1}{\alpha_{\rm eff} M_\chi \sqrt{kq}} + \frac{q}{(M_\chi \alpha_{\rm eff})^2} \delta(q-k) \ , \end{aligned} \tag{E.9}$$

which plugged into Eq. (E.5b) gives an estimate of $\mathcal{C}_{\rm free}$. All in all, plugging these estimates in Eq. (E.4) and replacing $q = M_\chi v_{\rm rel}$ we get that the contribution from NLO exchange of continuum states behaves similarly to the ones estimated in Eq. (E.3) up to subleading terms in the $v_{\rm rel} < \alpha_{\rm eff}$ regime.

Appendix F

More on WIMPs and DTs at future lepton colliders

In this Appendix we recast the two search strategies discussed in Ref. [322] that exploit the presence of a single short reconstructed disappearing track or a two-track analysis that require at least one of them to be a short disappearing track, in addition to a trigger photon. The requirements are summarized in Table F.1, taken from from Ref. [322].

	Single track (1T)	Double track (2T)
E_γ	> 25 GeV	> 25 GeV
$p_{\rm T}$ leading track	> 300 GeV	> 20 GeV
$p_{\rm T}$ subleding track	/	> 10 GeV
θ leading track	$\frac{2\pi}{9} < \theta < \frac{7\pi}{9}$	$\frac{2\pi}{9} < \theta < \frac{7\pi}{9}$
Δz tracks	/	< 0.1 mm

Table F.1: Event selections in the two signal regions considered in the original work [322].

Single-track search. For the single-track analysis we take the background cross-section quoted in [322]. This rate is mainly determined by the combinatorial of track reconstruction induced by beam-induced backgrounds.[1] To determine the rate of the single-track events, we compute the mono-photon cross-section doubly differential in the polar angles of the charged particles χ_1, χ_2. This $d\sigma/d\theta_1 d\theta_2$ is obtained at LO in perturbation theory with MadGraph5_aMC@NLO and is further reweighted to take into account angular and distance sensitivity to stub-tracks reported in Ref. [322]. Let $P(\theta_1)$ be the probability that the particle χ_1 is reconstructed as a track:

$$P(\theta, r_{\rm min}, r_{\rm max}) = \int_{r_{\rm min}}^{r_{\rm max}} \frac{{\rm d}r\, \epsilon_{\rm rec}(r,\theta)}{c\tau\beta\gamma \sin\theta} e^{-r/(c\tau\beta\gamma\sin\theta)}, \tag{F.1}$$

where r is the transverse radius and $\epsilon_{\rm rec}(r,\theta)$ is the probability to reconstruct as a track a particle travelling at an angle θ that decayed at a transverse radius r given in Fig. 11 of Ref. [322]. For single tracks $\epsilon_{\rm rec}(r,\theta)$ is 0 outside the interval $r \in [50\,{\rm mm}, 127\,{\rm mm}]$, and outside $\pi/6 < \theta < 5\pi/6$. The radial

[1] As acknowledged in [322], this estimate of the background is quite conservative because it is based on detailed beam dynamics simulation for $\sqrt{s} = 1.5$ TeV. Due to the relativistic dilution of muon decays, we expect smaller background cross-section at higher $\sqrt{s}$.

condition reflects the fact that tracks can only be reconstructed if the particles make at least 4 hits in the vertex detector, which for the considered geometry means that the particle must travel at least a minimum distance of 50 mm in the detector, while the upper limit stems from the disappearing condition of the track. The latter condition will be relaxed in the double-tracks search. With the knowledge of $\epsilon_{\rm rec}$ the integral in Eq. (F.1) can be performed numerically. As per Table F.1, the hard cross-section $\sigma_{S,\gamma}$ is subject to trigger requirements: the leading observed track is required to have

$$p_{\rm T} > 300 \text{ GeV} \tag{F.2}$$

to help discriminate it against fake tracks, and it must lie within the cone

$$\frac{2\pi}{9} < \theta < \frac{7\pi}{9}. \tag{F.3}$$

In our recast, due to lack of a detailed tracking and detector simulation, these cuts are implemented at parton level on the DM particles momenta, which leads us to overestimate the number of events that pass the selection. To account for this effect we assume that only a fraction $\epsilon_{\rm tran}$ of the events with parton $p_{\rm T} > 300$ GeV gives a track whose $p_{\rm T}$ fulfils the same conditions. The transfer factor $\epsilon_{\rm tran} \approx 0.5$ is estimated from the $p_{\rm T}$ distribution of χ obtained at generator level, and track $p_{\rm T}$ distribution given in Ref. [322]. We assume that tracks with $p_{\rm T} > 300$ GeV can only come from χ with $p_{\rm T} > 300$ GeV. To properly avoid over-counting events with two reconstructed tracks, we divide the final state phase space into two non-overlapping regions that require different reconstruction constraints:

i) Both χ fulfil the conditions to be considered as leading track (Eqs. (F.2) and (F.3)). In this case both tracks are subject to the detection and reconstruction efficiencies $\epsilon_{\rm tran}$ and $\epsilon_{\rm rec}(\theta, r)$. These events may give rise to zero, one, or two reconstructed stub-tracks. We count events with at least one stub-track.

ii) Exactly one χ fulfils the conditions to be considered as leading track. Only events in which this track is reconstructed according to detection and reconstruction efficiencies $\epsilon_{\rm tran}$ and $\epsilon_{\rm rec}(\theta, r)$ are counted. The fate of the sub-leading χ (if any) is irrelevant.

The largest contribution to the single-track cross-section comes from events in region i), where both DM particles satisfy the $p_{\rm T}$ and θ requirements to be considered as a leading track. The preference for this configuration reflects the approximate 2-body kinematics of the mono-γ events with small $p_{\rm T}$. In order to understand the nature of signal we can split it into two further sub-categories with: a) exactly one reconstructed track which fulfils the conditions Eq. (F.2) and Eq. (F.3); b) exactly 2 reconstructed stub-tracks, of which at least one fulfils the same conditions. The respective rates are given by:

$$\frac{\mathrm{d}^2\sigma^{\rm 1T}_{S,\gamma}}{\mathrm{d}\cos\theta_1 \mathrm{d}\cos\theta_2} \cdot \begin{cases} \epsilon_{\rm tran} 2P(\theta_1)(1-P(\theta_2)) & \text{1 track,} \\ \big(1-(1-\epsilon_{\rm tran})^2\big)P(\theta_1)P(\theta_2) & \text{2 tracks,} \end{cases}$$

where the hard cross-section $\sigma^{\rm 1T}_{S,\gamma}$ is restricted to the phase-space region where both χ particles fulfil the requirements of Eqs. (F.2) and (F.3). The boost factor $\beta\gamma$ and the angular distribution are both taken from a MC sample with cuts only on the photon at generator level. The resulting number of events is used to compute the reach on the DM mass reported in Fig. 10.6, according to Eq. (10.43) with $\epsilon_{\rm sys} = 0$.

Interestingly, the results obtained from the MC sample can also be understood semi-analytically thanks to the simple kinematics of the mono-photon process. Given that the photon tends to be soft, the kinematics of the three body process is not too different from direct production of a pair of

oppositely charged DM particles without the photon. Therefore a very good analytic approximation of the above results can be obtained, with the χ boost factor and flight directions approximated by the ones for pair-produced DM particles with energy $\sqrt{s}/2$,

$$\beta\gamma \approx \sqrt{\frac{s}{4M_\chi^2} - 1}\,, \qquad \theta_1 = \pi + \theta_2. \tag{F.4}$$

The angular distribution can also be computed analytically in the 2-body limit,

$$\frac{1}{\sigma_{S,\gamma}}\frac{\mathrm{d}\sigma_{S,\gamma}}{\mathrm{d}\cos\theta} \propto \begin{cases} 1 + 4\frac{M_\chi^2}{s} + \left(1 - 4\frac{M_\chi^2}{s}\right)\cos^2\theta\,, & \text{fermion,} \\ \sin^2\theta\,, & \text{scalar.} \end{cases}$$

Results obtained using the MC 3-body angular distributions are in good agreement with the ones obtained with this analytic two-body approximation.

Double-track search. The signal of the double tracks is computed by requiring both DM particles to be reconstructed as tracks. The rate in this case is

$$\frac{\mathrm{d}^2\sigma^{2\mathrm{T}}_{\mathrm{S},\gamma}}{\mathrm{d}\cos\theta_1\mathrm{d}\cos\theta_2}P(\theta_1)P(\theta_2)\,. \tag{F.5}$$

We additionally require the two tracks to originate from points that are close to each other along the direction of the beam axis, $\Delta z < 0.1$ mm (see Table F.1). This effectively reduces the background to negligible levels. In this limit, we use 4 signal events as a conservative estimate of the 95% C.L. exclusion for a Poissonian counting.

The angular cuts on the tracks are the same as in the single track case, while the p_T cuts are much milder: $p_\mathrm{T} > 10, 20$ GeV for the sub-leading and leading tracks, respectively. In this case the mismatch between the p_T of the reconstructed track and the p_T of the charged χ obtained at generator level is negligible. The additional cuts do not affect significantly the signal events. Note that, following Ref. [322], the disappearing condition is required on at least one track, i.e. this analysis includes in the signal all events in which the second track extends up to a transverse radius of $r = 1153$ mm. Following Ref. [322], we assumed for such long tracks a reconstruction efficiency equal to the tracks decaying between 101 mm $< r <$ 127 mm. Also for double tracks, the result obtained using the MC sample $\beta\gamma$ and θ distributions are in agreement with the ones computed analytically in the 2-body limit.

Appendix G

Details about the coupling of DM with $\ell\pi$

As explained in Chapter 11, below the QCD scale $\Lambda_{\rm QCD}$ the quarks are dresses into mesons and baryons, so that the terms in the effective Lagrangian (11.30) are substituted by the new ones in Eq. (11.31). These new interactions have been computed in chiral perturbation theory, as we will schematically show in this Appendix.

We start summarizing the pion action [406]. We define

$$U = \exp \frac{i\Pi}{f_\pi}\,, \qquad \Pi = \begin{pmatrix} \pi^0 & \sqrt{2}\pi^+ \\ \sqrt{2}\pi^- & -\pi^0 \end{pmatrix}\,, \tag{G.1}$$

where $f_\pi = 93\,\text{MeV}$. The SM pion Lagrangian is given by

$$\mathcal{L}_{\text{SM}\pi} = \frac{f_\pi^2}{4}\,\text{Tr}\left[|D_\mu U|^2 + m_\pi^2(U + U^\dagger)\right]\,, \tag{G.2}$$

where the covariant derivative is

$$D_\mu U = \partial_\mu U - i(r_\mu^A + r_\mu^W)U + iU(l_\mu^A + l_\mu^W)\,, \tag{G.3}$$

with

$$r_\mu^A = l_\mu^A = -eQA_\mu\,, \qquad r_\mu^W = 0\,, \qquad l_\mu^W = -\frac{gV_{ud}}{\sqrt{2}}(\sigma^+ W_\mu^+ + \sigma^- W_\mu^-) \tag{G.4}$$

and

$$Q = \frac{\sigma^3}{2} = \frac{1}{2}\begin{pmatrix} 1 & 0 \\ 0 & -1 \end{pmatrix}\,, \qquad \sigma^+ = \begin{pmatrix} 0 & 1 \\ 0 & 0 \end{pmatrix}\,, \qquad \sigma^- = \begin{pmatrix} 0 & 0 \\ 1 & 0 \end{pmatrix}\,. \tag{G.5}$$

The Lagrangian can be then expanded as

$$\begin{aligned}
\mathcal{L}_{\text{SM}\pi} \;=\; & \frac{1}{2}(\partial_\mu\pi^0)^2 + |\partial_\mu\pi^+|^2 - m_\pi^2\left(|\pi^+|^2 + \frac{1}{2}(\pi^0)^2\right) \\
& + \Big(-\frac{g}{2} f_\pi V_{ud} W_\mu^+ (\partial^\mu - ieA^\mu)\pi^- + ieA_\mu\pi^+(\partial^\mu - ieA^\mu)\pi^- \\
& \quad - \frac{ig}{2} V_{ud} W_\mu^+ \left[\pi^0(\partial^\mu - ieA^\mu)\pi^- - \pi^-\partial^\mu\pi^0\right] + \text{h.c.}\Big) + \\
& + \frac{1}{6f_\pi^2}\Big[\left((\pi^-\partial_\mu\pi^+)^2 + 2\pi^0\pi^-\partial_\mu\pi^+\partial^\mu\pi^0 + \text{h.c.}\right) +
\end{aligned}$$

$$- 2|\partial_\mu\pi^+|^2(|\pi^+|^2+(\pi^0)^2) - 2|\pi^+|^2(\partial_\mu\pi^0)^2 + m_\pi^2\left(|\pi^+|^2+\frac{1}{2}(\pi^0)^2\right)^2\Big] + \cdots$$

where we only wrote the relevant terms in the expansion. Integrating out the W gives the effective Fermi interaction of pions

$$\mathcal{L}^{\rm weak}_{{\rm SM}\pi} = 2G_F(\bar\nu_L\gamma^\mu\ell_L)\big(f_\pi\partial_\mu\pi^+ - i(\pi^0\partial_\mu\pi^+ - \pi^+\partial_\mu\pi^0)+\dots\big) + \text{h.c.} \tag{G.6}$$

Now, the vector-like DM interaction in Eq. (11.31) can be obtained in a very similar way, *i.e.* by replacing the left-handed current with $(\bar\chi\gamma^\mu\ell_R)$. The scalar interaction is obtained converting $(\bar\chi L_L)(Q_L u_R)$ into

$$(\bar\chi\nu_L)\frac{f_\pi^2 B_0}{2}{\rm Tr}\Big[\frac{\sigma^3}{2}U+\frac{1}{2}U\Big] + (\bar\chi\ell_L)\frac{f_\pi^2 B_0}{2}{\rm Tr}\Big[\sigma^+ U\Big]. \tag{G.7}$$

In what follows, we give some compact formulæ that, starting from the Lagrangian (11.31), allows to describe quantitatively the interactions of DM with pions and other SM particles.

G.1 Tree-level DM decay

If $M > m_\ell$, the DM can decay to a lepton and an off-shell pion (subsequently decaying to $e\bar\nu$) through the interaction in Eq. (11.31). The amplitude reads

$$\mathscr{A} = \sqrt{2}C_{\chi R}G_F\frac{i}{p_\pi^2-m_\pi^2}f_\pi^2 p_\pi^\mu(-p_\pi^\nu)\left[(\bar u_\chi\gamma_\mu P_R v_\ell)(\bar u_e\gamma_\nu P_L v_\nu)+(\bar u_\ell\gamma_\mu P_R v_\chi)(\bar u_e\gamma_\nu P_L v_\nu)\right], \tag{G.8}$$

where the second term is absent if χ is Dirac. The squared amplitude is

$$\overline{|\mathscr{A}|^2} = (2)\frac{2f_\pi^4 G_F^2 C_{\chi R}^2 m_e^2(p_\pi^2-m_e^2)}{(m_\pi^2-p_\pi^2)^2}\left[(M^2-m_\ell^2)^2 - p_\pi^2(M^2+m_\ell^2)\right] \tag{G.9}$$

where $p_\pi = p_e + p_\nu$ is the pion 4-momentum and the (2) holds only if χ is Majorana. The decay width is then

$$\Gamma(\chi\to\ell e\nu) = \frac{1}{2M}\int_{s_{12}^{\rm min}}^{s_{12}^{\rm max}}\int_{s_{23}^{\rm min}}^{s_{23}^{\rm max}} ds_{12}ds_{23}|\mathscr{A}|^2\frac{1}{128\pi^3M^2} \tag{G.10}$$

$$= \frac{1}{2M}\int_{m_e^2}^{(M-m_\ell)^2}\frac{dp_\pi^2}{128\pi^3M^2}|\mathscr{A}|^2\left(1-\frac{m_e^2}{p_\pi^2}\right)\sqrt{m_\ell^4-2m_\ell^2(M^2+p_\pi^2)+(M^2-p_\pi^2)^2}. \tag{G.11}$$

Note that the off-shell decay rates have been computed both analytically and numerically with MadGraph [375], after having implemented the interaction in Eq. (11.31) and the relevant SM pion interactions.

G.2 Scatterings among $\chi, \ell, \gamma, \pi^\pm$

The photon interacts with charged particles, π and ℓ. Furthermore a $\chi\ell\gamma\pi$ vertex arises from the gauge-covariantization of the $\chi\ell\partial_\mu\pi$ interaction. Taking this vertex into account, the total scattering

amplitude vanishes for longitudinal photons. In the non-relativistic limits the squared amplitudes summed over all initial-state and final states are

$$|\mathscr{A}|^2(\chi\gamma \to \pi^+\ell) = \frac{e^2 f_\pi^2 C_{\chi R}^2 (m_\ell + m_\pi)(m_\ell^2 + M^2)}{m_\ell}, \tag{G.12a}$$

$$|\mathscr{A}|^2(\chi\pi^- \to \gamma\ell) = \frac{e^2 f_\pi^2 C_{\chi R}^2 M(m_\ell^2 + M^2)}{m_\pi + M}, \tag{G.12b}$$

$$|\mathscr{A}|^2(\chi\ell \to \pi^-\gamma) = \frac{e^2 f_\pi^2 C_{\chi R}^2 M(m_\ell^2 + M^2)}{m_\ell}, \tag{G.12c}$$

with no contribution from the photon interaction to the π.

G.3 Scatterings among $\chi, \ell, \pi^0, \pi^\pm$

Only the quartic interaction among $\chi, \ell_R, \pi^0, \pi^\pm$ contributes to tree-level scatterings among these particles. All processes with different initial-state and final-state particles have the following squared amplitude, summed over all degrees of freedom, and here written assuming all incoming momenta, $p_\chi + p_\ell + p_{\pi^0} + p_{\pi^\pm} = 0$:

$$|\mathscr{A}|^2 = -2C_{\chi R}^2 \left\{ [p_\ell \cdot (p_{\pi^0} - p_{\pi^+})]\, [p_\chi \cdot (p_{\pi^0} - p_{\pi^+})] + \left(p_{\pi^+} \cdot p_{\pi^0} - m_\pi^2\right) (p_\ell \cdot p_\chi) \right\} . \tag{G.13}$$

So the squared amplitudes, summed over all degrees of freedom, are

$$|\mathscr{A}|^2_{\chi\ell\to\pi^-\pi^0} = -\frac{f_\pi^2 C_{\chi R}^2}{2}[4m_\pi^4 + 4t^2 + (m_\ell^2 + M^2)(m_\ell^2 + M^2 - s) + 4t(s - m_\ell^2 - M^2 - 2m_\pi^2)],$$

$$|\mathscr{A}|^2_{\chi\pi^+\to\bar{\ell}\pi^0} = -\frac{f_\pi^2 C_{\chi R}^2}{2}[4m_\pi^4 + m_\ell^4 + M^4 + m_\ell^2(2M^2 - 4s - t) + 4s(s + t - 2m_\pi^2) - M^2(4s + t)],$$

and the same for $\chi\pi^0 \to \bar{\ell}\pi^-$.

Bibliography

[1] M. Di Carlo, G. Martinelli, M. Naviglio, F. Sanfilippo, S. Simula, and L. Vittorio, "Unitarity bounds for semileptonic decays in lattice QCD," *Phys. Rev. D*, vol. 104, no. 5, p. 054502, 2021.

[2] G. Martinelli, S. Simula, and L. Vittorio, "Constraints for the semileptonic B→D(*) form factors from lattice QCD simulations of two-point correlation functions," *Phys. Rev. D*, vol. 104, no. 9, p. 094512, 2021.

[3] G. Martinelli, S. Simula, and L. Vittorio, "$|V_{cb}|$ and $R(D)^{(*)}$ using lattice QCD and unitarity," *Phys. Rev. D*, vol. 105, no. 3, p. 034503, 2022.

[4] S. Bottaro, D. Buttazzo, M. Costa, R. Franceschini, P. Panci, D. Redigolo, and L. Vittorio, "Closing the window on WIMP Dark Matter," *Eur. Phys. J. C*, vol. 82, no. 1, p. 31, 2022.

[5] G. Martinelli, S. Simula, and L. Vittorio, "Exclusive determinations of $|V_{cb}|$ and $R(D^*)$ through unitarity," 9 2021.

[6] B. Belfatto, D. Buttazzo, C. Gross, P. Panci, A. Strumia, N. Vignaroli, L. Vittorio, and R. Watanabe, "Dark Matter abundance via thermal decays and leptoquark mediators," 11 2021.

[7] G. Martinelli, S. Simula, and L. Vittorio, "Exclusive semileptonic $B \to \pi\ell\nu_\ell$ and $B_s \to K\ell\nu_\ell$ decays through unitarity and lattice QCD," 2 2022.

[8] J. Aalbers *et al.*, "A Next-Generation Liquid Xenon Observatory for Dark Matter and Neutrino Physics," 3 2022.

[9] C. Aimè *et al.*, "Muon Collider Physics Summary," 3 2022.

[10] J. De Blas *et al.*, "The physics case of a 3 TeV muon collider stage," in *2022 Snowmass Summer Study*, 3 2022.

[11] G. Martinelli, M. Naviglio, S. Simula, and L. Vittorio, "$|V_{cb}|$, Lepton Flavour Universality and $SU(3)_F$ symmetry breaking in semileptonic $B_s \to D_s^{(*)}\ell\nu_\ell$ decays through unitarity and lattice QCD," 4 2022.

[12] S. Bottaro, D. Buttazzo, M. Costa, R. Franceschini, P. Panci, D. Redigolo, and L. Vittorio, "The last Complex WIMPs standing," 5 2022.

[13] A. Abada *et al.*, "FCC Physics Opportunities: Future Circular Collider Conceptual Design Report Volume 1," *Eur. Phys. J. C*, vol. 79, no. 6, p. 474, 2019.

[14] A. Abada *et al.*, "FCC-ee: The Lepton Collider: Future Circular Collider Conceptual Design Report Volume 2," *Eur. Phys. J. ST*, vol. 228, no. 2, pp. 261–623, 2019.

[15] A. Abada *et al.*, "FCC-hh: The Hadron Collider: Future Circular Collider Conceptual Design Report Volume 3," *Eur. Phys. J. ST*, vol. 228, no. 4, pp. 755–1107, 2019.

[16] A. Abada *et al.*, "HE-LHC: The High-Energy Large Hadron Collider: Future Circular Collider Conceptual Design Report Volume 4," *Eur. Phys. J. ST*, vol. 228, no. 5, pp. 1109–1382, 2019.

[17] R. K. Ellis *et al.*, "Physics Briefing Book: Input for the European Strategy for Particle Physics Update 2020," 10 2019.

[18] P. D. Group, "Review of Particle Physics," *Progress of Theoretical and Experimental Physics*, vol. 2020, 08 2020. 083C01.

[19] P. Higgs, "Broken symmetries, massless particles and gauge fields," *Physics Letters*, vol. 12, no. 2, pp. 132–133, 1964.

[20] P. W. Higgs, "Broken symmetries and the masses of gauge bosons," *Phys. Rev. Lett.*, vol. 13, pp. 508–509, Oct 1964.

[21] F. Englert and R. Brout, "Broken symmetry and the mass of gauge vector mesons," *Phys. Rev. Lett.*, vol. 13, pp. 321–323, Aug 1964.

[22] N. Cabibbo, "Unitary symmetry and leptonic decays," *Phys. Rev. Lett.*, vol. 10, pp. 531–533, Jun 1963.

[23] M. Kobayashi and T. Maskawa, "CP-Violation in the Renormalizable Theory of Weak Interaction," *Progress of Theoretical Physics*, vol. 49, pp. 652–657, 02 1973.

[24] L. Wolfenstein, "Parametrization of the kobayashi-maskawa matrix," *Phys. Rev. Lett.*, vol. 51, pp. 1945–1947, Nov 1983.

[25] G. Aad, T. Abajyan, B. Abbott, J. Abdallah, S. Abdel Khalek, A. Abdelalim, O. Abdinov, R. Aben, B. Abi, M. Abolins, *et al.*, "Observation of a new particle in the search for the Standard Model Higgs boson with the ATLAS detector at the LHC," *Physics Letters B*, vol. 716, pp. 1–29, Sep 2012.

[26] G. Aad *et al.*, "A Particle Consistent with the Higgs Boson Observed with the ATLAS detector at the Large Hadron Collider," *Science*, vol. 338, no. 6114, pp. 1576–1582, 2012.

[27] P. Gambino and C. Schwanda, "Inclusive semileptonic fits, heavy quark masses, and V_{cb}," *Phys. Rev.*, vol. D89, no. 1, p. 014022, 2014.

[28] A. Alberti, P. Gambino, K. J. Healey, and S. Nandi, "Precision Determination of the Cabibbo-Kobayashi-Maskawa Element V_{cb}," *Phys. Rev. Lett.*, vol. 114, no. 6, p. 061802, 2015.

[29] P. Gambino, K. J. Healey, and S. Turczyk, "Taming the higher power corrections in semileptonic B decays," *Phys. Lett. B*, vol. 763, pp. 60–65, 2016.

[30] M. Bordone, B. Capdevila, and P. Gambino, "Three loop calculations and inclusive Vcb," *Phys. Lett. B*, vol. 822, p. 136679, 2021.

[31] B. Aubert *et al.*, "Measurement of the Decay $B^- \to D^{*0}\ e^-\bar{\nu}$," *Phys. Rev. Lett.*, vol. 100, p. 231803, 2008.

[32] B. Aubert *et al.*, "Determination of the form-factors for the decay $B^0 \to D^{*-}\ell^+\nu_l$ and of the CKM matrix element $|V_{cb}|$," *Phys. Rev.*, vol. D77, p. 032002, 2008.

[33] B. Aubert *et al.*, "Measurements of the Semileptonic Decays $\bar{B} \to D\ell\bar{\nu}$ and $\bar{B} \to D^*\ell\bar{\nu}$ Using a Global Fit to $DX\ell\bar{\nu}$ Final States," *Phys. Rev.*, vol. D79, p. 012002, 2009.

[34] B. Aubert *et al.*, "Measurement of $|V_{cb}|$ and the Form-Factor Slope in $\bar{B} \to Dl^-\bar{\nu}$ Decays in Events Tagged by a Fully Reconstructed B Meson," *Phys. Rev. Lett.*, vol. 104, p. 011802, 2010.

[35] W. Dungel *et al.*, "Measurement of the form factors of the decay $B^0 \to D^{*-}\ell^+\nu$ and determination of the CKM matrix element V_{cb}," *Phys. Rev.*, vol. D82, p. 112007, 2010.

[36] R. Glattauer *et al.*, "Measurement of the decay $B \to D\ell\nu_\ell$ in fully reconstructed events and determination of the Cabibbo-Kobayashi-Maskawa matrix element $|V_{cb}|$," *Phys. Rev.*, vol. D93, no. 3, p. 032006, 2016.

[37] A. Abdesselam *et al.*, "Precise determination of the CKM matrix element $|V_{cb}|$ with $\bar{B}^0 \to D^{*+}\ell^-\bar{\nu}_\ell$ decays with hadronic tagging at Belle," 2 2017.

[38] A. Abdesselam *et al.*, "Measurement of CKM Matrix Element $|V_{cb}|$ from $\bar{B} \to D^{*+}\ell^-\bar{\nu}_\ell$," 2018.

[39] Y. Aoki *et al.*, "FLAG Review 2021," 11 2021.

[40] Y. S. Amhis *et al.*, "Averages of b-hadron, c-hadron, and τ-lepton properties as of 2018," *Eur. Phys. J. C*, vol. 81, no. 3, p. 226, 2021.

[41] J. P. Lees *et al.*, "Evidence for an excess of $\bar{B} \to D^{(*)}\tau^-\bar{\nu}_\tau$ decays," *Phys. Rev. Lett.*, vol. 109, p. 101802, 2012.

[42] J. P. Lees *et al.*, "Measurement of an Excess of $\bar{B} \to D^{(*)}\tau^-\bar{\nu}_\tau$ Decays and Implications for Charged Higgs Bosons," *Phys. Rev.*, vol. D88, no. 7, p. 072012, 2013.

[43] R. Aaij *et al.*, "Measurement of the ratio of branching fractions $\mathcal{B}(\bar{B}^0 \to D^{*+}\tau^-\bar{\nu}_\tau)/\mathcal{B}(\bar{B}^0 \to D^{*+}\mu^-\bar{\nu}_\mu)$," *Phys. Rev. Lett.*, vol. 115, no. 11, p. 111803, 2015. [Erratum: Phys. Rev. Lett.115,no.15,159901(2015)].

[44] M. Huschle *et al.*, "Measurement of the branching ratio of $\bar{B} \to D^{(*)}\tau^-\bar{\nu}_\tau$ relative to $\bar{B} \to D^{(*)}\ell^-\bar{\nu}_\ell$ decays with hadronic tagging at Belle," *Phys. Rev.*, vol. D92, no. 7, p. 072014, 2015.

[45] Y. Sato *et al.*, "Measurement of the branching ratio of $\bar{B}^0 \to D^{*+}\tau^-\bar{\nu}_\tau$ relative to $\bar{B}^0 \to D^{*+}\ell^-\bar{\nu}_\ell$ decays with a semileptonic tagging method," *Phys. Rev.*, vol. D94, no. 7, p. 072007, 2016.

[46] S. Hirose *et al.*, "Measurement of the τ lepton polarization and $R(D^*)$ in the decay $\bar{B} \to D^*\tau^-\bar{\nu}_\tau$," *Phys. Rev. Lett.*, vol. 118, no. 21, p. 211801, 2017.

[47] R. Aaij *et al.*, "Measurement of the ratio of the $B^0 \to D^{*-}\tau^+\nu_\tau$ and $B^0 \to D^{*-}\mu^+\nu_\mu$ branching fractions using three-prong τ-lepton decays," *Phys. Rev. Lett.*, vol. 120, no. 17, p. 171802, 2018.

[48] S. Hirose *et al.*, "Measurement of the τ lepton polarization and $R(D^*)$ in the decay $\bar{B} \to D^*\tau^-\bar{\nu}_\tau$ with one-prong hadronic τ decays at Belle," *Phys. Rev.*, vol. D97, no. 1, p. 012004, 2018.

[49] R. Aaij *et al.*, "Test of Lepton Flavor Universality by the measurement of the $B^0 \to D^{*-}\tau^+\nu_\tau$ branching fraction using three-prong τ decays," *Phys. Rev.*, vol. D97, no. 7, p. 072013, 2018.

[50] D. Bigi and P. Gambino, "Revisiting $B \to D\ell\nu$," *Physical Review D*, vol. 94, Nov 2016.

[51] P. Gambino, M. Jung, and S. Schacht, "The V_{cb} puzzle: An update," *Phys. Lett. B*, vol. 795, pp. 386–390, 2019.

[52] M. Bordone, N. Gubernari, D. van Dyk, and M. Jung, "Heavy-Quark expansion for $\bar{B}_s \to D_s^{(*)}$ form factors and unitarity bounds beyond the $SU(3)_F$ limit," *Eur. Phys. J. C*, vol. 80, no. 4, p. 347, 2020.

[53] H. Na, C. M. Bouchard, G. P. Lepage, C. Monahan, and J. Shigemitsu, "$B \to Dl\nu$ form factors at nonzero recoil and extraction of $|V_{cb}|$," *Phys. Rev.*, vol. D92, no. 5, p. 054510, 2015. [Erratum: Phys. Rev.D93,no.11,119906(2016)].

[54] J. A. Bailey *et al.*, "$B \to D\ell\nu$ form factors at nonzero recoil and $|V_{cb}|$ from 2+1-flavor lattice QCD," *Phys. Rev.*, vol. D92, no. 3, p. 034506, 2015.

[55] A. Bazavov *et al.*, "Semileptonic form factors for $B \to D^*\ell\nu$ at nonzero recoil from 2 + 1-flavor lattice QCD," 5 2021.

[56] S. Okubo, "Exact bounds for K_{l3} decay parameters," *Phys. Rev. D*, vol. 3, pp. 2807–2813, Jun 1971.

[57] S. Okubo, "New improved bounds for K_{l3} parameters," *Phys. Rev. D*, vol. 4, pp. 725–733, 1971.

[58] S. Okubo and I.-F. Shih, "Exact inequality and test of chiral sw(3) theory in K_{l3} decay problem," *Phys. Rev. D*, vol. 4, pp. 2020–2029, Oct 1971.

[59] C. Bourrely, B. Machet, and E. de Rafael, "Semileptonic Decays of Pseudoscalar Particles ($M \to M^{'}\ell\nu_\ell$) and Short Distance Behavior of Quantum Chromodynamics," *Nucl. Phys. B*, vol. 189, pp. 157–181, 1981.

[60] L. Lellouch, "Lattice constrained unitarity bounds for $\bar{B}^0 \to \pi^+\ell^-\bar{\nu}_\ell$ decays," *Nucl. Phys. B*, vol. 479, pp. 353–391, 1996.

[61] C. G. Boyd, B. Grinstein, and R. F. Lebed, "Model independent extraction of $|V_{cb}|$ using dispersion relations," *Phys. Lett.*, vol. B353, pp. 306–312, 1995.

[62] C. G. Boyd, B. Grinstein, and R. F. Lebed, "Model independent determinations of $\bar{B} \to D\ell\bar{\nu}, D^*\ell\bar{\nu}$ form-factors," *Nucl. Phys.*, vol. B461, pp. 493–511, 1996.

[63] C. Boyd, B. Grinstein, and R. F. Lebed, "Precision corrections to dispersive bounds on form-factors," *Phys. Rev. D*, vol. 56, pp. 6895–6911, 1997.

[64] C. Bourrely, I. Caprini, and L. Lellouch, "Model-independent description of $B \to \pi\ell\nu$ decays and a determination of $|V_{ub}|$," *Phys. Rev. D*, vol. 79, p. 013008, 2009. [Erratum: Phys.Rev.D 82, 099902 (2010)].

[65] I. Caprini and M. Neubert, "Improved bounds for the slope and curvature of $\bar{B} \to D^{(*)}\ell\bar{\nu}$ form-factors," *Phys. Lett.*, vol. B380, pp. 376–384, 1996.

[66] I. Caprini, L. Lellouch, and M. Neubert, "Dispersive bounds on the shape of $\bar{B} \to D^{(*)}\ell\bar{\nu}$ form-factors," *Nucl. Phys.*, vol. B530, pp. 153–181, 1998.

[67] G. D'Agostini, "Skeptical combination of experimental results using JAGS/rjags with application to the $K^{\pm}$ mass determination," 1 2020.

[68] G. D'Agostini, "On a curious bias arising when the $\sqrt{\chi^2/\nu}$ scaling prescription is first applied to a sub-sample of the individual results," 1 2020.

[69] D. Bigi, P. Gambino, and S. Schacht, "$R(D^*)$, $|V_{cb}|$, and the heavy quark symmetry relations between form factors," *Journal of High Energy Physics*, vol. 2017, Nov 2017.

[70] G. Martinelli, M. Naviglio, S. Simula, and L. Vittorio, "Exclusive B-meson semileptonic decays from unitarity and lattice QCD," *PoS*, vol. CKM2021, p. 045, 2021.

[71] J. A. Bailey, A. Bazavov, C. Bernard, M. Bouchard, C., C. DeTar, D. Du, X. El-Khadra, A., J. Foley, D. Freeland, E., E. Gz, *et al.*, "$B \to D\ell\nu$ form factors at nonzero recoil and $|V_{cb}|$ from $2+1-$flavor lattice QCD," *Physical Review D*, vol. 92, Aug 2015.

[72] T. Kaneko, Y. Aoki, G. Bailas, B. Colquhoun, H. Fukaya, S. Hashimoto, and J. Koponen, "$B \to D^{(*)}\ell\nu$ form factors from lattice QCD with relativistic heavy quarks," *PoS*, vol. LATTICE2019, p. 139, 2019.

[73] H. Na, C. M. Bouchard, G. P. Lepage, C. Monahan, and J. Shigemitsu, "$B \to D\ell\nu$ form factors at nonzero recoil and extraction of $|V_{cb}|$," *Physical Review D*, vol. 92, Sep 2015.

[74] N. Gubernari, A. Kokulu, and D. van Dyk, "$B \to P$ and $B \to V$ Form Factors from B-Meson Light-Cone Sum Rules beyond Leading Twist," *JHEP*, vol. 01, p. 150, 2019.

[75] R. Glattauer, C. Schwanda, A. Abdesselam, I. Adachi, K. Adamczyk, H. Aihara, S. Al Said, M. Asner, D., T. Aushev, R. Ayad, *et al.*, "Measurement of the decay $B \to D\ell\nu_\ell$ in fully reconstructed events and determination of the cabibbo-kobayashi-maskawa matrix element $|V_{cb}|$," *Physical Review D*, vol. 93, Feb 2016.

[76] L. Riggio, G. Salerno, and S. Simula, "Extraction of $|V_{cd}|$ and $|V_{cs}|$ from experimental decay rates using lattice QCD $D \to \pi(K)\ell\nu$ form factors," *Eur. Phys. J. C*, vol. 78, no. 6, p. 501, 2018.

[77] M. Schmelling, "Averaging correlated data," *Phys. Scripta*, vol. 51, pp. 676–679, 1995.

[78] E. Waheed *et al.*, "Measurement of the CKM matrix element $|V_{cb}|$ from $B^0 \to D^{*-}\ell^+\nu_\ell$ at Belle," *Phys. Rev. D*, vol. 100, no. 5, p. 052007, 2019.

[79] G. D'Agostini, "On the use of the covariance matrix to fit correlated data," *Nucl. Instrum. Meth. A*, vol. 346, pp. 306–311, 1994.

[80] N. Carrasco *et al.*, "Up, down, strange and charm quark masses with $N_f = 2+1+1$ twisted mass lattice QCD," *Nucl. Phys. B*, vol. 887, pp. 19–68, 2014.

[81] E. Waheed, P. Urquijo, D. Ferlewicz, I. Adachi, K. Adamczyk, H. Aihara, S. Al Said, M. Asner, D., H. Atmacan, T. Aushev, *et al.*, "Erratum: Measurement of the CKM matrix element $|V_{cb}|$ from $B^0 \to D^{*-}\ell^+\nu_\ell$ at Belle [Phys. Rev. D 100, 052007 (2019)]," *Phys. Rev. D*, vol. 103, p. 079901, Apr 2021.

[82] M. A. Ivanov, J. G. Körner, and C.-T. Tran, "Analyzing new physics in the decays $\bar{B}^0 \to D^{(*)}\tau^-\bar{\nu}_\tau$ with form factors obtained from the covariant quark model," *Phys. Rev. D*, vol. 94, no. 9, p. 094028, 2016.

[83] S. Bhattacharya, S. Nandi, and S. Kumar Patra, "$b \to c\tau\nu_\tau$ Decays: a catalogue to compare, constrain, and correlate new physics effects," *Eur. Phys. J. C*, vol. 79, no. 3, p. 268, 2019.

[84] S. Hirose *et al.*, "Measurement of the τ lepton polarization and $R(D^*)$ in the decay $\bar{B} \to D^*\tau^-\bar{\nu}_\tau$," *Phys. Rev. Lett.*, vol. 118, no. 21, p. 211801, 2017.

[85] A. Abdesselam *et al.*, "Measurement of the D^{*-} polarization in the decay $B^0 \to D^{*-}\tau^+\nu_\tau$," in *10th International Workshop on the CKM Unitarity Triangle*, 3 2019.

[86] E. McLean, C. T. H. Davies, J. Koponen, and A. T. Lytle, "$B_s \to D_s\ell\nu$ Form Factors for the full q^2 range from Lattice QCD with non-perturbatively normalized currents," *Phys. Rev. D*, vol. 101, no. 7, p. 074513, 2020.

[87] J. Harrison and C. T. H. Davies, "$B_s \to D_s^*$ Form Factors for the full q^2 range from Lattice QCD," 5 2021.

[88] R. Aaij *et al.*, "Measurement of $|V_{cb}|$ with $B_s^0 \to D_s^{(*)-}\mu^+\nu_\mu$ decays," *Phys. Rev. D*, vol. 101, no. 7, p. 072004, 2020.

[89] R. Aaij *et al.*, "Measurement of the shape of the $B_s^0 \to D_s^{*-}\mu^+\nu_\mu$ differential decay rate," *JHEP*, vol. 12, p. 144, 2020.

[90] P. A. Zyla *et al.*, "Review of Particle Physics," *PTEP*, vol. 2020, no. 8, p. 083C01, 2020.

[91] S. Jaiswal, S. Nandi, and S. K. Patra, "Extraction of $|V_{cb}|$ from $B \to D^{(*)}\ell\nu_\ell$ and the standard model predictions of $R(D^{(*)})$," *Journal of High Energy Physics*, vol. 2017, Dec 2017.

[92] S. Aoki *et al.*, "FLAG Review 2019: Flavour Lattice Averaging Group (FLAG)," *Eur. Phys. J. C*, vol. 80, no. 2, p. 113, 2020.

[93] B. Aubert *et al.*, "Measurement of $|V_{cb}|$ and the Form-Factor Slope in $\bar{B} \to D\ell^-\bar{\nu}_\ell$ Decays in Events Tagged by a Fully Reconstructed B Meson," *Phys. Rev. Lett.*, vol. 104, p. 011802, 2010.

[94] S. Jaiswal, S. Nandi, and S. K. Patra, "Updates on extraction of $|V_{cb}|$ and SM prediction of $R(D^*)$ in $B \to D^*\ell\nu_\ell$ decays," *JHEP*, vol. 06, p. 165, 2020.

[95] Y. Amhis *et al.*, "Averages of b-hadron, c-hadron, and τ-lepton properties as of 2021," 6 2022.

[96] L. Cao *et al.*, "Measurements of partial branching fractions of inclusive $B \to X_u\ell^+\nu_\ell$ decays with hadronic tagging," *Phys. Rev. D*, vol. 104, no. 1, p. 012008, 2021.

[97] B. O. Lange, M. Neubert, and G. Paz, "Theory of charmless inclusive B decays and the extraction of V(ub)," *Phys. Rev. D*, vol. 72, p. 073006, 2005.

[98] J. R. Andersen and E. Gardi, "Inclusive spectra in charmless semileptonic B decays by dressed gluon exponentiation," *JHEP*, vol. 01, p. 097, 2006.

[99] P. Gambino, P. Giordano, G. Ossola, and N. Uraltsev, "Inclusive semileptonic B decays and the determination of $|V_{ub}|$," *JHEP*, vol. 10, p. 058, 2007.

[100] U. Aglietti, G. Ferrera, and G. Ricciardi, "Semi-Inclusive B Decays and a Model for Soft-Gluon Effects," *Nucl. Phys. B*, vol. 768, pp. 85–115, 2007.

[101] U. Aglietti, F. Di Lodovico, G. Ferrera, and G. Ricciardi, "Inclusive measure of $|V_{ub}|$ with the analytic coupling model," *Eur. Phys. J. C*, vol. 59, pp. 831–840, 2009.

[102] D. Leljak, B. Melić, and D. van Dyk, "The $\bar{B} \to \pi$ form factors from QCD and their impact on $|V_{ub}|$," 2 2021.

[103] A. Biswas, S. Nandi, S. K. Patra, and I. Ray, "A closer look at the extraction of $|V_{ub}|$ from $B \to \pi l \nu$," 3 2021.

[104] S. Gonzàlez-Solís, P. Masjuan, and C. Rojas, "Padé approximants to $B \to \pi \ell \nu_\ell$ and $B_s \to \ell \nu_\ell$ and determination of $|V_{ub}|$," *Phys. Rev. D*, vol. 104, no. 11, p. 114041, 2021.

[105] A. Bharucha, D. M. Straub, and R. Zwicky, "$B \to V \ell^+ \ell^-$ in the Standard Model from light-cone sum rules," *JHEP*, vol. 08, p. 098, 2016.

[106] S. Gonzàlez-Solís and P. Masjuan, "Study of $B \to \pi \ell \nu_\ell$ and $B^+ \to \eta^{(\prime)} \ell^+ \nu_\ell$ decays and determination of $|V_{ub}|$," *Phys. Rev. D*, vol. 98, no. 3, p. 034027, 2018.

[107] J. M. Flynn, T. Izubuchi, T. Kawanai, C. Lehner, A. Soni, R. S. Van de Water, and O. Witzel, "$B \to \pi \ell \nu$ and $B_s \to K \ell \nu$ form factors and $|V_{ub}|$ from 2+1-flavor lattice QCD with domain-wall light quarks and relativistic heavy quarks," *Phys. Rev. D*, vol. 91, no. 7, p. 074510, 2015.

[108] J. A. Bailey *et al.*, "$|V_{ub}|$ from $B \to \pi \ell \nu$ decays and (2+1)-flavor lattice QCD," *Phys. Rev. D*, vol. 92, no. 1, p. 014024, 2015.

[109] C. M. Bouchard, G. P. Lepage, C. Monahan, H. Na, and J. Shigemitsu, "$B_s \to K \ell \nu$ form factors from lattice QCD," *Phys. Rev. D*, vol. 90, p. 054506, 2014.

[110] A. Bazavov *et al.*, "$B_s \to K \ell \nu$ decay from lattice QCD," *Phys. Rev. D*, vol. 100, no. 3, p. 034501, 2019.

[111] Z. Gelzer *et al.*, "B-meson semileptonic form factors on (2+1+1)-flavor HISQ ensembles," *PoS*, vol. LATTICE2019, p. 236, 2019.

[112] J. M. Flynn, R. C. Hill, A. Jüttner, A. Soni, J. T. Tsang, and O. Witzel, "Nonperturbative calculations of form factors for exclusive semileptonic $B_{(s)}$ decays," *PoS*, vol. ICHEP2020, p. 436, 2021.

[113] A. Khodjamirian and A. V. Rusov, "$B_s \to K \ell \nu_\ell$ and $B_{(s)} \to \pi(K) \ell^+ \ell^-$ decays at large recoil and CKM matrix elements," *JHEP*, vol. 08, p. 112, 2017.

[114] P. del Amo Sanchez *et al.*, "Study of $B \to \pi \ell \nu$ and $B \to \rho \ell \nu$ Decays and Determination of $|V_{ub}|$," *Phys. Rev. D*, vol. 83, p. 032007, 2011.

[115] H. Ha *et al.*, "Measurement of the decay $B^0 \to \pi^- \ell^+ \nu$ and determination of $|V_{ub}|$," *Phys. Rev. D*, vol. 83, p. 071101, 2011.

[116] J. P. Lees *et al.*, "Branching fraction and form-factor shape measurements of exclusive charmless semileptonic B decays, and determination of $|V_{ub}|$," *Phys. Rev. D*, vol. 86, p. 092004, 2012.

[117] A. Sibidanov *et al.*, "Study of Exclusive $B \to X_u \ell \nu$ Decays and Extraction of $|V_{ub}|$ using Full Reconstruction Tagging at the Belle Experiment," *Phys. Rev. D*, vol. 88, no. 3, p. 032005, 2013.

[118] R. Aaij *et al.*, "First observation of the decay $B_s^0 \to K^- \mu^+ \nu_\mu$ and Measurement of $|V_{ub}|/|V_{cb}|$," *Phys. Rev. Lett.*, vol. 126, no. 8, p. 081804, 2021.

[119] U.-G. Meißner and W. Wang

[120] N. Rajeev and R. Dutta, "Impact of vector new physics couplings on $B_s \to (K, K^*)\tau\nu$ and $B \to \pi\tau\nu$ decays," *Phys. Rev. D*, vol. 98, no. 5, p. 055024, 2018.

[121] A. Biswas and S. Nandi, "A closer look at observables from exclusive semileptonic $B \to (\pi, \rho)\ell\nu_\ell$ decays," *JHEP*, vol. 09, p. 127, 2021.

[122] P. Hamer *et al.*, "Search for $B^0 \to \pi^- \tau^+ \nu_\tau$ with hadronic tagging at Belle," *Phys. Rev. D*, vol. 93, no. 3, p. 032007, 2016.

[123] W. Altmannshofer *et al.*, "The belle ii physics book," *PTEP*, vol. 2019, no. 12, p. 123C01, 2019. [Erratum: PTEP 2020, 029201 (2020)].

[124] M. Ciuchini, G. D'Agostini, E. Franco, V. Lubicz, G. Martinelli, F. Parodi, P. Roudeau, and A. Stocchi, "2000 CKM triangle analysis: A Critical review with updated experimental inputs and theoretical parameters," *JHEP*, vol. 07, p. 013, 2001.

[125] M. Bona *et al.*, "The 2004 UTfit collaboration report on the status of the unitarity triangle in the standard model," *JHEP*, vol. 07, p. 028, 2005.

[126] M. Bona *et al.*, "Unitarity Triangle global fits testing the Standard Model: UTfit 2021 SM update," *PoS*, vol. EPS-HEP2021, p. 512, 2022.

[127] F. Gabbiani, E. Gabrielli, A. Masiero, and L. Silvestrini, "A Complete analysis of FCNC and CP constraints in general SUSY extensions of the standard model," *Nucl. Phys. B*, vol. 477, pp. 321–352, 1996.

[128] A. J. Buras, M. Misiak, and J. Urban, "Two loop QCD anomalous dimensions of flavor changing four quark operators within and beyond the standard model," *Nucl. Phys. B*, vol. 586, pp. 397–426, 2000.

[129] J. Aebischer, M. Fael, C. Greub, and J. Virto, "B physics Beyond the Standard Model at One Loop: Complete Renormalization Group Evolution below the Electroweak Scale," *JHEP*, vol. 09, p. 158, 2017.

[130] A. J. Buras, "Weak Hamiltonian, CP violation and rare decays," in *Les Houches Summer School in Theoretical Physics, Session 68: Probing the Standard Model of Particle Interactions*, pp. 281–539, 6 1998.

[131] A. J. Buras, "Flavour dynamics: CP violation and rare decays," *Theory and Experiment Heading for New Physics*, Jan 2002.

[132] L. Silvestrini, "Effective Theories for Quark Flavour Physics," 5 2019.

[133] G. D'Ambrosio, G. F. Giudice, G. Isidori, and A. Strumia, "Minimal flavor violation: An Effective field theory approach," *Nucl. Phys. B*, vol. 645, pp. 155–187, 2002.

[134] G. Isidori and D. M. Straub, "Minimal Flavour Violation and Beyond," *Eur. Phys. J. C*, vol. 72, p. 2103, 2012.

[135] R. Barbieri, G. Isidori, J. Jones-Perez, P. Lodone, and D. M. Straub, "$U(2)$ and Minimal Flavour Violation in Supersymmetry," *Eur. Phys. J. C*, vol. 71, p. 1725, 2011.

[136] R. Aaij *et al.*, "Test of lepton universality in beauty-quark decays," *Nature Phys.*, vol. 18, no. 3, pp. 277–282, 2022.

[137] R. Aaij *et al.*, "Test of lepton universality with $B^0 \to K^{*0}\ell^+\ell^-$ decays," *JHEP*, vol. 08, p. 055, 2017.

[138] J. P. Lees *et al.*, "Measurement of branching fractions and rate asymmetries in the rare decays $B \to K^{(*)}\ell^+\ell^-$," *Phys. Rev. D*, vol. 86, p. 032012, Aug 2012.

[139] S. Choudhury *et al.*, "Test of lepton flavor universality and search for lepton flavor violation in $B \to K\ell\ell$ decays," *JHEP*, vol. 03, p. 105, 2021.

[140] J. P. Lees *et al.*, "Measurement of Branching Fractions and Rate Asymmetries in the Rare Decays $B \to K^{(*)}l^+l^-$," *Phys. Rev. D*, vol. 86, p. 032012, 2012.

[141] J. T. Wei *et al.*, "Measurement of the Differential Branching Fraction and Forward-Backward Asymmetry for $B \to K^{(*)}\ell^+\ell^-$," *Phys. Rev. Lett.*, vol. 103, p. 171801, 2009.

[142] M. Ciuchini, M. Fedele, E. Franco, A. Paul, L. Silvestrini, and M. Valli, "New Physics without bias: Charming Penguins and Lepton Universality Violation in $b \to s\ell^+\ell^-$ decays," 10 2021.

[143] G. Isidori, D. Lancierini, A. Mathad, P. Owen, N. Serra, and R. S. Coutinho, "A general effective field theory description of $b \to sl^+l^-$ lepton universality ratios," 10 2021.

[144] "Physics case for an LHCb Upgrade II - opportunities in flavour physics, and beyond, in the HL-LHC era," 2018.

[145] E. Kou, P. Urquijo, W. Altmannshofer, F. Beaujean, G. Bell, M. Beneke, I. I. Bigi, F. Bishara, M. Blanke, C. Bobeth, *et al.*, "The belle ii physics book," *Progress of Theoretical and Experimental Physics*, vol. 2019, Dec 2019.

[146] W. Altmannshofer and D. M. Straub, "Cornering new physics in $b \to s$ transitions," *Journal of High Energy Physics*, vol. 2012, Aug 2012.

[147] M. Chrzaszcz, A. Mauri, N. Serra, R. S. Coutinho, and D. van Dyk, "Prospects for disentangling long- and short-distance effects in the decays $B \to K^*\mu^+\mu^-$," *Journal of High Energy Physics*, vol. 2019, Oct 2019.

[148] M. Artuso, G. Borissov, and A. Lenz, "CP violation in the B_s^0 system," *Rev. Mod. Phys.*, vol. 88, p. 045002, Oct 2016.

[149] U. Collaboration, M. Bona, M. Ciuchini, E. Franco, V. Lubicz, G. Martinelli, F. Parodi, M. Pierini, P. Roudeau, C. Schiavi, L. Silvestrini, A. Stocchi, and V. Vagnoni, "The UTfit collaboration report on the status of the unitarity triangle beyond the standard model I. model-independent analysis and minimal flavour violation," *Journal of High Energy Physics*, vol. 2006, pp. 080–080, mar 2006.

[150] M. Bona *et al.*, "Model-independent constraints on $\Delta F = 2$ operators and the scale of new physics," *JHEP*, vol. 03, p. 049, 2008.

[151] G. Isidori, Y. Nir, and G. Perez, "Flavor physics constraints for physics beyond the standard model," *Annual Review of Nuclear and Particle Science*, vol. 60, no. 1, pp. 355–380, 2010.

[152] J. Charles, S. Descotes-Genon, Z. Ligeti, S. Monteil, M. Papucci, and K. Trabelsi, "Future sensitivity to new physics inbd,bs, andkmixings," *Physical Review D*, vol. 89, Feb 2014.

[153] A. J. Buras, D. Buttazzo, J. Girrbach-Noe, and R. Knegjens, "Can we reach the zeptouniverse with rare K and $B_{s,d}$ decays?," *Journal of High Energy Physics*, vol. 2014, Nov 2014.

[154] N. Vignaroli, "$\Delta F = 1$ constraints on composite Higgs models with left-right parity," *Physical Review D*, vol. 86, Dec 2012.

[155] W. Altmannshofer, P. Ball, A. Bharucha, A. J. Buras, D. M. Straub, and M. Wick, "Symmetries and Asymmetries of $B \to K^* \mu^+ \mu^-$ Decays in the Standard Model and Beyond," *JHEP*, vol. 01, p. 019, 2009.

[156] M. Misiak, M. Asatrian, H., R. Boughezal, M. Czakon, T. Ewerth, A. Ferroglia, P. Fiedler, P. Gambino, C. Greub, U. Haisch, *et al.*, "Updated next-to-next-to-leading-order qcd predictions for the weak radiative b -meson decays," *Physical Review Letters*, vol. 114, Jun 2015.

[157] A. Paul and D. M. Straub, "Constraints on new physics from radiative b decays," *Journal of High Energy Physics*, vol. 2017, Apr 2017.

[158] A. Ali and A. Parkhomenko, "Branching ratios for $B \to K^* \gamma$ and $B \to \rho \gamma$ decays in next-to-leading order in the large energy effective theory," *The European Physical Journal C*, vol. 23, pp. 89–112, Mar 2002.

[159] P. D. Group, "Review of particle physics," *Phys. Rev. D*, vol. 98, p. 030001, Aug 2018.

[160] P. Ball, G. W. Jones, and R. Zwicky, "$B \to V \gamma$ beyond QCD factorization," *Physical Review D*, vol. 75, Mar 2007.

[161] Y. Amhis, S. Banerjee, E. Ben-Haim, F. Bernlochner, A. Bozek, C. Bozzi, M. Chrz, szcz, J. Dingfelder, S. Duell, *et al.*, "Averages of b-hadron, c-hadron, and τ-lepton properties as of summer 2016," *The European Physical Journal C*, vol. 77, Dec 2017.

[162] D. Bečirević and E. Schneider, "On transverse asymmetries in $B \to K^* \ell^+ \ell^-$," *Nuclear Physics B*, vol. 854, pp. 321–339, Jan 2012.

[163] S. Jr and J. Martin Camalich, "Reassessing the discovery potential of the $B \to K^* \ell^+ \ell^-$ decays in the large-recoil region: SM challenges and BSM opportunities," *Physical Review D*, vol. 93, Jan 2016.

[164] R. Contino, "Tasi 2009 lectures: The higgs as a composite nambu-goldstone boson," 2010.

[165] G. Panico and A. Wulzer, "The composite nambu-goldstone higgs," *Lecture Notes in Physics*, 2016.

[166] K. Agashe, R. Contino, and A. Pomarol, "The minimal composite higgs model," *Nuclear Physics B*, vol. 719, pp. 165–187, Jul 2005.

[167] D. B. Kaplan and H. Georgi, "$SU(2) \times U(1)$ breaking by vacuum misalignment," *Physics Letters B*, vol. 136, no. 3, pp. 183 – 186, 1984.

[168] D. B. Kaplan, H. Georgi, and S. Dimopoulos, "Composite higgs scalars," *Physics Letters B*, vol. 136, no. 3, pp. 187 – 190, 1984.

[169] M. J. Dugan, H. Georgi, and D. B. Kaplan, "Anatomy of a composite higgs model," *Nuclear Physics B*, vol. 254, pp. 299 – 326, 1985.

[170] D. B. Kaplan, "Flavor at SSC energies: A new mechanism for dynamically generated fermion masses," *Nuclear Physics B*, vol. 365, no. 2, pp. 259 – 278, 1991.

[171] R. Barbieri, D. Buttazzo, F. Sala, D. M. Straub, and A. Tesi, "A 125 GeV composite higgs boson versus flavour and electroweak precision tests," *Journal of High Energy Physics*, vol. 2013, May 2013.

[172] Y. Grossman and M. Neubert, "Neutrino masses and mixings in nonfactorizable geometry," *Phys. Lett. B*, vol. 474, pp. 361–371, 2000.

[173] S. J. Huber and Q. Shafi, "Fermion masses, mixings and proton decay in a Randall-Sundrum model," *Physics Letters B*, vol. 498, pp. 256–262, Jan 2001.

[174] T. Gherghetta and A. Pomarol, "Bulk fields and supersymmetry in a slice of AdS," *Nucl. Phys. B*, vol. 586, pp. 141–162, 2000.

[175] K. Agashe, G. Perez, and A. Soni, "Flavor structure of warped extra dimension models," *Physical Review D*, vol. 71, Jan 2005.

[176] M. Blanke, A. J. Buras, B. Duling, S. Gori, and A. Weiler, "$\Delta F = 2$ observables and fine-tuning in a warped extra dimension with custodial protection," *Journal of High Energy Physics*, vol. 2009, p. 001, Mar 2009.

[177] M. Bauer, S. Casagrande, U. Haisch, and M. Neubert, "Flavor Physics in the Randall-Sundrum Model: II. Tree-Level Weak-Interaction Processes," *JHEP*, vol. 09, p. 017, 2010.

[178] B. Keren-Zur, P. Lodone, M. Nardecchia, D. Pappadopulo, R. Rattazzi, and L. Vecchi, "On partial compositeness and the CP asymmetry in charm decays," *Nuclear Physics B*, vol. 867, no. 2, pp. 394 – 428, 2013.

[179] C. Cs, A. Falkowski, and A. Weiler, "The flavor of the composite pseudo-goldstone Higgs," *Journal of High Energy Physics*, vol. 2008, p. 008, Sep 2008.

[180] J. C. Pati and A. Salam, "Unified lepton-hadron symmetry and a gauge theory of the basic interactions," *Phys. Rev. D*, vol. 8, pp. 1240–1251, Aug 1973.

[181] J. C. Pati and A. Salam, "Lepton number as the fourth "color"," *Phys. Rev. D*, vol. 10, pp. 275–289, Jul 1974.

[182] J. C. Pati and A. Salam, "Erratum: Lepton number as the fourth "color"," *Phys. Rev. D*, vol. 11, pp. 703–703, Feb 1975.

[183] O. Shanker, "Flavour violation, scalar particles and leptoquarks," *Nuclear Physics B*, vol. 206, no. 2, pp. 253–272, 1982.

[184] O. Shanker, "2, k3and k0k0 constraints on leptoquarks and supersymmetric particles," *Nuclear Physics B*, vol. 204, no. 3, pp. 375–386, 1982.

[185] J. L. Hewett and S. Pakvasa, "Scalar-leptoquark production at hadron colliders," *Phys. Rev. D*, vol. 37, pp. 3165–3171, Jun 1988.

[186] M. Leurer, "Comprehensive study of leptoquark bounds," *Phys. Rev. D*, vol. 49, pp. 333–342, Jan 1994.

[187] M. Leurer, "Bounds on vector leptoquarks," *Phys. Rev. D*, vol. 50, pp. 536–541, Jul 1994.

[188] W. Buchmüller and D. Wyler, "Constraints on SU(5)-type leptoquarks," *Physics Letters B*, vol. 177, no. 3, pp. 377–382, 1986.

[189] W. Buchmüller, R. Rückl, and D. Wyler, "Leptoquarks in lepton-quark collisions," *Physics Letters B*, vol. 191, no. 4, pp. 442–448, 1987.

[190] J. L. Hewett and T. G. Rizzo, "Much ado about leptoquarks: A comprehensive analysis," *Phys. Rev. D*, vol. 56, pp. 5709–5724, Nov 1997.

[191] I. Doršner, S. Fajfer, A. Greljo, J. F. Kamenik, and N. Košnik, "Physics of leptoquarks in precision experiments and at particle colliders," *Phys. Rept.*, vol. 641, pp. 1–68, 2016.

[192] C. Cornella, J. Fuentes-Martin, and G. Isidori, "Revisiting the vector leptoquark explanation of the B-physics anomalies," *JHEP*, vol. 07, p. 168, 2019.

[193] C. Cornella, D. A. Faroughy, J. Fuentes-Martin, G. Isidori, and M. Neubert, "Reading the footprints of the B-meson flavor anomalies," *JHEP*, vol. 08, p. 050, 2021.

[194] A. Crivellin, C. Greub, D. Müller, and F. Saturnino, "Importance of Loop Effects in Explaining the Accumulated Evidence for New Physics in B Decays with a Vector Leptoquark," *Phys. Rev. Lett.*, vol. 122, no. 1, p. 011805, 2019.

[195] M. Bordone, G. Isidori, and A. Pattori, "On the Standard Model predictions for R_K and R_{K^*}," *Eur. Phys. J. C*, vol. 76, no. 8, p. 440, 2016.

[196] M. Tanaka and R. Watanabe, "New physics in the weak interaction of $\bar{B} \to D^{(*)}\tau\bar{\nu}$," *Phys. Rev. D*, vol. 87, no. 3, p. 034028, 2013.

[197] Y. Sakaki, M. Tanaka, A. Tayduganov, and R. Watanabe, "Testing leptoquark models in $\bar{B} \to D^{(*)}\tau\bar{\nu}$," *Phys. Rev. D*, vol. 88, no. 9, p. 094012, 2013.

[198] Y. Sakaki, M. Tanaka, A. Tayduganov, and R. Watanabe, "Probing New Physics with q^2 distributions in $\bar{B} \to D^{(*)}\tau\bar{\nu}$," *Phys. Rev. D*, vol. 91, no. 11, p. 114028, 2015.

[199] R. Alonso, B. Grinstein, and J. Martin Camalich, "Lepton universality violation and lepton flavor conservation in B-meson decays," *JHEP*, vol. 10, p. 184, 2015.

[200] M. Freytsis, Z. Ligeti, and J. T. Ruderman, "Flavor models for $\bar{B} \to D^{(*)}\tau\bar{\nu}$," *Phys. Rev. D*, vol. 92, no. 5, p. 054018, 2015.

[201] X.-Q. Li, Y.-D. Yang, and X. Zhang, "Revisiting the one leptoquark solution to the R($D^{(*)}$) anomalies and its phenomenological implications," *JHEP*, vol. 08, p. 054, 2016.

[202] J. P. Saha, B. Misra, and A. Kundu, "Constraining Scalar Leptoquarks from the K and B Sectors," *Phys. Rev. D*, vol. 81, p. 095011, 2010.

[203] N. Kosnik, "Model independent constraints on leptoquarks from $b \to s\ell^+\ell^-$ processes," *Phys. Rev. D*, vol. 86, p. 055004, 2012.

[204] S. Sahoo and R. Mohanta, "Leptoquark effects on $b \to s\boldsymbol{\nu\bar{\nu}}$ and $B \to Kl^+l^-$ decay processes," *New J. Phys.*, vol. 18, no. 1, p. 013032, 2016.

[205] S. Sahoo and R. Mohanta, "Scalar leptoquarks and the rare B meson decays," *Phys. Rev. D*, vol. 91, no. 9, p. 094019, 2015.

[206] D. Bečirević, S. Fajfer, and N. Košnik, "Lepton flavor nonuniversality in $b \to s\ell^+\ell^-$ processes," *Phys. Rev. D*, vol. 92, no. 1, p. 014016, 2015.

[207] G. Hiller and M. Schmaltz, "Diagnosing lepton-nonuniversality in $b \to s\ell\ell$," *JHEP*, vol. 02, p. 055, 2015.

[208] G. Hiller and M. Schmaltz, "R_K and future $b \to s\ell\ell$ physics beyond the standard model opportunities," *Phys. Rev. D*, vol. 90, p. 054014, 2014.

[209] B. Gripaios, M. Nardecchia, and S. A. Renner, "Composite leptoquarks and anomalies in B-meson decays," *JHEP*, vol. 05, p. 006, 2015.

[210] S. Fajfer and N. Košnik, "Vector leptoquark resolution of R_K and $R_{D^{(*)}}$ puzzles," *Phys. Lett. B*, vol. 755, pp. 270–274, 2016.

[211] M. Bauer and M. Neubert, "Minimal Leptoquark Explanation for the $R_{D^{(*)}}$, R_K , and $(g-2)_\mu$ Anomalies," *Phys. Rev. Lett.*, vol. 116, no. 14, p. 141802, 2016.

[212] R. Barbieri, G. Isidori, A. Pattori, and F. Senia, "Anomalies in B-decays and $U(2)$ flavour symmetry," *Eur. Phys. J. C*, vol. 76, no. 2, p. 67, 2016.

[213] V. Gherardi, D. Marzocca, and E. Venturini, "Low-energy phenomenology of scalar leptoquarks at one-loop accuracy," *JHEP*, vol. 01, p. 138, 2021.

[214] H. Georgi and S. L. Glashow, "Unity of all elementary-particle forces," *Phys. Rev. Lett.*, vol. 32, pp. 438–441, Feb 1974.

[215] H. Georgi, "The State of the Art—Gauge Theories," *AIP Conf. Proc.*, vol. 23, pp. 575–582, 1975.

[216] H. Fritzsch and P. Minkowski, "Unified interactions of leptons and hadrons," *Annals of Physics*, vol. 93, no. 1, pp. 193–266, 1975.

[217] S. P. Martin, "A supersymmetry primer," *Advanced Series on Directions in High Energy Physics*, pp. 1–98, Jul 1998.

[218] G. R. Farrar and P. Fayet, "Phenomenology of the Production, Decay, and Detection of New Hadronic States Associated with Supersymmetry," *Phys. Lett. B*, vol. 76, pp. 575–579, 1978.

[219] S. Dimopoulos and H. Georgi, "Softly broken supersymmetry and SU(5)," *Nuclear Physics B*, vol. 193, no. 1, pp. 150–162, 1981.

[220] S. Dimopoulos, S. Raby, and F. Wilczek, "Proton decay in supersymmetric models," *Physics Letters B*, vol. 112, no. 2, pp. 133–136, 1982.

[221] S. Weinberg, "Supersymmetry at ordinary energies. masses and conservation laws," *Phys. Rev. D*, vol. 26, pp. 287–302, Jul 1982.

[222] N. Sakai and T. Yanagida, "Proton Decay in a Class of Supersymmetric Grand Unified Models," *Nucl. Phys. B*, vol. 197, p. 533, 1982.

[223] F. Zwirner, "Observable $\Delta B = 2$ transitions without nucleon decay in a minimal supersymmetric extension of the standard model," *Physics Letters B*, vol. 132, no. 1, pp. 103–106, 1983.

[224] R. Barbieri and A. Masiero, "Supersymmetric models with low-energy baryon number violation," *Nuclear Physics B*, vol. 267, no. 3, pp. 679–689, 1986.

[225] S. Dimopoulos and L. J. Hall, "Lepton-and baryon-number violating collider signatures from supersymmetry," *Physics Letters B*, vol. 207, no. 2, pp. 210–216, 1988.

[226] L. J. Hall and M. Suzuki, "Explicit R-parity breaking in supersymmetric models," *Nuclear Physics B*, vol. 231, no. 3, pp. 419–444, 1984.

[227] S. Dawson, "R-parity breaking in supersymmetric theories," *Nuclear Physics B*, vol. 261, pp. 297–318, 1985.

[228] G. F. Giudice and R. Rattazzi, "R-parity violation and unification," *Phys. Lett. B*, vol. 406, pp. 321–327, 1997.

[229] C. Csaki, Y. Grossman, and B. Heidenreich, "MFV SUSY: A Natural Theory for R-Parity Violation," *Phys. Rev. D*, vol. 85, p. 095009, 2012.

[230] B. Bajc and L. Di Luzio, "R-parity violation in SU(5)," *JHEP*, vol. 07, p. 123, 2015.

[231] B. C. Allanach, A. Dedes, and H. K. Dreiner, "Bounds on R-parity violating couplings at the weak scale and at the GUT scale," *Phys. Rev. D*, vol. 60, p. 075014, 1999.

[232] M. Chemtob, "Phenomenological constraints on broken R parity symmetry in supersymmetry models," *Prog. Part. Nucl. Phys.*, vol. 54, pp. 71–191, 2005.

[233] R. Barbier *et al.*, "R-parity violating supersymmetry," *Phys. Rept.*, vol. 420, pp. 1–202, 2005.

[234] H. K. Dreiner, M. Kramer, and B. O'Leary, "Bounds on R-parity violating supersymmetric couplings from leptonic and semi-leptonic meson decays," *Phys. Rev. D*, vol. 75, p. 114016, 2007.

[235] P. Fileviez Perez and S. Spinner, "The Fate of R-Parity," *Phys. Rev. D*, vol. 83, p. 035004, 2011.

[236] H. K. Dreiner, K. Nickel, F. Staub, and A. Vicente, "New bounds on trilinear R-parity violation from lepton flavor violating observables," *Phys. Rev. D*, vol. 86, p. 015003, 2012.

[237] G. Ferretti and D. Karateev, "Fermionic UV completions of Composite Higgs models," *JHEP*, vol. 03, p. 077, 2014.

[238] G. Ferretti, "UV Completions of Partial Compositeness: The Case for a SU(4) Gauge Group," *JHEP*, vol. 06, p. 142, 2014.

[239] G. Cacciapaglia and F. Sannino, "Fundamental Composite (Goldstone) Higgs Dynamics," *JHEP*, vol. 04, p. 111, 2014.

[240] L. Vecchi, "A dangerous irrelevant UV-completion of the composite Higgs," *JHEP*, vol. 02, p. 094, 2017.

[241] T. Ma and G. Cacciapaglia, "Fundamental Composite 2HDM: SU(N) with 4 flavours," *JHEP*, vol. 03, p. 211, 2016.

[242] G. Ferretti, "Gauge theories of Partial Compositeness: Scenarios for Run-II of the LHC," *JHEP*, vol. 06, p. 107, 2016.

[243] F. Sannino, A. Strumia, A. Tesi, and E. Vigiani, "Fundamental partial compositeness," *JHEP*, vol. 11, p. 029, 2016.

[244] A. Agugliaro, O. Antipin, D. Becciolini, S. De Curtis, and M. Redi, "UV complete composite Higgs models," *Phys. Rev. D*, vol. 95, no. 3, p. 035019, 2017.

[245] D. Buttazzo, A. Greljo, G. Isidori, and D. Marzocca, "Toward a coherent solution of diphoton and flavor anomalies," *JHEP*, vol. 08, p. 035, 2016.

[246] D. Buttazzo, A. Greljo, G. Isidori, and D. Marzocca, "B-physics anomalies: a guide to combined explanations," *JHEP*, vol. 11, p. 044, 2017.

[247] N. Aghanim *et al.*, "Planck 2018 results. VI. Cosmological parameters," *Astron. Astrophys.*, vol. 641, p. A6, 2020. [Erratum: Astron.Astrophys. 652, C4 (2021)].

[248] F. Zwicky, "Die Rotverschiebung von extragalaktischen Nebeln," *Helvetica Physica Acta*, vol. 6, pp. 110–127, Jan. 1933.

[249] F. Zwicky, "On the Masses of Nebulae and of Clusters of Nebulae," , vol. 86, p. 217, Oct. 1937.

[250] A. V. Zasov, A. S. Saburova, A. V. Khoperskov, and S. A. Khoperskov, "Dark matter in galaxies," *Physics Uspekhi*, vol. 60, p. 3, Apr. 2017.

[251] E. Zackrisson and T. Riehm, "Gravitational Lensing as a Probe of Cold Dark Matter Subhalos," *Advances in Astronomy*, vol. 2010, p. 478910, Jan. 2010.

[252] D. Clowe, A. Gonzalez, and M. Markevitch, "Weak-Lensing Mass Reconstruction of the Interacting Cluster 1E 0657-558: Direct Evidence for the Existence of Dark Matter," , vol. 604, pp. 596–603, Apr. 2004.

[253] D. Clowe, M. Bradac, A. H. Gonzalez, M. Markevitch, S. W. Randall, C. Jones, and D. Zaritsky, "A direct empirical proof of the existence of dark matter," *Astrophys. J. Lett.*, vol. 648, pp. L109–L113, 2006.

[254] G. Bertone, D. Hooper, and J. Silk, "Particle dark matter: Evidence, candidates and constraints," *Phys. Rept.*, vol. 405, pp. 279–390, 2005.

[255] S. Hawking, "Gravitationally Collapsed Objects of Very Low Mass," *Monthly Notices of the Royal Astronomical Society*, vol. 152, pp. 75–78, 04 1971.

[256] B. J. Carr and S. W. Hawking, "Black Holes in the Early Universe," *Monthly Notices of the Royal Astronomical Society*, vol. 168, pp. 399–415, 08 1974.

[257] B. J. Carr, "The primordial black hole mass spectrum.," , vol. 201, pp. 1–19, Oct. 1975.

[258] B. Carr, F. Kuhnel, and M. Sandstad, "Primordial Black Holes as Dark Matter," *Phys. Rev. D*, vol. 94, no. 8, p. 083504, 2016.

[259] J. García-Bellido, "Massive Primordial Black Holes as Dark Matter and their detection with Gravitational Waves," *J. Phys. Conf. Ser.*, vol. 840, no. 1, p. 012032, 2017.

[260] B. Carr, K. Kohri, Y. Sendouda, and J. Yokoyama, "Constraints on primordial black holes," *Rept. Prog. Phys.*, vol. 84, no. 11, p. 116902, 2021.

[261] T. Nihei, L. Roszkowski, and R. Ruiz de Austri, "Towards an accurate calculation of the neutralino relic density," *JHEP*, vol. 05, p. 063, 2001.

[262] G. Gelmini and P. Gondolo, "DM Production Mechanisms," pp. 121–141, 9 2010.

[263] L. Baudis, "Dark matter searches," *Annalen der Physik*, vol. 528, no. 1-2, pp. 74–83, 2016.

[264] T. Cohen, K. Murase, N. L. Rodd, B. R. Safdi, and Y. Soreq, "γ -ray Constraints on Decaying Dark Matter and Implications for IceCube," *Phys. Rev. Lett.*, vol. 119, no. 2, p. 021102, 2017.

[265] M. Cirelli, N. Fornengo, and A. Strumia, "Minimal dark matter," *Nucl. Phys. B*, vol. 753, pp. 178–194, 2006.

[266] M. Cirelli, A. Strumia, and M. Tamburini, "Cosmology and Astrophysics of Minimal Dark Matter," *Nucl. Phys. B*, vol. 787, pp. 152–175, 2007.

[267] M. Cirelli and A. Strumia, "Minimal Dark Matter: Model and results," *New J. Phys.*, vol. 11, p. 105005, 2009.

[268] T. Hambye, F. S. Ling, L. Lopez Honorez, and J. Rocher, "Scalar Multiplet Dark Matter," *JHEP*, vol. 07, p. 090, 2009. [Erratum: JHEP 05, 066 (2010)].

[269] E. Del Nobile, M. Nardecchia, and P. Panci, "Millicharge or Decay: A Critical Take on Minimal Dark Matter," *JCAP*, vol. 04, p. 048, 2016.

[270] H.-C. Cheng, B. A. Dobrescu, and K. T. Matchev, "Generic and chiral extensions of the supersymmetric standard model," *Nucl. Phys. B*, vol. 543, pp. 47–72, 1999.

[271] J. L. Feng, T. Moroi, L. Randall, M. Strassler, and S.-f. Su, "Discovering supersymmetry at the Tevatron in wino LSP scenarios," *Phys. Rev. Lett.*, vol. 83, pp. 1731–1734, 1999.

[272] T. Gherghetta, G. F. Giudice, and J. D. Wells, "Phenomenological consequences of supersymmetry with anomaly induced masses," *Nucl. Phys. B*, vol. 559, pp. 27–47, 1999.

[273] M. Ibe, S. Matsumoto, and R. Sato, "Mass Splitting between Charged and Neutral Winos at Two-Loop Level," *Phys. Lett. B*, vol. 721, pp. 252–260, 2013.

[274] J. McKay and P. Scott, "Two-loop mass splittings in electroweak multiplets: winos and minimal dark matter," *Phys. Rev. D*, vol. 97, no. 5, p. 055049, 2018.

[275] M. Low and L.-T. Wang, "Neutralino dark matter at 14 TeV and 100 TeV," *JHEP*, vol. 08, p. 161, 2014.

[276] M. Cirelli, F. Sala, and M. Taoso, "Wino-like Minimal Dark Matter and future colliders," *JHEP*, vol. 10, p. 033, 2014. [Erratum: JHEP 01, 041 (2015)].

[277] R. Capdevilla, F. Meloni, R. Simoniello, and J. Zurita, "Hunting wino and higgsino dark matter at the muon collider with disappearing tracks," 2 2021.

[278] T. Han, Z. Liu, L.-T. Wang, and X. Wang, "WIMPs at High Energy Muon Colliders," *Phys. Rev. D*, vol. 103, no. 7, p. 075004, 2021.

[279] B. Audren, J. Lesgourgues, G. Mangano, P. D. Serpico, and T. Tram, "Strongest model-independent bound on the lifetime of Dark Matter," *JCAP*, vol. 12, p. 028, 2014.

[280] E. Aubourg *et al.*, "Cosmological implications of baryon acoustic oscillation measurements," *Phys. Rev. D*, vol. 92, no. 12, p. 123516, 2015.

[281] S. Ando and K. Ishiwata, "Constraints on decaying dark matter from the extragalactic gamma-ray background," *JCAP*, vol. 05, p. 024, 2015.

[282] M. Cirelli, E. Moulin, P. Panci, P. D. Serpico, and A. Viana, "Gamma ray constraints on Decaying Dark Matter," *Phys. Rev. D*, vol. 86, p. 083506, 2012.

[283] L. Di Luzio, R. Gröber, J. F. Kamenik, and M. Nardecchia, "Accidental matter at the LHC," *JHEP*, vol. 07, p. 074, 2015.

[284] K. Griest and M. Kamionkowski, "Unitarity Limits on the Mass and Radius of Dark Matter Particles," *Phys. Rev. Lett.*, vol. 64, p. 615, 1990.

[285] Y. Meng *et al.*, "Dark Matter Search Results from the PandaX-4T Commissioning Run," 7 2021.

[286] M. W. Goodman and E. Witten, "Detectability of Certain Dark Matter Candidates," *Phys. Rev. D*, vol. 31, p. 3059, 1985.

[287] E. Aprile *et al.*, "Dark Matter Search Results from a One Ton-Year Exposure of XENON1T," *Phys. Rev. Lett.*, vol. 121, no. 11, p. 111302, 2018.

[288] J. Bramante, P. J. Fox, G. D. Kribs, and A. Martin, "Inelastic frontier: Discovering dark matter at high recoil energy," *Phys. Rev. D*, vol. 94, no. 11, p. 115026, 2016.

[289] N. Song, S. Nagorny, and A. C. Vincent, "Pushing the frontier of WIMPy inelastic dark matter: Journey to the end of the periodic table," *Phys. Rev. D*, vol. 104, no. 10, p. 103032, 2021.

[290] C. Amole *et al.*, "Dark matter search results from the PICO-60 CF_3I bubble chamber," *Phys. Rev. D*, vol. 93, no. 5, p. 052014, 2016.

[291] G. Angloher *et al.*, "Results on light dark matter particles with a low-threshold CRESST-II detector," *Eur. Phys. J. C*, vol. 76, no. 1, p. 25, 2016.

[292] A. Münster *et al.*, "Radiopurity of CaWO4 crystals for direct dark matter search with CRESST and EURECA," *JCAP*, vol. 05, p. 018, 2014.

[293] J. W. Beeman *et al.*, "New experimental limits on the alpha decays of lead isotopes," *Eur. Phys. J. A*, vol. 49, p. 50, 2013.

[294] B. Lehnert, H. Ramani, M. Hult, G. Lutter, M. Pospelov, S. Rajendran, and K. Zuber, "Search for Dark Matter Induced Deexcitation of $^{180}\mathrm{Ta}^{\mathrm{m}}$," *Phys. Rev. Lett.*, vol. 124, no. 18, p. 181802, 2020.

[295] B. Broerman, M. Laubenstein, S. Nagorny, N. Song, and A. C. Vincent, "A search for rare and induced nuclear decays in hafnium," *Nucl. Phys. A*, vol. 1012, p. 122212, 2021.

[296] P. Belli *et al.*, "Search for α decay of naturally occurring osmium nuclides accompanied by γ quanta," *Phys. Rev. C*, vol. 102, no. 2, p. 024605, 2020.

[297] H. E. Haber and D. Wyler, "RADIATIVE NEUTRALINO DECAY," *Nucl. Phys. B*, vol. 323, pp. 267–310, 1989.

[298] A. Mitridate, M. Redi, J. Smirnov, and A. Strumia, "Cosmological Implications of Dark Matter Bound States," *JCAP*, vol. 05, p. 006, 2017.

[299] J. Harz and K. Petraki, "Radiative bound-state formation in unbroken perturbative non-Abelian theories and implications for dark matter," *JHEP*, vol. 07, p. 096, 2018.

[300] S. Cassel, "Sommerfeld factor for arbitrary partial wave processes," *J. Phys. G*, vol. 37, p. 105009, 2010.

[301] J. Smirnov and J. F. Beacom, "TeV-Scale Thermal WIMPs: Unitarity and its Consequences," *Phys. Rev. D*, vol. 100, no. 4, p. 043029, 2019.

[302] N. Cabibbo and R. Gatto, "Electron Positron Colliding Beam Experiments," *Phys. Rev.*, vol. 124, pp. 1577–1595, 1961.

[303] N. Cabibbo, G. Karl, and L. Wolfenstein, "A New Unitarity Bound on e+ e- Annihilation," *Phys. Lett. B*, vol. 51, pp. 387–389, 1974.

[304] L. D. Landau, *Quantum Mechanics: Non-Relativistic Theory*, vol. v.3 of *Course of Theoretical Physics*. Oxford: Butterworth-Heinemann, 1991.

[305] M. Beneke, R. Szafron, and K. Urban, "Sommerfeld-corrected relic abundance of wino dark matter with NLO electroweak potentials," *JHEP*, vol. 02, p. 020, 2021.

[306] B. Ostdiek, "Constraining the minimal dark matter fiveplet with LHC searches," , vol. 92, p. 055008, Sept. 2015.

[307] M. Low and L.-T. Wang, "Neutralino dark matter at 100 TeV," Apr 2014.

[308] European Strategy for Particle Physics Preparatory Group, "Physics Briefing Book," Oct 2019. Physics Briefing Book - Input for the European Strategy for Particle Physics Update 2020.

[309] K. Harigaya, K. Ichikawa, A. Kundu, S. Matsumoto, and S. Shirai, "Indirect probe of electroweak-interacting particles at future lepton colliders," *Journal of High Energy Physics*, vol. 9, p. 105, Sept. 2015.

[310] L. Di Luzio, R. Gröber, and G. Panico, "Probing new electroweak states via precision measurements at the LHC and future colliders," *JHEP*, vol. 01, p. 011, 2019.

[311] J. P. Delahaye, M. Diemoz, K. Long, B. Mansoulié, N. Pastrone, L. Rivkin, D. Schulte, A. Skrinsky, and A. Wulzer, "Muon Colliders," 1 2019.

[312] M. Boscolo, J. P. Delahaye, and M. Palmer, "The future prospects of muon colliders and neutrino factories," Aug 2018.

[313] R. B. Palmer, "Muon colliders," *Reviews of Accelerator Science and Technology*, vol. 07, pp. 137–159, Jan 2014.

[314] P. J. Fox, R. Harnik, J. Kopp, and Y. Tsai, "LEP Shines Light on Dark Matter," *Phys. Rev. D*, vol. 84, p. 014028, 2011.

[315] C. Bartels, M. Berggren, and J. List, "Characterising WIMPs at a future e^+e^- Linear Collider," *Eur. Phys. J. C*, vol. 72, p. 2213, 2012.

[316] J. de Blas *et al.*, "The CLIC Potential for New Physics," vol. 3/2018, 12 2018.

[317] J. Alwall, M. Herquet, F. Maltoni, O. Mattelaer, and T. Stelzer, "MadGraph 5 : Going Beyond," *JHEP*, vol. 06, p. 128, 2011.

[318] J. Alwall, R. Frederix, S. Frixione, V. Hirschi, F. Maltoni, O. Mattelaer, H. S. Shao, T. Stelzer, P. Torrielli, and M. Zaro, "The automated computation of tree-level and next-to-leading order differential cross sections, and their matching to parton shower simulations," *JHEP*, vol. 07, p. 079, 2014.

[319] S. Frixione, M. L. Mangano, P. Nason, and G. Ridolfi, "Improving the Weizsacker-Williams approximation in electron - proton collisions," *Phys. Lett. B*, vol. 319, pp. 339–345, 1993.

[320] U. Schnoor, "Long-lived particle reconstruction at CLIC," *Linear Collider Workshop 2019.*

[321] Erica Brondolin, "Disappearing tracks at CLIC," *LLP workshop 2020.*

[322] R. Capdevilla, F. Meloni, R. Simoniello, and J. Zurita, "Hunting wino and higgsino dark matter at the muon collider with disappearing tracks," Feb 2021.

[323] V. Khachatryan *et al.*, "Search for long-lived charged particles in proton-proton collisions at $\sqrt{s} = 13$ TeV," *Phys. Rev. D*, vol. 94, no. 11, p. 112004, 2016.

[324] M. Aaboud *et al.*, "Search for heavy charged long-lived particles in the ATLAS detector in 36.1 fb^{-1} of proton-proton collision data at $\sqrt{s} = 13$ TeV," *Phys. Rev. D*, vol. 99, no. 9, p. 092007, 2019.

[325] V. Lefranc, E. Moulin, P. Panci, F. Sala, and J. Silk, "Dark Matter in γ lines: Galactic Center vs dwarf galaxies," *JCAP*, vol. 09, p. 043, 2016.

[326] M. Cirelli, T. Hambye, P. Panci, F. Sala, and M. Taoso, "Gamma ray tests of Minimal Dark Matter," *JCAP*, vol. 10, p. 026, 2015.

[327] C. Garcia-Cely, A. Ibarra, A. S. Lamperstorfer, and M. H. G. Tytgat, "Gamma-rays from Heavy Minimal Dark Matter," *JCAP*, vol. 10, p. 058, 2015.

[328] M. Cirelli, G. Corcella, A. Hektor, G. Hutsi, M. Kadastik, P. Panci, M. Raidal, F. Sala, and A. Strumia, "PPPC 4 DM ID: A Poor Particle Physicist Cookbook for Dark Matter Indirect Detection," *JCAP*, vol. 03, p. 051, 2011. [Erratum: JCAP 10, E01 (2012)].

[329] L. Rinchiuso, N. L. Rodd, I. Moult, E. Moulin, M. Baumgart, T. Cohen, T. R. Slatyer, I. W. Stewart, and V. Vaidya, "Hunting for Heavy Winos in the Galactic Center," *Phys. Rev. D*, vol. 98, no. 12, p. 123014, 2018.

[330] F. Iocco, M. Pato, and G. Bertone, "Evidence for dark matter in the inner Milky Way," *Nature Phys.*, vol. 11, pp. 245–248, 2015.

[331] C. Wegg, O. Gerhard, and M. Portail, "MOA-II Galactic microlensing constraints: the inner Milky Way has a low dark matter fraction and a near maximal disc," *mnras*, vol. 463, pp. 557–570, Nov. 2016.

[332] M. Pato, F. Iocco, and G. Bertone, "Dynamical constraints on the dark matter distribution in the Milky Way," *JCAP*, vol. 12, p. 001, 2015.

[333] Y. Huang, X. W. Liu, H. B. Yuan, M. S. Xiang, H. W. Zhang, B. Q. Chen, J. J. Ren, C. Wang, Y. Zhang, Y. H. Hou, Y. F. Wang, and Z. H. Cao, "The Milky Way's rotation curve out to 100 kpc and its constraint on the Galactic mass distribution," *mnras*, vol. 463, pp. 2623–2639, Dec. 2016.

[334] V. Lefranc, G. A. Mamon, and P. Panci, "Prospects for annihilating Dark Matter towards Milky Way's dwarf galaxies by the Cherenkov Telescope Array," *JCAP*, vol. 09, p. 021, 2016.

[335] P. Ullio and M. Valli, "A critical reassessment of particle Dark Matter limits from dwarf satellites," *JCAP*, vol. 07, p. 025, 2016.

[336] K. Hayashi, K. Ichikawa, S. Matsumoto, M. Ibe, M. N. Ishigaki, and H. Sugai, "Dark matter annihilation and decay from non-spherical dark halos in galactic dwarf satellites," *Mon. Not. Roy. Astron. Soc.*, vol. 461, no. 3, pp. 2914–2928, 2016.

[337] M. Baumgart, T. Cohen, I. Moult, N. L. Rodd, T. R. Slatyer, M. P. Solon, I. W. Stewart, and V. Vaidya, "Resummed Photon Spectra for WIMP Annihilation," *JHEP*, vol. 03, p. 117, 2018.

[338] A. Hryczuk and R. Iengo, "The one-loop and Sommerfeld electroweak corrections to the Wino dark matter annihilation," *JHEP*, vol. 01, p. 163, 2012. [Erratum: JHEP 06, 137 (2012)].

[339] G. Ovanesyan, T. R. Slatyer, and I. W. Stewart, "Heavy Dark Matter Annihilation from Effective Field Theory," *Phys. Rev. Lett.*, vol. 114, no. 21, p. 211302, 2015.

[340] M. Baumgart, I. Z. Rothstein, and V. Vaidya, "Constraints on Galactic Wino Densities from Gamma Ray Lines," *JHEP*, vol. 04, p. 106, 2015.

[341] M. Baumgart and V. Vaidya, "Semi-inclusive wino and higgsino annihilation to LL'," *JHEP*, vol. 03, p. 213, 2016.

[342] G. Ovanesyan, N. L. Rodd, T. R. Slatyer, and I. W. Stewart, "One-loop correction to heavy dark matter annihilation," *Phys. Rev. D*, vol. 95, no. 5, p. 055001, 2017. [Erratum: Phys.Rev.D 100, 119901 (2019)].

[343] H. Abdalla *et al.*, "Searches for gamma-ray lines and 'pure WIMP' spectra from Dark Matter annihilations in dwarf galaxies with H.E.S.S," *JCAP*, vol. 11, p. 037, 2018.

[344] R. Mahbubani, M. Redi, and A. Tesi, "Indirect detection of composite asymmetric dark matter," *Phys. Rev. D*, vol. 101, no. 10, p. 103037, 2020.

[345] E. Aprile *et al.*, "Dark Matter Search Results from a One Ton-Year Exposure of XENON1T," *Phys. Rev. Lett.*, vol. 121, no. 11, p. 111302, 2018.

[346] B. J. Mount *et al.*, "LUX-ZEPLIN (LZ) Technical Design Report," 3 2017.

[347] J. Aalbers *et al.*, "DARWIN: towards the ultimate dark matter detector," *JCAP*, vol. 11, p. 017, 2016.

[348] J. Billard, L. Strigari, and E. Figueroa-Feliciano, "Implication of neutrino backgrounds on the reach of next generation dark matter direct detection experiments," *Phys. Rev. D*, vol. 89, no. 2, p. 023524, 2014.

[349] E. Aprile *et al.*, "Projected WIMP sensitivity of the XENONnT dark matter experiment," *JCAP*, vol. 11, p. 031, 2020.

[350] J. Hisano, S. Matsumoto, M. M. Nojiri, and O. Saito, "Direct detection of the Wino and Higgsino-like neutralino dark matters at one-loop level," *Phys. Rev. D*, vol. 71, p. 015007, 2005.

[351] J. Hisano, K. Ishiwata, and N. Nagata, "A complete calculation for direct detection of Wino dark matter," *Phys. Lett. B*, vol. 690, pp. 311–315, 2010.

[352] M. Cirelli, E. Del Nobile, and P. Panci, "Tools for model-independent bounds in direct dark matter searches," *JCAP*, vol. 10, p. 019, 2013.

[353] J. Hisano, K. Ishiwata, N. Nagata, and T. Takesako, "Direct Detection of Electroweak-Interacting Dark Matter," *JHEP*, vol. 07, p. 005, 2011.

[354] J. Hisano, K. Ishiwata, and N. Nagata, "QCD Effects on Direct Detection of Wino Dark Matter," *JHEP*, vol. 06, p. 097, 2015.

[355] C. Alexandrou, V. Drach, K. Jansen, C. Kallidonis, and G. Koutsou, "Baryon spectrum with $N_f = 2 + 1 + 1$ twisted mass fermions," *Phys. Rev. D*, vol. 90, no. 7, p. 074501, 2014.

[356] W. Freeman and D. Toussaint, "Intrinsic strangeness and charm of the nucleon using improved staggered fermions," *Phys. Rev. D*, vol. 88, p. 054503, 2013.

[357] T. Katayose, S. Matsumoto, S. Shirai, and Y. Watanabe, "Thermal Real Scalar Triplet Dark Matter," 5 2021.

[358] G. Arcadi, A. Djouadi, and M. Raidal, "Dark Matter through the Higgs portal," *Phys. Rept.*, vol. 842, pp. 1–180, 2020.

[359] T. Hambye, "Hidden vector dark matter," *JHEP*, vol. 01, p. 028, 2009.

[360] F. D'Eramo and J. Thaler, "Semi-annihilation of Dark Matter," *JHEP*, vol. 06, p. 109, 2010.

[361] T. Bringmann, P. F. Depta, M. Hufnagel, J. T. Ruderman, and K. Schmidt-Hoberg, "Dark Matter from Exponential Growth," *Phys. Rev. Lett.*, vol. 127, no. 19, p. 191802, 2021.

[362] M. Farina, D. Pappadopulo, J. T. Ruderman, and G. Trevisan, "Phases of Cannibal Dark Matter," *JHEP*, vol. 12, p. 039, 2016.

[363] R. Mandal, "Fermionic dark matter in leptoquark portal," *Eur. Phys. J. C*, vol. 78, no. 9, p. 726, 2018.

[364] M. J. Baker, D. A. Faroughy, and S. Trifinopoulos, "Collider signatures of coannihilating dark matter in light of the B-physics anomalies," *JHEP*, vol. 11, p. 084, 2021.

[365] G. Belanger *et al.*, "Leptoquark manoeuvres in the dark: a simultaneous solution of the dark matter problem and the $R_{D^{(*)}}$ anomalies," *JHEP*, vol. 02, p. 042, 2022.

[366] R. Essig, E. Kuflik, S. D. McDermott, T. Volansky, and K. M. Zurek, "Constraining Light Dark Matter with Diffuse X-Ray and Gamma-Ray Observations," *JHEP*, vol. 11, p. 193, 2013.

[367] M. Boudaud, J. Lavalle, and P. Salati, "Novel cosmic-ray electron and positron constraints on MeV dark matter particles," *Phys. Rev. Lett.*, vol. 119, no. 2, p. 021103, 2017.

[368] H. Liu, W. Qin, G. W. Ridgway, and T. R. Slatyer, "Lyman-α constraints on cosmic heating from dark matter annihilation and decay," *Phys. Rev. D*, vol. 104, no. 4, p. 043514, 2021.

[369] L. J. Hall, K. Jedamzik, J. March-Russell, and S. M. West, "Freeze-In Production of FIMP Dark Matter," *JHEP*, vol. 03, p. 080, 2010.

[370] A. Boyarsky, M. Drewes, T. Lasserre, S. Mertens, and O. Ruchayskiy, "Sterile neutrino Dark Matter," *Prog. Part. Nucl. Phys.*, vol. 104, pp. 1–45, 2019.

[371] W. Altmannshofer and P. Stangl, "New physics in rare B decays after Moriond 2021," *Eur. Phys. J. C*, vol. 81, no. 10, p. 952, 2021.

[372] F. del Aguila, S. Bar-Shalom, A. Soni, and J. Wudka, "Heavy Majorana Neutrinos in the Effective Lagrangian Description: Application to Hadron Colliders," *Phys. Lett. B*, vol. 670, pp. 399–402, 2009.

[373] T. R. Slatyer and C.-L. Wu, "General Constraints on Dark Matter Decay from the Cosmic Microwave Background," *Phys. Rev. D*, vol. 95, no. 2, p. 023010, 2017.

[374] G. Aad *et al.*, "Search for a heavy charged boson in events with a charged lepton and missing transverse momentum from pp collisions at $\sqrt{s} = 13$ TeV with the ATLAS detector," *Phys. Rev. D*, vol. 100, no. 5, p. 052013, 2019.

[375] J. Alwall, R. Frederix, S. Frixione, V. Hirschi, F. Maltoni, O. Mattelaer, H. S. Shao, T. Stelzer, P. Torrielli, and M. Zaro, "The automated computation of tree-level and next-to-leading order differential cross sections, and their matching to parton shower simulations," *JHEP*, vol. 07, p. 079, 2014.

[376] A. Salvio, P. Lodone, and A. Strumia, "Towards leptogenesis at NLO: the right-handed neutrino interaction rate," *JHEP*, vol. 08, p. 116, 2011.

[377] G. Jackson and M. Laine, "Efficient numerical integration of thermal interaction rates," *JHEP*, vol. 09, p. 125, 2021.

[378] B. Bhattacharya, A. Datta, J.-P. Guévin, D. London, and R. Watanabe, "Simultaneous Explanation of the R_K and $R_{D^{(*)}}$ Puzzles: a Model Analysis," *JHEP*, vol. 01, p. 015, 2017.

[379] A. Greljo, G. Isidori, and D. Marzocca, "On the breaking of Lepton Flavor Universality in B decays," *JHEP*, vol. 07, p. 142, 2015.

[380] J. Kumar, D. London, and R. Watanabe, "Combined Explanations of the $b \to s\mu^+\mu^-$ and $b \to c\tau^-\bar{\nu}$ Anomalies: a General Model Analysis," *Phys. Rev. D*, vol. 99, no. 1, p. 015007, 2019.

[381] M. Bordone, C. Cornella, J. Fuentes-Martin, and G. Isidori, "A three-site gauge model for flavor hierarchies and flavor anomalies," *Phys. Lett. B*, vol. 779, pp. 317–323, 2018.

[382] A. Greljo and B. A. Stefanek, "Third family quark–lepton unification at the TeV scale," *Phys. Lett. B*, vol. 782, pp. 131–138, 2018.

[383] J. Fuentes-Martin, G. Isidori, J. Pagès, and B. A. Stefanek, "Flavor non-universal Pati-Salam unification and neutrino masses," *Phys. Lett. B*, vol. 820, p. 136484, 2021.

[384] C. Froggatt and H. Nielsen, "Hierarchy of quark masses, cabibbo angles and CP violation," *Nuclear Physics B*, vol. 147, no. 3, pp. 277–298, 1979.

[385] D. B. Kaplan, "Flavor at ssc energies: A new mechanism for dynamically generated fermion masses," *Nuclear Physics B*, vol. 365, no. 2, pp. 259–278, 1991.

[386] R. Contino, T. Kramer, M. Son, and R. Sundrum, "Warped/composite phenomenology simplified," *JHEP*, vol. 05, p. 074, 2007.

[387] K. Agashe, G. Perez, and A. Soni, "Flavor structure of warped extra dimension models," *Phys. Rev. D*, vol. 71, p. 016002, 2005.

[388] B. Sekhar Chivukula and H. Georgi, "Composite-technicolor standard model," *Physics Letters B*, vol. 188, no. 1, pp. 99–104, 1987.

[389] L. J. Hall and L. Randall, "Weak-scale effective supersymmetry," *Phys. Rev. Lett.*, vol. 65, pp. 2939–2942, Dec 1990.

[390] R. Barbieri, D. Buttazzo, F. Sala, and D. M. Straub, "Flavour physics from an approximate $U(2)^3$ symmetry," *JHEP*, vol. 07, p. 181, 2012.

[391] A. Kusenko, "Sterile neutrinos, dark matter, and the pulsar velocities in models with a Higgs singlet," *Phys. Rev. Lett.*, vol. 97, p. 241301, 2006.

[392] A. Czarnecki, W. J. Marciano, and A. Sirlin, "Neutron Lifetime and Axial Coupling Connection," *Phys. Rev. Lett.*, vol. 120, no. 20, p. 202002, 2018.

[393] J. A. Dror, G. Elor, and R. Mcgehee, "Absorption of Fermionic Dark Matter by Nuclear Targets," *JHEP*, vol. 02, p. 134, 2020.

[394] E. Aprile *et al.*, "Excess electronic recoil events in XENON1T," *Phys. Rev. D*, vol. 102, no. 7, p. 072004, 2020.

[395] S. Haselschwardt, B. Lenardo, P. Pirinen, and J. Suhonen, "Solar neutrino detection in liquid xenon detectors via charged-current scattering to excited states," *Phys. Rev. D*, vol. 102, no. 7, p. 072009, 2020.

[396] E. Bulbul, M. Markevitch, A. Foster, R. K. Smith, M. Loewenstein, and S. W. Randall, "Detection of An Unidentified Emission Line in the Stacked X-ray spectrum of Galaxy Clusters," *Astrophys. J.*, vol. 789, p. 13, 2014.

[397] A. Boyarsky, O. Ruchayskiy, D. Iakubovskyi, and J. Franse, "Unidentified Line in X-Ray Spectra of the Andromeda Galaxy and Perseus Galaxy Cluster," *Phys. Rev. Lett.*, vol. 113, p. 251301, 2014.

[398] L. Covi, J. E. Kim, and L. Roszkowski, "Axinos as cold dark matter," *Phys. Rev. Lett.*, vol. 82, pp. 4180–4183, 1999.

[399] J. L. Feng, A. Rajaraman, and F. Takayama, "SuperWIMP dark matter signals from the early universe," *Phys. Rev. D*, vol. 68, p. 063504, 2003.

[400] N. Isgur and M. B. Wise, "WEAK TRANSITION FORM-FACTORS BETWEEN HEAVY MESONS," *Phys. Lett. B*, vol. 237, pp. 527–530, 1990.

[401] D. Bernecker and H. B. Meyer, "Vector Correlators in Lattice QCD: Methods and applications," *Eur. Phys. J. A*, vol. 47, p. 148, 2011.

[402] D. Giusti, V. Lubicz, G. Martinelli, F. Sanfilippo, and S. Simula, "Strange and charm HVP contributions to the muon $(g-2)$ including QED corrections with twisted-mass fermions," *JHEP*, vol. 10, p. 157, 2017.

[403] M. Bochicchio, L. Maiani, G. Martinelli, G. Rossi, and M. Testa, "Chiral symmetry on the lattice with wilson fermions," *Nuclear Physics B*, vol. 262, no. 2, pp. 331–355, 1985.

[404] F. Burger, G. Hotzel, K. Jansen, and M. Petschlies, "The hadronic vacuum polarization and automatic $\mathcal{O}(a)$ improvement for twisted mass fermions," *JHEP*, vol. 03, p. 073, 2015.

[405] M. Constantinou, M. Costa, M. Göckeler, R. Horsley, H. Panagopoulos, H. Perlt, P. E. L. Rakow, G. Schierholz, and A. Schiller, "Perturbatively improving regularization-invariant momentum scheme renormalization constants," *Phys. Rev. D*, vol. 87, no. 9, p. 096019, 2013.

[406] S. Scherer and M. R. Schindler, "A Chiral perturbation theory primer," 5 2005.